Thermal and Mechanical Response of Curved Composite Panels

Nicole L. Breivik

Dissertation submitted to the Faculty of the Virginia Polytechnic Institute and State University in partial fufillment of the requirements for the degree of

Doctor of Philosophy
in
Engineering Mechanics

Michael W. Hyer, Chair
Mark S. Cramer
O. Hayden Griffin, Jr.
Zafer Gürdal
Elaine P. Scott

June 4, 1997
Blacksburg, VA

Keywords: buckling, postbuckling, thermal structures, nonlinear response, imperfections

Thermal and Mechanical Response of Curved Composite Panels

Nicole L. Breivik

(ABSTRACT)

Curved panels constructed of laminated graphite-epoxy composite material are of potential interest in airframe fuselage applications. An understanding of structural response at elevated temperatures is required for anticipated future high speed aircraft applications. This study concentrates on the response of unstiffened, curved composite panels subjected to combinations of thermal and mechanical loading conditions. Mechanical loading is due to compressive end-shortening and thermal loading is due to a uniform temperature increase. Thermal stresses, which are induced by mechanical restraints against thermal expansions or contractions, cause buckling and postbuckling panel responses. Panels with three different lamination sequences are considered, including a quasi-isotropic laminate, an axially soft laminate, and an axially stiff laminate. These panels were chosen because they exhibit a range of stiffnesses and a wide variation in laminate coefficients of thermal expansion. The panels have dimensions of 10 in. by 10 in. with a base radius of 60 in. The base boundary conditions are clamped along the curved ends, and simply supported along the straight edges. Three methods are employed to study the panel response, including a geometrically nonlinear Rayleigh-Ritz solution, a finite element solution using the commercially available code STAGS, and an experimental program. The effects of inplane boundary conditions and radius of curvature are studied analytically, along with consideration of order of application in combined loading. A substantial difference is noted in the nonlinear load vs. axial strain

responses of panels loaded in end-shortening and panels loaded with uniform temperature change, depending on the specific lamination sequence, boundary conditions, and radius of curvature. Experiments are conducted and results are presented for both room temperature end-shortening tests and elevated temperature tests with accompanying end-shortening. The base finite element model is modified to include measured panel thicknesses, boundary conditions representative of the experimental apparatus, measured initial geometric imperfections, and measured temperature gradients. With these modifications, and including an inherent end displacement of the panel present during thermal loading, good correlation is obtained between the experimental and numerically predicted load vs. axial strain responses from initial loading through postbuckling.

Acknowledgments

Table of Contents

Table of Contents

Table of Contents

List of Figures

List of Figures

List of Figures

List of Figures

List of Figures

List of Tables

List of Tables

Chapter 1 - Introduction

Future high-speed supersonic civil aircraft are expected to operate in an elevated temperature environment, resulting in simultaneous thermal and mechanical loading [1]. In order to reduce overall weight and cost of the aircraft, organic matrix composites appear to be an attractive option for both wing and fuselage structures. Simulating fuselage sections between stringers, this study concentrates on the geometrically nonlinear response of unstiffened, curved, laminated graphite-epoxy composite panels. Geometrically nonlinear response is considered because buckling and postbuckling behavior are felt to be the most important response of such panels. Thermal stresses, which are induced by mechanical restraints against thermal expansions or contractions, cause buckling and postbuckling behavior. Response due to thermal stresses at temperatures up to 350°F is of particular interest. Mechanical loading in the form of end-shortening is considered separately for comparison to thermal loading response, and in combination with elevated temperatures to better simulate an actual loading environment. Understanding the interaction of thermal expansion and Poisson's expansion is key to understanding the behavior of such structures.

Literature relevant to this study includes the buckling response of curved panels due to both axial compression and thermal stresses. A review of this literature follows, along with a review of some recent summary papers on the topic of thermal structural response. Although little has been published recently in the area of thermal structural testing, a review of past studies is included here.

1.1 Literature Survey

Although axial compression of flat plates and complete circular cylinders has been considered extensively in the literature, the response of cylindrically curved panels has received less attention. The study of curved panels incorporates substantially different issues than the study of either flat panels or complete circular cylinders, requiring coupling of membrane and bending in the equilibrium equations and boundary conditions on four edges. Therefore, the literature surveyed for this study is focused on the response of cylindrically curved panels to axial compression and/or thermal stresses.

Chapter 1 - Introduction

1.1.1 Thermal Response Review Papers

A number of review papers which detail progress in thermal-structural interaction have appeared in recent years. Thorton [2] considered advancements in high temperature structures from a historical perspective through 1990. A number of future research directions were suggested, including the need for further experimental studies at elevated temperatures. Tauchert [3] reviewed the response of flat plates to thermal loading in studies conducted prior to 1991. References were included on thermally induced bending, bucking, postbuckling, and vibrations. Noor and Burton [4] reviewed thermal modeling approaches for both flat plates and shell structures, with an emphasis on multilayered composite structures. A variety of applications, including heat transfer, curing stresses, buckling, vibration, and transient problems, were included. A review focusing on the thermal buckling characteristics of plates and shells was published by Thorton [5] in 1993. An examination of experimental studies up to that time revealed very limited data, and lacked any results for composite shells.

1.1.2 Axial Compression of Curved Panels

The buckling response of curved panels has been considered either in terms of a bifurcation buckling analysis, or by solution of the geometrically nonlinear equilibrium equations. Linear bifurcation buckling analyses often begin by assuming a membrane prebuckling solution, as occurs for flat plates.

Early studies on the response of isotropic cylindrically curved panels were based on the shell equations formulated by Donnell [6] in terms of radial displacement and a stress function. Levy [7] considered a Fourier series bifurcation buckling solution for a panel of infinite length with simply supported edges. Leggett [8] used linear bifurcation buckling equations in terms of displacements to study the response of an infinite length panel with either clamped or simply supported sides. Koiter [9] presented an exact bifurcation buckling solution for an isotropic curved panel with all four edges simply supported. Initial geometric imperfections were included in the form of the first buckling mode. An initial postbuckling theory was presented based on the sign of the second derivative of the total potential energy in the vicinity of buckling. Tamate and Sekine [10] presented an approximate solution to the geometrically nonlinear equilibrium equations based on Galerkin's method for very shallow, simply supported panels under compression. Due to the shallow geometry, postbuckling response was stable so solution beyond buckling was presented with no particular difficulties. Hsueh and Chajes [11] considered linear bifurcation buckling of curved panels with 8 different sets of boundary conditions using a finite difference solution

scheme. Postbuckling was studied using geometrically nonlinear Donnell-type equilibrium equations with initial geometric imperfections.

Early studies on the buckling response of curved composite panels were conducted by Wilkins [12, 13]. Experimental end conditions were clamped, and straight edges were either simply supported or clamped. Results were compared to an approximate linear bifurcation buckling analysis based on a Rayleigh-Ritz solution for clamped ends and simply supported straight edges. Analytical predictions were substantially higher than experimentally measured collapse loads. Soldatos and Tzivanidis [14] presented an exact linear buckling solution for the special case of cross-ply laminates with simply supported edges. Donnell shell theory and membrane prebuckling response was assumed. Soldatos [15] later expanded the study to incorporate the effects of transverse shear deformations and angle ply stacking sequence, which required Galerkin's method to obtain a solution. Whitney [16] presented linear bifurcation buckling solutions for two types of simple support boundary conditions. An approximate Galerkin's method was required for general laminates, but for specially orthotropic laminates the solution was reduced to an exact linear buckling solution. Reddy and Liu [17] expanded on this exact solution using Sander's shell theory [18] and incorporating the effects of parabolically distributed transverse shear strains. Palazotto and Linnemann [19] used the formulation presented by Reddy and Liu [17] with a modified Galerkin's solution technique to study the linear bifurcation buckling of cross-ply and angle-ply laminates. Hui [20] considered linear bifurcation buckling of cross-ply laminates with simply supported edges and applied Koiter's initial postbuckling theory.

Solution of the geometrically nonlinear equilibrium equations can also lead to a buckling solution. Satyamurthy, Khot, and Bauld [21], Bauld and Khot [22], and Khot and Bauld [23] noted that buckling of curved panels may be due to a bifurcation, a limit point, or excessive displacements, and a geometrically nonlinear analysis is required to predict buckling that is not attributed to bifurcation. A finite difference code based on Sander's nonlinear shell theory was presented. Measured imperfections were incorporated into the model [22] to improve correlation with experimentally determined load vs. end-shortening response. Becker, Palazotto, and Khot [24] compared experimental buckling loads to buckling predictions from linear bifurcation and nonlinear collapse analyses conducted with a finite element program. Nonlinear analysis with assumed geometric imperfections provided the best correlation. Zhang and Matthews [25, 26] presented a nonlinear solution, formulated in terms of radial displacement and a stress function, for a curved panel with simply supported boundary conditions. The effects of assumed geometric imperfections were included. Snell and Morley [27] compared linear and nonlinear analyses to experimen-

tally determined buckling loads and load vs. end-shortening responses for panels with general symmetric stacking. Nonlinear analysis resulted in better agreement with experiments than linear analysis methods. The effects of initial imperfections were studied both analytically and experimentally, by intentionally manufacturing panels with known geometric shape imperfections. Imperfections of magnitudes up to one half of the panel thickness had little effect on the buckling load. Kobayashi, Sumihara, and Koyama [28] compared experimental buckling loads and load vs. end-shortening responses to a nonlinear 1-mode Galerkin solution and a nonlinear finite element solution. Good agreement was obtained between the finite element solution and experimentally determined buckling load. Knight and Starnes [29] used a geometrically nonlinear finite element model to predict the postbuckling response of symmetric laminated curved panels. Load vs. end-shortening numerical results and postbuckling mode predictions compared favorably to experiments. The nonlinear analysis included measured geometric imperfections and used Riks' method [30] to obtain solutions beyond the nonlinear collapse load.

1.1.3 Thermal Response of Curved Panels

The thermal buckling response of doubly curved isotropic panels was studied by Mahayni [31] using Galerkin's method to solve nonlinear equilibrium equations. A nonuniform temperature distribution was considered along with two types of simple support boundary conditions, one with tangential edge restraint and one without. It was found that both boundary conditions resulted in snap-buckling, with a lower value in critical temperature when the edges were free to translate in the tangential directions.

The thermal response of laminated composite panels can be studied using linear equilibrium equations to find deformations and stresses below the level of buckling. Birman, Bert, and Elishakoff [32] studied the linear prebuckling response of composite cylindrical panels subjected to thermal loading. Specially orthotropic panels were considered using Galerkin's method with simple support boundary conditions and a parabolic temperature distribution. Khdeir, Rajab, and Reddy [33] also studied the linear prebuckling deformations of specially orthotropic panels, this time using Levy's method to determine the effects of variations in the boundary conditions along two opposite edges. A higher order shear deformation theory was compared to first order shear deformation theory and classical theory.

Thermal buckling of laminated composite cylindrical panels was studied by Chen and Chen [34], using a linear bifurcation analysis. For loading due to a uniform change in temperature, a membrane prebuckling solution was assumed, and Galerkin's method was used to solve the buckling

equations. Both clamped and simply supported boundary conditions were considered. Chen and Chen [35] improved on their previous study by including a nonlinear prestress solution with a nonuniform thermal gradient, and using the finite element method to find the bifurcation point. Chandrashekhara [36] considers linear bifurcation buckling accounting for transverse shear deformations by using a finite element solution. Chang and Chui [37] used a higher order transverse shear deformation theory in conjunction with the finite element method to study bifurcation buckling due to a uniform temperature change. A nonlinear prestress solution was used for the study of simply supported, angle-ply laminates.

For thermal buckling due to a limit point or excessive deformations, a geometrically nonlinear analysis is required. Huang and Tauchert [38] used the finite element method to conduct a geometrically nonlinear analysis that incorporated Riks' method to allow solution into the postbuckling region. Depending on the panel geometry, it was noted that either limit point or bifurcation buckling might occur. Kossira and Haupt [39] conducted a geometrically nonlinear analysis using the finite element method to study the effects of nonuniform temperature distributions and shear loading on an angle-ply laminate. Averill and Reddy [40] used a higher order shear deformation theory with the finite element method to study postbuckling of cylindrical panels subjected to uniform temperature distribution and a transverse normal strain at the panel edges. The effect of restricting transverse normal strain was to reduce the center deflection of the panel, as compared to previous studies which neglected this strain. Patlashenko and Weller [41] used a spline collocation solution method with a geometrically nonlinear formulation including transverse shear deformations. Temperature dependent material properties and initial geometric imperfections were found to reduce the buckling loads due to either axial compression or uniform temperature change. Librescu et al. [42] considered the effect of nonuniform temperature distributions, compressive edge loads, and transverse pressure on transversely isotropic three-layer panels. Simple support boundary conditions with different levels of tangential restraint were studied using Galerkin's method for solution of the geometrically nonlinear equilibrium equations.

The geometrically nonlinear thermal response of composite cylindrical panels with a hole was considered by Madenci and Barut [43] using the finite element method. Noor, Starnes and Peters [44] considered combined thermal loading and compressive end shortening of a composite cylindrical panel with a hole. The finite element method was used to study postbuckling response and the effect of variations in panel geometry and laminate stacking sequence.

Chapter 1 - Introduction

1.1.4 Thermal-Structural Testing

Early work in the area of thermal structural testing was concerned both with structural response and appropriate measurement techniques. Heldenfels and Roberts [45] present results for flat aluminum-alloy panels heated along a centerline with parallel edges water cooled to provide an inplane thermal gradient. A technique is presented for measurement of the thermal response characteristics of wire strain gages by initial uniform heating of the test panel. Measured thermal stresses correlate well with theoretical stresses.

After Heldenfels and Roberts, thermal structural testing focused primarily on the response of unstiffened isotropic cylinders to non-uniform heating. In 1959, Hill [46] conducted thermal buckling tests on simply supported aluminum and steel cylinders heated along a 1 in. wide axial strip. Heating was accomplished using two quartz lamps in the interior of the 4 ft. long by 10.375 in. diameter cylinders. Cylinders were heated quickly until buckling occurred. Johns [47] reports experimental results for thermal buckling of a steel cylinder with clamped ends and an axially varying temperature distribution. A rare study on stiffened cylinders was presented by Anderson and Card [48], who tested stainless steel ring-stiffened cylinders in pure bending then applied a nonuniform temperature distribution until buckling occurred. Cylinders were 45.75 in. long with 19 in. diameters and either five or nine ring stiffeners. Two heating schemes were achieved by selective placement of axially aligned quartz lamp heaters around the circumference of the cylinders. The first configuration involved heating only the portion of the cylinder circumference that was under compressive stresses during bending, while the other configuration used equally spaced lamps all the way around the circumference to achieve circumferentially uniform heating. All heating was conducted rapidly to achieve a thermal gradient in the skin and between the skin and stiffeners of the stiffened cylinders.

Returning to unstiffened shells, Ross, Mayers, and Jaworski [49] extended the study by Hill on the buckling of cylinders heated along an axial strip to include strips of various widths. Heating was from both interior and exterior quartz lamps. Different widths of black strips were painted on the surface of the cylinder to obtain different heating widths. Ross, Hoff, and Horton [50] considered uniformly heated cylinders with the ends restricted from axial expansion and circumferential expansion, resulting in compressive thermal stresses that eventually led to buckling. The 48 in. long by 10.375 in. diameter stainless steel and cold-rolled steel cylinders were heated rapidly using interior quartz lamp heaters. Although the cylinders were found to buckle at the same stress whether the load was applied as axial compression or thermal stress, the temperatures that produced the buckling stress were higher than the predictions from linear theory due the substantial

circumferential expansion that occurs with uniform heating. In an analytical study by Bushnell and Smith [51], a finite difference based code called BOSOR3 was used to interpret some of the experimental results published in refs. [46], [48], [49], and [50].

Somewhat more recently, Frum and Baruch [52] studied combined thermal and mechanical loading for clamped cylindrical shells preloaded in axial compression, then heated along two opposite generators. Results are presented for 46 tests on aluminum-alloy cylinders that were 26.4 in. long, 0.025 in. thick, and had a diameter of 15.0 in. After an initial axial preload, additional end-displacement during heating was prevented by making manual corrections. The amount of axial displacement during heating was found to significantly effect the buckling results. Ari-Bur, Baruch, and Singer [53] continued this study by adding torsional preloading. Aluminum-alloy cylinders of the same dimensions as ref. [52] were used, with the testing apparatus modified slightly to allow for the introduction of torque. For small torques, the critical temperature was not significantly affected. For medium torques, a buckling mode interaction of local and torsional patterns was believed to have contributed to the observed decrease in buckling temperatures. For large torques, the buckling mode was torsional and the buckling temperatures were further reduced.

Combined thermal and mechanical loading was addressed for a flat stiffened panel by Percy and Fields [54] for a 24 in. square titanium hat-stiffened panel. Uniform heating to 500°F was achieved using quartz lamps inside a ceramic insulation box. For some tests, an inplane temperature gradient was applied by use of heated and water-cooled platens. The panel and heating apparatus were placed within a hydraulic uniaxial load frame in order to apply axial compression. Testing was stopped prior to buckling so that additional tests could be conducted with the same panel, though buckling was estimated from strain gage bending data. Linear predictions using a finite element model compared well to the estimated buckling loads. Extending this study to composite materials, Thompson and Richards [55] tested a 24 in. square titanium matrix composite hat-stiffened panel using the methods developed for the titanium panel. Heating to 500°F and 1200°F was achieved, and the resulting temperature gradient was measured. Tests were conducted by first allowing the panel to reach an equilibrium temperature, then applying a compressive load, with data presented only after an equilibrium temperature had been achieved. Correlation to analysis was not presented.

Returning to the problem initially proposed in ref. [45], Thorton, Coyle and McLeod [56] conducted tests of flat panels which were heated transiently along their centerlines while two parallel edges were water cooled to maintain a constant temperature. Test panels measured 10 in. wide by 15 in. long measured parallel to the lamp, with a 0.125 in. thickness. Except for the heated center-

line strip, the remainder of the panel was thermally insulated from the outside environment. Results demonstrated that localized heating can result in buckling and substantial out-of-plane deformation for freely supported flat panels.

1.2 Objective and Approach

Experimental results for the thermal buckling response of curved composite panels are not available in the open literature. Although numerous analytical results have been presented, the effects of boundary conditions, stacking sequence, and curvature are not fully understood in the context of cylindrically curved panels subjected to thermal loading. Room temperature experimental results are available for the end-shortening of curved panels with clamped curved ends and simply supported straight edges, along with successful nonlinear analyses using the finite element method, although this method often obscures the equations required to formulate the problem. Less cumbersome but equally accurate approximate solutions have not been presented.

The objective of the present work is to study the thermal, mechanical, and combined thermal/mechanical response of curved laminated composite panels. Three different laminates, $[\pm45/0/90]_s$, $[\pm45/90_2]_s$, and $[\pm45/0_2]_s$, are considered. The effects of inplane boundary conditions and radius of curvature are considered, along with the effects of combined loading, including consideration of the order of application of the combined loading. An approximate solution to the geometrically nonlinear response problem, based on the Rayleigh-Ritz approach, is presented for a shallow curved panels with clamped curved ends and simply supported straight edges. Numerical results based on the STAGS finite element code [57] are presented to provide comparison with the Rayleigh-Ritz solution, and to provide additional insight into the problem by considering several boundary conditions and several radii of curvature. As part of this study, ten curved panels were fabricated and tested at room temperature and elevated temperatures. A fixture was constructed for supporting the panels and mechanically loading them by way of end-shortening. An insulated and heated enclosure, in addition to the support fixtures, provided a temperature increase to the panels so that thermal loading, combined with mechanical loading, could be studied. Experimental results are presented and compared to predictions from the finite element analysis.

The formulation of the specific problem is presented in Chapter 2. A simplified linear bifurcation buckling solution is presented that is used as a basis for comparison with the nonlinear solutions obtained using the Rayleigh-Ritz method and the finite element program STAGS. The approximate nonlinear Rayleigh-Ritz solution is described, along with some theory behind the selected finite element analyses. Convergence of the Rayleigh-Ritz solution is discussed in Appendix A.

Chapter 1 - Introduction

Analytical results are presented in Chapter 3, including results from the simplified linear solution, results from the Rayleigh-Ritz solution, and finite element results. End-shortening and uniform temperature change are considered for three stacking sequences and variations of the boundary conditions. Additional parametric studies are presented on the effects of radius and combined thermal and mechanical loading.

The experimental apparatus and procedure are described in Chapter 4, and experimental results are presented. The measured geometric shape imperfections are discussed in Appendix B, and measured thermal gradients are presented in Appendix C.

Chapter 5 begins with an analytical study of modeling refinements that became necessary due to the nature of the experimental apparatus. These include modified boundary conditions to represent the finite dimensions of the support fixtures, measured thicknesses, measured geometric imperfections and measured temperature gradients. Analytical predictions which incorporate these modeling refinements are compared to the experimental responses.

Concluding remarks are presented in Chapter 6 regarding the analytical parametric studies, the experimental results, and the correlation between analysis and experiment. Suggestions are made for future improvements to the study.

Chapter 2 - Formulation

The curved cylindrical panel considered in this study is analyzed by a combination of methods. An approximate solution to the geometrically nonlinear equilibrium equations is obtained by the Rayleigh-Ritz method, with instability predicted by considering the determinant of the Jacobian matrix. The equations are formulated using Donnell's shell theory and Kirchhoff-Love approximations. The geometrically nonlinear equilibrium equations are also studied using the finite element code STAGS (STructural Analysis of General Shells) [57]. A simplified linear buckling solution is obtained for specially orthotropic stacking with membrane prebuckling. It is presented to provide a normalization for the more rigorous results.

The coordinate system and loading for the specific problem studied are shown in Fig. 2-1. The cylindrical panel is of length a, opening angle β, arc length b, and thickness H. The reference surface, which is at mid-thickness of the panel, has radius R. The origin of the coordinate system is in the corner. The mechanical loading is represented by a spatially uniform end-shortening Δu, and the thermal loading is represented by a spatially uniform temperature change ΔT.
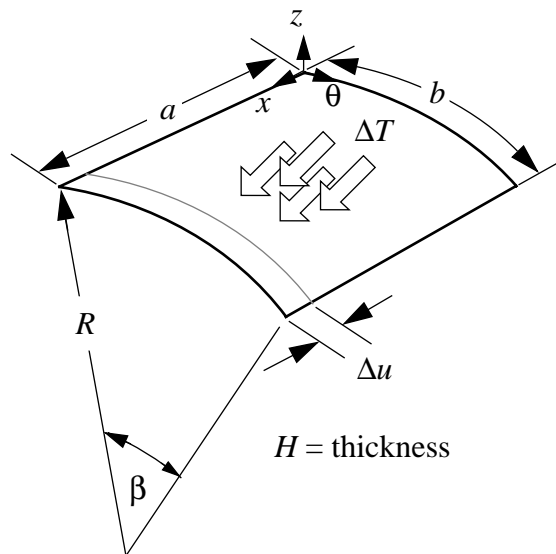
Figure 2-1 Coordinate system and loading convention

2.1 Kinematics and Constitutive Relations

The kinematic relations according to Donnell's assumptions can be expressed as

$$u(x, \theta, z) = u^{\circ}(x, \theta) + z\, \beta_x^{\circ}(x, \theta)$$
$$v(x, \theta, z) = v^{\circ}(x, \theta) + z\, \beta_\theta^{\circ}(x, \theta)$$
$$w(x, \theta, z) = w^{\circ}(x, \theta),$$

(2.1)

with the superscript zero signifying displacements and rotations at the reference surface. Following the Kirchhoff-Love hypothesis, the reference surface rotations are defined as

$$\beta_x^{\circ} = -\frac{\partial w^{\circ}}{\partial x} \qquad \text{and} \qquad \beta_\theta^{\circ} = -\frac{\partial w^{\circ}}{R \partial \theta}.$$

(2.2)

The nonlinear strain-displacement relations can be expressed as

$$\varepsilon_x = \varepsilon_x^{\circ} + z\kappa_x^{\circ}$$
$$\varepsilon_\theta = \varepsilon_\theta^{\circ} + z\kappa_\theta^{\circ}$$
$$\gamma_{x\theta} = \gamma_{x\theta}^{\circ} + z\kappa_{x\theta}^{\circ},$$

(2.3)

where the midsurface strains and curvatures are given by

$$\varepsilon_x^{\circ} = \frac{\partial u^{\circ}}{\partial x} + \frac{1}{2}\left(\frac{\partial w^{\circ}}{\partial x}\right)^2$$

$$\varepsilon_\theta^{\circ} = \frac{\partial v^{\circ}}{R \partial \theta} + \frac{w^{\circ}}{R} + \frac{1}{2}\left(\frac{\partial w^{\circ}}{R \partial \theta}\right)^2$$

$$\gamma_{x\theta}^{\circ} = \frac{\partial v^{\circ}}{\partial x} + \frac{\partial u^{\circ}}{R \partial \theta} + \frac{\partial w^{\circ}}{R \partial \theta}\frac{\partial w^{\circ}}{\partial x}$$

(2.4)

$$\kappa_x^{\circ} = -\frac{\partial^2 w^{\circ}}{\partial x^2}$$

$$\kappa_\theta^{\circ} = -\frac{\partial^2 w^{\circ}}{R^2 \partial \theta^2}$$

$$\kappa_{x\theta}^{\circ} = -2\frac{\partial^2 w^{\circ}}{R \partial x \partial \theta}.$$

(2.5)

It is seen that geometric nonlinearities in the sense of von Karman are included. The stress-strain relations for the *k*th ply of the laminate are given by

$$
\left\{
\begin{array}{c}
\sigma_x \\
\sigma_\theta \\
\tau_{x\theta}
\end{array}
\right\}_k
=
\begin{bmatrix}
\bar{Q}_{11} & \bar{Q}_{12} & \bar{Q}_{16} \\
\bar{Q}_{12} & \bar{Q}_{22} & \bar{Q}_{26} \\
\bar{Q}_{16} & \bar{Q}_{26} & \bar{Q}_{66}
\end{bmatrix}_k
\left\{
\begin{array}{c}
(\varepsilon_x - \varepsilon_x^T) \\
(\varepsilon_\theta - \varepsilon_\theta^T) \\
(\gamma_{x\theta} - \gamma_{x\theta}^T)
\end{array}
\right\},
\tag{2.6}
$$

where $\{\varepsilon_x^T, \varepsilon_\theta^T, \gamma_{x\theta}^T\}$ are the free thermal strains. For this study, the free thermal strains will be assumed to be a linear function of temperature change, namely,

$$
\varepsilon_x^T = \alpha_x \Delta T
$$
$$
\varepsilon_\theta^T = \alpha_\theta \Delta T
$$
$$
\gamma_{x\theta}^T = \alpha_{x\theta} \Delta T,
\tag{2.7}
$$

where α_x, α_θ, and $\alpha_{x\theta}$ are the coefficients of thermal expansion. Defining

$$
\left\{
\begin{array}{c}
\sigma_x^T \\
\sigma_\theta^T \\
\tau_{x\theta}^T
\end{array}
\right\}_k
=
\begin{bmatrix}
\bar{Q}_{11} & \bar{Q}_{12} & \bar{Q}_{16} \\
\bar{Q}_{12} & \bar{Q}_{22} & \bar{Q}_{26} \\
\bar{Q}_{16} & \bar{Q}_{26} & \bar{Q}_{66}
\end{bmatrix}_k
\left\{
\begin{array}{c}
\alpha_x \Delta T \\
\alpha_\theta \Delta T \\
\alpha_{x\theta} \Delta T
\end{array}
\right\}_k,
\tag{2.8}
$$

the stress-strain relation can be written as

$$
\left\{
\begin{array}{c}
\sigma_x \\
\sigma_\theta \\
\tau_{x\theta}
\end{array}
\right\}_k
=
\begin{bmatrix}
\bar{Q}_{11} & \bar{Q}_{12} & \bar{Q}_{16} \\
\bar{Q}_{12} & \bar{Q}_{22} & \bar{Q}_{26} \\
\bar{Q}_{16} & \bar{Q}_{26} & \bar{Q}_{66}
\end{bmatrix}_k
\left\{
\begin{array}{c}
\varepsilon_x \\
\varepsilon_\theta \\
\gamma_{x\theta}
\end{array}
\right\}
-
\left\{
\begin{array}{c}
\sigma_x^T \\
\sigma_\theta^T \\
\tau_{x\theta}^T
\end{array}
\right\}_k.
\tag{2.9}
$$

The force and moment resultants are defined as

$$
\left\{
\begin{array}{c}
N_x \\
N_\theta \\
N_{x\theta}
\end{array}
\right\}
\equiv
\int_{-h/2}^{h/2}
\left\{
\begin{array}{c}
\sigma_x \\
\sigma_\theta \\
\tau_{x\theta}
\end{array}
\right\} dz
\quad \text{and} \quad
\left\{
\begin{array}{c}
M_x \\
M_\theta \\
M_{x\theta}
\end{array}
\right\}
\equiv
\int_{-h/2}^{h/2}
\left\{
\begin{array}{c}
\sigma_x \\
\sigma_\theta \\
\tau_{x\theta}
\end{array}
\right\} z \, dz.
\tag{2.10}
$$

Performing the integration results in the classical lamination theory relations

$$
\left\{ \begin{array}{c} N_x \\ N_\theta \\ N_{x\theta} \end{array} \right\} = \begin{bmatrix} A_{11} & A_{12} & A_{16} \\ A_{12} & A_{22} & A_{26} \\ A_{16} & A_{26} & A_{66} \end{bmatrix} \left\{ \begin{array}{c} \varepsilon_x^\circ \\ \varepsilon_\theta^\circ \\ \gamma_{x\theta}^\circ \end{array} \right\} + \begin{bmatrix} B_{11} & B_{12} & B_{16} \\ B_{12} & B_{22} & B_{26} \\ B_{16} & B_{26} & B_{66} \end{bmatrix} \left\{ \begin{array}{c} \kappa_x^\circ \\ \kappa_\theta^\circ \\ \kappa_{x\theta}^\circ \end{array} \right\} - \left\{ \begin{array}{c} N_x^T \\ N_\theta^T \\ N_{x\theta}^T \end{array} \right\}
$$

$$
\left\{ \begin{array}{c} M_x \\ M_\theta \\ M_{x\theta} \end{array} \right\} = \begin{bmatrix} B_{11} & B_{12} & B_{16} \\ B_{12} & B_{22} & B_{26} \\ B_{16} & B_{26} & B_{66} \end{bmatrix} \left\{ \begin{array}{c} \varepsilon_x^\circ \\ \varepsilon_\theta^\circ \\ \gamma_{x\theta}^\circ \end{array} \right\} + \begin{bmatrix} D_{11} & D_{12} & D_{16} \\ D_{12} & D_{22} & D_{26} \\ D_{16} & D_{26} & D_{66} \end{bmatrix} \left\{ \begin{array}{c} \kappa_x^\circ \\ \kappa_\theta^\circ \\ \kappa_{x\theta}^\circ \end{array} \right\} - \left\{ \begin{array}{c} M_x^T \\ M_\theta^T \\ M_{x\theta}^T \end{array} \right\}. \tag{2.11}
$$

The thermal force and moment resultants are given by

$$
\left\{ \begin{array}{c} N_x^T \\ N_\theta^T \\ N_{x\theta}^T \end{array} \right\} \equiv \int_{-h/2}^{h/2} \left\{ \begin{array}{c} \sigma_x^T \\ \sigma_\theta^T \\ \tau_{x\theta}^T \end{array} \right\} dz = \int_{-h/2}^{h/2} \begin{bmatrix} \overline{Q}_{11} & \overline{Q}_{12} & \overline{Q}_{16} \\ \overline{Q}_{12} & \overline{Q}_{22} & \overline{Q}_{26} \\ \overline{Q}_{16} & \overline{Q}_{26} & \overline{Q}_{66} \end{bmatrix} \left\{ \begin{array}{c} \alpha_x \\ \alpha_\theta \\ \alpha_{x\theta} \end{array} \right\} \Delta T \, dz
$$

$$
\left\{ \begin{array}{c} M_x^T \\ M_\theta^T \\ M_{x\theta}^T \end{array} \right\} \equiv \int_{-h/2}^{h/2} \left\{ \begin{array}{c} \sigma_x^T \\ \sigma_\theta^T \\ \tau_{x\theta}^T \end{array} \right\} dz = \int_{-h/2}^{h/2} \begin{bmatrix} \overline{Q}_{11} & \overline{Q}_{12} & \overline{Q}_{16} \\ \overline{Q}_{12} & \overline{Q}_{22} & \overline{Q}_{26} \\ \overline{Q}_{16} & \overline{Q}_{26} & \overline{Q}_{66} \end{bmatrix} \left\{ \begin{array}{c} \alpha_x \\ \alpha_\theta \\ \alpha_{x\theta} \end{array} \right\} \Delta T z \, dz . \tag{2.12}
$$

When the temperature change ΔT is uniform, the thermal force and moment resultants can be expressed as

$$
\left\{ \begin{array}{c} N_x^T \\ N_\theta^T \\ N_{x\theta}^T \end{array} \right\} = \Delta T \int_{-h/2}^{h/2} \begin{bmatrix} \overline{Q}_{11} & \overline{Q}_{12} & \overline{Q}_{16} \\ \overline{Q}_{12} & \overline{Q}_{22} & \overline{Q}_{26} \\ \overline{Q}_{16} & \overline{Q}_{26} & \overline{Q}_{66} \end{bmatrix} \left\{ \begin{array}{c} \alpha_x \\ \alpha_\theta \\ \alpha_{x\theta} \end{array} \right\} dz = \left\{ \begin{array}{c} \hat{N}_x^T \\ \hat{N}_\theta^T \\ \hat{N}_{x\theta}^T \end{array} \right\} \Delta T
$$

$$
\left\{ \begin{array}{c} M_x^T \\ M_\theta^T \\ M_{x\theta}^T \end{array} \right\} = \Delta T \int_{-h/2}^{h/2} \begin{bmatrix} \overline{Q}_{11} & \overline{Q}_{12} & \overline{Q}_{16} \\ \overline{Q}_{12} & \overline{Q}_{22} & \overline{Q}_{26} \\ \overline{Q}_{16} & \overline{Q}_{26} & \overline{Q}_{66} \end{bmatrix} \left\{ \begin{array}{c} \alpha_x \\ \alpha_\theta \\ \alpha_{x\theta} \end{array} \right\} z \, dz = \left\{ \begin{array}{c} \hat{M}_x^T \\ \hat{M}_\theta^T \\ \hat{M}_{x\theta}^T \end{array} \right\} \Delta T , \tag{2.13}
$$

where the hatted quantities are referred to as unit thermal force and moment resultants, but they are strictly material properties.

2.2 Exact Buckling Solution for a Simplified Problem

An exact analytical buckling solution can be found for a curved panel subject to a number of simplifying assumptions. Begin by considering the linearized Donnell shell equilibrium equations to determine the prebuckling response. These linear equations are given by

$$\frac{\partial N_x}{\partial x} + \frac{\partial N_{x\theta}}{R\partial \theta} = 0$$

$$\frac{\partial N_{x\theta}}{\partial x} + \frac{\partial N_\theta}{R\partial \theta} = 0$$

$$\frac{\partial^2 M_x}{\partial x^2} + 2\frac{\partial^2 M_{x\theta}}{R\partial\theta\partial x} + \frac{\partial^2 M_\theta}{R^2\partial\theta^2} - \frac{N_\theta}{R} = 0. \tag{2.14}$$

For the special case of balanced, symmetric, specially orthotropic laminates with $A_{16} = A_{26} = D_{16} = D_{26} = B_{ij} = 0$, the linear force resultants can be written as

$$N_x = A_{11}\left(\frac{\partial u^\circ}{\partial x}\right) + A_{12}\left(\frac{\partial v^\circ}{R\partial\theta} + \frac{w^\circ}{R}\right) - \hat{N}_x^T\Delta T$$

$$N_\theta = A_{12}\left(\frac{\partial u^\circ}{\partial x}\right) + A_{22}\left(\frac{\partial v^\circ}{R\partial\theta} + \frac{w^\circ}{R}\right) - \hat{N}_\theta^T\Delta T$$

$$N_{x\theta} = A_{66}\left(\frac{\partial u^\circ}{R\partial\theta} + \frac{\partial v^\circ}{\partial x}\right). \tag{2.15}$$

If we further consider a membrane, or momentless, prebuckling solution, the equilibrium equations reduce to

$$\frac{\partial N_x}{\partial x} + \frac{\partial N_{x\theta}}{R\partial\theta} = 0$$

$$\frac{\partial N_{x\theta}}{\partial x} + \frac{\partial N_\theta}{R\partial\theta} = 0$$

$$N_\theta = 0. \tag{2.16}$$

The boundary conditions for a membrane solution with axial end-shortening are:

at $x = 0$,   at $x = a$,

$$u^\circ = 0 \qquad\qquad\qquad\qquad u^\circ = \Delta u$$

$$N_{x\theta} = 0 \qquad\qquad\qquad\qquad N_{x\theta} = 0 \tag{2.17}$$

at $\theta = 0$,   at $\theta = \beta$,

$$N_{x\theta} = 0 \qquad\qquad\qquad\qquad N_{x\theta} = 0$$

$$N_\theta = 0 \qquad\qquad\qquad\qquad N_\theta = 0 \; . \tag{2.18}$$

To satisfy the displacement boundary conditions at $x = 0$ and $x = a$, let

$$u^\circ(x, \theta) = \left(\frac{\Delta u}{a}\right) x \; . \tag{2.19}$$

Then the stress resultants which satisfy the equilibrium equations and remaining boundary conditions are given by

$$N_x = \frac{A_{11}A_{22} - A_{12}^2}{A_{22}}\left(\frac{\Delta u}{a}\right) + \Delta T\left(\frac{A_{12}}{A_{22}}\hat{N}_\theta^T - \hat{N}_x^T\right)$$

$$N_\theta = 0$$

$$N_{x\theta} = 0. \tag{2.20}$$

The buckling equations, based on Donnell shell theory, can be written as

$$\frac{\partial N_{x_1}}{\partial x} + \frac{\partial N_{x\theta_1}}{R\partial\theta} = 0$$

$$\frac{\partial N_{x\theta_1}}{\partial x} + \frac{\partial N_{\theta_1}}{R\partial\theta} = 0$$

$$\frac{\partial^2 M_{x_1}}{\partial x^2} + 2\frac{\partial^2 M_{x\theta_1}}{R\partial\theta\partial x} + \frac{\partial^2 M_{\theta_1}}{R^2\partial\theta^2} + N_x\frac{\partial^2 w_1}{\partial x^2} + 2N_{x\theta}\frac{\partial^2 w_1}{R\partial\theta\partial x} + N_\theta\frac{\partial^2 w_1}{R^2\partial\theta^2} - \frac{N_{\theta_1}}{R} = 0, \tag{2.21}$$

where the subscript 1 denotes a buckling, or incremental, quantity and no subscript denotes a pre-buckling quantity. The force and moment resultant increments can be written as

$$N_{x_1} = A_{11}\frac{\partial u_1}{\partial x} + A_{12}\left(\frac{\partial v_1}{R\partial\theta} + \frac{w_1}{R}\right)$$

$$N_{\theta_1} = A_{12}\frac{\partial u_1}{\partial x} + A_{22}\left(\frac{\partial v_1}{R\partial\theta} + \frac{w_1}{R}\right)$$

$$N_{x\theta_1} = A_{66}\left(\frac{\partial u_1}{R\partial\theta} + \frac{\partial v_1}{\partial x}\right)$$

(2.22)

$$M_{x_1} = -D_{11}\frac{\partial^2 w_1}{\partial x^2} - D_{12}\frac{\partial^2 w_1}{R^2\partial\theta^2}$$

$$M_{\theta_1} = -D_{12}\frac{\partial^2 w_1}{\partial x^2} - D_{22}\frac{\partial^2 w_1}{R^2\partial\theta^2}$$

$$M_{x\theta_1} = -2D_{66}\frac{\partial^2 w_1}{R\partial\theta\partial x} .$$

(2.23)

Writing the buckling equations in terms of displacement increments, and noting that, according to the prebuckling solution, $N_\theta = N_{x\theta} = 0$,

$$A_{11}\frac{\partial^2 u_1}{\partial x^2} + A_{12}\left(\frac{\partial^2 v_1}{R\partial\theta\partial x} + \frac{1}{R}\frac{\partial w_1}{\partial x}\right) + A_{66}\left(\frac{\partial^2 u_1}{R^2\partial\theta^2} + \frac{\partial^2 v_1}{R\partial\theta\partial x}\right) = 0$$

$$A_{66}\left(\frac{\partial^2 u_1}{R\partial\theta\partial x} + \frac{\partial^2 v_1}{\partial x^2}\right) + A_{12}\frac{\partial^2 u_1}{R\partial\theta\partial x} + A_{22}\left(\frac{\partial^2 v_1}{R^2\partial\theta^2} + \frac{1}{R}\frac{\partial w_1}{R\partial\theta}\right) = 0$$

$$D_{11}\frac{\partial^4 w_1}{\partial x^4} + 2(D_{12} + 2D_{66})\frac{\partial^4 w_1}{R^2\partial\theta^2\partial x^2} + D_{22}\frac{\partial^4 w_1}{R^4\partial\theta^4}$$

$$- N_x\frac{\partial^2 w_1}{\partial x^2} + \frac{A_{12}}{R}\frac{\partial u_1}{\partial x} + \frac{A_{22}}{R}\left(\frac{\partial v_1}{R\partial\theta} + \frac{w_1}{R}\right) = 0.$$

(2.24)

Next, assume buckling displacements of the form

$$u_1 = U_{mn}\cos\left(\frac{m\pi x}{a}\right)\sin\left(\frac{n\pi\theta}{\beta}\right)$$

$$v_1 = V_{mn}\sin\left(\frac{m\pi x}{a}\right)\cos\left(\frac{n\pi\theta}{\beta}\right)$$

$$w_1 = W_{mn}\sin\left(\frac{m\pi x}{a}\right)\sin\left(\frac{n\pi\theta}{\beta}\right)$$

(2.25)

and substitute them into Eq. (2.24) to obtain

$$
\begin{bmatrix}
C_{11} & C_{12} & C_{13} \\
C_{12} & C_{22} & C_{23} \\
C_{13} & C_{23} & (C_{33} - P_{cr})
\end{bmatrix}
\begin{Bmatrix}
U_{mn} \\
V_{mn} \\
W_{mn}
\end{Bmatrix}
=
\begin{Bmatrix}
0 \\
0 \\
0
\end{Bmatrix},
\tag{2.26}
$$

where

$$
C_{11} = A_{11}\left(\frac{m\pi}{a}\right)^2 + A_{66}\left(\frac{n\pi}{\beta R}\right)^2
$$

$$
C_{12} = (A_{12} + A_{66})\left(\frac{m\pi}{a}\right)\left(\frac{n\pi}{\beta R}\right)
$$

$$
C_{13} = -\frac{A_{12}}{R}\left(\frac{m\pi}{a}\right)
$$

$$
C_{22} = A_{22}\left(\frac{n\pi}{\beta R}\right)^2 + A_{66}\left(\frac{m\pi}{a}\right)^2
$$

$$
C_{23} = -\frac{A_{22}}{R}\left(\frac{n\pi}{\beta R}\right)
$$

$$
C_{33} = D_{11}\left(\frac{m\pi}{a}\right)^4 + 2(D_{12} + 2D_{66})\left(\frac{m\pi}{a}\right)^2\left(\frac{n\pi}{\beta R}\right)^2 + D_{22}\left(\frac{n\pi}{\beta R}\right)^4 + \frac{A_{22}}{R^2}
$$

$$
P_{cr} = N_x\left(\frac{m\pi}{a}\right)^2.
\tag{2.27}
$$

To solve for P_{cr}, set $\det[C_{ij}] = 0$ to obtain

$$
P_{cr} = C_{33} + \frac{(2C_{12}C_{13}C_{23} - C_{11}C_{23}^2 - C_{22}C_{13}^2)}{(C_{11}C_{22} - C_{12}^2)},
\tag{2.28}
$$

where the subscript cr denotes a critical, or buckling, quantity. Substituting the expressions for C_{ij} and P_{cr} from Eq. (2.27) and solving for the axial end load per unit length $N_x = -N_{cr}$ gives

$$
-N_{cr} = \left[D_{11}\left(\frac{m\pi}{a}\right)^2 + 2(D_{12} + 2D_{66})\left(\frac{n\pi}{\beta R}\right)^2 + D_{22}\left(\frac{a}{m\pi}\right)^2\left(\frac{n\pi}{\beta R}\right)^4\right]
$$

$$
+ \frac{1}{R^2}\left[\frac{(A_{11}A_{22} - A_{12}^2)}{A_{11}\left(\frac{m\pi}{a}\right) + \left(\frac{A_{11}A_{22} - A_{12}^2}{A_{66}} - 2A_{12}\right)\left(\frac{n\pi}{\beta R}\right)^2 + A_{22}\left(\frac{a}{m\pi}\right)^2\left(\frac{n\pi}{\beta R}\right)^4}\right].
\tag{2.29}
$$

Notice that the first bracketed term in Eq. (2.29) represents the buckling solution for a flat plate. For an isotropic shell with $a = \beta R$ and $m = n = 1$, Eq. (2.29) simplifies to

$$-N_{cr} = \frac{Eh^3}{3(1-v^2)}\left(\frac{\pi}{a}\right)^2 + \frac{1}{R^2}\left(\frac{a}{\pi}\right)^2\frac{Eh}{4} \, , \tag{2.30}$$

which was obtained by Koiter in ref. [9]. Notice that the first term of Eq. (2.30) is the buckling solution of a square, isotropic flat plate.

The buckling solution occurs when m and n are chosen to give a minimum value of N_{cr}. For a square, flat, isotropic plate, the buckling solution is obtained when $m = n = 1$, however this is not true for a cylindrically curved panel. The minimum value of N_{cr} can be found trying different integer values for m and n, and selecting the values that gives the lowest value of N_{cr}. When end-shortening and temperature change are applied separately, their critical values are obtained from Eq. (2.20) for a specially orthotropic curved panel as

$$\Delta u_{cr} = \frac{N_{cr}aA_{22}}{(A_{11}A_{22} - A_{12}^2)} \qquad \text{and} \qquad \Delta T_{cr} = \frac{N_{cr}A_{22}}{A_{12}\hat{N}_\theta^T - A_{22}\hat{N}_x^T} \, . \tag{2.31}$$

2.3 Rayleigh-Ritz Solution to Nonlinear Response Problem

The total potential energy of a cylinder according to Donnell's assumptions can be expressed as

$$\pi = \frac{1}{2}\iiint_{x\theta z}[(\sigma_x - \sigma_x^T)\varepsilon_x + (\sigma_\theta - \sigma_\theta^T)\varepsilon_\theta +$$

$$(\tau_{x\theta} - \tau_{x\theta}^T)\gamma_{x\theta}]R\,dz\,d\theta\,dx + \pi_{load} \tag{2.32}$$

where π_{load} is the total potential energy of the applied load. Inplane axial and circumferential edge loads are included by

$$\pi_{load} = \int_\theta N_x^-(\theta)u^\circ(0, \theta)R\,d\theta - \int_\theta N_x^+(\theta)u^\circ(a, \theta)R\,d\theta$$

$$+ \int_x N_\theta^-(x)v^\circ(x, 0)dx - \int_x N_\theta^+(x)v^\circ(x, \beta)dx \, , \tag{2.33}$$

inplane shear loading is included by

$$\pi_{load} = \int_\theta N_{x\theta}^-(\theta)v^\circ(0, \theta)R\,d\theta - \int_\theta N_{x\theta}^+(\theta)v^\circ(a, \theta)R\,d\theta$$

$$+ \int_x N_{x\theta}^-(x)u^\circ(x, 0)dx - \int_x N_{x\theta}^+(x)u^\circ(x, \beta)dx, \tag{2.34}$$

and outward radial loading is included by

$$\pi_{load} = -\iint_{x\,\theta} q(x, \theta) w^{\circ}(x, \theta) R d\theta dx \ . \tag{2.35}$$

The terms N^{+} and N^{-} refer to applied edge loads per unit length, and $q(x, \theta)$ is a load per unit area. This study focuses on panel response due to a combination of a known end shortening and temperature change. As a result, $\pi_{load} = 0$. Integrating Eq. (2.32) through the thickness with no applied edge loads results in

$$\pi = \frac{1}{2}\iint_{\theta\,x} [(N_x - N_x^T)\varepsilon_x^{\circ} + (N_{\theta} - N_{\theta}^T)\varepsilon_{\theta}^{\circ} + (N_{x\theta} - N_{x\theta}^T)\gamma_{x\theta}^{\circ}$$

$$+ (M_x - M_x^T)\kappa_x^{\circ} + (M_{\theta} - M_{\theta}^T)\kappa_{\theta}^{\circ} + (M_{x\theta} - N_{x\theta}^T)\kappa_{x\theta}^{\circ}] R d\theta \iota. \tag{2.36}$$

Using Eqs. (2.4), (2.5), and (2.11), the total potential energy π can be written as a function of the reference surface displacements u°, v°, and w°. The first variation in the total potential energy with respect to displacements can be found by incrementing each of the displacements an infinitesimally small amount ε. Operationally, the incrementing can be expressed as the following substitutions:

$$u^{\circ} \rightarrow u^{\circ} + \varepsilon u_1^{\circ}$$

$$v^{\circ} \rightarrow v^{\circ} + \varepsilon v_1^{\circ}$$

$$w^{\circ} \rightarrow w^{\circ} + \varepsilon w_1^{\circ}, \tag{2.37}$$

where ε is a small scaler quantity and, as mentioned previously, the subscript 1 is associated with incremental quantities. Incrementing the displacements results in increments for other quantities that are functions of displacement, including strains and stress resultants. In terms of these increments, an expression for the incremented total potential energy is given by

$$\pi + \Delta\pi =$$

$$\frac{1}{2}\iint_{\theta\,x} \{(N_x + \Delta N_x - N_x^T)(\varepsilon_x^{\circ} + \Delta\varepsilon_x^{\circ}) + (N_{\theta} + \Delta N_{\theta} - N_{\theta}^T)(\varepsilon_{\theta}^{\circ} + \Delta\varepsilon_{\theta}^{\circ})$$

$$+ (N_{x\theta} + \Delta N_{x\theta} - N_{x\theta}^T)(\gamma_{x\theta}^{\circ} + \Delta\gamma_{x\theta}^{\circ})$$

$$+ (M_x + \Delta M_x - M_x^T)(\kappa_x^{\circ} + \Delta\kappa_x^{\circ}) + (M_{\theta} + \Delta M_{\theta} - M_{\theta}^T)(\kappa_{\theta}^{\circ} + \Delta\kappa_{\theta}^{\circ})$$

$$+ (M_{x\theta} + \Delta M_{x\theta} - M_{x\theta}^T)(\kappa_{x\theta}^{\circ} + \Delta\kappa_{x\theta}^{\circ})\} R d\theta dx \ . \tag{2.38}$$

Substitution of the displacement increments of Eq. (2.37) into the definitions of strains and curvatures from Eq. (2.4) results in

$$\varepsilon_x^\circ + \Delta\varepsilon_x^\circ = \frac{\partial(u^\circ + \varepsilon u_1^\circ)}{\partial x} + \frac{1}{2}\left[\frac{\partial(w^\circ + \varepsilon w_1^\circ)}{\partial x}\right]^2$$

$$\varepsilon_\theta^\circ + \Delta\varepsilon_\theta^\circ = \frac{\partial(v^\circ + \varepsilon v_1^\circ)}{R\partial\theta} + \frac{(w^\circ + \varepsilon w_1^\circ)}{R} + \frac{1}{2}\left[\frac{\partial(w^\circ + \varepsilon w_1^\circ)}{R\partial\theta}\right]^2$$

$$\gamma_{x\theta}^\circ + \Delta\gamma_{x\theta}^\circ = \frac{\partial(u^\circ + \varepsilon u_1^\circ)}{R\partial\theta} + \frac{\partial(v^\circ + \varepsilon v_1^\circ)}{\partial x} + \left[\frac{\partial(w^\circ + \varepsilon w_1^\circ)}{\partial x}\right]\left[\frac{\partial(w^\circ + \varepsilon w_1^\circ)}{R\partial\theta}\right] \tag{2.39}$$

$$\kappa_x^\circ + \Delta\kappa_x^\circ = -\frac{\partial^2(w^\circ + \varepsilon w_1^\circ)}{\partial x^2}$$

$$\kappa_\theta^\circ + \Delta\kappa_\theta^\circ = -\frac{\partial^2(w^\circ + \varepsilon w_1^\circ)}{R^2\partial\theta^2}$$

$$\kappa_{x\theta}^\circ + \Delta\kappa_{x\theta}^\circ = -2\frac{\partial^2(w^\circ + \varepsilon w_1^\circ)}{R\partial\theta\partial x}. \tag{2.40}$$

By grouping powers of ε, the strain and curvature increments can be written as

$$\Delta\varepsilon_x^\circ = \varepsilon(\varepsilon_{x_1}^\circ) + \varepsilon^2(\varepsilon_{x_2}^\circ)$$

$$\Delta\varepsilon_\theta^\circ = \varepsilon(\varepsilon_{\theta_1}^\circ) + \varepsilon^2(\varepsilon_{\theta_2}^\circ)$$

$$\Delta\gamma_{x\theta}^\circ = \varepsilon(\gamma_{x\theta_1}^\circ) + \varepsilon^2(\gamma_{x\theta_2}^\circ) \tag{2.41}$$

$$\Delta\kappa_x^\circ = \varepsilon(\kappa_{x_1}^\circ)$$

$$\Delta\kappa_\theta^\circ = \varepsilon(\kappa_{\theta_1}^\circ)$$

$$\Delta\kappa_{x\theta}^\circ = \varepsilon(\kappa_{x\theta_1}^\circ), \tag{2.42}$$

where

$$\varepsilon_{x_1}^\circ = \frac{\partial u_1^\circ}{\partial x} + \frac{\partial w^\circ}{\partial x}\frac{\partial w_1^\circ}{\partial x}$$

$$\varepsilon_{\theta_1}^\circ = \frac{\partial v_1^\circ}{R\partial\theta} + \frac{w_1^\circ}{R} + \frac{\partial w^\circ}{R\partial\theta}\frac{\partial w_1^\circ}{R\partial\theta}$$

$$\gamma_{x\theta_1}^\circ = \frac{\partial v_1^\circ}{\partial x} + \frac{\partial u_1^\circ}{R\partial\theta} + \frac{\partial w^\circ}{\partial x}\frac{\partial w_1^\circ}{R\partial\theta} + \frac{\partial w^\circ}{R\partial\theta}\frac{\partial w_1^\circ}{\partial x}, \tag{2.43}$$

$$\varepsilon_{x_2}^{\circ} = \frac{1}{2}\left(\frac{\partial w_1^{\circ}}{\partial x}\right)^2$$

$$\varepsilon_{\theta_2}^{\circ} = \frac{1}{2}\left(\frac{\partial w_1^{\circ}}{R\partial \theta}\right)^2$$

$$\gamma_{x\theta_2}^{\circ} = \frac{\partial w_1^{\circ}}{\partial x}\frac{\partial w_1^{\circ}}{R\partial \theta},$$
(2.44)

and

$$\kappa_{x_1}^{\circ} = -\frac{\partial^2 w_1^{\circ}}{\partial x^2}$$

$$\kappa_{\theta_1}^{\circ} = -\frac{\partial^2 w_1^{\circ}}{R^2\partial \theta^2}$$

$$\kappa_{x\theta_1}^{\circ} = -2\frac{\partial^2 w_1^{\circ}}{R\partial \theta \partial x}.$$
(2.45)

Now the increments in the force and moment resultants can be written in terms of the strain and curvature increments to obtain

$$\begin{Bmatrix} \Delta N_x \\ \Delta N_\theta \\ \Delta N_{x\theta} \end{Bmatrix} = \begin{bmatrix} A_{11} & A_{12} & A_{16} \\ A_{12} & A_{22} & A_{26} \\ A_{16} & A_{26} & A_{66} \end{bmatrix} \begin{Bmatrix} \Delta\varepsilon_x^{\circ} \\ \Delta\varepsilon_\theta^{\circ} \\ \Delta\gamma_{x\theta}^{\circ} \end{Bmatrix} + \begin{bmatrix} B_{11} & B_{12} & B_{16} \\ B_{12} & B_{22} & B_{26} \\ B_{16} & B_{26} & B_{66} \end{bmatrix} \begin{Bmatrix} \Delta\kappa_x^{\circ} \\ \Delta\kappa_\theta^{\circ} \\ \Delta\kappa_{x\theta}^{\circ} \end{Bmatrix}$$

$$\begin{Bmatrix} \Delta M_x \\ \Delta M_\theta \\ \Delta M_{x\theta} \end{Bmatrix} = \begin{bmatrix} B_{11} & B_{12} & B_{16} \\ B_{12} & B_{22} & B_{26} \\ B_{16} & B_{26} & B_{66} \end{bmatrix} \begin{Bmatrix} \Delta\varepsilon_x^{\circ} \\ \Delta\varepsilon_\theta^{\circ} \\ \Delta\gamma_{x\theta}^{\circ} \end{Bmatrix} + \begin{bmatrix} D_{11} & D_{12} & D_{16} \\ D_{12} & D_{22} & D_{26} \\ D_{16} & D_{26} & D_{66} \end{bmatrix} \begin{Bmatrix} \Delta\kappa_x^{\circ} \\ \Delta\kappa_\theta^{\circ} \\ \Delta\kappa_{x\theta}^{\circ} \end{Bmatrix}.$$
(2.46)

Making use of Eq. (2.41) and grouping powers of ε, the incremented force and moment resultants can be rewritten as

$$\Delta N_x = \varepsilon(N_{x_1}) + \varepsilon^2(N_{x_2})$$

$$\Delta N_\theta = \varepsilon(N_{\theta_1}) + \varepsilon^2(N_{\theta_2})$$

$$\Delta N_{x\theta} = \varepsilon(N_{x\theta_1}) + \varepsilon^2(N_{x\theta_2})$$

$$\Delta M_x = \varepsilon(M_{x_1}) + \varepsilon^2(M_{x_2})$$

$$\Delta M_\theta = \varepsilon(M_{\theta_1}) + \varepsilon^2(M_{\theta_2})$$

$$\Delta M_{x\theta} = \varepsilon(M_{x\theta_1}) + \varepsilon^2(M_{x\theta_2}) , \tag{2.47}$$

where

$$\begin{Bmatrix} N_{x_1} \\ N_{\theta_1} \\ N_{x\theta_1} \end{Bmatrix} = \begin{bmatrix} A_{11} & A_{12} & A_{16} \\ A_{12} & A_{22} & A_{26} \\ A_{16} & A_{26} & A_{66} \end{bmatrix} \begin{Bmatrix} \varepsilon^\circ_{x_1} \\ \varepsilon^\circ_{\theta_1} \\ \gamma^\circ_{x\theta_1} \end{Bmatrix} + \begin{bmatrix} B_{11} & B_{12} & B_{16} \\ B_{12} & B_{22} & B_{26} \\ B_{16} & B_{26} & B_{66} \end{bmatrix} \begin{Bmatrix} \kappa^\circ_{x_1} \\ \kappa^\circ_{\theta_1} \\ \kappa^\circ_{x\theta_1} \end{Bmatrix}$$

$$\begin{Bmatrix} M_{x_1} \\ M_{\theta_1} \\ M_{x\theta_1} \end{Bmatrix} = \begin{bmatrix} B_{11} & B_{12} & B_{16} \\ B_{12} & B_{22} & B_{26} \\ B_{16} & B_{26} & B_{66} \end{bmatrix} \begin{Bmatrix} \varepsilon^\circ_{x_1} \\ \varepsilon^\circ_{\theta_1} \\ \gamma^\circ_{x\theta_1} \end{Bmatrix} + \begin{bmatrix} D_{11} & D_{12} & D_{16} \\ D_{12} & D_{22} & D_{26} \\ D_{16} & D_{26} & D_{66} \end{bmatrix} \begin{Bmatrix} \kappa^\circ_{x_1} \\ \kappa^\circ_{\theta_1} \\ \kappa^\circ_{x\theta_1} \end{Bmatrix} \tag{2.48}$$

and

$$\begin{Bmatrix} N_{x_2} \\ N_{\theta_2} \\ N_{x\theta_2} \end{Bmatrix} = \begin{bmatrix} A_{11} & A_{12} & A_{16} \\ A_{12} & A_{22} & A_{26} \\ A_{16} & A_{26} & A_{66} \end{bmatrix} \begin{Bmatrix} \varepsilon^\circ_{x_2} \\ \varepsilon^\circ_{\theta_2} \\ \gamma^\circ_{x\theta_2} \end{Bmatrix}$$

$$\begin{Bmatrix} M_{x_2} \\ M_{\theta_2} \\ M_{x\theta_2} \end{Bmatrix} = \begin{bmatrix} B_{11} & B_{12} & B_{16} \\ B_{12} & B_{22} & B_{26} \\ B_{16} & B_{26} & B_{66} \end{bmatrix} \begin{Bmatrix} \varepsilon^\circ_{x_2} \\ \varepsilon^\circ_{\theta_2} \\ \gamma^\circ_{x\theta_2} \end{Bmatrix} . \tag{2.49}$$

Substituting Eqs. (2.41), (2.42), and (2.47) into Eq. (2.38) gives an expression for the total potential energy that can be written in shorthand notation as

$$\pi + \Delta\pi = \pi + \varepsilon\pi_1 + \varepsilon^2\pi_2 + \varepsilon^3\pi_3 + \varepsilon^4\pi_4 \tag{2.50}$$

where π_1 is the first variation in the total potential energy, π_2 is the second variation, π_3 is the

third variation, and π_4 is the fourth variation. Equilibrium is obtained when the first variation is equal to zero. The first variation is given by

$$
\pi_1 = \frac{1}{2}\iint\limits_{x\,\theta}[(N_x - N_x^T)\varepsilon_{x_1}^\circ + N_{x_1}\varepsilon_x^\circ + (N_\theta - N_\theta^T)\varepsilon_{\theta_1}^\circ + N_{\theta_1}\varepsilon_\theta^\circ
$$
$$
+ (N_{x\theta} - N_{x\theta}^T)\gamma_{x\theta_1}^\circ + N_{x\theta_1}\gamma_{x\theta}^\circ + (M_x - M_x^T)\kappa_{x_1}^\circ + M_{x_1}\varepsilon_x^\circ
$$
$$
+ (M_\theta - M_\theta^T)\kappa_{\theta_1}^\circ + M_{\theta_1}\varepsilon_\theta^\circ + (M_{x\theta} - M_{x\theta}^T)\kappa_{x\theta_1}^\circ + M_{x\theta_1}\gamma_{x\theta}^\circ]Rd\theta dx\,. \tag{2.51}
$$

This expression can be further simplified by substituting the expressions for N_{x_1}, N_{θ_1}, $N_{x\theta_1}$, M_{x_1}, M_{θ_1}, and $M_{x\theta_1}$ from Eq. (2.48) and regrouping to obtain

$$
\pi_1 = \iint\limits_{x\,\theta}(N_x\varepsilon_{x_1}^\circ + N_\theta\varepsilon_{\theta_1}^\circ + N_{x\theta}\gamma_{x\theta_1}^\circ + M_x\kappa_{x_1}^\circ + M_\theta\kappa_{\theta_1}^\circ + M_{x\theta}\kappa_{x\theta_1}^\circ)Rd\theta dx\,. \tag{2.52}
$$

This expression plays a key roll for approximate solutions, such as the Rayleigh-Ritz approach.

For a Rayleigh-Ritz solution, the assumed solution the must satisfy the essential boundary conditions. For this formulation, the essential boundary conditions involve the displacements and the first derivative of w°. The first set of boundary conditions considered is denoted as clamped/sliding simple supports, and is defined by

at $x = 0$,   at $x = a$,

$$
\begin{aligned}
u^\circ &= 0 & u^\circ &= \Delta u \\
v^\circ &= 0 & v^\circ &= 0 \\
w^\circ &= 0 & w^\circ &= 0 \\
\frac{\partial w^\circ}{\partial x} &= 0 & \frac{\partial w^\circ}{\partial x} &= 0
\end{aligned} \tag{2.53}
$$

at $\theta = 0$,   at $\theta = \beta$,

$$
\begin{aligned}
N_{x\theta} &= 0 & N_{x\theta} &= 0 \\
N_\theta &= 0 & N_\theta &= 0 \\
w^\circ &= 0 & w^\circ &= 0 \\
M_\theta &= 0 & M_\theta &= 0\,.
\end{aligned} \tag{2.54}
$$

The assumed forms of the displacements which satisfy the essential boundary conditions of clamped/sliding simple supports are

$$u^\circ(x, \theta) = \frac{x\Delta u}{a} + \sum_{i=1}^{2N}\sum_{j=0}^{2N} U_{ij}^c \sin\left(\frac{i\pi x}{a}\right)\cos\left(\frac{j\pi\theta}{\beta}\right) + \sum_{i=1}^{2N}\sum_{j=1}^{2N} U_{ij}^s \sin\left(\frac{i\pi x}{a}\right)\sin\left(\frac{j\pi\theta}{\beta}\right)$$

$$v^\circ(x, \theta) = \sum_{i=1}^{2N}\sum_{j=0}^{2N} V_{ij}^c \sin\left(\frac{i\pi x}{a}\right)\cos\left(\frac{j\pi\theta}{\beta}\right) + \sum_{i=1}^{2N}\sum_{j=1}^{2N} V_{ij}^s \sin\left(\frac{i\pi x}{a}\right)\sin\left(\frac{j\pi\theta}{\beta}\right)$$

$$w^\circ(x, \theta) = \sum_{i=1}^{N}\sum_{j=1}^{N} W_{ij}\left[\cos\left(\frac{(i-1)\pi x}{a}\right) - \cos\left(\frac{(i+1)\pi x}{a}\right)\right]\sin\left(\frac{j\pi\theta}{\beta}\right)$$

(2.55)

Notice that the non-essential or natural boundary conditions, those involving the stress resultants, are not satisfied on a term-by-term basis.

The second set of boundary conditions considered is denoted clamped/fixed simple supports. These boundary conditions differ from clamped/sliding simple supports in the amount of tangential restraint along the straight edges. Clamped/fixed simple supports are defined by

at $x = 0$,   at $x = a$,

$$u^\circ = 0 \qquad\qquad\qquad u^\circ = \Delta u$$
$$v^\circ = 0 \qquad\qquad\qquad v^\circ = 0$$
$$w^\circ = 0 \qquad\qquad\qquad w^\circ = 0$$
$$\frac{\partial w^\circ}{\partial x} = 0 \qquad\qquad\qquad \frac{\partial w^\circ}{\partial x} = 0$$

(2.56)

at $\theta = 0$,   at $\theta = \beta$,

$$N_{x\theta} = 0 \qquad\qquad\qquad N_{x\theta} = 0$$
$$v^\circ = 0 \qquad\qquad\qquad v^\circ = 0$$
$$w^\circ = 0 \qquad\qquad\qquad w^\circ = 0$$
$$M_\theta = 0 \qquad\qquad\qquad M_\theta = 0$$

(2.57)

The assumed forms of the displacements for clamped/fixed simple supports are

$$u^\circ(x, \theta) = \frac{x\Delta u}{a} + \sum_{i=1}^{2N}\sum_{j=0}^{2N} U_{ij}^c \sin\left(\frac{i\pi x}{a}\right)\cos\left(\frac{j\pi\theta}{\beta}\right)$$

$$v^\circ(x, \theta) = \sum_{i=1}^{2N}\sum_{j=1}^{2N} V_{ij}^s \sin\left(\frac{i\pi x}{a}\right)\sin\left(\frac{j\pi\theta}{\beta}\right)$$

$$w^\circ(x, \theta) = \sum_{i=1}^{N}\sum_{j=1}^{N} W_{ij}\left[\cos\left(\frac{(i-1)\pi x}{a}\right) - \cos\left(\frac{(i+1)\pi x}{a}\right)\right]\sin\left(\frac{j\pi\theta}{\beta}\right). \tag{2.58}$$

In addition to satisfying the essential boundary conditions, this form of the assumed displacements also satisfies the natural boundary condition $N_{x\theta} = 0$ at $\theta = 0, \beta$. The natural boundary condition $M_\theta = 0$ at $\theta = 0, \beta$ is not satisfied on a term-by-term basis except for the special case of balanced, symmetric, specially orthotropic laminates with $D_{16} = D_{26} = 0$.

The Rayleigh-Ritz solutions are obtained by substituting the assumed forms for the displacements, Eqs. (2.55) or (2.58), into the expression for the first variation in total potential energy, Eq. (2.52). The displacement increments are assumed to have the same form as the displacements. By carrying out the integration and grouping the coefficients of the displacement increments, nonlinear algebraic equations are obtained in terms of the unknown coefficients in the assumed forms for the displacements. The number of equations is equal to the total number of terms in the displacement series, which is also the number of unknown coefficients. The substitution, integration, and grouping of coefficients into equations was accomplished using the symbolic manipulator *Mathematica*® [58]. From the equations obtained with *Mathematica*®, a FORTRAN computer program was developed to account for an theoretically unlimited number of terms in the approximation series. The nonlinear equations are solved using the IMSL [59] subroutine DNEQNJ, which is based on a variation of Newton's method, and requires a user supplied Jacobian matrix. Further description of the algorithm for the subroutine DNEQNJ is documented in reference [60]. The Jacobian matrix is also used to access stability of the curved panel by computing the determinant of the Jacobian matrix using IMSL subroutines DLFTRG and DLFDRG.

2.4 The Finite Element Code STAGS

The finite element code STAGS is also used to predict the nonlinear response. The code is particularly useful for predicting response in the postbuckling range. A corotational formulation [61] is included to account for large rotations, and Riks' method [30] is incorporated to allow solution along an unstable loading path.

25

The cylindrically curved panels considered here are modeled with 411 type elements, according to the STAGS naming convention. These elements are 8-noded quadrilateral faceted shell elements which are identical to the 4-noded 410 element [62], but with the addition of midside nodes. Both the 410 and 411 elements are formulated according to the Kirchhoff-Love hypothesis with Lagrangian nonlinear strain-displacement relations. Each node is allowed 6 degrees of freedom, comprised of three translations and three rotations. The three rotations are β_x and β_θ, and a "drilling" rotation β_z. Nodal degrees of freedom as shown in Fig. 2-2.

For panels in the parametric study section, a uniform grid of 20 elements by 20 elements will be used. When using STAGS to predict experimental results, a mesh of 23 elements by 23 elements will be used, with smaller elements near the edges to better represent the boundary conditions due to the testing fixture. This will be discussed in a later chapter.

Buckling is predicted with a nonlinear STAGS analysis by noting the number of negative roots, or eigenvalues, in the reformed tangent stiffness matrix. The tangent stiffness matrix, which is equivalent to the Jacobian matrix, is reformed after each load step to represent the current deformed configuration of the structure. When the determinant of the reformed tangent stiffness matrix changes sign from positive to negative, a change in the stability of the load path is indicated. For a stable prebuckling solution, the tangent stiffness matrix has zero negative eigenvalues. When a secondary load path is encountered, points on an unstable path will have one negative eigenvalue. Points on a stable secondary load path, if such a path exists, will have zero negative eigenvalues.

Consider geometrically nonlinear inplane load vs. inplane strain relations, as in Fig. 2-3. For the flat panel response shown in Fig. 2-3(a), point A is the bifurcation point marking the intersection of the primary and secondary equilibrium paths. The portion of the primary path from the origin to point A represents the panel remaining flat prior to buckling, which is a stable prebuckling
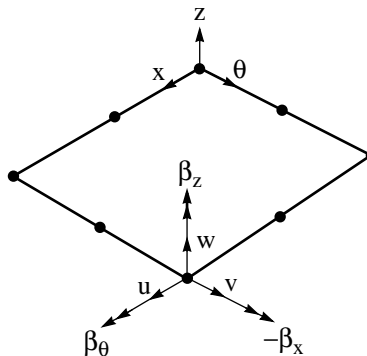
Figure 2-2 Nodal degrees of freedom

response. The portion of the primary path between points A and C represents an unstable config-
uration, with one negative eigenvalue in the reformed tangent stiffness matrix. This represents the
panel remaining flat even though the load is above the buckling load, which is an unstable
response. From point A to point B is the secondary equilibrium path, which is a stable configura-
tion with no negative eigenvalues.

The geometrically nonlinear inplane load vs. inplane strain relation for a typical cylindrically
curved panel is shown in Fig. 2-3(b). The line from the origin to point A represents stable behav-
ior. Unlike the flat panel, deflections perpendicular to the panel do occur in this load range due to
curvature, Poisson effects, and boundary effects. Point A again represents a bifurcation between
the primary and secondary paths. The portion of the primary path from point A to point D is an
unstable configuration with one negative eigenvalue in the reformed stiffness matrix. On the sec-
ondary loading path, the path between points A and B is also unstable, indicated by the appear-
ance of one negative eigenvalue. However beyond point B, the region from point B to point C
again represents a stable configuration with no negative eigenvalues in the reformed tangent stiff-
ness matrix.

Koiter [9] suggests a determination of stable or unstable postbuckling response based on the slope
of the initial postbuckling curve, i.e., from point A to point B in Fig. 2-4. When strain is pre-
scribed, as opposed to load being prescribed, a vertical downward slope in the immediate vicinity
of the bifurcation point is the limiting case separating stable from unstable response. In Fig. 2-4,
the vertical path from A to B represents this transition, with stable configurations to the right, and

(a) Flat Panel   (b) Curved Panel
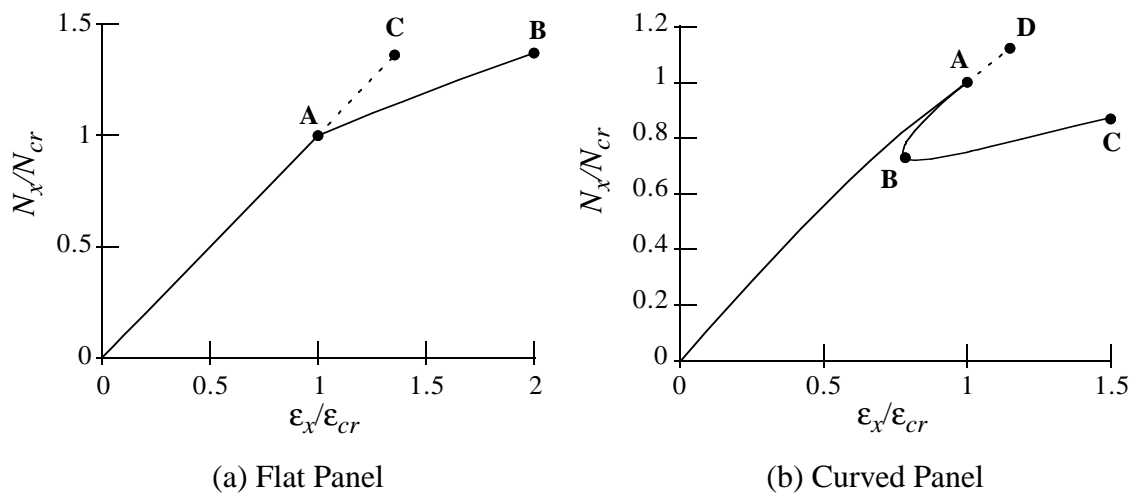
Figure 2-3 Typical postbuckling response, normalized load vs. axial strain

unstable configurations to the left. For unstable response after point A, a decrease in applied strain is required to stay on the response path, while for stable response after point A, an increase in applied strain is required.
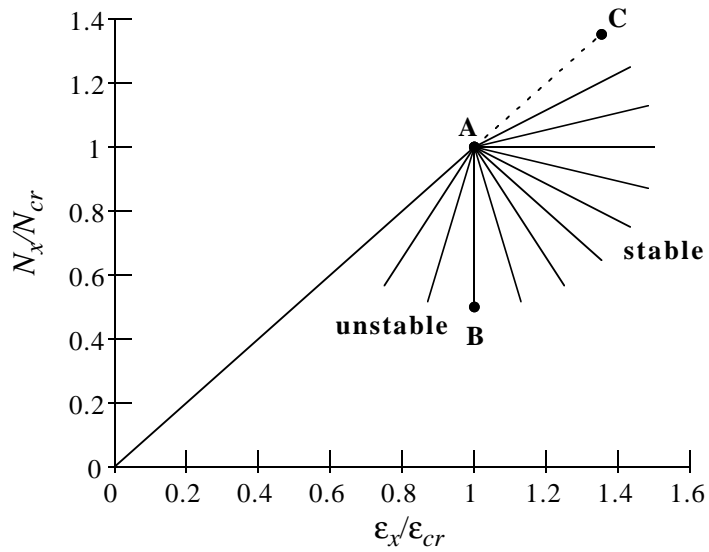
Figure 2-4 Postbuckling stability according to initial slope, prescribed inplane strain

Chapter 3 - Analytical and Numerical Results

Results presented in this section consider the influence of a variety of boundary conditions and panel geometries. The boundary conditions considered cover the range of possibilities that may be seen in the experimental portion of the study. For example, although the goal is to keep the curved edges clamped, they may in fact slide in the circumferential direction. Different values of the radius of curvature are considered to determine how the observed responses depend on the shallowness of the panels. End-shortening and uniform temperature change are considered separately and in combination.

For this portion of the study, only geometrically perfect panels with 10 in. by 10 in. rectangular planforms are considered. Only three laminates are considered, but they represent a range of levels of orthotropy. Where the 0 deg. is the axial direction, the stacking sequences are: $[\pm45/0/90]_s$, a quasi-isotropic lay-up; $[\pm45/0_2]_s$, an axially stiff lay-up; and $[\pm45/90_2]_s$, an axially soft lay-up. The panels are assumed to be fabricated from IM7/5260 with a layer thickness of 0.005 in. Analytical results are based on material properties for IM7/5260 from ref. [44]. These properties are given in Table 3-1.

Table 3-1 Material properties for analytical studies

E_1	22.1 Msi
E_2	1.457 Msi
ν_{12}	0.258
G_{12}	0.860 Msi
α_1	$0.01250 \times 10^{-6}/°F$
α_2	$14.91 \times 10^{-6}/°F$

Interpretation of the results also requires laminate coefficients of thermal expansion, which are defined as

$$\alpha_x = \frac{A_{22}N_x^T - A_{12}N_y^T}{(A_{11}A_{22} - A_{12}^2)}$$

$$\alpha_y = \frac{A_{11}N_y^T - A_{12}N_x^T}{(A_{11}A_{22} - A_{12}^2)}$$

(3.1)

and the laminate major Poisson's ratio, which is given by

$$\nu_{xy} = \frac{A_{12}}{A_{22}}.$$

(3.2)

For the laminates of interest, the coefficients of thermal expansion and Poisson's ratios are given in Table 3-2. The thermal expansion characteristics and the Poisson's ratios of these three laminates offer a contrast. Note that the Poisson's ratio of the quasi-isotropic laminate is very similar to that of a metal, such as aluminum, for example. The coefficients of thermal expansion for that laminate, on the other hand, are an order of magnitude less than aluminum. The Poisson's ratio for the axially soft $[\pm 45/90_2]_s$ laminate is smaller than that of the quasi-isotropic laminate, and the coefficient of thermal expansion in the y-direction is actually negative. On the other hand, the coefficient of thermal expansion in the x-direction is positive and much larger than for the quasi-isotropic laminate, although still less than aluminum. The Poisson's ratio for the axially stiff $[\pm 45/0_2]_s$ laminate is quite large, being greater than the value of 0.5, the upper limit for isotropic materials. The coefficients of thermal expansion of the axially stiff laminate are reversed from those of the axially soft laminate.

Table 3-2 Laminate coefficients of thermal expansion and Poisson's ratios

	α_x	α_y	ν_{xy}
$[\pm 45/0/90]_s$	$1.136 \times 10^{-6}/°F$	$1.136 \times 10^{-6}/°F$	0.299
$[\pm 45/90_2]_s$	$4.34 \times 10^{-6}/°F$	$-0.1590 \times 10^{-6}/°F$	0.193
$[\pm 45/0_2]_s$	$-0.1590 \times 10^{-6}/°F$	$4.34 \times 10^{-6}/°F$	0.667
Aluminum	$13.0 \times 10^{-6}/°F$	$13.0 \times 10^{-6}/°F$	0.330

3.1 Simplified Linear Analysis

The results from the simplified linear buckling analysis for 10 in. by 10 in. curved panels with radii of 60 in. are given in Table 3-3. The value of the critical, or buckling, load is derived from Eq. (2.29), independent of whether the loading is due to thermal effects or mechanical effects. The number of half waves in the axial (m) and circumferential (n) directions is indicated. Note the multiple half waves in the axial direction. Note also that Eq. (2.31) predicts a negative buckling temperature for the $[\pm 45/0_2]_s$ laminate, indicating that raising the temperature will not cause thermal buckling. This is because of the coefficient of thermal expansion of this laminate in the axial direction is negative, whereas with the other two laminates the axial expansion coefficient is positive. Since in the solution to Eq. (2.29) only the axial prebuckling force resultant is involved, it is the axial coefficient of thermal expansion that is important. Recall that this solution assumes a membrane prebuckling state, that D_{16} and D_{26} are zero, and that the boundaries are simply supported. The load N_{cr} from this solution will be used to normalize the results of nonlinear analyses from the STAGS and Rayleigh-Ritz solutions.

Table 3-3 Buckling values from simplified linear analysis

		N_{cr}, lbs./in.	Δu_{cr}, in.	ΔT_{cr}, °F
$[\pm 45/0/90]_s$	$m = 4, n = 1$	-141.0	-0.00412	362.9
$[\pm 45/90_2]_s$	$m = 4, n = 1$	-145.0	-0.00988	227.5
$[\pm 45/0_2]_s$	$m = 3, n = 1$	-100.3	-0.00197	-1242.4

3.2 Effect of Boundary Conditions

The boundary condition that is of primary interest has clamped supports on the curved edges, with simple supports that allow circumferential displacement on the straight edges. It is hoped that this set of conditions, referred to earlier as clamped/sliding simple support, will be provided by the experimental set-up. Before broad generalizations are made about the behavior of curved panels, it is important to understand the sensitivity of thermal and mechanical response to specific boundary conditions. Because the effects of circumferential restraint are expected to substantially effect response, boundary conditions which vary this restraint are studied.

3.2.1 Clamped/Sliding Simple Support Boundary Conditions

Clamped/sliding simple support boundary conditions are defined for use in STAGS as shown in Fig. 3-1. For end-shortening, the specified displacement u^+ is equal to the prescribed end-shorten-

ing Δu along the curved end at $x = a$, and it is equal to zero at $x = 0$. For elevated temperature loading, u^+ is equal to zero along both curved ends. Because u^+ is required to be uniform along the curved edge, the drilling degree of freedom β_z is set to zero there. Along the straight edge, the sliding simple support boundary condition includes β_x being set equal to zero, which is not explicitly required by the Rayleigh-Ritz solution. This rotation is not part of the variationally consistent boundary conditions, Eqs. (2.53) and (2.54), but is required by the finite element analysis to accurately model the physical testing conditions. And although the Rayleigh-Ritz solution is not required to match this boundary condition, the particular choice of assumed displacements, Eq. (2.55), does result in β_x being equal to zero along the straight edges.
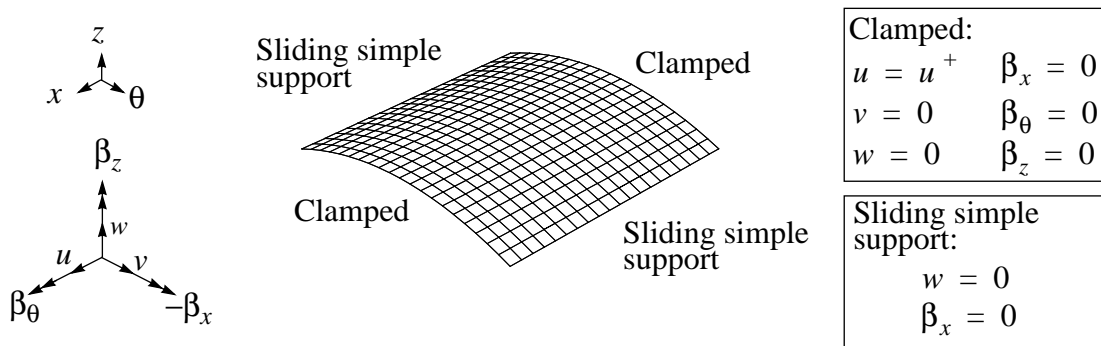
Figure 3-1 Clamped/sliding simple support boundary conditions for STAGS analysis

Table 3-4 gives the buckling results for the Rayleigh-Ritz and STAGS nonlinear analyses for clamped/sliding simple support boundary conditions. Buckling is predicted by the Rayleigh-Ritz solution when the determinant of the Jacobian matrix changes sign, and by STAGS when the reformed tangent stiffness matrix has one negative root. This behavior is characteristic of bifurcation buckling, defined earlier as the intersection between the primary load path and a secondary load path.

Again, 10 in. by 10 in. IM7/5260 panels with radii of 60 in. are considered. Axial force resultants, N_x, are normalized by the buckling load, N_{cr}, from the simplified linear solution of Table 3-3. In Table 3-4, and other results that follow, N_x is the average axial force along the curved end of the panel, divided by the arc length b. The assumed displacements for the Rayleigh-Ritz solution with clamped/sliding simple support boundary conditions are given in Eq. (2.55). The results presented in this section are for $N = 5$, which gives a total of 445 unknown constants to be determined in the solution of the nonlinear equations. Results using less terms did not compare as favorably to STAGS, as shown Appendix A, where convergence of the Rayleigh-Ritz solution is considered.

Table 3-4 Buckling values from STAGS and Rayleigh-Ritz nonlinear analysis solutions, clamped/sliding simple support boundary conditions

		Mechanical loading		Thermal loading	
		Δu_{max}, in.	N_x / N_{cr}	ΔT_{max},°F	N_x / N_{cr}
$[\pm 45/0/90]_s$	STAGS	-0.00404 (b)*	0.964	512.8 (b)	1.087
	Rayleigh-Ritz	-0.00403 (b)	0.963	522.2 (b)	1.117
$[\pm 45/90_2]_s$	STAGS	-0.00906 (b)	0.910	206.7 (b)	0.905
	Rayleigh-Ritz	-0.00901 (b)	0.907	206.1 (b)	0.903
$[\pm 45/0_2]_s$	STAGS	-0.00254 (b)	1.184	1150.0 (b)	-1.36
	Rayleigh-Ritz	-0.00254 (b)	1.186	does not buckle	

* Bifurcation buckling is indicated by a (b), limit point buckling is indicated by an (l).

For the axially stiff $[\pm 45/0_2]_s$ laminate, the Rayleigh-Ritz solution does not predict buckling when $N = 5$ terms are used, although the STAGS solution predicts a buckling temperature of 1150.0°F. A further increase in the number of terms in the Rayleigh-Ritz solution exceeds current computer limitations. More insight on this convergence problem will be provided in the discussion of clamped/fixed simple support boundary conditions.

It is important to note that with the nonlinear analysis, either the end-shortening Δu is prescribed, or the temperature increase ΔT is prescribed, depending on whether a mechanical or thermal loading is being considered. Critical, or buckling, values of these parameters are sought. The value of N_x at the critical values of these parameters is an outcome of the analysis. Comparison between the simplified linear and nonlinear analyses reveals a weakness in the linear approach. For the $[\pm 45/0/90]_s$ laminate, for example, the value of N_x when Δu reaches its critical value is not the same as the value of N_x when ΔT reaches its critical value. The simplified linear analysis predicts one axial buckling load N_{cr} regardless of whether the loading was introduced through end-shortening or temperature change, as is apparent from Eq. (2.29). In the nonlinear analysis the magnitude of the buckling load N_x is seen to depend on how the load was introduced.

Nonlinear Response

The nonlinear response predicted by STAGS is shown in Fig. 3-2(a) for the quasi-isotropic $[\pm 45/0/90]_s$ laminate. The average force resultant on the curved end is normalized by the simplified linear buckling values of Table 3-3 to form the vertical axis. The horizontal axis has the
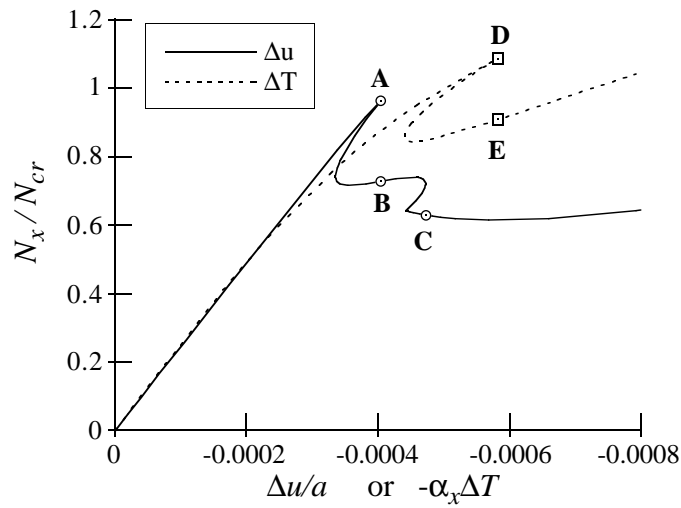
(a) Normalized axial force resultant vs. average mechanical strain response
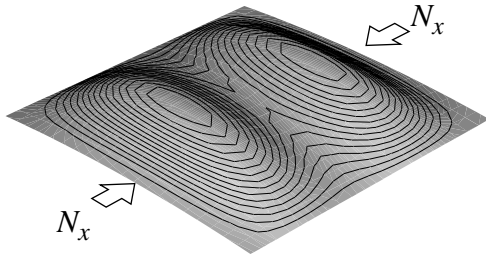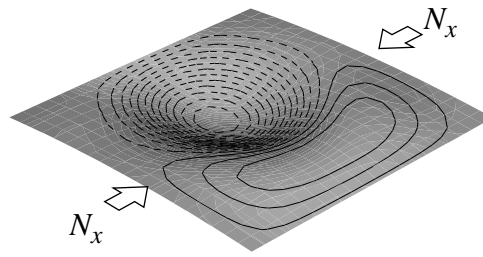
(b) Deformation at point A, Δu = -0.00404 in. (c) Deformation at point B, Δu = -0.00404 in.
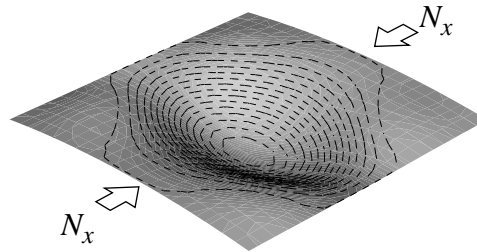
(d) Deformation at point C, Δu = -0.00473 in.
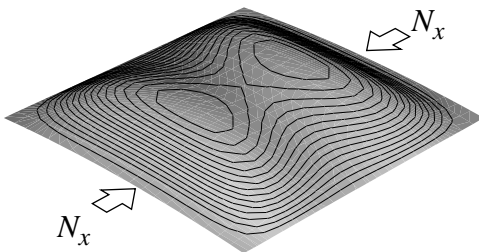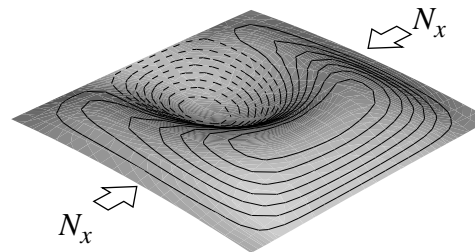
(e) Deformation at point D, ΔT = 512.8°F   (f) Deformation at point E, ΔT = 512.8°F

Figure 3-2 Nonlinear response for a [±45/0/90]$_\mathrm{s}$ laminate, clamped/sliding simple support boundary conditions

dimensions of axial strain. The average inplane axial strain due to end-shortening can be expressed as $\Delta u/a$, which is often referred to as the total strain. The average inplane axial strain due to temperature change can be expressed as $-\alpha_x\Delta T$, referred to as the thermal strain. The super-position of these two average strains gives the average elastic, or mechanical, strain. This average mechanical strain is conveniently used as the horizontal axis. By comparing Tables 3-3 and 3-4, the simplified linear analysis is seen to provide a reasonable prediction for buckling due to end-shortening, $\Delta u = -0.00412$ for the simplified linear analysis vs. $\Delta u = -0.00404$ in. for the geo-metrically nonlinear analysis. The simplified linear buckling temperature of 362.9°F, however, is far from the buckling temperature of 512.8°F predicted by the geometrically nonlinear analysis. Returning to Fig. 3-2(a), it is seen that the panel subjected to end-shortening reaches a bifurcation point at A on the solid line, then collapses with an unstable postbuckling behavior. When N_x reaches the first local minimum just before point B, the panel becomes stable until a second unsta-ble collapse occurs just after point B. After N_x reaches its second minimum near point C, the panel returns to a stable response. In contrast, the panel subjected to uniform temperature change continues along the primary loading path well beyond the bucking load predicted by the simplified linear analysis. At point D, the bifurcation point, unstable collapse occurs and the response remains unstable until N_x reaches a minimum. Stable panel response continues for the remainder of the temperature range considered.

Prebuckling and postbuckling deformed shapes are shown in Fig. 3-2(b-f). The prebuckling defor-mations at points A and D exhibit similar shapes. The initial postbuckling response at points B and E is also similar in terms of deformed shapes, although the end-shortening panel eventually reaches the shape at point C.

For the axially soft $[\pm 45/90_2]_s$ laminate, the buckling value from the simplified linear analysis somewhat overestimates both the maximum end-shortening and the maximum temperature found in the nonlinear analyses, as shown in Tables 3-3 and 3-4. From Fig. 3-3, it is seen that the ther-mal response is nearly identical to the mechanical response. That is because the laminate thermal expansion coefficient in the circumferential direction, α_y is nearly zero. For both loading condi-tions, the panel reaches a bifurcation point and collapses onto an unstable postbuckling path. Deformations for prebuckling and stable postbuckling response are shown in Fig. 3-3(b-e). Like the load vs. strain responses, the deformations are very similar for both thermal and mechanical loading.

For the axially stiff $[\pm 45/0_2]_s$ laminate, the response is shown in Fig. 3-4. The thermal and mechanical responses are entirely different due to the very small but negative coefficient of ther-
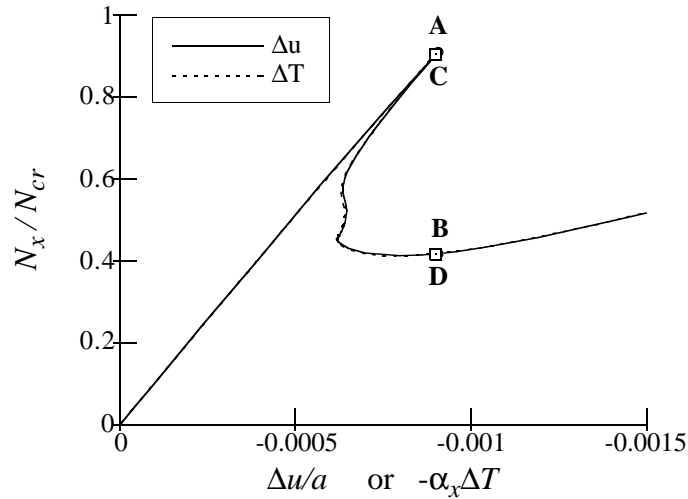
(a) Normalized axial force resultant vs. average mechanical strain response
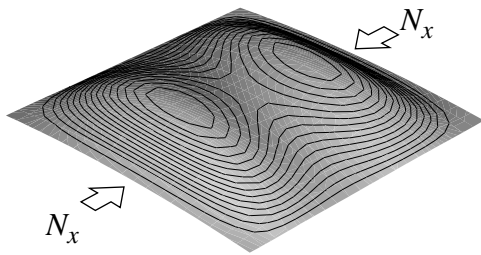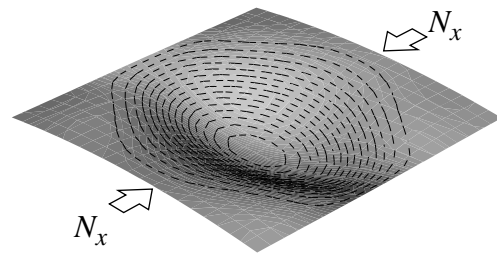
(b) Deformation at point A, $\Delta u = $ -0.00906 in. (c) Deformation at point B, $\Delta u = $ -0.00906 in.
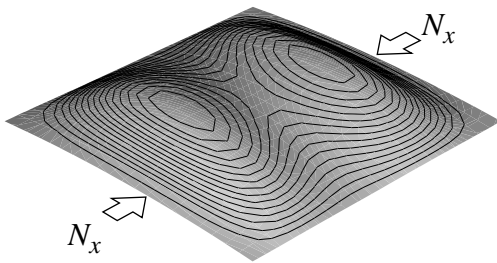
(d) Deformation at point C, $\Delta T = 206.7°F$ (e) Deformation at point D, $\Delta T = 206.7°F$
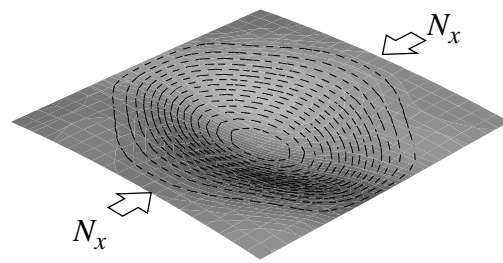
Figure 3-3 Nonlinear response for a $[\pm45/90_2]_s$ laminate, clamped/sliding simple support boundary conditions

mal expansion in the axial direction, α_x. The mechanical response is similar to the response seen for the other two stacking sequences, but the thermal response indicates that an increase in temperature produces a decrease in axial load N_x. For both thermal and mechanical loading, buckling occurs at a bifurcation point. The deformation shapes in Fig. 3-4(b-d) indicate that the mechanically induced deformations are similar to the mechanically induced deformations for the
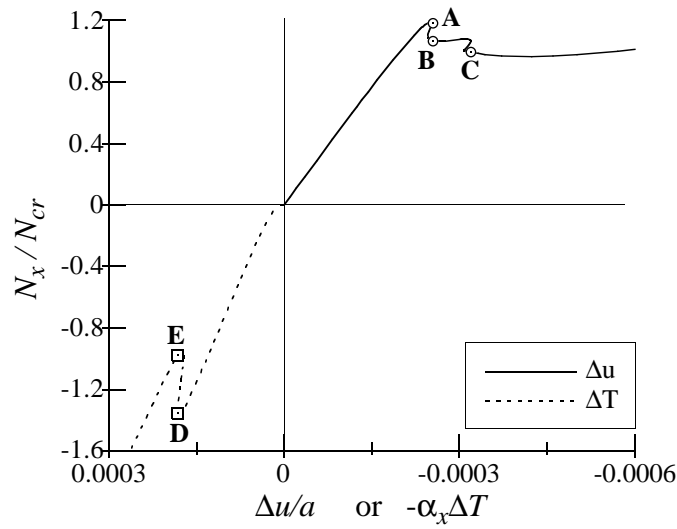
(a) Normalized axial force resultant vs. average mechanical strain response
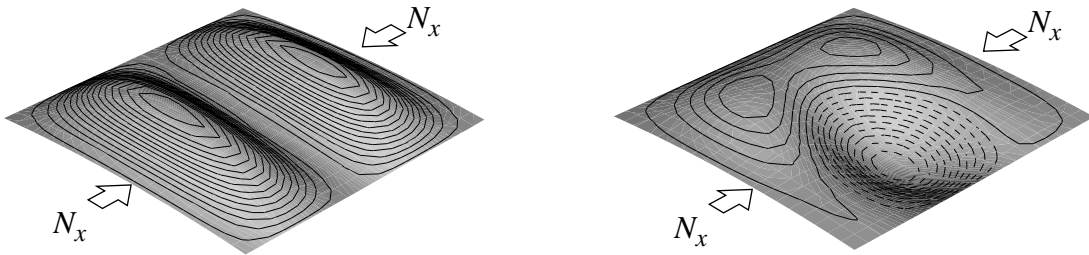
(b) Deformation at point A, Δu = -0.00254 in.   (c) Deformation at point B, Δu = -0.00254 in.
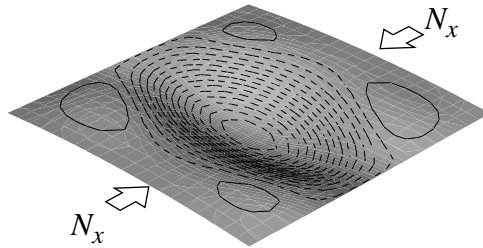
(d) Deformation at point C, Δu = -0.00319 in.
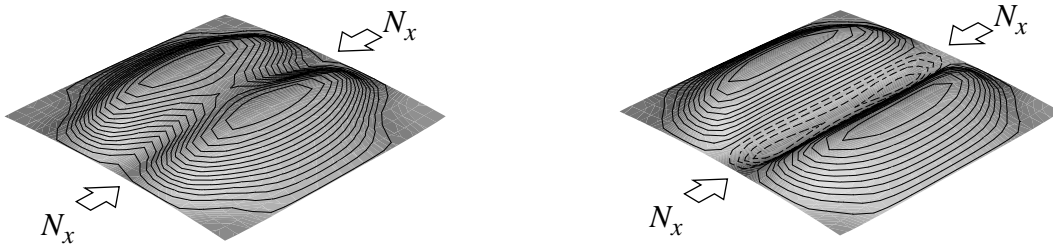
(e) Deformation at point D, ΔT = 1150°F   (f) Deformation at point E, ΔT = 1150°F

Figure 3-4 Nonlinear response for a $[\pm45/0_2]_s$ laminate, clamped/sliding simple support boundary conditions

quasi-isotropic $[\pm45/0/90]_s$ laminate, Fig. 3-2(b-d). The thermally induced deformation, Fig. 3-4(e), retains the same general shape for the range of temperatures considered.

Force Resultant Distributions

The difference in the thermal and mechanical responses can be better understood by examining the force resultant distributions of the curved panels immediately prior to buckling. These force distributions are shown in Figs. 3-5, 3-6, and 3-7, where the buckling load from the simplified linear analysis is used for normalization. For the quasi-isotropic panel, the force resultant N_θ is much higher along the curved ends for the panel subjected to uniform temperature change, Fig. 3-5(d), than for the panel loaded with end-shortening, Fig. 3-5(b). In the simplified linear analysis, the membrane prebuckling assumption required N_θ to be zero throughout the panel. This, apparently, is not a good assumption, particularly for the thermal case. For the end-shortening problem, interaction between N_x and N_θ is through the Poisson's ratio of the laminate. For the temperature problem, the coefficients of thermal expansion in both the axial and circumferential directions, as well as Poisson's ratio, are important in controlling interaction between responses in the axial and circumferential directions. The coefficients of thermal expansion are particularly important at the boundary, where boundary conditions may run counter to the natural tendency of the material to expand or contract as the temperature is changed.

Consider the definition of N_θ as given in sec. 2.1 and repeated here in terms of displacements as

$$N_\theta = A_{12}\left[\frac{\partial u^\circ}{\partial x} + \frac{1}{2}\left(\frac{\partial w^\circ}{\partial x}\right)^2\right] + A_{22}\left[\frac{\partial v^\circ}{R\partial\theta} + \frac{w^\circ}{R} + \frac{1}{2}\left(\frac{\partial w^\circ}{R\partial\theta}\right)^2\right] - \hat{N}_\theta^T\Delta T \qquad (3.3)$$

Using the assumed form of the displacements from the Rayleigh-Ritz solution, and considering N_θ along the curved edges results in

$$N_\theta\big|_{x=0,a} = A_{12}\frac{\partial u^\circ}{\partial x} - \hat{N}_\theta^T\Delta T \qquad (3.4)$$

Then for mechanical loading considered alone, A_{12} governs the magnitude of N_θ along the curved edges. For thermal loading, both A_{12} and $\hat{N}_\theta^T$ are involved, so the value of N_θ along the curved edges is a function of Poisson's ratio and the coefficients of thermal expansion. Note in Fig. 3-5 the spikes, or sharp peaks, in the value of the force resultants at the corners. These are due to the restraint in v-displacement in the corners at the ends of the straight edges. There is no restraint in v-displacement along the straight edges except in the corners, and this is due to the restraint in v-displacement along the clamped curved edges, the corner point being common to the

38
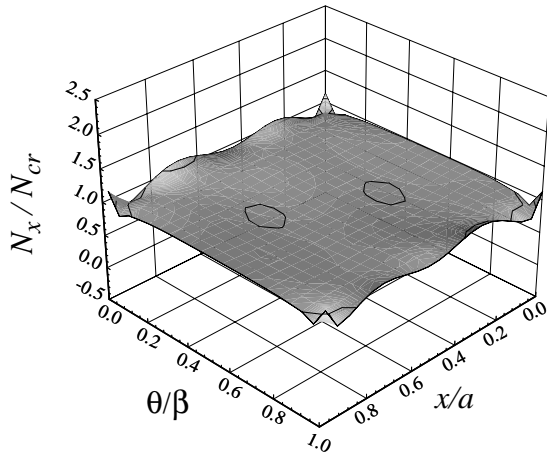
(a) Distribution of N_x, Δu = -0.00404 in.
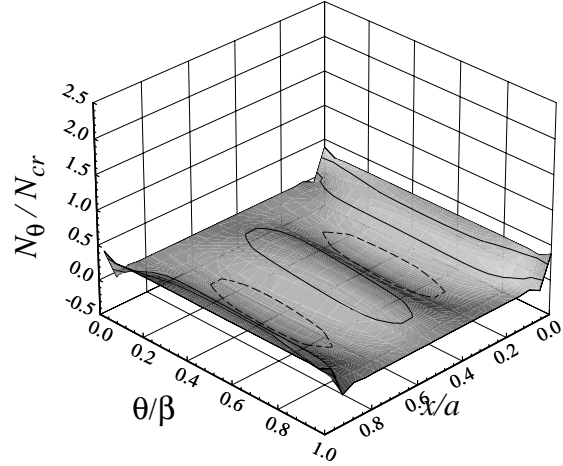
(b) Distribution of N_θ, Δu = -0.00404 in.
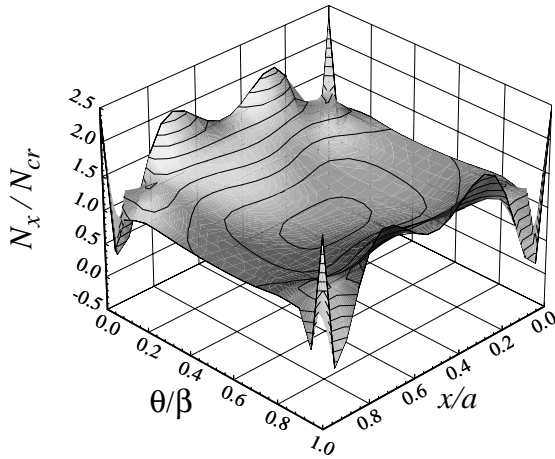
(c) Distribution of N_x, ΔT = 512.8°F
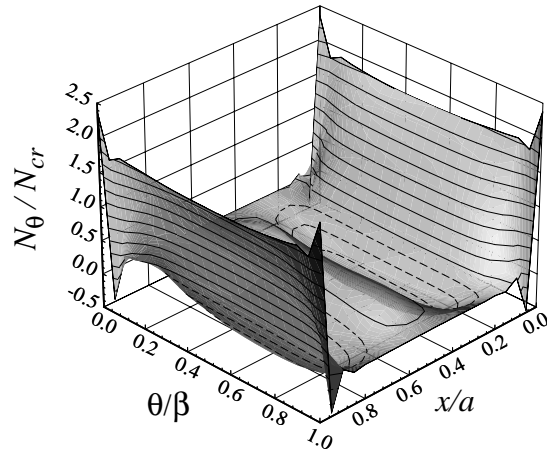
(d) Distribution of N_θ, ΔT = 512.8°F

Figure 3-5 Distribution of force resultants immediately prior to buckling for a [±45/0/90]$_s$ laminate, clamped/sliding simple support boundary conditions

simply supported straight edge and the clamped curved edge. The fact that the straight edge has no circumferential restraint on it except at the corner points leads to the sharp peaks in the force resultants there.

The distributions of force resultants for the axially soft [±45/90$_2$]$_s$ laminate are shown in Fig. 3-6. Just as the thermal and mechanical responses for this laminate were seen to be the same in Fig. 3-3, the force resultant distributions are also nearly the same for the two different loading conditions.
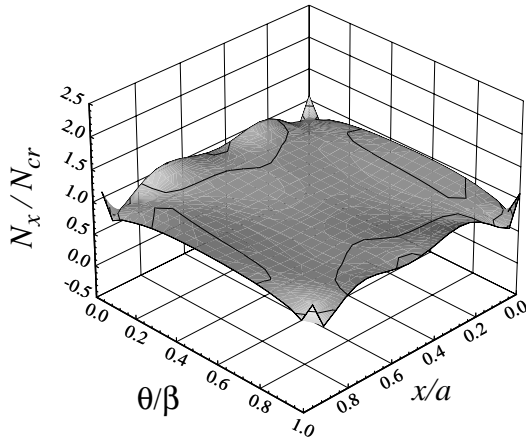
(a) Distribution of N_x, $\Delta u = -0.00906$ in.
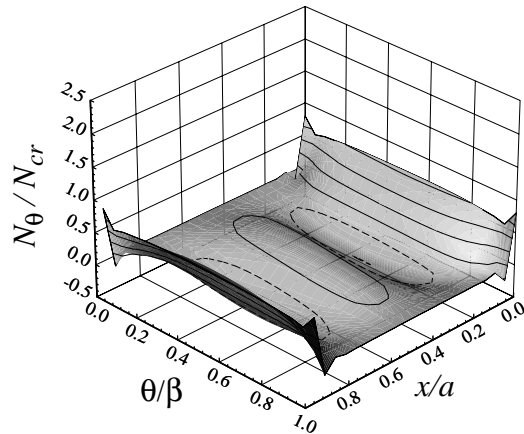
(b) Distribution of N_θ, $\Delta u = -0.00906$ in.
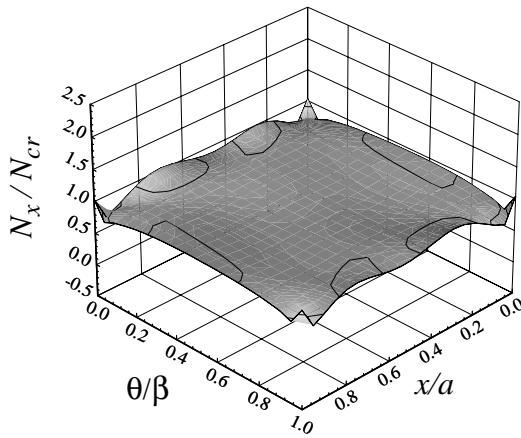
(c) Distribution of N_x, $\Delta T = 206.7°F$
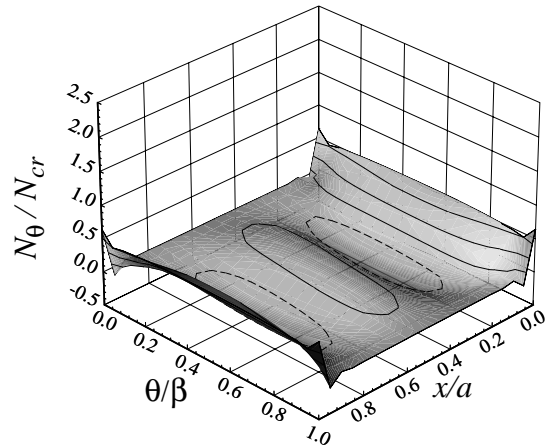
(d) Distribution of N_θ, $\Delta T = 206.7°F$

Figure 3-6 Distribution of force resultants immediately prior to buckling for a $[\pm45/90_2]_s$ laminate, clamped/sliding simple support boundary conditions

For the axially stiff $[\pm45/0_2]_s$ laminate, the force resultants for mechanical response immediately prior to buckling are shown in Fig. 3-7(a) and (b), while the force resultants for thermal response at 300°F are shown in Fig. 3-7(c) and (d). Keeping in mind that the normalization factor N_{cr} for this panel is negative, from Fig. 3-7(c) we can see that N_x is generally positive, or tensile, for thermal response. This is the opposite sense as the force resultant distribution of N_x for mechanical response. From Fig. 3-7(d), N_θ is seen to be always negative, or compressive, for thermal response.
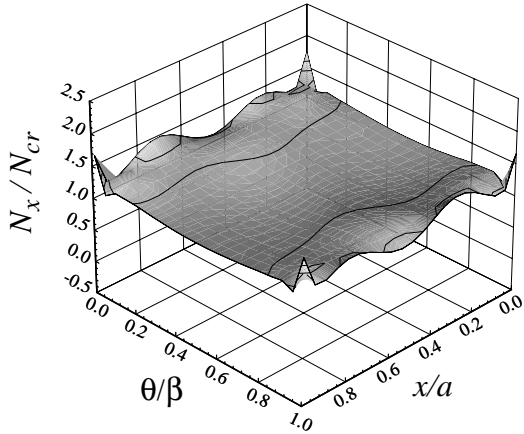
(a) Distribution of N_x immediately prior to buckling, $\Delta u = -0.00254$ in.
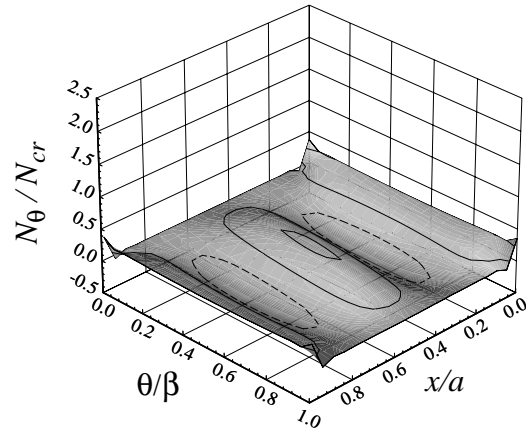
(b) Distribution of N_θ immediately prior to buckling, $\Delta u = -0.00254$ in.
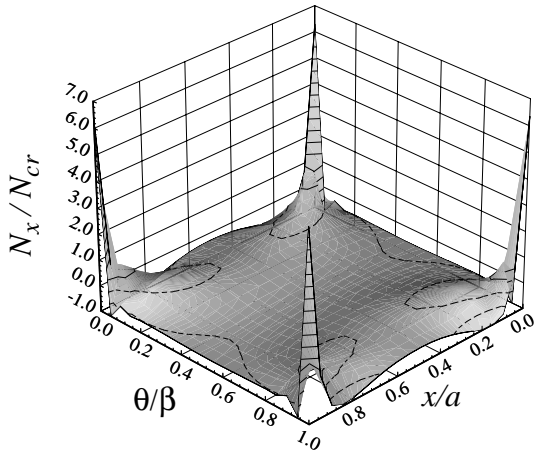
(c) Distribution of N_x at $\Delta T = 300°F$
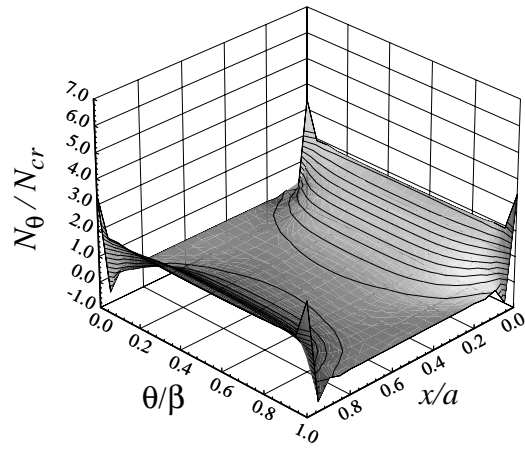
(d) Distribution of N_θ at $\Delta T = 300°F$

Figure 3-7 Distribution of force resultants for a $[\pm45/0_2]_s$ laminate, clamped/sliding simple support boundary conditions

Summary

Buckling of curved panels with clamped/sliding simple support boundary conditions loaded with end-shortening or temperature change is due to bifurcation. For the $[\pm45/0/90]_s$ laminate and the $[\pm45/0_2]_s$ laminate, the nonlinear response due to end-shortening is not the same as the nonlinear response due to temperature change. Response due to end-shortening is the same as response due to temperature change for the $[\pm45/90_2]_s$ laminate. Force resultant distributions are characterized by sharp peaks in the corners, due to the restriction of v-displacement imposed by the clamped

curved ends. The peaks are most pronounced in the thermal loading response of the $[\pm45/0/90]_s$ and $[\pm45/0_2]_s$ laminates.

3.2.2 Clamped/Fixed Simple Support Boundary Conditions

In order to determine the effects of in-plane boundary conditions on the response of curved panels, the boundary conditions on the straight edges were changed to give clamped/fixed simple support conditions, as defined for use in STAGS in Fig. 3-8. As discussed earlier for clamped/sliding simple supports, the straight edges of the panel were allowed to expand freely in the circumferential direction except at the ends, where the clamped curved edge restricted expansion. For clamped/fixed simple supports, circumferential expansion all along the straight edges is restricted by specifying $v = 0$ there. The variationally consistent boundary conditions used in the equivalent Rayleigh-Ritz solution are given by Eqs. (2.56) and (2.57).
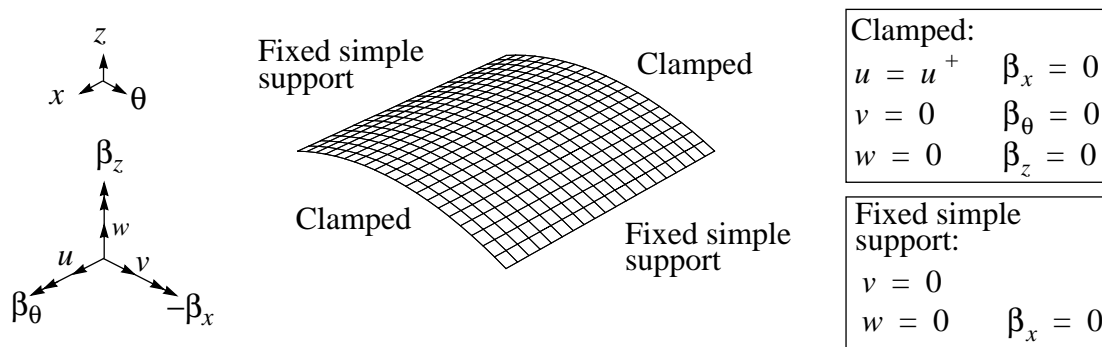
Figure 3-8 Clamped/fixed simple support boundary conditions

The buckling results for the Rayleigh-Ritz and STAGS nonlinear analyses with clamped/fixed simple support boundary conditions are given in Table 3-6. The assumed displacements for the Rayleigh-Ritz solution with clamped/fixed simple support boundary conditions are given in Eq. (2.58). Results are again presented for $N = 5$, yielding 235 unknown constants to be determined in the solution of the nonlinear equations. For the particular case of a $[\pm45/0_2]_s$ laminate subjected to uniform temperature change, because of convergence difficulties, additional terms were required in the assumed displacement series to predict a buckling temperature.

Buckling for clamped/fixed simple support boundary conditions generally occurs when the response curve reaches a limit point. In the Rayleigh-Ritz solution, limit point buckling with unstable postbuckling results in an inability of the solution to converge. When the postbuckling path is stable, solution can continue and buckling is determined by a local maximum in the load

vs. mechanical strain response. Buckling is indicated in the STAGS solution by a local maximum, which may be followed by a stable solution, or an unstable solution with one negative root in the tangent stiffness matrix. More will be said shortly of the convergence difficulties for thermal loading of the axially stiff $[\pm 45/0_2]_s$ laminate.

Table 3-5 Buckling values from STAGS and Rayleigh-Ritz solutions, clamped/fixed simple support boundary conditions

		Mechanical loading		Thermal loading	
		Δu_{max}, in.	N_x / N_{cr}	ΔT_{max},°F	N_x / N_{cr}
$[\pm 45/0/90]_s$	STAGS	-0.00459 (l)*	1.050	does not buckle	
	Rayleigh-Ritz	-0.00456 (l)	1.049	does not buckle	
$[\pm 45/90_2]_s$	STAGS	-0.01039 (l)	1.029	236.0 (l)	1.020
	Rayleigh-Ritz	-0.01036 (l)	1.029	235.0 (l)	1.020
$[\pm 45/0_2]_s$	STAGS	-0.00358 (b)	1.346	799.8 (l)	-1.434
	Rayleigh-Ritz	-0.00359 (b)	1.354	835.0** (l)	-1.529**

* Bifurcation buckling is indicated by a (b), limit point buckling is indicated by an (l).

** Uses $N = 7$ in the assumed form for the displacements, Eq. (2.58).

The simplified linear solution provides a reasonable estimate for the mechanically induced buckling load, except for the $[\pm 45/0_2]_s$ laminate, as shown in Table 3-6. By comparing Tables 3-3, 3-4, and 3-6, it can be seen that the simplified linear thermal solution is better at predicting the occurrence of buckling for clamped/sliding simple support boundaries than for clamped/fixed simple support boundaries. The simplified linear solution predicts buckling for a positive temperature changes for both the $[\pm 45/0/90]_s$ and $[\pm 45/90_2]_s$ laminates, as occurs for the clamped/sliding simple supports boundaries in Table 3-4, but not for the clamped/fixed simple support boundaries in Table 3-6. This is because the circumferential restraint conditions for the simplified linear solution were equivalent to sliding simple supports on the straight edges. For clamped/fixed simple supports, the axially stiff $[\pm 45/0_2]_s$ laminate buckles with elevated temperature, while the quasi-isotropic $[\pm 45/0/90]_s$ laminate does not. Buckling of the $[\pm 45/0_2]_s$ laminate can be expected due to the large coefficient of thermal expansion in the circumferential direction opposed by the restraint in circumferential displacement along the straight edges. That the quasi-isotropic laminate does not buckle cannot be explained without more detailed investigation.

Nonlinear Response

The nonlinear response as predicted by STAGS for the quasi-isotropic [±45/0/90]$_\text{s}$ laminate with clamped/fixed simple supports is shown in Fig. 3-9(a). Normalization of the axial force resultant on the vertical axis is again with respect to the simplified linear buckling values of Table 3-3. The simplified linear analysis predicts a buckling value associated with thermal loading, but nonlinear analysis shows that buckling does not occur. The panel subjected to thermal loading responds to elevated temperatures without encountering a secondary load path or reaching a limit point. Additionally, the postbuckling response is stable for mechanical loading, so the Rayleigh-Ritz solution is able to continue into the postbuckling range. For both thermal and mechanical loading, the panel exhibits significant load carrying capacity beyond the bifurcation load predicted by the simplified linear analysis.

Deformations at various stages of loading are shown in Fig. 3-9(b-d). The panel subjected to mechanical loading is seen to approach its postbuckling shape before it reaches buckling, as shown in Fig. 3-9(b) and (c). The panel subjected to elevated temperatures shows only radial outward deformations, Fig. 3-9(d).

The nonlinear response of the axially soft [±45/90$_2$]$_\text{s}$ laminate with clamped/fixed simple support boundary conditions is shown in Fig. 3-10(a). Thermal and mechanical response are seen to be nearly identical, as they were for the clamped/sliding simple support boundary conditions shown in Fig. 3-3. The laminate circumferential coefficient of thermal expansion, α_y, is nearly zero, so thermal expansion is essentially uniaxial. Both end-shortening and elevated temperatures cause the development of axial strains much greater in magnitude than the circumferential strains. For both loading conditions, the panel reaches a limit point before collapse to an unstable postbuckling path. Deformations are also seen to be similar for both loading conditions, as shown in Fig. 3-10(b-e).

For the axially stiff [±45/0$_2$]$_\text{s}$ laminate with clamped/fixed simple supports, nonlinear response is shown in Fig. 3-11. The mechanical response shows a change in stiffness between points A and B, then bifurcation buckling at point C. Even after passing the bifurcation point, mechanical response continues to be stable. Note the similarity of the slope of the postbuckling path from point C to point D as compared to the stable postbuckling paths shown in Fig. 2-4. Thermal response again indicates that an increase in temperature results in a tensile axial force resultant N_x along the curved edge, as was seen for clamped/sliding simple support boundary conditions in Fig. 3-4. Thermal buckling occurs at a limit point, and postbuckling is stable.
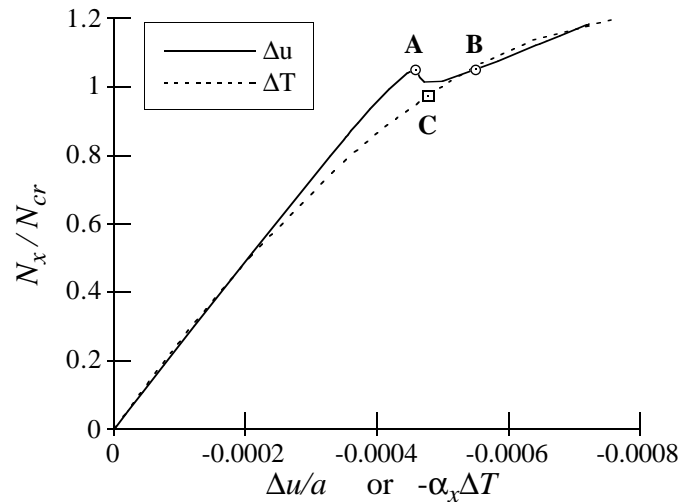
(a) Normalized axial force resultant vs. average mechanical strain response
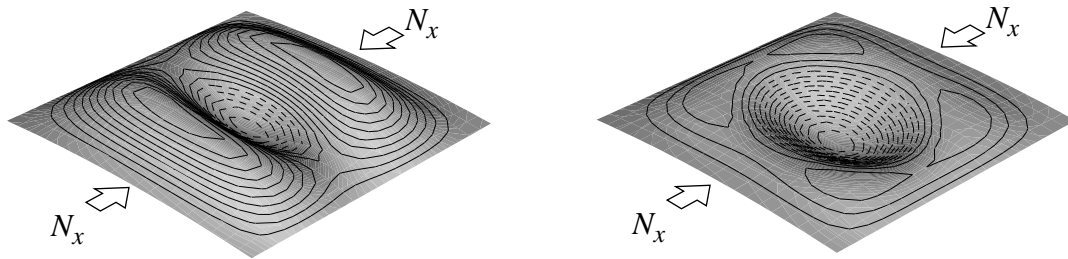
(b) Deformation at point A, Δu = -0.00459 in.   (c) Deformation at point B, Δu = -0.00550 in.
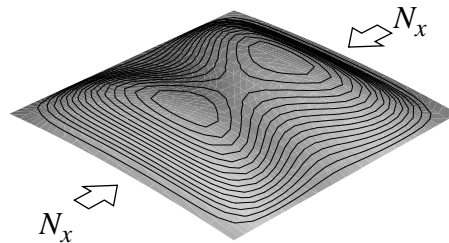
(d) Deformation at point C, ΔT = 420°F

Figure 3-9 Nonlinear response for a [±45/0/90]$_s$ laminate, clamped/fixed simple support boundary conditions

Deformations corresponding to the nonlinear response are shown in Fig. 3-11(b-g). Notice that the prebuckling deformation for the thermal response, Fig. 3-11(f), is similar to the prebuckling deformation for mechanical response, Fig. 3-11(b), but rotated by 90°. This is because the circumferential coefficient of thermal expansion, α_y, is much larger than the axial coefficient of thermal expansion. As a result, the panel behaves as though loaded in compression in the circumferential direction.
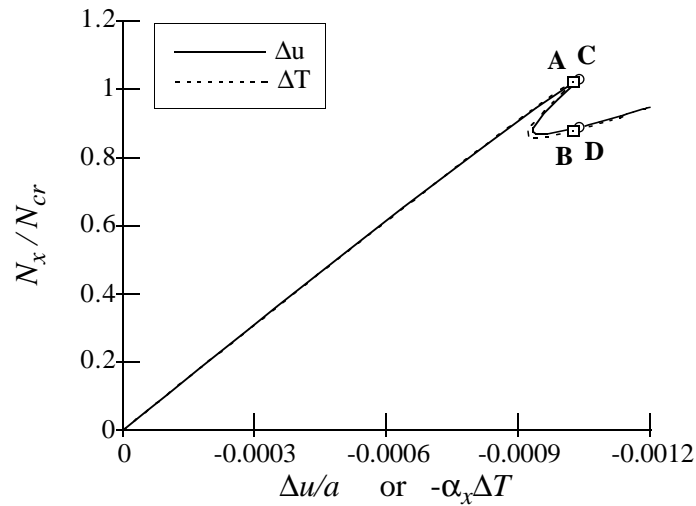
45

(a) Normalized axial force resultant vs. average mechanical strain response
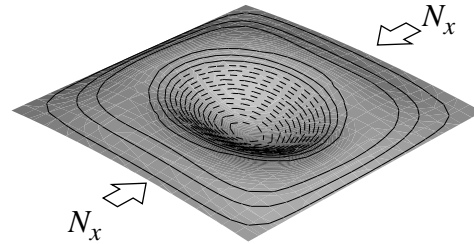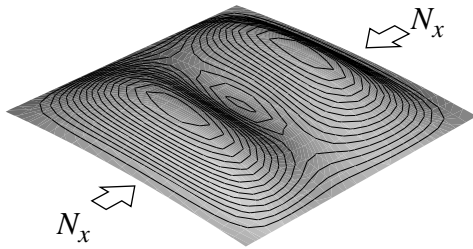
(b) Deformation at point A, Δu = -0.01039 in.

(c) Deformation at point B, Δu = -0.01039 in.
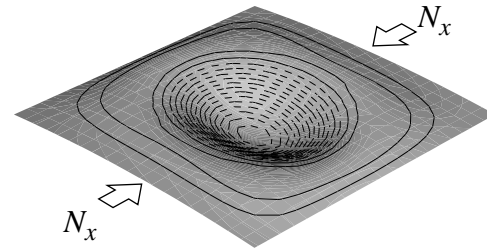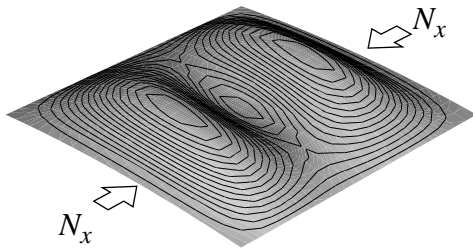
(d) Deformation at point C, ΔT = 236.0°F

(e) Deformation at point D, ΔT = 236.0°F

Figure 3-10 Nonlinear response for a $[\pm 45/90_2]_s$ laminate, clamped/fixed simple support boundary conditions

Force Resultant Distributions

The force resultant distributions immediately prior to buckling are given in Figs. 3-12, 3-13 and 3-14 for clamped/fixed simple supports, where the buckling solution N_{cr} from the simplified linear analysis is used for normalization. Notice that the force resultants have no sharp peaks in the cor-
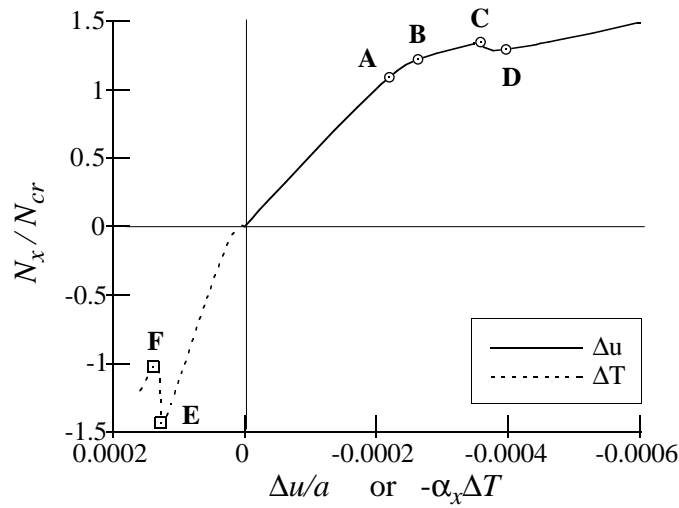
(a) Normalized axial force resultant vs. average mechanical strain response
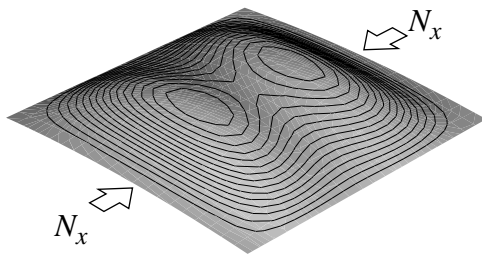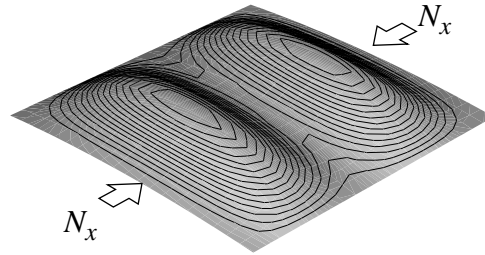
(b) Deformation at point A, Δu = -0.00219 in.   (c) Deformation at point B, Δu = -0.00263 in.
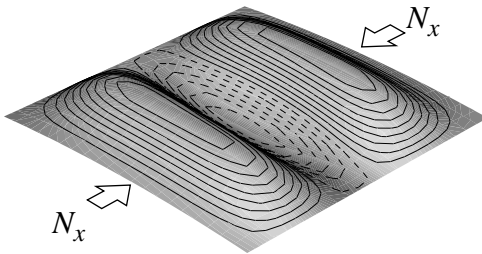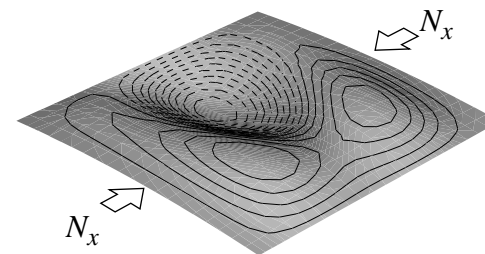
(d) Deformation at point C, Δu = -0.00358 in.   (e) Deformation at point D, Δu = -0.00396 in.
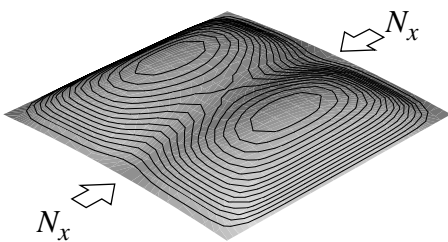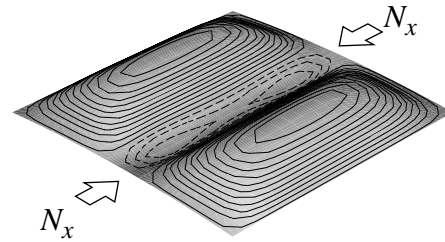
(f) Deformation at point E, ΔT = 799.8°F   (g) Deformation at point F, ΔT = 870.1°F

Figure 3-11 Thermal and mechanical response for a $[\pm 45/0_2]_s$ laminate, clamped/fixed simple supports

ners, as they did for clamped/sliding simple support boundary conditions of Figs. 3-5, 3-6 and 3-7. This is because the v-displacement has been restrained to be zero along the straight edge, just as it is at the corner points.   For both thermal and mechanical loading, the distribution of N_x is relatively uniform. However, the distribution of N_θ shows substantial gradients in the axial direction, particularly for the thermal response. Since the v-displacement was specified to be zero at all four edges, the force resultant N_θ is expected to be non-zero. The gradient in the axial direction can be attributed to the coupling between N_θ and moment resultant M_x along the curved ends due to the clamped boundary condition. These two resultants are coupled in the third equilibrium equation, which is given in linear form in Eq. (2.14).
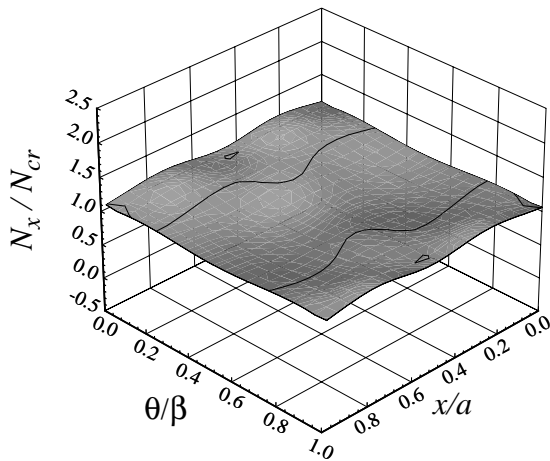
(a) Distribution of N_x immediately prior to
buckling, $\Delta u = $ -0.00459 in.
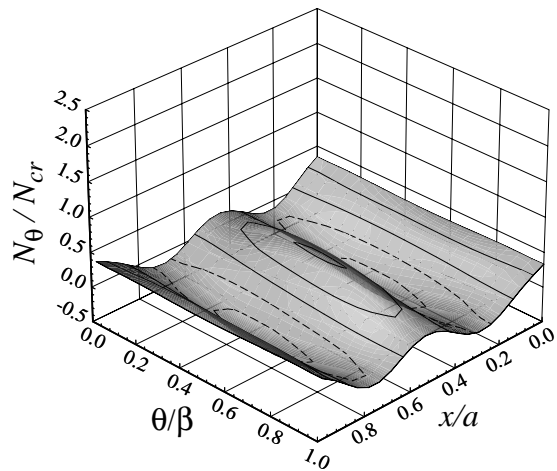
(b) Distribution of N_θ immediately prior to
buckling, $\Delta u = $ -0.00459 in.
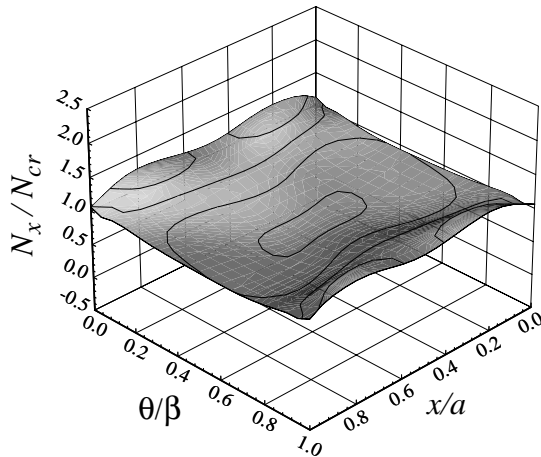
(c) Distribution of N_x, $\Delta T = 420°F$
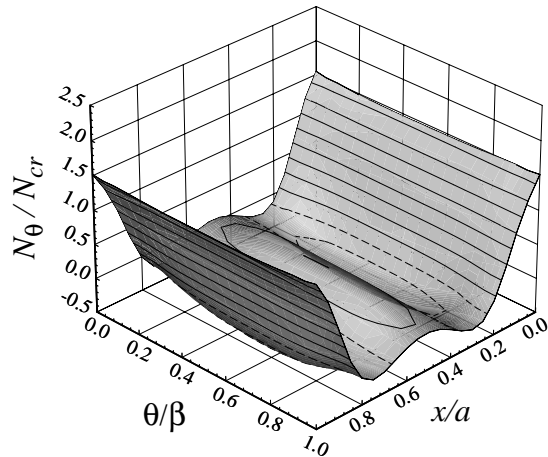
(d) Distribution of N_θ, $\Delta T = 420°F$

**Figure 3-12 Distribution of force resultants for a $[\pm 45/0/90]_s$ laminate, clamped/fixed
simple support boundary conditions**

Force resultant distributions for the $[\pm 45/90_2]_s$ laminate are shown in Fig. 3-13. The force result-ant distributions for thermal and mechanical loading are essentially the same, just as they were for the clamped/sliding simple support boundary conditions. Again there are gradients in the x-direc-tion for force resultant N_θ.

For the axially stiff $[\pm 45/0_2]_s$ laminate, the force resultants immediately prior to buckling are shown in Fig. 3-14. The force resultant distributions for the mechanical response are seen to be similar to the distributions observed for the other stacking sequences. The distribution of N_x is generally negative, or compressive, over the panel, and the distribution of N_θ is near zero. The resultant N_x, however, is not nearly as uniform as for the other laminates. Recalling that the nor-
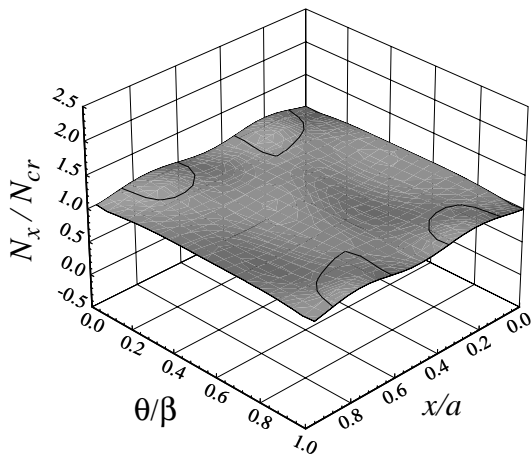
(a) Distribution of N_x, $\Delta u = -0.01039$ in.
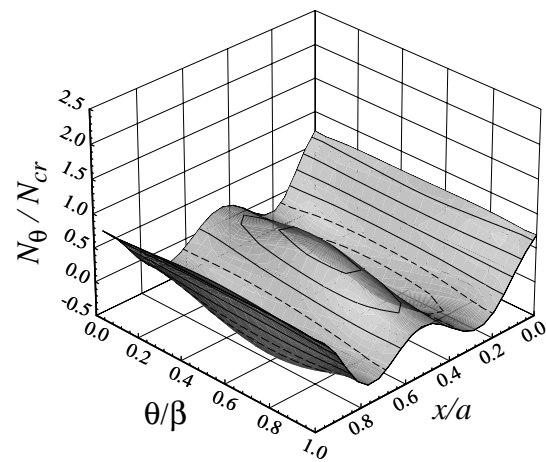
(b) Distribution of N_θ, $\Delta u = -0.01039$ in.
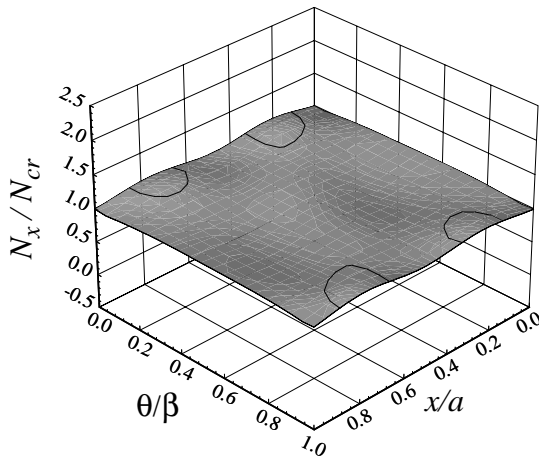
(c) Distribution of N_x, $\Delta T = 236.0°F$
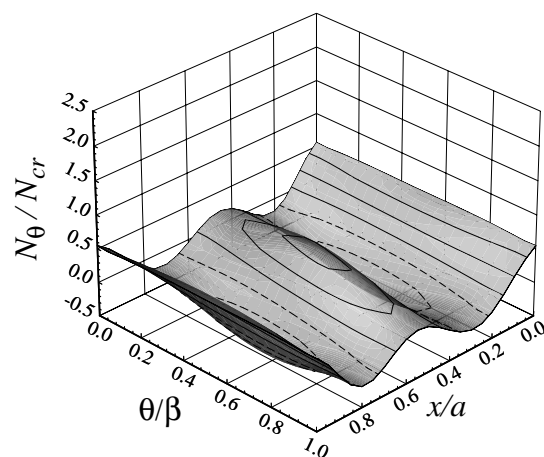
(d) Distribution of N_θ, $\Delta T = 236.0°F$

Figure 3-13 Distribution of force resultants immediately prior to buckling for a $[\pm 45/90_2]_s$ laminate, clamped/fixed simple support boundary conditions
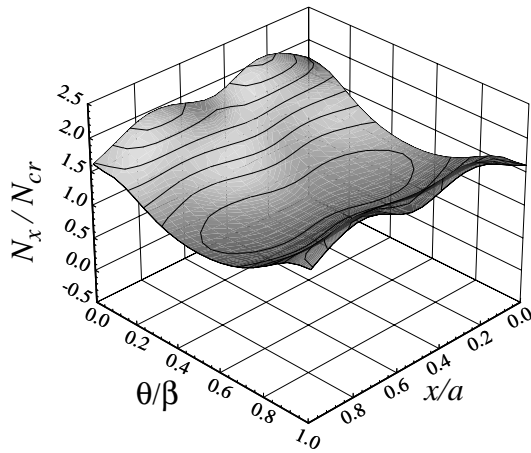
(a) Distribution of N_x, $\Delta u = -0.00358$ in.
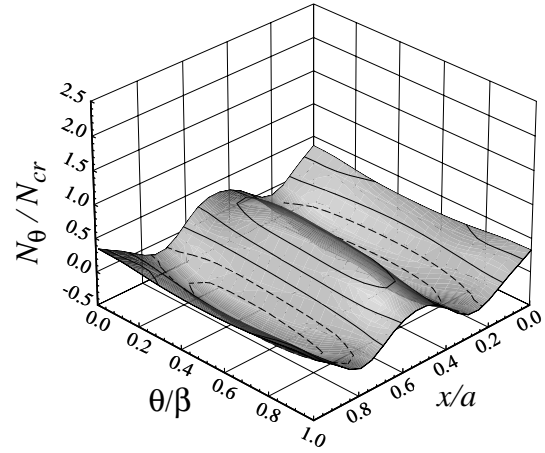
(b) Distribution of N_θ, $\Delta u = -0.00358$ in.
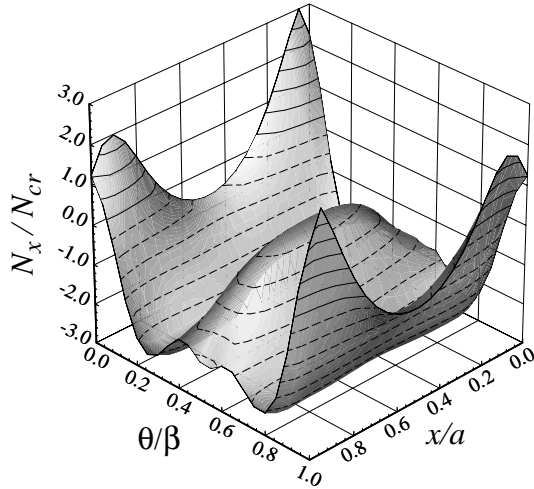
(c) Distribution of N_x, $\Delta T = 799.8°F$
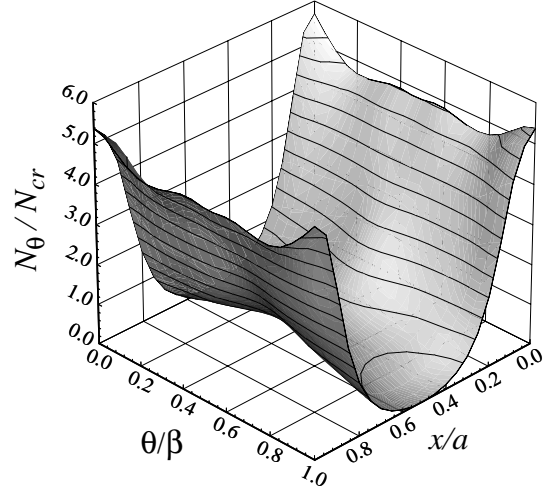
(d) Distribution of N_θ, $\Delta T = 799.8°F$

Figure 3-14 Distribution of force resultants immediately prior to buckling for a $[\pm 45/0_2]_s$ laminate, clamped/fixed simple support boundary conditions

malization factor N_{cr} is negative for this stacking sequence, we note that N_x from the thermal response is generally positive, or tensile, as it was for the clamped/sliding simple support boundary conditions. Also similar to the thermal response of clamped/sliding simple support boundary conditions, N_θ is seen to be always negative, or compressive, but here N_θ is much larger in magnitude due to the explicit enforcement of $v = 0$ along the straight edges.

In order to better understand the convergence difficulties encountered in the Rayleigh-Ritz solution for thermal loading of the axially stiff $[\pm 45/0_2]_s$ laminate, a comparison of the force and moment resultant distributions for both the STAGS and Rayleigh-Ritz solutions is shown in Fig.

3-15. Rayleigh-Ritz solutions with $N = 5$ and $N = 7$ are considered, using the assumed displacements given in Eq. (2.58). Since for this case buckling is dominated by expansion in the circumferential direction, which is opposed by the v-displacement restriction along the straight edges, distributions of N_θ and M_θ are considered. The postbuckling deformation, Fig. 3-11(g), is seen to resemble the prebuckling deformation, Fig. 3-11(f), but with the addition of a depression in the center of the panel. This implies that the distribution of force and moment resultants near the center of the panel are critical to panel buckling. In Fig. 3-15, the distributions of N_θ from the Rayleigh-Ritz solutions for $N = 5$ and $N = 7$ are seen to closely resemble the distribution of N_θ from STAGS. However, the distribution of M_θ for the Rayleigh-Ritz solution with $N = 5$ differs from the distribution of M_θ from STAGS, particularly near $\theta = \beta/2$, where the Rayleigh-Ritz distribution indicates a positive moment and STAGS indicates a negative moment. The Rayleigh-Ritz solution for $N = 5$ does not give a buckling solution for this panel with thermal loading. The distribution of M_θ for the Rayleigh-Ritz solution with $N = 7$ shows a closer match with the distribution of M_θ from STAGS, particularly near $\theta = \beta/2$ where both solutions indicate a negative moment. The Rayleigh-Ritz solution with $N = 7$ gives a reasonable solution for buckling, as was shown in Table 3-6, though it is less accurate than the solutions for the other stacking sequences. The Rayleigh-Ritz solution for $N = 6$ did not differ significantly from the solution for $N = 5$.

Summary

Curved panels with clamped/fixed simple support boundary conditions loaded with end-shortening or temperature change generally exhibit limit point buckling, when buckling occurs. The nonlinear responses due to end-shortening and due to temperature change are not the same for the $[\pm45/0/90]_s$ and $[\pm45/0_2]_s$ laminates. For the $[\pm45/90_2]_s$ laminate, responses due to end-shortening and due to temperature change are the same. Force resultant distributions are smooth, but with substantial gradients in N_θ in the axial direction. As compared to clamped/sliding simple support boundary conditions, curved panels with clamped/fixed simple support boundary conditions generally buckle at higher loads, and exhibit a different response character.

3.2.3 Sliding Clamped/Sliding Simple Support Boundary Conditions

In contrast to the boundary condition termed clamped/fixed simple supports, which has complete restriction of v-displacement on the boundaries, the effects of unrestricted v-displacement are considered with the boundary condition termed sliding clamped/sliding simple supports, as defined in Fig. 3-16. This boundary condition is studied only with STAGS. It differs from the original clamped/sliding simple support boundary condition of sec. 3.2.1 only in the amount of circumfer-
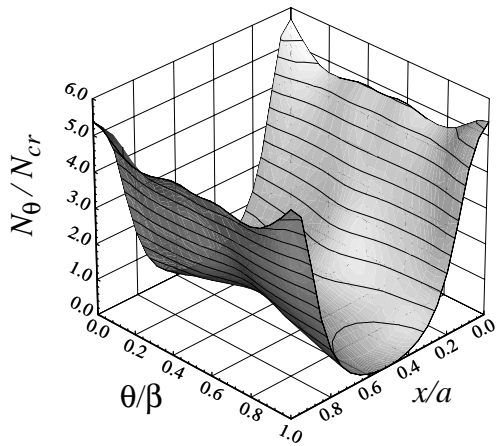
(a) Distribution of N_θ, $\Delta T = 799.8°F$, STAGS
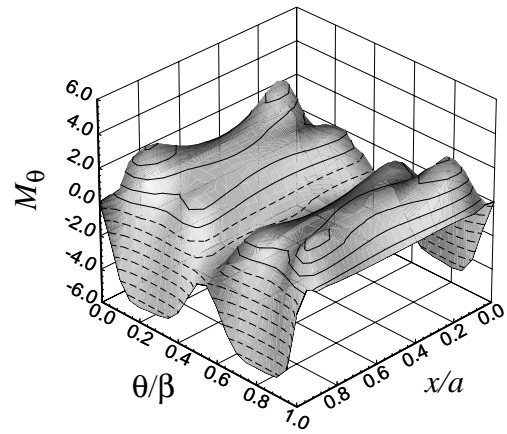
(b) Distribution of M_θ, $\Delta T = 799.8°F$, STAGS
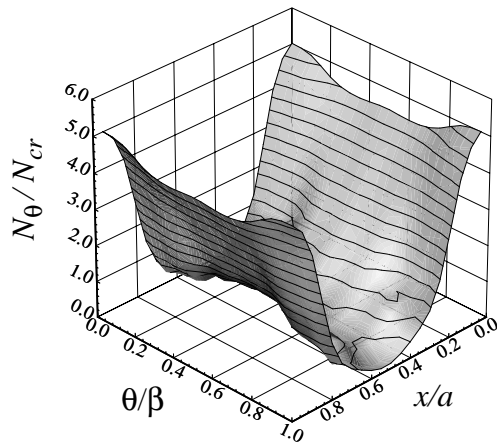
(c) Distribution of N_θ, $\Delta T = 800°F$,
Rayleigh-Ritz with $N = 5$
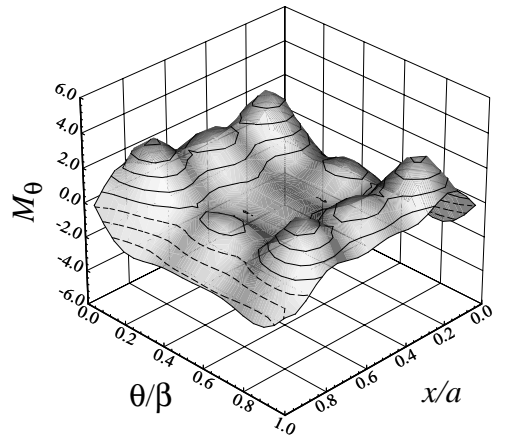
(d) Distribution of M_θ, $\Delta T = 800°F$,
Rayleigh-Ritz with $N = 5$
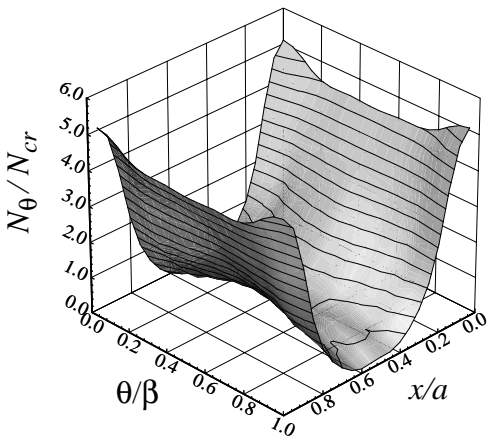
(e) Distribution of N_θ, $\Delta T = 800°F$,
Rayleigh-Ritz with $N = 7$
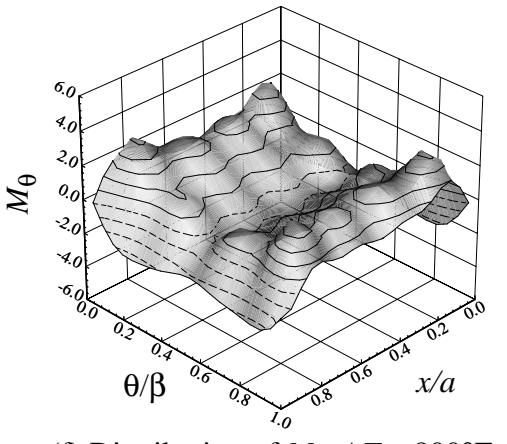
(f) Distribution of M_θ, $\Delta T = 800°F$,
Rayleigh-Ritz with $N = 7$

Figure 3-15 Distribution of force and moment resultants immediately prior to buckling for a $[\pm 45/0_2]_s$ laminate, clamped/fixed simple support boundary conditions
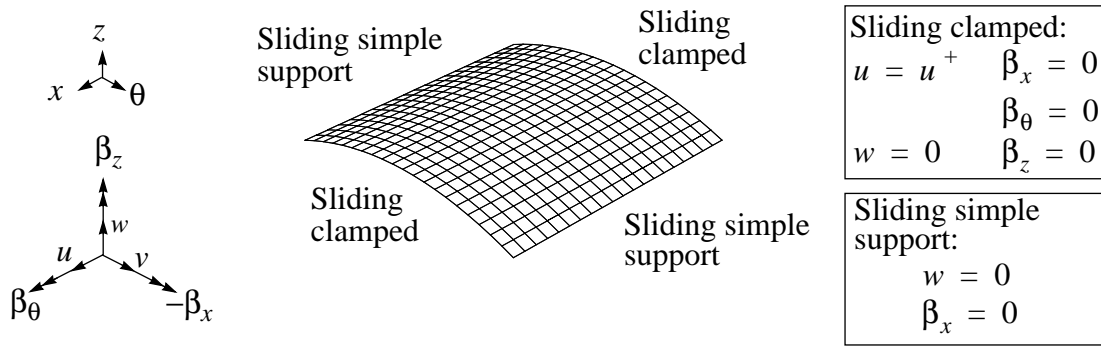
Figure 3-16 Sliding clamped/sliding simple support boundary conditions

ential restraint provided along the curved edges. The curved end boundary condition is termed sliding clamped because, like the clamped condition, radial w-displacement and all of the rotations are restricted, but unlike the clamped condition, circumferential v-displacement is allowed. Such a situation might occur in an experiment when the clamps were sufficiently tight to prevent rotation of the curved ends, but would not prevent tangential displacement due to Poisson or thermal expansion effects. In fact, these boundary conditions closely match the prebuckling membrane boundary conditions of the simplified linear analysis.

Buckling results from STAGS are given in Table 3-6. The buckling force N_{cr} from the simplified linear solution of Table 3-3 is used to normalize the axial force resultants, N_x. Buckling for sliding clamped/sliding simple support boundary conditions occurs at a bifurcation point followed by an unstable postbuckling response.

Table 3-6 Buckling values from STAGS solution, sliding clamped/sliding simple support boundary conditions

		Mechanical loading		Thermal loading	
		Δu_{max}, in.	N_x / N_{cr}	ΔT_{max},°F	N_x / N_{cr}
$[\pm 45/0/90]_s$	STAGS	-0.00386 (b)	0.936	339.9 (b)	0.936
$[\pm 45/90_2]_s$	STAGS	-0.00888 (b)	0.898	204.4 (b)	0.898
$[\pm 45/0_2]_s$	STAGS	-0.00199 (b)	1.008	does not buckle	

* Bifurcation buckling is indicated by a (b), limit point buckling is indicated by an (l).

For the quasi-isotropic $[\pm 45/0/90]_s$ laminate and the axially soft $[\pm 45/90_2]_s$ laminate, the axial force resultant at bucking, N_x, is the same for both mechanical and thermal loading, as seen in

Table 3-6. This can be attributed to the uniaxial character of the loading, either thermal or mechanical, that occurs when circumferential *v*-displacement is unrestricted. Since both thermal and mechanical loading produce uniaxial stresses, both also give the same buckling load N_x. The axially stiff $[\pm 45/0_2]_s$ laminate does not buckle due to an increase in temperature. This is because the thermal expansion in the axial direction is negative, while the positive thermal expansion in the circumferential direction encounters no resistance. Recall the coefficients of thermal expansion given in Table 3-2. For all three laminates, the buckling displacements, temperatures, and force resultants are lower than those seen in Table 3-6 for clamped/sliding simple supports. A decrease in the amount of restraint at the edges results in a decrease in the buckling values.

Nonlinear Response

The geometrically nonlinear response predicted by STAGS for the quasi-isotropic $[\pm 45/0/90]_s$ laminate with sliding clamped/sliding simple supports is shown in Fig. 3-17(a). As with previous responses, the axial force resultant on the vertical axis is normalized by the simplified linear buckling values of Table 3-3. The geometrically nonlinear responses for mechanical loading, Δu, and thermal loading, ΔT, are the same. This is unlike the responses of the $[\pm 45/0/90]_s$ laminate for the other two boundary conditions, Figs. 3-2(a) and 3-9(a), which were different for mechanical vs. thermal loading. The character of the response is very similar to the response for clamped/sliding simple supports shown in Fig. 3-2(a), except that the prebuckling response for both loadings is linear, with no radial *w*-displacement. Identical postbuckling deformations are shown in Fig. 3-17(b) for end-shortening and Fig. 3-17(c) for uniform temperature change.

The nonlinear response of the axially soft $[\pm 45/90_2]_s$ laminate is shown in Fig. 3-18(a) for sliding clamped/sliding simple supports. The thermal and mechanical responses are nearly identical, as was observed for the $[\pm 45/90_2]_s$ laminate with clamped/sliding simple supports, Fig. 3-3(a), and clamped/fixed simple supports, Fig. 3-10(a). The response is very similar to the response observed for clamped/sliding simple supports, Fig. 3-3(a), with bifurcation buckling followed by an unstable postbuckling response. Prebuckling response is linear, with no radial *w*-displacements. Postbuckling deformations for end-shortening are shown in Fig. 3-18(b), and for uniform temperature change in Fig. 3-18(c). The deformations are again the same for both loading conditions.

Nonlinear response of the axially stiff $[\pm 45/0_2]_s$ laminate with sliding clamped/sliding simple supports is shown in Fig. 3-19(a). For end-shortening, bifurcation buckling occurs at a lower load than it did for the clamped/sliding simple supports of Fig. 3-4(a), and just after the point where
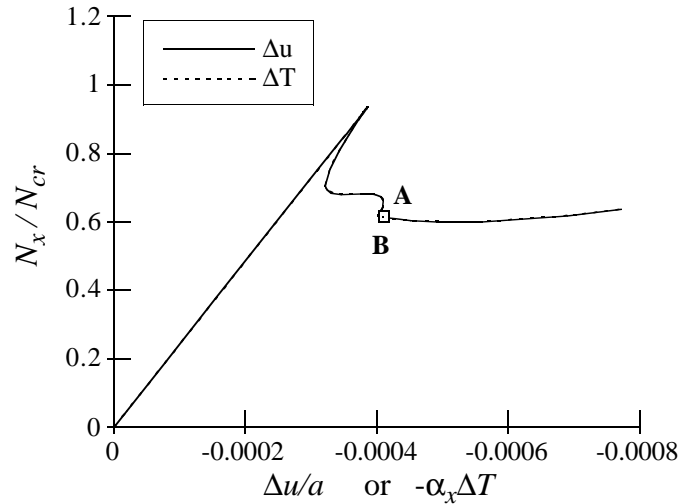
(a) Normalized axial force resultant vs. average mechanical strain response
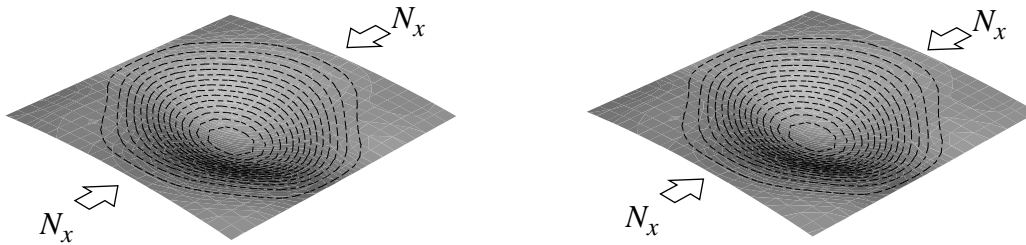
(b) Deformation at point A, Δu = -0.00410 in.   (c) Deformation at point B, ΔT = 361.3°F

Figure 3-17 Nonlinear response for a [±45/0/90]$_s$ laminate, sliding clamped/sliding simple support boundary conditions

stiffness changed in the response of the clamped/fixed simple support laminate, point A of Fig. 3-11(a). Buckling due to mechanical loading is followed by a collapse to an unstable postbuckling configuration, which quickly regains stability as the end-shortening is further increased. The thermal response does not indicate buckling with an increase in temperature, and instead indicates a decrease in axial load with the same load vs. strain slope as the mechanical response. Postbuckling deformations are shown in Fig. 3-19(b) and (c). The postbuckling deformation for mechanical response is similar to the final postbuckling deformation for the mechanical response of clamped/sliding simple supports, Fig. 3-4(d). The panel subjected to uniform temperature change does not exhibit any radial w-displacement, similar to the prebuckling response of all the laminates with sliding clamped/sliding simple supports. Because the coefficient of thermal expansion in the axial direction, α_x, is negative, an increase in temperature will results in a positive axial force N_x. With circumferential v-displacement unrestricted, no circumferential force N_θ devel-
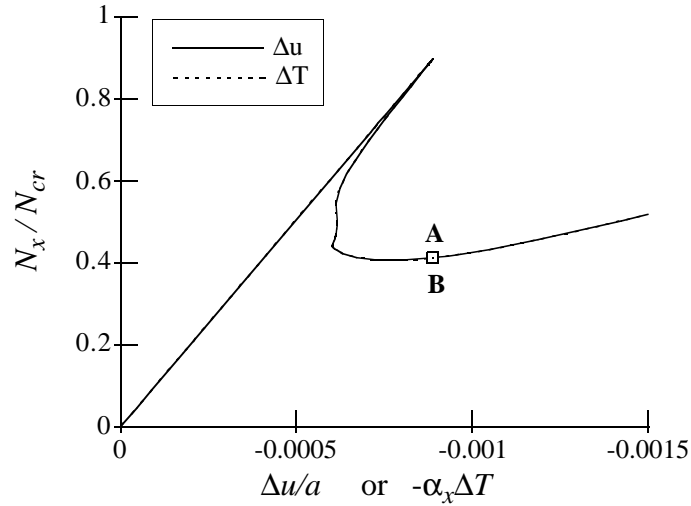
(a) Normalized axial force resultant vs. average mechanical strain response
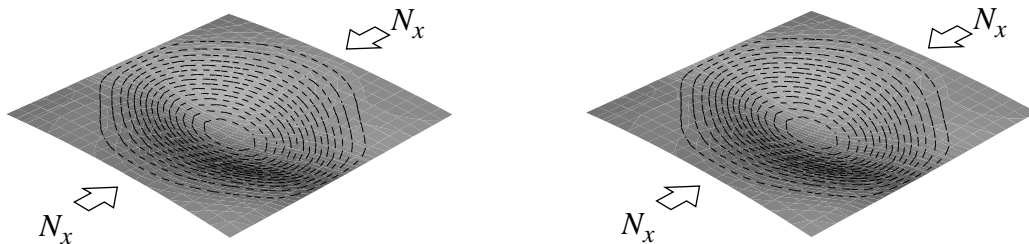
(b) Deformation at point A, $\Delta u = -0.00888$ in. (c) Deformation at point B, $\Delta T = 204.4°F$

Figure 3-18 Nonlinear response for a [$\pm 45/90_2$]$_s$ laminate, sliding clamped/sliding simple support boundary conditions

ops, so the panel tends to shrink in the axial direction and expand in the circumferential direction without resistance and without occurrence of radial *w*-displacements.

Force Resultant Distributions

The force resultant distributions for sliding clamped/sliding simple support boundary conditions are essentially uniform. Since circumferential *v*-displacement is unrestricted all along the straight edges, including the corners, the circumferential force resultant N_θ is zero both at the edges and over the interior of the panel. The unrestricted circumferential expansion also results in a uniform axial force resultant N_x.
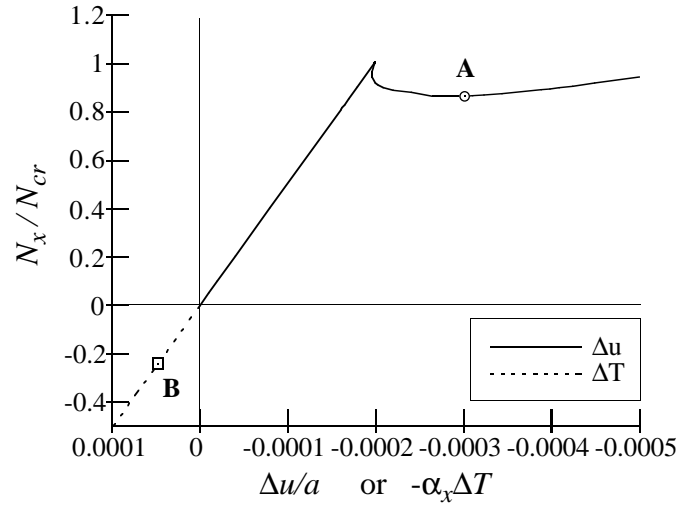
(a) Normalized axial force resultant vs. average mechanical strain response
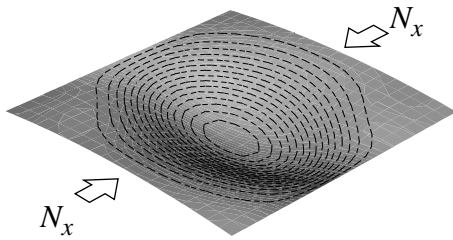
(b) Deformation at point A, $\Delta u = $ -0.00301 in.
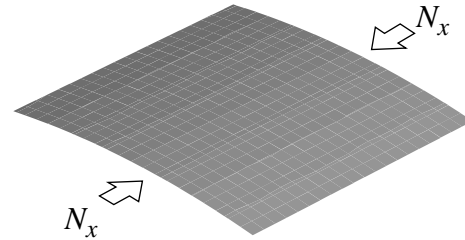
(c) Deformation at point B, $\Delta T = 300°$F

Figure 3-19 Nonlinear response for a $[\pm 45/0_2]_s$ laminate, sliding clamped/sliding simple support boundary conditions

Summary

Curved panels with sliding clamped/sliding simple support boundary conditions loaded with end-shortening or temperature change buckle due to bifurcation, when buckling occurs. The non-linear responses for the $[\pm 45/0/90]_s$ and $[\pm 45/90_2]_s$ laminates due to end-shortening and due to temperature change are the same. For the $[\pm 45/0_2]_s$ laminate, responses due to end-shortening and due to temperature change are different, since a positive temperature change results in a positive axial force. The force resultant distribution of N_x is uniform, and N_θ is equal to zero. As compared to clamped/sliding simple support boundary conditions, curved panels with sliding clamped/sliding simple support boundary conditions buckle at lower loads.

3.3 Effect of Panel Radius

Before generalizations can be made about the behavior of curved panels, the effects of panel radius need to be considered. With the panel dimensions of 10 in. by 10 in. held constant, and considering the clamped/sliding simple support boundary conditions, the panel radius was gradually changed from 60 in. to 20 in. The resulting buckling values are listed in Table 3-7. For both mechanical and thermal loading, the buckling load increases with decreasing radius. The

Table 3-7 Buckling values from STAGS solution, radius effect, clamped/sliding simple support boundary conditions

		Mechanical loading		Thermal loading	
		Δu_{max}, in.	N_x, lbs./in.	ΔT_{max},°F	N_x, lbs./in.
$[\pm45/0/90]_s$	$R = 60$ in.	-0.00404	-135.9	512.8	-153.3
	$R = 50$ in.	-0.00447	-151.5	468.0	-157.0
	$R = 40$ in.	-0.00535	-182.3	511.4	-180.0
	$R = 30$ in.	-0.00743	-252.8	682.3	-240.8
	$R = 20$ in.	-0.01064	-362.4	959.3	-345.6
$[\pm45/90_2]_s$	$R = 60$ in.	-0.00906	-132.0	206.7	-131.2
	$R = 50$ in.	-0.01008	-147.0	231.4	-147.5
	$R = 40$ in.	-0.01204	-176.0	276.5	-176.6
	$R = 30$ in.	-0.01560	-229.0	358.5	-229.0
	$R = 20$ in.	-0.02256	-331.1	520.8	-332.5
$[\pm45/0_2]_s$	$R = 60$ in.	-0.00254	-118.7	1150.0	136.0
	$R = 50$ in.	-0.00273	-129.4	1276.8	148.7
	$R = 40$ in.	-0.00312	-149.5	1495.1	172.4
	$R = 30$ in.	-0.00397	-192.6	1759.2	257.7
	$R = 20$ in.	-0.00605	-288.6	2465.0	372.2

end-shortening at buckling also increases with decreasing radius, while the temperature at buckling generally increases except for the change from R=60 in. to R=50 in. for the $[\pm45/0/90]_s$ laminate, when buckling temperature decreases slightly.

The nonlinear response of the quasi-isotropic $[\pm45/0/90]_s$ laminate subjected to uniform end-shortening is shown in Fig. 3-20(a) for various radii. The slope of the prebuckling response remains constant with changes in radius, but the postbuckling response shows a change in character from $R = 40$ in. to $R = 30$ in. and again for $R = 20$ in. This corresponds to the changes in postbuckling deformed shapes, as shown in Fig. 3-20(b-f). Postbuckling deformed shapes are shown at three times the end-shortening at buckling, Δu_{max}, from Table 3-7. As the radius decreases, the postbuckling deformation pattern approaches the diamond-shaped pattern commonly observed in postbuckling of complete cylinders, see refs. [63, 64] for example.

For the quasi-isotropic $[\pm45/0/90]_s$ laminate subjected to temperature change, the nonlinear responses for various radii are shown in Fig. 3-21(a). The initial slope of the prebuckling response is the same for all radii. The slope of the prebuckling response near buckling changes slightly depending on the radius, particularly for $R = 60$ in., $R = 50$ in., and $R = 40$ in., which all buckle at similar temperatures. The character of the postbuckling response and the postbuckling deformed shapes remain essentially the same for all the radii considered. Postbuckling deformed shapes, Fig. 3-21(b-f) are shown at three times the temperature change at buckling, ΔT_{max}, from Table 3-7. The postbuckling responses for the thermal case are somewhat simpler than for the end-shortening case, there not being as many secondary instabilities with the thermal case.

The nonlinear response of the axially soft $[\pm45/90_2]_s$ laminate subjected to uniform end-shortening is shown in Fig. 3-22(a) for various radii. For all radii considered, the prebuckling stiffness is the same, although the postbuckling response changes character for $R = 20$ in. as compared to $R = 30$ in. or more. Correspondingly, the postbuckling deformation pattern for $R = 20$ in. has three inward buckles as shown in Fig. 3-22(f). The postbuckling deformation patterns for $R = 30$ in. and greater have just one inward buckle each as shown in Fig. 3-22(b-e). As with the $[\pm45/0/90]_s$ laminate, a decrease in radius to 20 in. results in postbuckling behavior for a curved panel similar to the postbuckling behavior of a complete cylinder.

For loading due to temperature change, the nonlinear response of the axially soft $[\pm45/90_2]_s$ laminate for various radii is shown in Fig. 3-23(a). By comparing Figs. 3-22(a) and 3-23(a), the response due to thermal loading is seen to be nearly identical to the response due to end-shortening for each radius considered, as has been the case for the this laminate throughout the study. Postbuckling deformation patterns also correspond for thermal and mechanical loading of this laminate, with the deformation pattern notably changing for $R = 20$ in., Fig. 3-23(f) as compared to $R = 30$ in. and greater, Fig. 3-23(b-e).

(a) Axial force resultant vs. average mechanical strain response

(b) Deformation at $\Delta u/\Delta u_{max} = 3.0$, $R = 60$ in. (c) Deformation at $\Delta u/\Delta u_{max} = 3.0$, $R = 50$ in.

(d) Deformation at $\Delta u/\Delta u_{max} = 3.0$, $R = 40$ in. (e) Deformation at $\Delta u/\Delta u_{max} = 3.0$, $R = 30$ in.

(f) Deformation at $\Delta u/\Delta u_{max} = 3.0$, $R = 20$ in.

Figure 3-20 Nonlinear response for [±45/0/90]$_s$ laminates with different radii due to end-shortening

(a) Axial force resultant vs. average mechanical strain response

(b) Deformation at $\Delta T/\Delta T_{max} = 3.0$, $R = 60$ in.   (c) Deformation at $\Delta T/\Delta T_{max} = 3.0$, $R = 50$ in.

(d) Deformation at $\Delta T/\Delta T_{max} = 3.0$, $R = 40$ in.   (e) Deformation at $\Delta T/\Delta T_{max} = 3.0$, $R = 30$ in.

(f) Deformation at $\Delta T/\Delta T_{max} = 3.0$, $R = 20$ in.

Figure 3-21 Nonlinear response for $[\pm 45/0/90]_s$ laminates with different radii due to temperature change

(a) Axial force resultant vs. average mechanical strain response

(b) Deformation at $\Delta u/\Delta u_{max} = 3.0$, $R = 60$ in.

(c) Deformation at $\Delta u/\Delta u_{max} = 3.0$, $R = 50$ in.

(d) Deformation at $\Delta u/\Delta u_{max} = 3.0$, $R = 40$ in.

(e) Deformation at $\Delta u/\Delta u_{max} = 3.0$, $R = 30$ in.

(f) Deformation at $\Delta u/\Delta u_{max} = 3.0$, $R = 20$ in.

Figure 3-22 Nonlinear response for [±45/90$_2$]$_s$ laminates with different radii due to end-shortening

(a) Axial force resultant vs. average mechanical strain response

(b) Deformation at $\Delta T/\Delta T_{max} = 3.0$, $R = 60$ in. (c) Deformation at $\Delta T/\Delta T_{max} = 3.0$, $R = 50$ in.

(d) Deformation at $\Delta T/\Delta T_{max} = 3.0$, $R = 40$ in. (e) Deformation at $\Delta T/\Delta T_{max} = 3.0$, $R = 30$ in.

(f) Deformation at $\Delta T/\Delta T_{max} = 3.0$, $R = 20$ in.

Figure 3-23 Nonlinear response for $[\pm 45/90_2]_s$ laminates with different radii due to temperature change

The nonlinear response of the axially stiff $[\pm 45/0_2]_s$ laminate with various radii loaded in uniform end-shortening is shown in Fig. 3-24(a). Again, the prebuckling stiffness is the same for all radii. The character of the postbuckling response changes from $R = 40$ in. to $R = 30$ in., and appears to change again from $R = 30$ in. to $R = 20$ in., although the postbuckling solution for $R = 20$ in. could not be completed due to the close proximity of many solution paths. The postbuckling deformation pattern for $R = 30$ in., Fig. 3-24(e), is correspondingly different than the postbuckling deformation patterns for $R = 40$ in. and more, Fig. 3-24(b-d). The deformation for $R = 30$ in. is
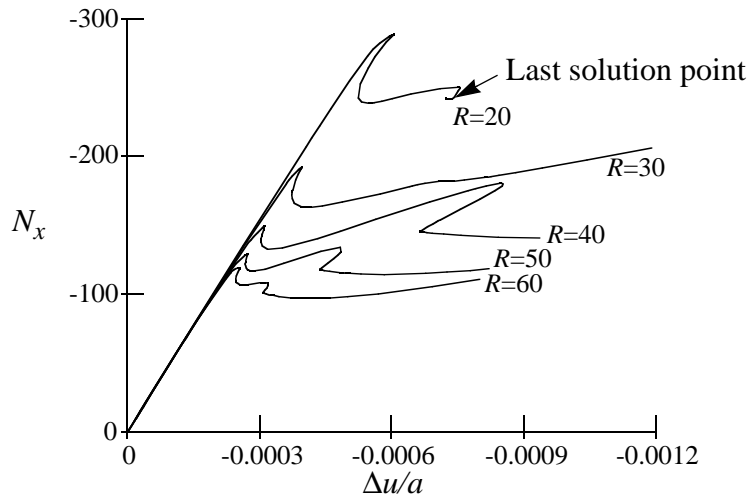
(a) Axial force resultant vs. average mechanical strain response
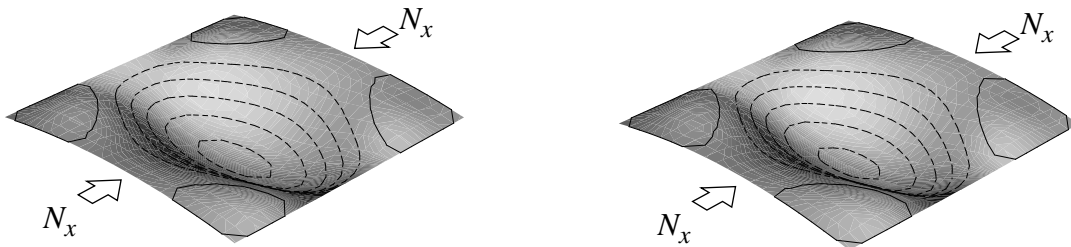
(b) Deformation at $\Delta u/\Delta u_{max} = 3.0$, $R = 60$ in. (c) Deformation at $\Delta u/\Delta u_{max} = 3.0$, $R = 50$ in.
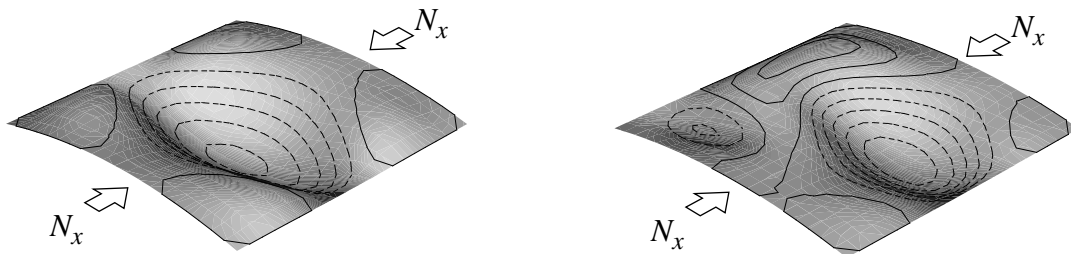
(d) Deformation at $\Delta u/\Delta u_{max} = 3.0$, $R = 40$ in. (e) Deformation at $\Delta u/\Delta u_{max} = 3.0$, $R = 30$ in.

Figure 3-24 Nonlinear response for $[\pm 45/0_2]_s$ laminates with different radii due to end-shortening

approaching the diamond pattern typically associated with the postbuckling of complete cylinders.

The nonlinear response due to temperature change for the axially stiff $[\pm45/0_2]_s$ laminate with various radii is shown in Fig. 3-25(a). For $R = 60$ in. through $R = 30$ in. the prebuckling stiffness is the same, but for $R = 20$ in. the prebuckling stiffness is slightly softer. Although the character of the postbuckling response changes slightly from $R = 40$ in. to $R = 30$ in., the corresponding postbuckling deformations, Fig. 3-25(d-e) are essentially the same. For $R = 20$ in., the postbuckling solution again could not be completed due to the close proximity of multiple solutions. Even at $R = 30$ in., the postbuckling deformation pattern still appears similar to the postbuckling pattern of the original shallow curved panel, $R = 60$ in. in Fig. 3-25(b). This is because the buckling of this laminate under thermal loading is dominated by circumferential strains due to this laminates large, positive α_y and small, negative α_x. A complete cylinder would not experience the same circumferential strains as this curved panel with clamped supports along the curved ends and sliding simple supports along the straight edges.

3.4 Combined Loading

The effects of combined thermal and mechanical loading are studied using geometrically nonlinear analysis conducted with STAGS for clamped/sliding simple support boundary conditions as defined in Fig. 3-1. End-shortening and temperature change are applied sequentially, with their magnitudes based on the buckling values, Δu_{max} and ΔT_{max}, predicted for end-shortening and temperature change applied separately, as listed in Table 3-6. Six loading combinations are considered, including three with end-shortening, Δu, applied first, and three with temperature change, ΔT, applied first. The initial loading is held at either 25%, 50% or 75% of the buckling value, followed by the other loading applied until the panel buckles and achieves a stable postbuckling response. Buckling combinations of $\Delta u/\Delta u_{max}$, $\Delta T/\Delta T_{max}$, and the normalized load at buckling are listed in Tables 3-8, 3-9, and 3-10. The buckling load N_x is normalized by the buckling load from the simplified linear analysis N_{cr} as listed originally in Table 3-3.

By examining Table 3-8 for the quasi-isotropic $[\pm45/0/90]_s$ laminate, buckling due to combined thermal and mechanical loading is seen to occur at lower axial strains than when loading was applied separately, as indicated by $\Delta u/\Delta u_{cr} + \Delta T/\Delta T_{cr} < 1.0$. The load at buckling due to combined end-shortening and temperature change falls between the predicted load for end-shortening alone and temperature change alone, as seen by comparison between Table 3-8 and 3-4.
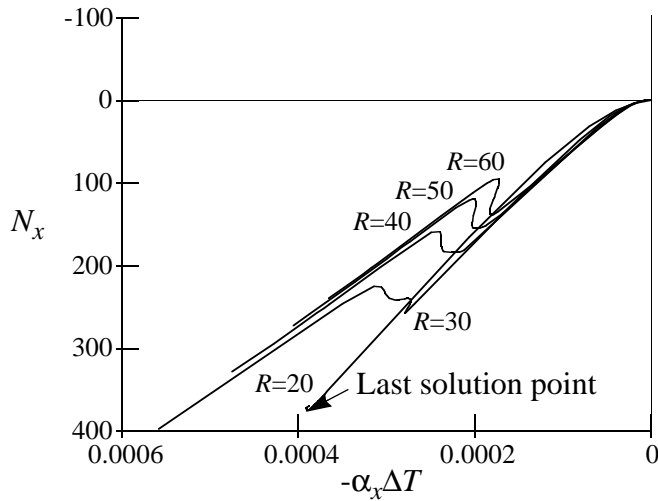
(a) Axial force resultant vs. average mechanical strain response
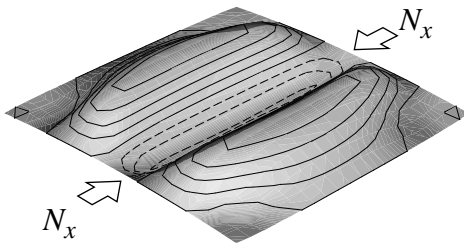
(b) Deformation at $\Delta T/\Delta T_{max} = 3.0$, $R = 60$ in. (c) Deformation at $\Delta T/\Delta T_{max} = 3.0$, $R = 50$ in.
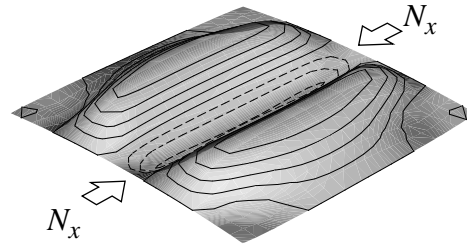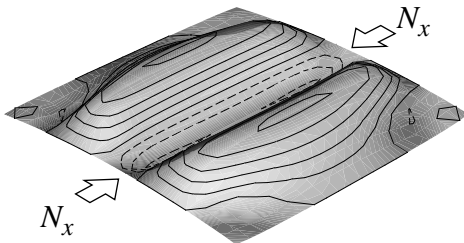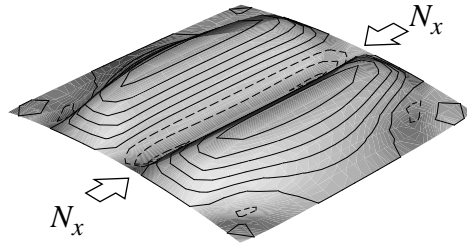
(d) Deformation at $\Delta T/\Delta T_{max} = 3.0$, $R = 40$ in. (e) Deformation at $\Delta T/\Delta T_{max} = 3.0$, $R = 30$ in.

Figure 3-25 Nonlinear response for $[\pm45/0_2]_s$ laminates with different radii due to temperature change

From Table 3-9 for the axially soft $[\pm45/90_2]_s$ laminate, note that buckling occurs when $\Delta u/\Delta u_{cr}$ + $\Delta T/\Delta T_{cr} = 1.0$. This indicates that the axial strain required for buckling is the same for combined end-shortening and temperature change or loading applied separately. This is very interesting but is to be expected, since the axial strains and loads at buckling were the same for end-shortening alone and temperature change alone, as shown in Fig. 3-3(a).

Table 3-8 Buckling combinations from STAGS solution, $[\pm45/0/90]_s$, combined loading

	$\Delta u/\Delta u_{max}$ $\Delta u_{max} = -0.00404$	$\Delta T/\Delta T_{max}$ $\Delta T_{max} = 512.8°F$	N_x/N_{cr} $N_{cr} = -141.0$ lbs./in.
$[\pm45/0/90]_s$ Initial loading ΔT	0.217	0.750	1.054
	0.450	0.500	1.021
	0.707	0.250	0.988
$[\pm45/0/90]_s$ Initial loading Δu	0.250	0.713	1.049
	0.500	0.449	1.014
	0.750	0.211	0.984

Table 3-9 Buckling combinations from STAGS solution, $[\pm45/90_2]_s$, combined loading

	$\Delta u/\Delta u_{max}$ $\Delta u_{max} = -0.00906$	$\Delta T/\Delta T_{max}$ $\Delta T_{max} = 206.7°F$	N_x/N_{cr} $N_{cr} = -145.0$ lbs./in.
$[\pm45/90_2]_s$ Initial loading ΔT	0.250	0.750	0.906
	0.500	0.500	0.907
	0.750	0.250	0.909
$[\pm45/90_2]_s$ Initial loading Δu	0.250	0.750	0.906
	0.500	0.500	0.907
	0.750	0.250	0.909

Table 3-10 Buckling combinations from STAGS solution, $[\pm45/0_2]_s$, combined loading

	$\Delta u/\Delta u_{max}$ $\Delta u_{max} = -0.00254$	$\Delta T/\Delta T_{max}$ $\Delta T_{max} = 1150.0°F$	N_x/N_{cr} $N_{cr} = -100.3$ lbs./in.
$[\pm45/0_2]_s$ Initial loading ΔT	does not buckle	0.750	does not buckle
	does not buckle	0.500	does not buckle
	does not buckle	0.250	does not buckle
$[\pm45/0_2]_s$ Initial loading Δu	0.250	1.027	-1.217
	0.500	1.059	-1.088
	0.750	1.094	-0.979

The buckling combinations for the axially stiff $[\pm45/0_2]_s$ laminate are listed in Table 3-10. When initial loading is due to temperature change, buckling does not occur. This is likely due to the radial deformations that occurs during thermal loading, shown in Fig. 3-4(e), which are never overcome by the axially applied end-shortening. When initial loading is due to end-shortening, buckling still occurs at very near the same temperature, ΔT_{max}, as when no initial mechanical loading was present, as indicated by values of $\Delta T/\Delta T_{max}$ near 1.0. This is because thermal buckling of this laminate is dominated by strain in the circumferential direction, which is influenced only through Poisson's ratio during end-shortening. Therefore, since the circumferential strain induced by axial end-shortening is small compared to the circumferential strain induced by temperature change, the initial axial end-shortening has little effect on buckling temperature. However, since initial end-shortening causes a compressive endload on the panel, increasing levels of initial end-shortening reduce the tensile buckling load N_x due to thermal loading.

The nonlinear responses for the $[\pm45/0/90]_s$ laminate subjected to combined loading are shown in Fig. 3-26. The solid line indicates that initial loading is due to temperature change, followed by loading due to end-shortening, as in Fig. 3-26(a), (c), and (e). Since $\Delta u/a$ is plotted along the horizontal axis, the initial thermal loading portion of the response appears as a vertical line at $\Delta u/a = 0$. For these three cases, notice that the character of the postbuckling response is quite similar. The dashed line indicates that initial loading is due to end-shortening, followed by loading due to temperature change, as in Fig. 3-26(b), (d), and (f). These response curves are plotted with $-\alpha_x\Delta T$ on the horizontal axis, so the initial end-shortening portion of the response appears as a vertical line at $-\alpha_x\Delta T = 0$. Comparing the postbuckling response for these three cases, note that for a large initial end-shortening, Fig. 3-26(f), the response takes on the character of mechanical loading alone, and for a small initial end-shortening, Fig. 3-26(b), the response is similar in character to thermal loading alone, (see Fig. 3-2(a)).

Points A-F represents solutions where $\Delta u/\Delta u_{cr} + \Delta T/\Delta T_{cr} = 1.0$. These correspond to the deformation patterns of Fig. 3-27. Although the nonlinear responses in Fig. 3-26(a) and (b) are quite different, the postbuckling deformation patterns at points A and B are identical, Fig. 3-27(a) and (b), as are their corresponding loads, N_x / N_{cr}. This indicates that a particular solution is independent of load path, since for $\Delta u/\Delta u_{cr} = 0.25$ and $\Delta T/\Delta T_{cr} = 0.75$, only one postbuckling solution exists with one unique load and deformation pattern. This observation regarding path independence is further supported by the examining the deformation patterns of Fig. 3-27(c) and (d) and Fig. 3-27(e) and (f).

(a) $\Delta T/\Delta T_{cr} = 0.75$, then Δu

(b) $\Delta u/\Delta u_{cr} = 0.25$, then ΔT

(c) $\Delta T/\Delta T_{cr} = 0.5$, then Δu

(d) $\Delta u/\Delta u_{cr} = 0.5$, then ΔT

(e) $\Delta T/\Delta T_{cr} = 0.25$, then Δu

(f) $\Delta u/\Delta u_{cr} = 0.75$, then ΔT
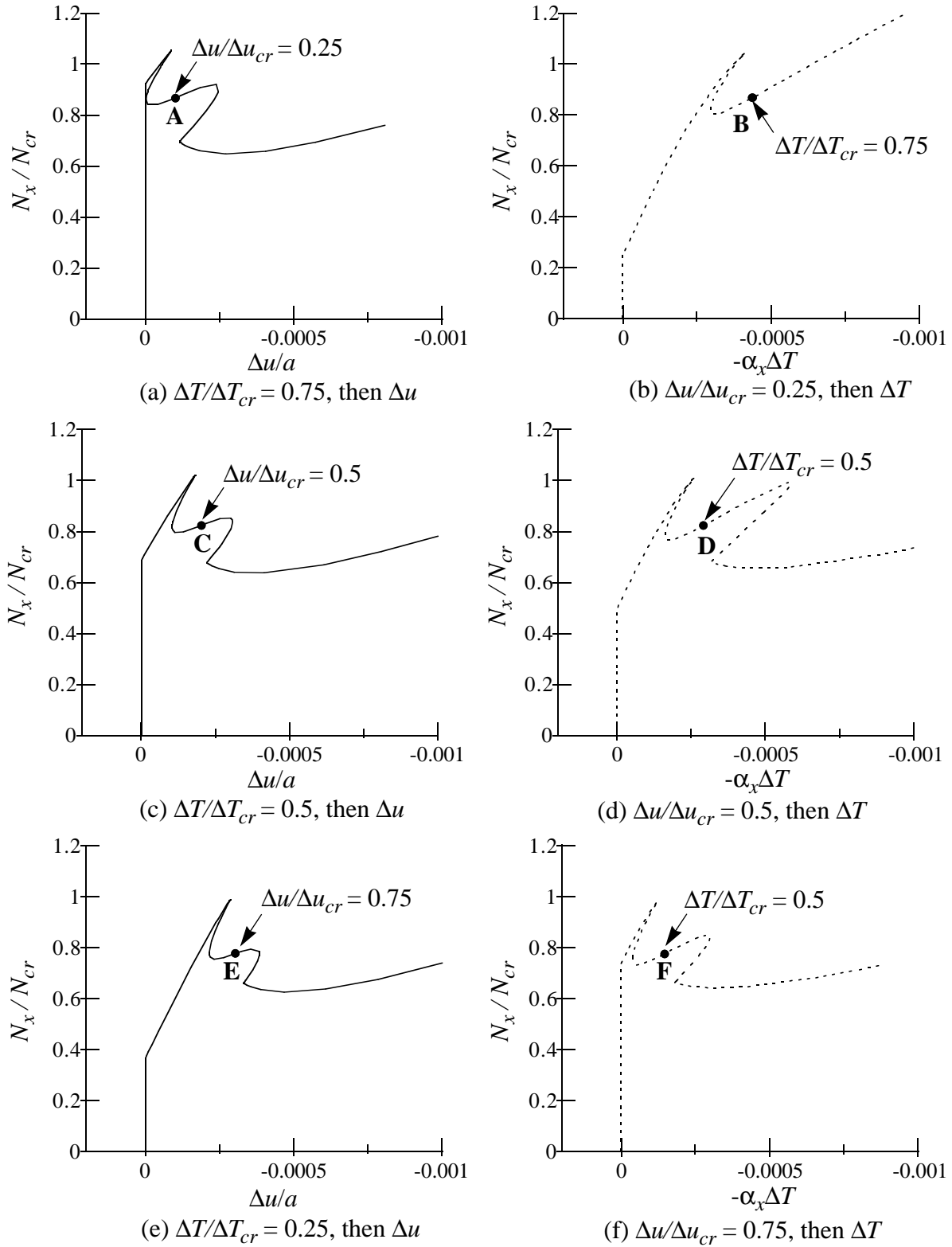
Figure 3-26 Nonlinear response for a $[\pm 45/0/90]_s$ laminate due to combined loading

(a) Point A, $\Delta T/\Delta T_{cr} = 0.75$, $\Delta u/\Delta u_{cr} = 0.25$, $N_x/N_{cr} = 0.868$

(b) Point B, $\Delta u/\Delta u_{cr} = 0.25$, $\Delta T/\Delta T_{cr} = 0.75$, $N_x/N_{cr} = 0.868$

(c) Point C, $\Delta T/\Delta T_{cr} = 0.5$, $\Delta u/\Delta u_{cr} = 0.5$, $N_x/N_{cr} = 0.823$

(d) Point D, $\Delta u/\Delta u_{cr} = 0.5$, $\Delta T/\Delta T_{cr} = 0.5$, $N_x/N_{cr} = 0.823$

(e) Point E, $\Delta T/\Delta T_{cr} = 0.25$, $\Delta u/\Delta u_{cr} = 0.75$, $N_x/N_{cr} = 0.776$

(f) Point F, $\Delta u/\Delta u_{cr} = 0.75$, $\Delta T/\Delta T_{cr} = 0.25$, $N_x/N_{cr} = 0.776$
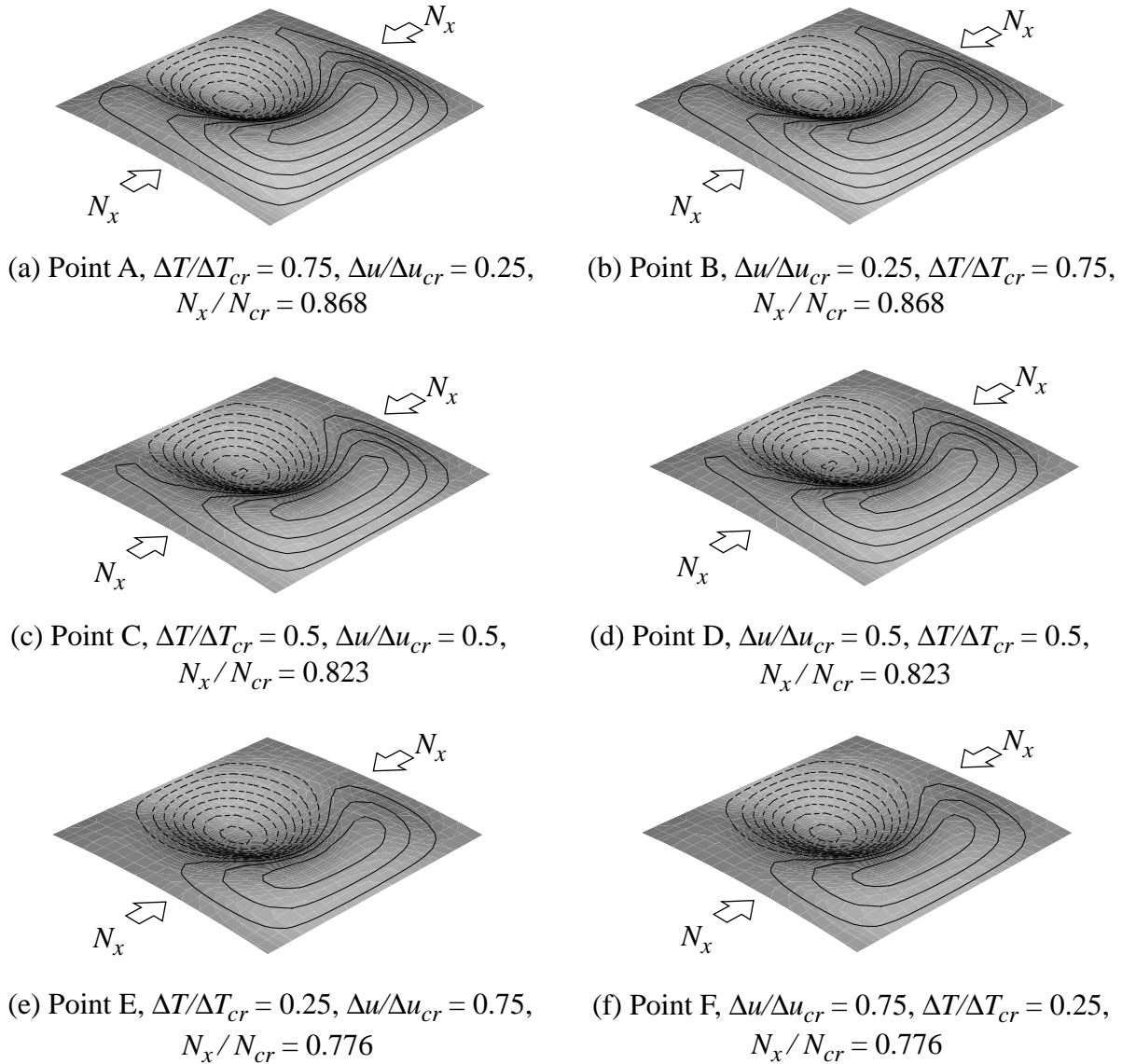
Figure 3-27 Postbuckling deformations for a $[\pm 45/0/90]_s$ laminate at
$\Delta u/\Delta u_{cr} + \Delta T/\Delta T_{cr} = 1.0$

The nonlinear combined loading responses for the axially soft $[\pm 45/90_2]_s$ laminate are shown in Fig. 3-28. Again, solid lines indicate that initial loading is due to temperature change, and dashed lines indicate that initial loading is due to end-shortening. For all six combined loading cases, the character of the postbuckling response is the same, since the responses due to end-shortening alone and temperature change alone were also the same. Points A-F again represent solutions where $\Delta u/\Delta u_{cr} + \Delta T/\Delta T_{cr} = 1.0$. The corresponding deformation patterns are shown in Fig. 3-29. Although all of the deformation patterns appear alike, the deformation patterns and loads are iden-

(a) $\Delta T/\Delta T_{cr} = 0.75$, then Δu

(b) $\Delta u/\Delta u_{cr} = 0.25$, then ΔT

(c) $\Delta T/\Delta T_{cr} = 0.5$, then Δu

(d) $\Delta u/\Delta u_{cr} = 0.5$, then ΔT

(e) $\Delta T/\Delta T_{cr} = 0.25$, then Δu

(f) $\Delta u/\Delta u_{cr} = 0.75$, then ΔT
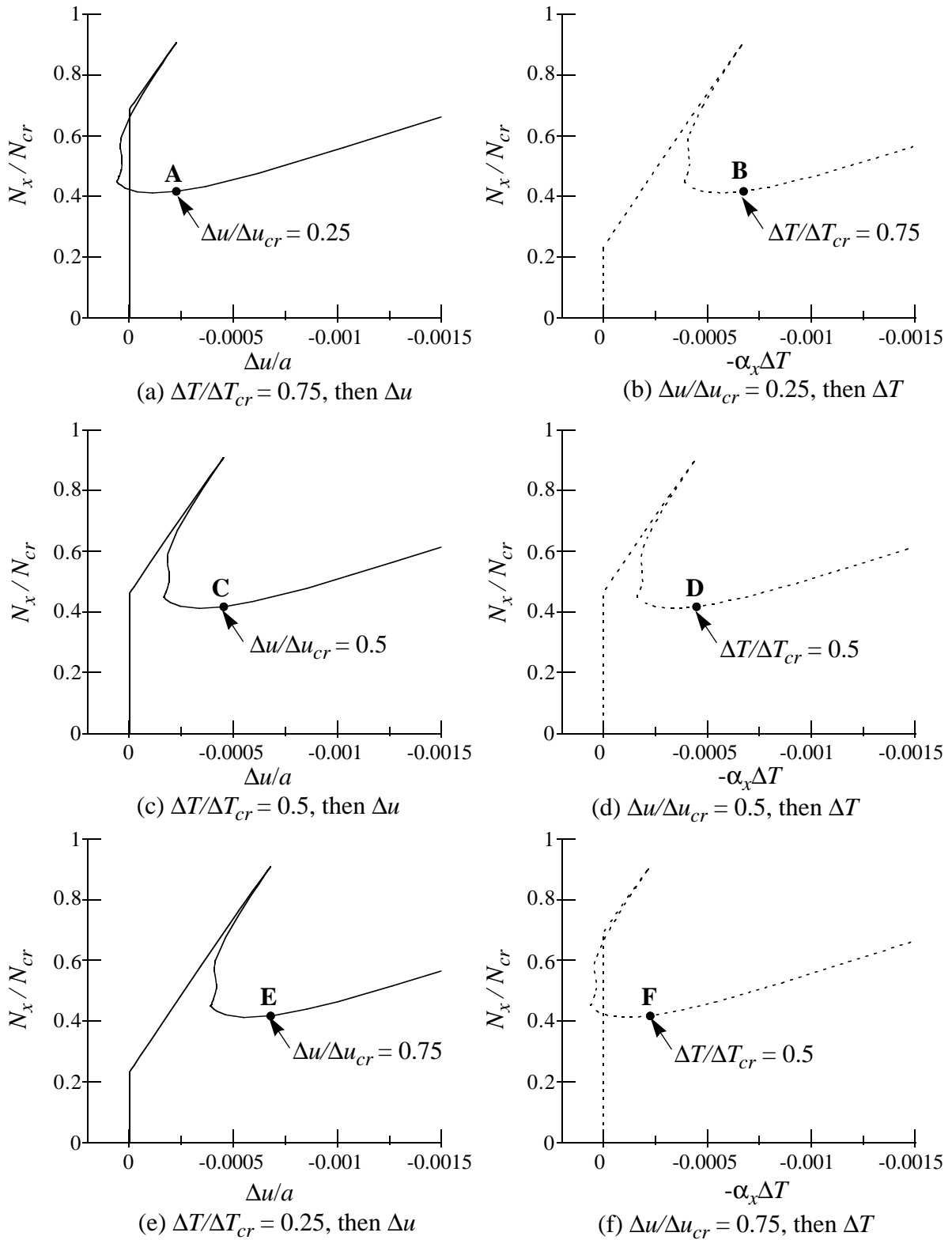
Figure 3-28 Nonlinear response for a $[\pm 45/90_2]_s$ laminate due to combined loading

(a) Point A, $\Delta T/\Delta T_{cr} = 0.75$, $\Delta u/\Delta u_{cr} = 0.25$, $N_x/N_{cr} = 0.417$

(b) Point B, $\Delta u/\Delta u_{cr} = 0.25$, $\Delta T/\Delta T_{cr} = 0.75$, $N_x/N_{cr} = 0.417$

(c) Point C, $\Delta T/\Delta T_{cr} = 0.5$, $\Delta u/\Delta u_{cr} = 0.5$, $N_x/N_{cr} = 0.417$

(d) Point D, $\Delta u/\Delta u_{cr} = 0.5$, $\Delta T/\Delta T_{cr} = 0.5$, $N_x/N_{cr} = 0.417$

(e) Point E, $\Delta T/\Delta T_{cr} = 0.25$, $\Delta u/\Delta u_{cr} = 0.75$, $N_x/N_{cr} = 0.418$

(f) Point F, $\Delta u/\Delta u_{cr} = 0.75$, $\Delta T/\Delta T_{cr} = 0.25$, $N_x/N_{cr} = 0.418$
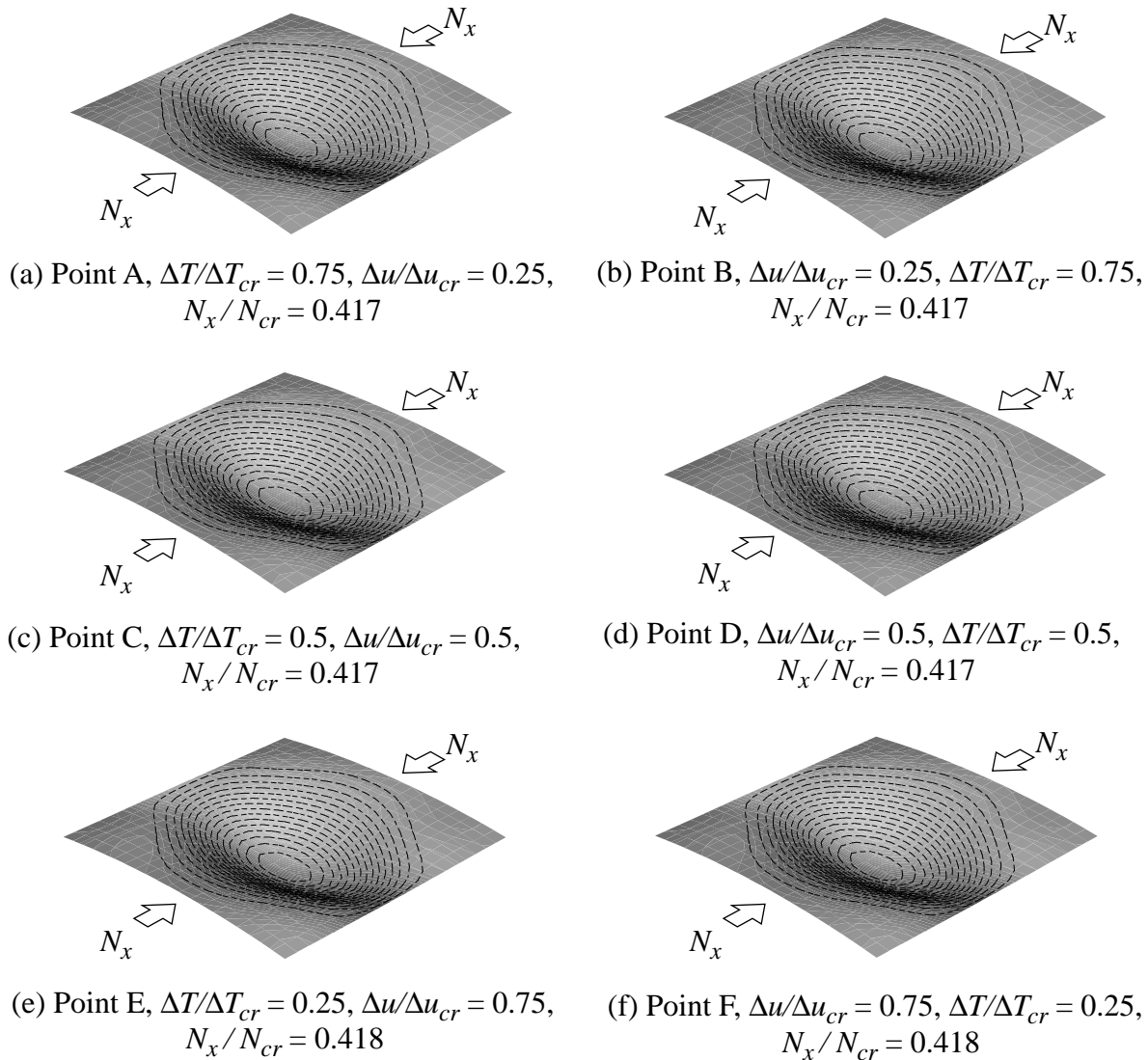
Figure 3-29 Postbuckling deformations for a $[\pm 45/90_2]_s$ laminate at
$\Delta u/\Delta u_{cr} + \Delta T/\Delta T_{cr} = 1.0$

tical for pairs that also share the same values of $\Delta u/\Delta u_{cr}$ and $\Delta T/\Delta T_{cr}$, such as Fig. 3-29(a) and (b), Fig. 3-29(c) and (d), and Fig. 3-29(e) and (f). This observation supports the earlier conclusion that a particular solution is independent of the order of loading. Equally interesting is the similarity in the postbuckling paths for the cases represented by Fig. 3-28(a) and (f), and (e) and (b), where the proportion of initial thermal loading for one of the cases that are paired is the same as the proportion of initial end-shortening for the other case.

The nonlinear response for the axially stiff $[\pm 45/0_2]_s$ laminate subjected to combined loading are shown in Fig. 3-30. For initial loading due to temperature change, represented by the solid lines

(a) $\Delta T/\Delta T_{cr} = 0.75$, then Δu

(b) $\Delta u/\Delta u_{cr} = 0.25$, then ΔT

(c) $\Delta T/\Delta T_{cr} = 0.5$, then Δu

(d) $\Delta u/\Delta u_{cr} = 0.5$, then ΔT

(e) $\Delta T/\Delta T_{cr} = 0.25$, then Δu

(f) $\Delta u/\Delta u_{cr} = 0.75$, then ΔT
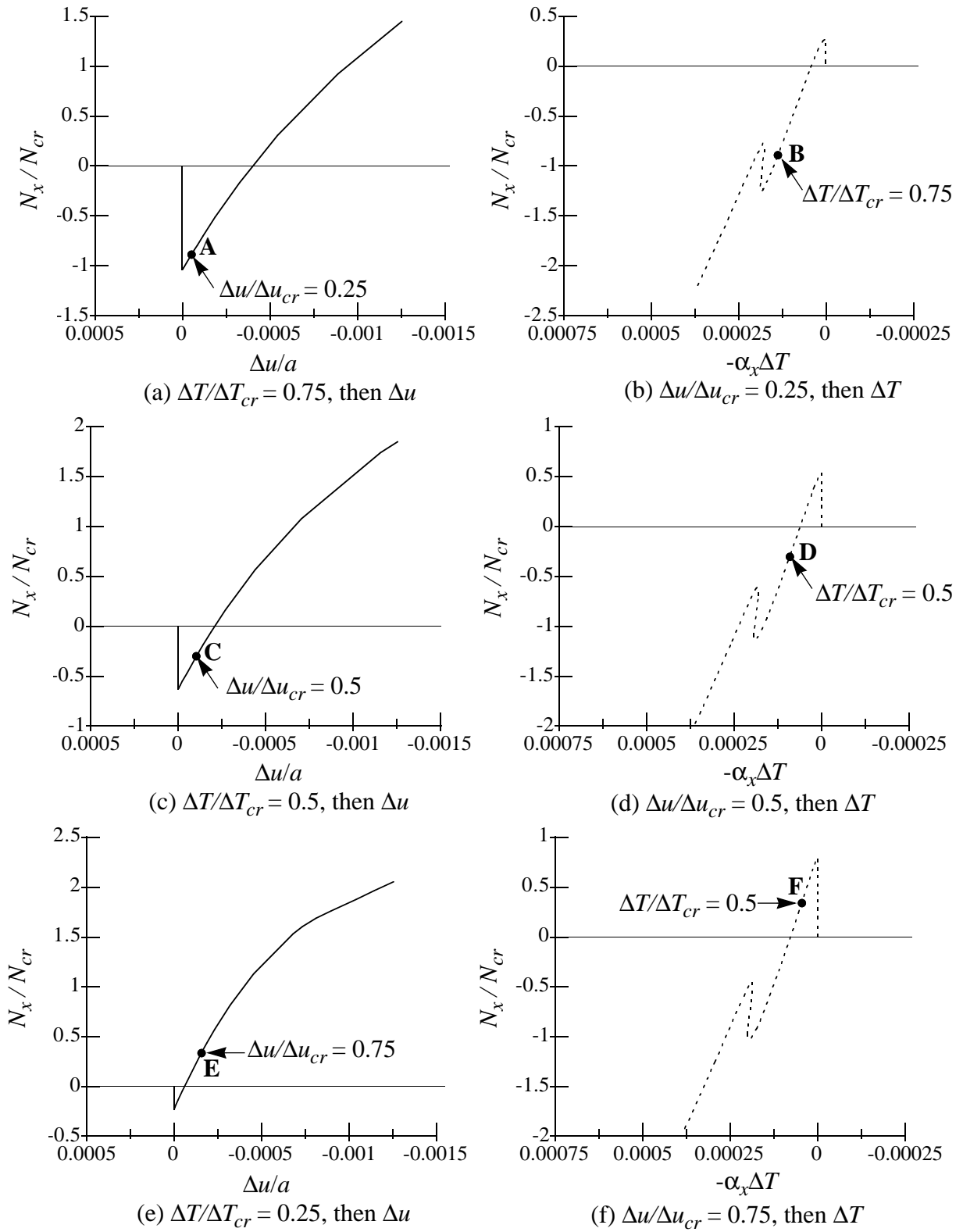
Figure 3-30 Nonlinear response for a $[\pm 45/0_2]_s$ laminate due to combined loading

in Fig. 3-30(a), (c), and (e), buckling does not occur, but instead the panel stiffness slowly diminishes. For initial loading due to end-shortening, Fig. 3-30(b), (d), and (f), the initial loading causes a shift of the response but no significant difference in the character of the response. For all cases, the points A-F where $\Delta u/\Delta u_{cr} + \Delta T/\Delta T_{cr} = 1.0$ occur in the prebuckling range of loading, suggesting that combined loading results in a increased resistance to buckling than either of the loading conditions applied separately. Deformation patterns corresponding to points A-F are shown in Fig. 3-31. As with the previous laminates, the solutions for a particular $\Delta u/\Delta u_{cr}$ and

(a) Point A, $\Delta T/\Delta T_{cr} = 0.75$, $\Delta u/\Delta u_{cr} = 0.25$, $N_x/N_{cr} = -0.888$

(b) Point B, $\Delta u/\Delta u_{cr} = 0.25$, $\Delta T/\Delta T_{cr} = 0.75$, $N_x/N_{cr} = -0.888$

(c) Point C, $\Delta T/\Delta T_{cr} = 0.5$, $\Delta u/\Delta u_{cr} = 0.5$, $N_x/N_{cr} = -0.299$

(d) Point D, $\Delta u/\Delta u_{cr} = 0.5$, $\Delta T/\Delta T_{cr} = 0.5$, $N_x/N_{cr} = -0.299$

(e) Point E, $\Delta T/\Delta T_{cr} = 0.25$, $\Delta u/\Delta u_{cr} = 0.75$, $N_x/N_{cr} = 0.338$

(f) Point F, $\Delta u/\Delta u_{cr} = 0.75$, $\Delta T/\Delta T_{cr} = 0.25$, $N_x/N_{cr} = 0.338$
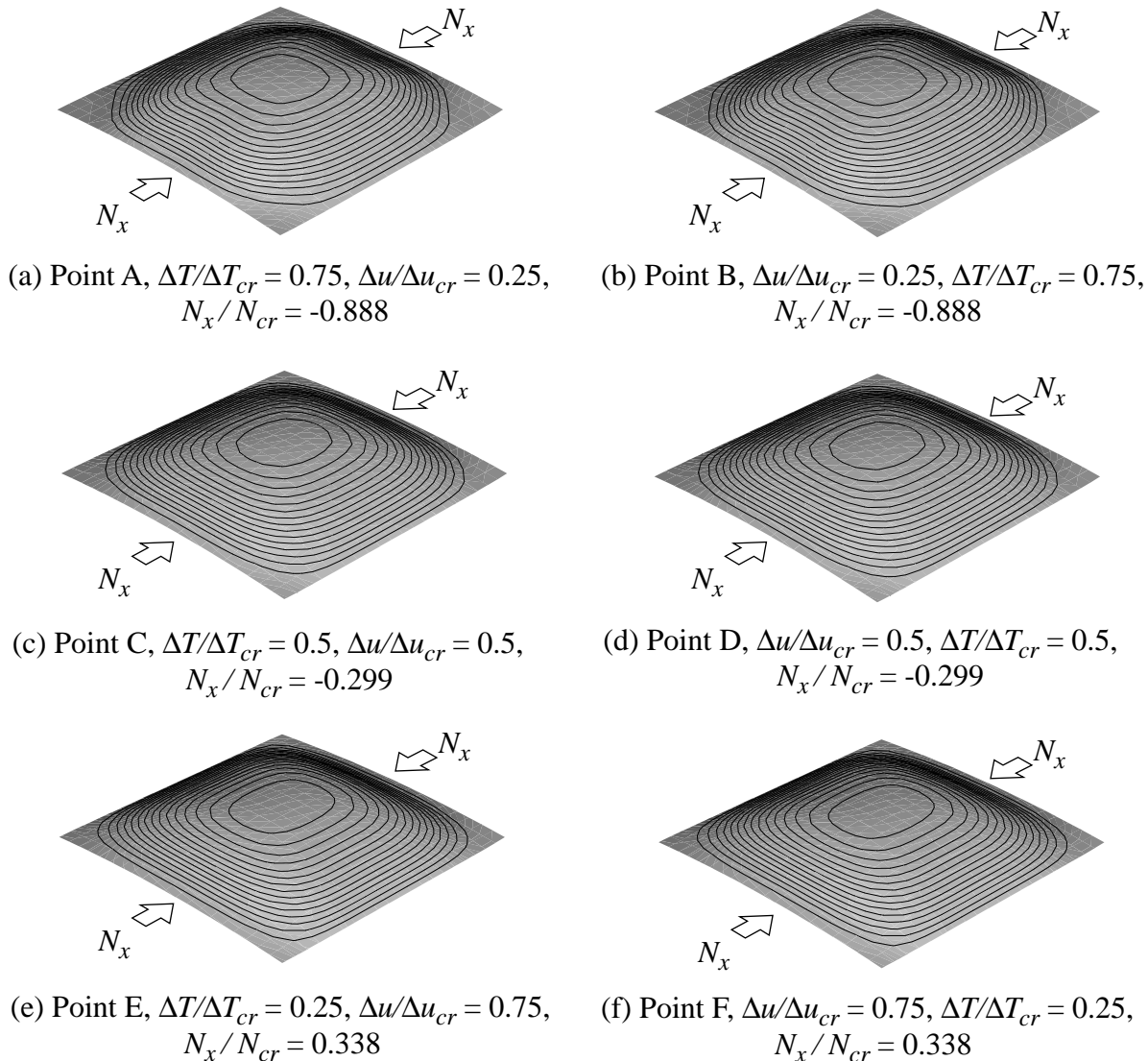
Figure 3-31 Postbuckling deformations for a $[\pm 45/0_2]_s$ laminate at
$$\Delta u/\Delta u_{cr} + \Delta T/\Delta T_{cr} = 1.0$$

$\Delta T/\Delta T_{cr}$ combination are unique, as indicated by the identical deformation patterns and loads in Fig. 3-31(a) and (b), Fig. 3-31(c) and (d), and Fig. 3-31(e) and (f).

This concludes the discussion of some of the important issues in curved panel response due to axial end-shortening and uniform temperature change. The results have shown that there is a significant range of response, and that the influence of boundary conditions, lamination sequence, and panel radius of curvature are considerable. The discussion now turns to the experimental aspects of the study, where parameter studies are much more difficult. In addition, testing under a thermal environment offers a number of challenges. Therefore, the experiments will be limited to panels with $R = 60$ in., the three lamination sequences, simulation of clamped/sliding simple supports conditions, and a few important loading conditions.

Chapter 4 - Experimental Considerations

The experimental phase of this study consumed a considerable portion of the total effort. Manufacturing of the curved panels introduced unwanted effects, as it is virtually impossible to manufacture perfect composite specimens. Machining tolerances are always an issue in experimental work, but with buckling studies involving small end-shortening displacements (see Table 3-4), machining tolerances with the loading fixtures can lead to nonuniform load introduction, and the fixtures have compliances that are often difficult to quantify. Application of loads, both mechanical and thermal, is challenging, particularly when heat conduction and thermal expansion are involved. Here, thermal expansion of the composite panels was a major focus of the study, but thermal expansion of the fixtures accompanies thermal expansion of the composite panels and could influence the results. Finally, control of the end-shortening and temperature is important, and is only possible to within a certain tolerance. This chapter discusses these and other relevant issues, and provides insight into structural testing in a thermal environment.

4.1 Overview of the Experimental Setup

To provide axial end-shortening, a hydraulic load frame with flat and parallel loading platens was used in conjunction with a specially designed elevated temperature testing apparatus. Panels were supported with a stainless steel fixture designed to accommodate the curvature. The fixture provided clamped boundary conditions on the loaded curved ends and sliding simple supports on the straight unloaded edges. The introduction of temperature change into the composite panels was accomplished by heating and circulating the air inside an insulated box, and providing additional localized heating of the test fixture supporting the panel. The size of the insulated box was determined by the maximum width between the supports of the load frame platens. The composite panels were sized to fit within the insulated box, while still allowing sufficient space for air movement and instrumentation wiring.

Twelve separate tests were conducted on test specimens measuring 10 in. long by 10 in. along the arc length, and with a radius of 60 in. The following sections provide a further description of the required test apparatus, test panels, instrumentation, and testing procedure.

Preliminary design and development of the insulated box was conducted by Waters and Sikora [65] in anticipation of future high temperature testing.

4.2 Apparatus

Tests on the end-shortening of curved composite panels have been conducted previously, see, for example, refs. [12], [22-24], and [27-29]. The fixture designed for the present study was a smaller version of the curved panel compression test fixture used by Knight and Starnes [29]. Because the present fixture was to be used at elevated temperatures, it was constructed of stainless steel. Details of the support conditions are provided in Fig. 4-1. The panel was held in curved end grip
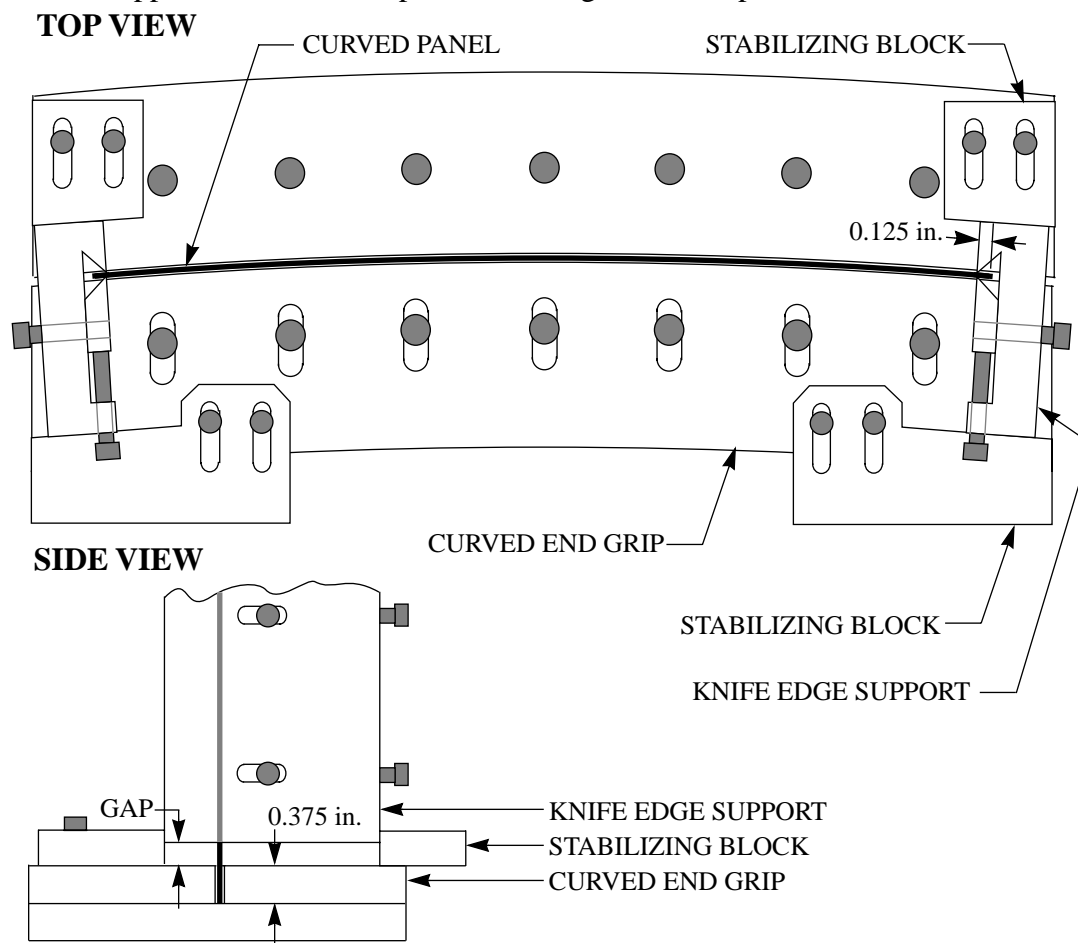
Figure 4-1 Schematic of curved panel compression test fixture

fixtures to provide clamped boundary conditions. All displacements and rotations were restricted on the curved ends. The curved end grips provided support over 0.375 in. of the panel length on each end. The straight edges of the panel were held in knife edge supports, which provide restric-

tion from radial displacement approximately 0.125 in. inward circumferentially from the edges. The knife edge support was held in place by stabilizing blocks.

The insulated box and curved panel compression test fixture assembly is shown schematically in Fig. 4-2, with a corresponding photograph shown in Fig. 4-3. The interior of the insulated box is 20 in. wide by 26 in. deep by approximately 11 in. high. The walls are made of two layers of 1 in. thick ceramic board[1]. The top and bottom of the oven are made from the same board except for a 12 in. by 5 in. hole in the center of each for introduction of the load by the load frame platens. Inside each of the two side walls of the insulated box is a coil resistance heater. Air is circulated over the heaters and around the box by a fan and baffle combination located at the back of the oven.

Two layers of ceramic[2], cut into small blocks, fit inside the 12 in. by 5 in. holes in the top and bottom of the insulated box. The ceramic is meant to thermally isolate for the curved end grips from the massive heat sink potential of the load frame platens, and transfer the load from the load frame platen to the curved end grips. Because a single, larger piece of ceramic tended to warp out-of-plane when heated, it was cut into a number of smaller blocks measuring 2.0 in. by 2.5 in.
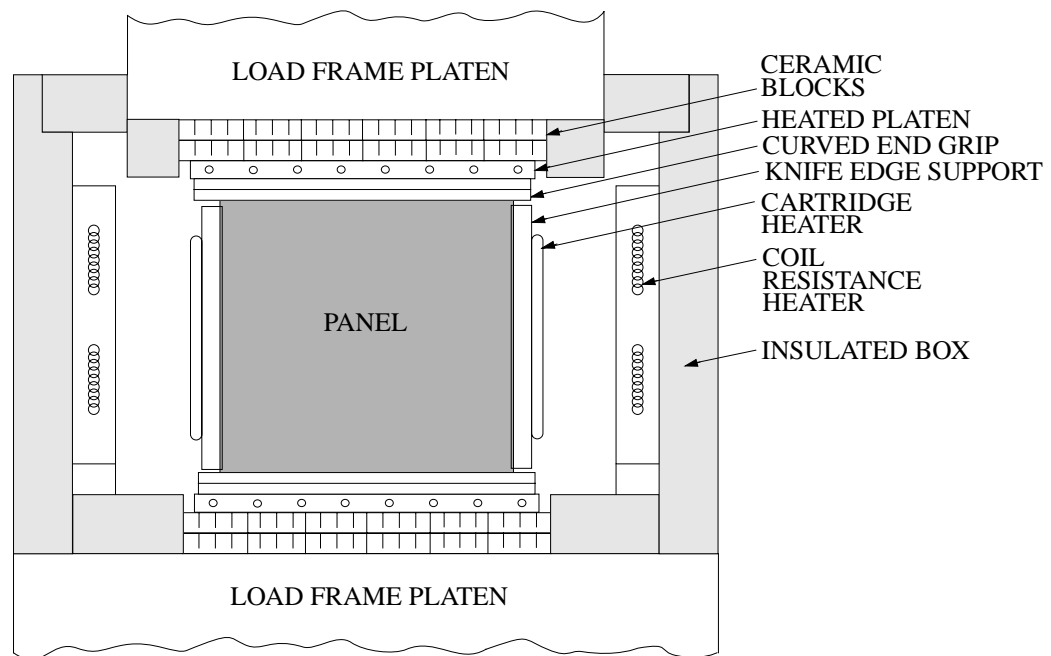
Figure 4-2 Schematic of thermal test apparatus

1. Cotronics, 360-4 ceramic board
2. Mycroy/Mycalex Ceramics, grade 500 Supra Mica
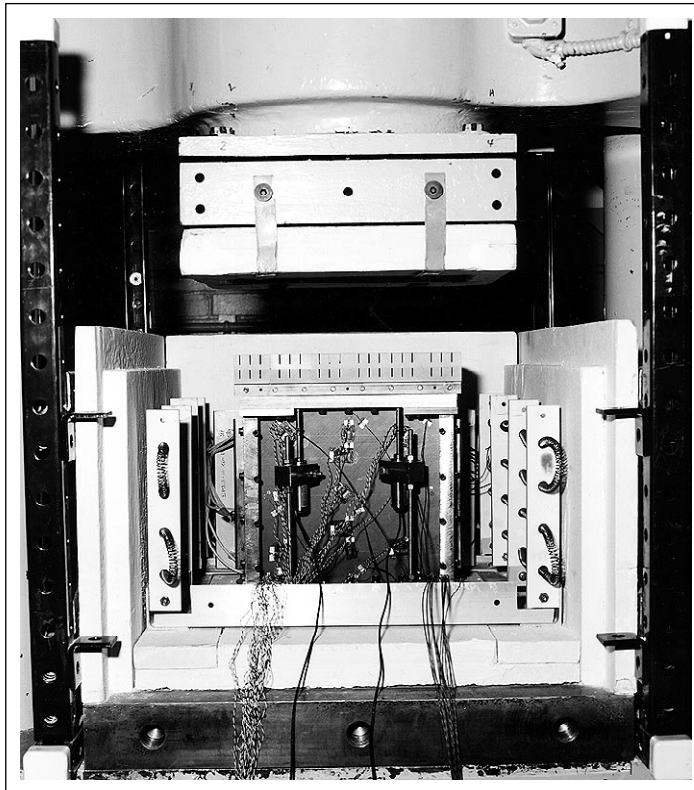
Figure 4-3 Photograph of thermal test apparatus

by 0.75 in. thick, with 0.5 in. deep grooves cut in a 0.5 in. grid pattern. Measurement of the deflection of the ceramic at elevated temperatures up to 450°F indicated that the ceramic blocks deflect from flat and parallel less than the machining tolerances of ±0.003 in.

To further insure that the thermal environment of the panel is controlled, a set of heated platens is inserted between the ceramic blocks and the curved end grips. Each heated platen contains eight cartridge heaters, which are meant to provide additional heating to the curved end grips. By including this additional conduction source, the temperature increase of the curved end grips can be controlled to be the same as the increase in air temperature, rather than lagging behind due to the substantial mass of the stainless steel. Each of the knife edge support pieces is heated by a cartridge heater attached along the length of the support.

4.3 Test Panels and Test Matrix

The panels are made from unidirectional layers of IM7/5260 BMI. Three panels, with stacking sequences $[\pm45/0/90]_s$, $[\pm45/0_2]_s$, and $[\pm45/90_2]_s$, were layed up on a curved base plate to form 22 in. by 22 in. panels with 60 in. radii. Each large panel was cut into four 10 in. by 10 in. test pan-

els, with the edges ground flat and parallel to within ±0.003 in. An ultrasonic scan was conducted for each test panel to search for manufacturing imperfections such as excessive voids, delaminations, or embedded materials. Of the original twelve panels, only ten were used in the experimental study.   The remaining two panels were failed prematurely while developing the test methodology.   The corner displacement listed in Table 4-1 is a measure of the initial warpage observed in the panels at room temperature. The warpage was measured by noting the maximum deflection at one corner of the panel, $x = a$ and $\theta = 0$, when the other three corners were held down against a flat surface.   Radial imperfections were measured at 0.125 in. increments in the axial and circumferential directions on both the inside radius and outside radius surfaces of the panels. The thickness at each point was calculated by the difference between the two measurements. The average measured thickness for each panel is given in Table 4-1. The average radial imperfections are shown in Appendix B.

Table 4-1 Summary of measured panel geometry

	Panel Number	Average Measured Thickness, in.	Corner Displacement, in.
$[\pm45/0/90]_s$	1	0.0431	0.192
	2	0.0430	0.106
	3	0.0431	0.108
$[\pm45/90_2]_s$	4	0.0428	0.102
	5	0.0428	0.072
	6	0.0432	0.098
	7	0.0429	0.039
$[\pm45/0_2]_s$	8	0.0429	0.085
	9	0.0425	0.096
	10	0.0428	0.115

The panel numbers and corresponding test numbers and test descriptions are listed in Table 4-2. Four tests with four different loading sequences were run for each type of laminate. The first loading sequence was axial end-shortening with no temperature change, denoted Δu only. The next loading sequence was temperature change with axial end-shortening restricted, denoted ΔT only. Two combined loading cases were considered, axial end-shortening followed by tempera-

Table 4-2 Panel identification and test description

	Panel Number	Test Number	Loading
$[\pm 45/0/90]_s$	1	Q1	Δu only
	2	Q2	ΔT only
	3	Q3	Δu then ΔT
	1	Q4	ΔT then Δu
$[\pm 45/90_2]_s$	4	N1	Δu only
	5	N2	ΔT only
	6	N3	Δu then ΔT
	7	N4	ΔT then Δu
$[\pm 45/0_2]_s$	8	Z1	Δu only
	10	Z2	free thermal expansion
	9	Z3	Δu then ΔT
	10	Z4	ΔT then Δu

ture change, denoted Δu then ΔT, or temperature change followed by axial end-shortening, denoted ΔT then Δu. Axial end-shortening was restricted during all loading by temperature change. For the $[\pm 45/0_2]_s$ laminates, the test with temperature change only was not run because the test apparatus was not equipped to handle the predicted tensile loads, but a free thermal expansion test was substituted instead.

4.4 Instrumentation

Room temperature tests and elevated temperature tests required different instrumentation. All panels were instrumented with forty-two back-to-back strain gages, as shown in Fig. 4-4. Axial and circumferential gages had 0.25 in. gage lengths, and rosettes had 0.125 in. gage lengths. For tests N1 and Z1, tested only at room temperature, Micromeasurements, Inc. gages CEA-06 were used. For all other tests, Micromeasurements, Inc. gages WK-00 were used. These gages were designated to compensate for a coefficient of thermal expansion of zero.

For the room temperature tests, one direct current differential transformer (DCDT) was used to measure radial displacement at the center of the panel, and three DCDT's were placed on the cor-

ners of the load platen to measure axial end-shortening. Shadow moiré interferometry equipment was used to qualitatively view the postbuckling mode shape. Axial load was determined from the load cell of the hydraulic load frame.
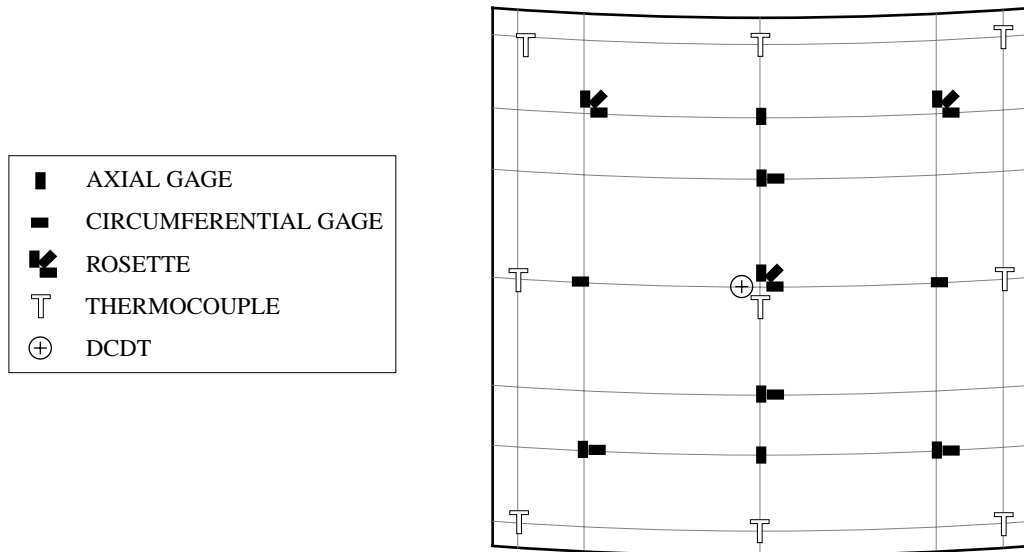
Figure 4-4 Typical instrumentation pattern

For elevated temperature tests, panels were instrumented with eighteen back-to-back thermocouples, type K, to map the axial, circumferential, and through the thickness thermal gradients of the panel. Shadow moiré was not available through the insulated box. No direct measure of axial end-shortening was obtained during thermal loading, although two linear variable differential transformers (LVDT's) were placed inside the insulated box with the intention of measuring end-shortening. The LVDT's did not give a satisfactory measurement of end-shortening because they were not thermally compensated, only high temperature tolerant. During changing temperatures, the LVDT's changed calibration, resulting in unreliable results. The LVDT's could be used at a constant temperature to provide a relative measure of axial displacement, assuming that calibration had been conducted at temperature. For this study, the LVDT measurements were disregarded.

4.5 Test Procedure

Testing was conducted at NASA-Langley Research Center in the Structural Mechanics Laboratory. Testing for this study can be broken into two groups: end-shortening only, and elevated-temperature testing.

Chapter 4 - Experimental Considerations

For end-shortening tests conducted at room temperature, a 120-kip hydraulic load frame was used. Special attention was given to the installation of the panels in the compression test fixture, including careful alignment of the upper and lower curved end grips under a compressive load of -50 lbs. to avoid testing the panel with an initial twist. The knife edge supports were adjusted until they were perpendicular to the loading surface. Panels were compressed at a rate of 0.002 in. per minute.

Panel failure for this type of load fixture initiates in the corners, where a gap exists between the curved end fixture and the knife edge supports. Since this type of failure gives no information about curved panels in general, testing was stopped prior to panel failure. Loading was continued beyond buckling until the slope of the postbuckling response could be fully determined. The end displacement was reversed and returned to zero before noticeable failure occurred, allowing further examination of the panel in its original state after testing.

Elevated temperature testing was conducted in a larger, 300-kip hydraulic load frame to restrict axial expansion. The larger load frame was required to provide sufficient space for the elevated temperature testing apparatus. Specimen alignment was assured by applying a compressive load of -50 lbs. then checking the knife edge supports for perpendicular alignment using a 90° bubble level. Testing began with axial end-shortening to a compressive load of -1000 lbs., then back to zero. This provided a measure of room temperature stiffness for each panel. For tests that began with a thermal loading phase, a small end-shortening was applied until a compressive load of -50 lbs. was reached to assure that all the layers of ceramic and steel between the load frame platens and the panel were making good contact. For thermal loading, temperature was increased slowly, requiring two hours to heat up from room temperature to 400°F. Data were recorded during panel heat up.

An attempt was made to restrict axial end-shortening during thermal loading, but this was not possible with the particular experimental apparatus. First, the load frame was designed to apply load by moving the lower load frame platen while the upper platen remained fixed. Unfortunately, when the load frame was held at a constant level, a small leak in the hydraulic system allowed the lower load frame platen to drift slowly downward with time. For these thermal tests, the hydraulic leak resulted in a small axial displacement in the tensile direction during thermal loading. This displacement was measured with an external DCDT which measured the drop of the lower load frame platen. In addition to the downward displacement of the lower load frame platen, the panel experienced axial compression from the steel fixtures inside the insulated box. When the temperature inside the box was increased, the steel curved end fixtures and the steel heated platens

expanded thermally. This expansion caused a compressive shortening of the test panel. Proper accounting for these two competing displacements was necessary to understand the thermal response of the panels.

4.6 Postprocessing of Experimental Results

The experimental data in raw form contained information about response of the test fixture, strain gages, and load frame that needed to be separated from the response of the panels. The thermal expansion of the strain gages, the displacement of the lower load frame platen, the thermal expansion of the steel end fixtures, and the compliance of the end fixtures and ceramic insulation combination were extracted from the original data to provide panel load, displacement, and temperature change results.

To account for the influence of temperature change on the strain gages, two reference gages of the same type as used on the panels were mounted on a piece of glass ceramic[1] with a near zero coefficient of thermal expansion. Since the glass ceramic did not expand, the apparent strain recorded for the reference gages was due to the resistivity of the gages changing with temperature, as shown in Fig. 4-5. By subtracting the apparent thermal expansion of the reference gages from the strain recorded by the panel gages, the resulting strain represents the change in length per initial length of the panel.
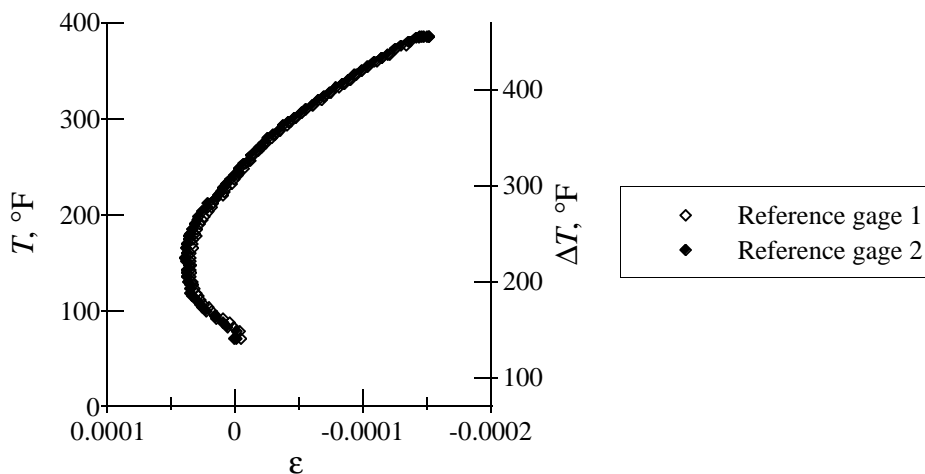
Figure 4-5 Apparent thermal expansion of reference strain gages

1. Schott Glass Technologies, Inc., Zerodur, $\alpha=0\pm0.55\text{x}10^{-9}/°F$

Chapter 4 - Experimental Considerations

To find the net axial displacement of the panels, three different methods were employed. During the prebuckling phase of loading, the end-shortening can be obtained from the average axial strain gage readings by multiplying the strain by the length of the panel. This provides a measure of end-shortening for either mechanical or thermal loading. After buckling, the strain gages can no longer be used to measure axial end-shortening because substantial bending occurs.

The second method for determining axial displacement is based on the superposition of the measured downward drift of the lower load platen, and a calculated thermal expansion of the steel fixtures. However, the steel fixtures were located between the ceramic insulation and the end of the panel, as shown in Fig. 4-2. When the steel expanded, some of the expansion shortened the panel, while some of the expansion compressed the ceramic insulation. The ceramic insulation had a stiffness based on the geometry of the multiple layers of insulation. Because the individual blocks of ceramic were not perfectly flat and parallel, and because each block was not of the identical thickness as its neighboring blocks, the stiffness of the ceramic reflects not only the compressive modulus of the ceramic, but also some settling and bending of the ceramic blocks. The stiffness of the panel is known from the strain gage data, and the stiffness of the overall system is known from the external DCDT. The stiffness of the insulation and steel fixture combination can be found as the difference between the panel stiffness and the overall system stiffness. By comparing the stiffness of the panel to the stiffness of the insulation/steel fixture combination, an estimate can be made of the percentage of steel expansion that contributes to panel end-shortening.

The third method for calculating end-shortening is even more indirect, and requires the room-temperature panel stiffness obtained from the initial compressive preload of -1000 lbs. Using the average of the axial strain gages during preload, the slope of axial strain vs. load can be found. With this slope and a calculated value of α_x for the panel, the panel end-shortening can be written as a function of load and temperature as

$$\Delta u = \left[\left(\frac{\varepsilon}{P} \right)_{preload} \cdot P + \alpha_x \Delta T \right] a . \tag{4.1}$$

Since this calculation is based on the prebuckling stiffness due to end-shortening, the resulting axial displacement Δu is valid only up to buckling for loading due to end-shortening. For post-buckling due to thermal loading, this calculation of axial displacement is also valid, since nothing has been assumed about panel stiffness in the thermal strain portion of the calculation.

4.7 Experimental Results

Experimental results are presented for global load vs. strain responses. Because all tests conducted at elevated temperatures included both thermal and mechanical loading, response is presented for both load vs. displacement and load vs. temperature. For comparison purposes, displacement is normalized by panel length, and temperature change is multiplied by the computed axial coefficient of thermal expansion of the panel.

The load vs. strain responses from tests Q1 and Q4, with $[\pm45/0/90]_s$ stacking sequences, are shown in Fig. 4-6. These two tests are presented together to allow comparison between loading in end-shortening only, test Q1, and heating first to 240°F then loading in end-shortening, test Q4. Notice that the prebuckling and postbuckling stiffnesses are the same for both tests, although the buckling load is greater for test Q4 than for test Q1. This discrepancy in buckling loads is likely due to both the difference between predicted thermal and mechanical buckling loads for a $[\pm45/0/90]_s$ laminate, and the fact that both tests were run on the same specimen, with test Q4 run before test Q1. A small amount of damage may have occurred in the panel during the first test, test Q4, resulting in a lower buckling load for the second test, test Q1.

The load vs. strain responses from tests Q2 and Q3, with $[\pm45/0/90]_s$ stacking sequences, are shown in Fig. 4-7. Both of these tests have thermal loading as the final loading phase. Test Q2 begins with a -50 lb. load due to end-shortening, then temperature is increased slowly to 400°F. Test Q3 is loaded in end-shortening to an initial load of -800 lbs. before being heated slowly to
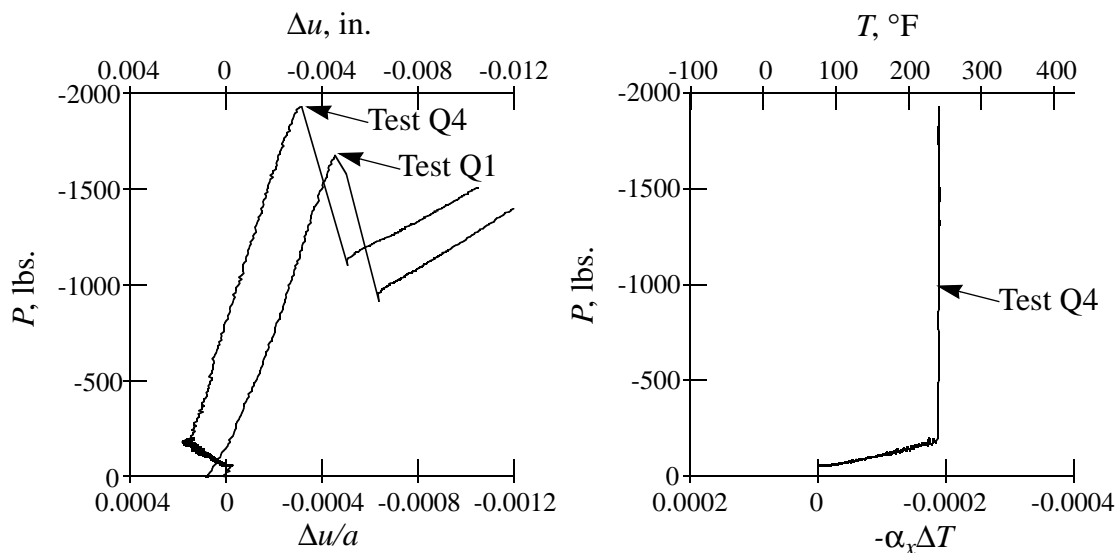
Figure 4-6 Load vs. strain responses for $[\pm45/0/90]_s$ laminates, test Q1 and test Q4
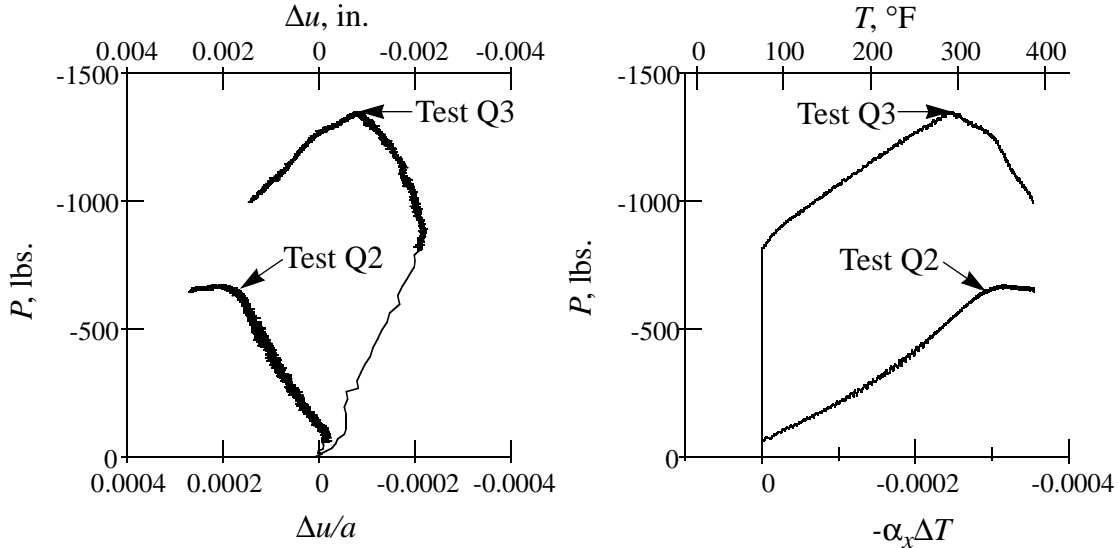
Figure 4-7 Load vs. strain responses for [±45/0/90]$_s$ laminates, test Q2 and test Q3

400°F. Note that the slopes of the load vs. displacement curves during thermal loading are differ-ent for the two tests, due to the different rates of downward drift of the lower load frame platen. The different slopes of the load vs. displacement curves correspond to different slopes of the load vs. temperature curves for the two tests. Test Q3 reaches a buckling load, but test Q2, which never exceeds an axial load of -700 lbs., does not reach a buckling load in the temperature range consid-ered. Both test Q2 and test Q3 experience a change is stiffness at a temperature of approximately 330°F, which may be due to temperature dependent material properties.

The load vs. strain responses from test N1 and test N4, with [±45/90$_2$]$_s$ stacking sequences, are shown in Fig. 4-8. Test N1 is an end-shortening only test, and test N4 is heated to 240°F, then loaded in end-shortening. The end-shortening portions of the tests are nearly identical, with both tests have the same prebuckling stiffnesses, nearly the same buckling loads, and nearly the same postbuckling stiffnesses.

The load vs. strain responses for tests N2 and N3, with [±45/90$_2$]$_s$ stacking sequences, are shown in Fig. 4-9. Test N2 begins with a -50 lbs. load due to end-shortening before the temperature is increased slowly to 400°F. Test N3 is loaded to -800 lbs. with end-shortening, then heated slowly to 400°F. The slope of the load vs. displacement curves are slightly different during the thermal loading portions of the tests, indicating a different rate of lower platen downward drift from test to test. The slopes of the load vs. temperature curves are correspondingly different between the two tests. The buckling load of test N2 is less than the buckling load of test N3, although after buck-
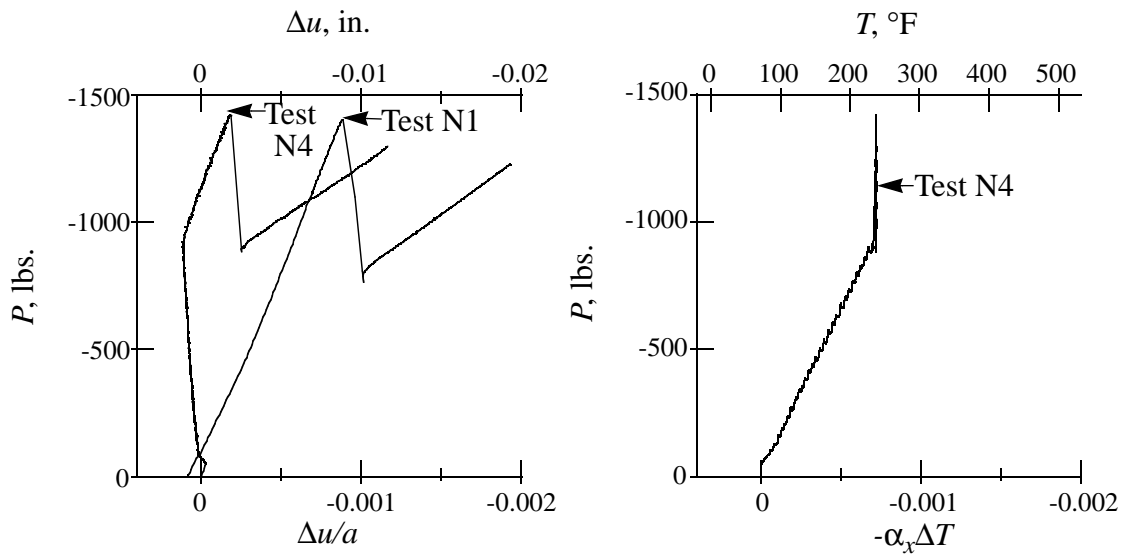
Figure 4-8 Load vs. strain responses for $[\pm 45/90_2]_s$ laminates, test N1 and test N4
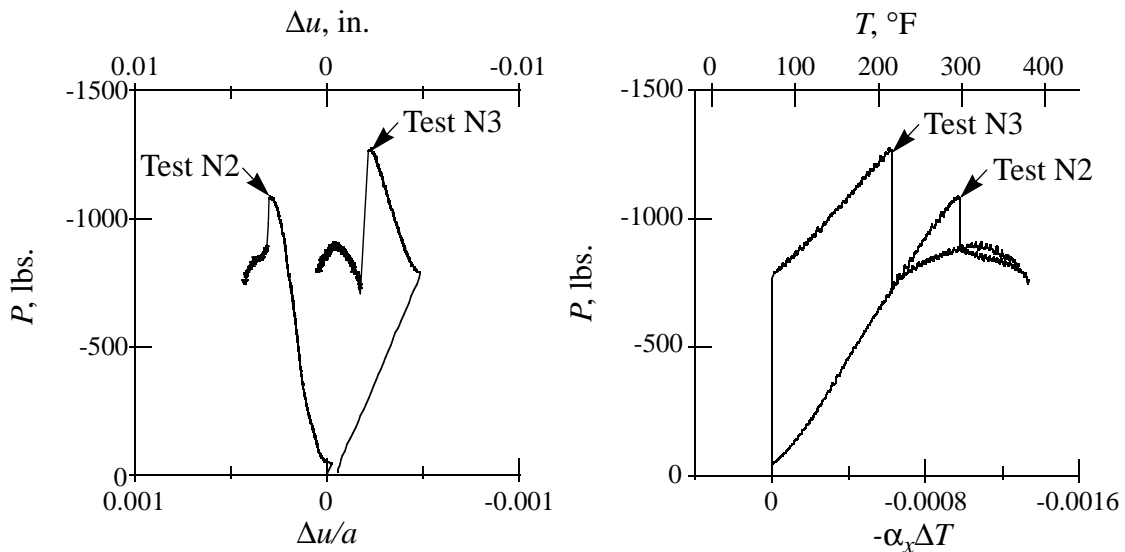
Figure 4-9 Load vs. strain responses for $[\pm 45/90_2]_s$ laminates, test N2 and test N3

ling, both reach the same postbuckling load. The difference in buckling loads is not expected from the analytical studies of $[\pm 45/90_2]_s$ panels, which indicated the same buckling load for thermal and mechanical loading. The difference may therefore be due to experimental differences between the tests, including initial geometric imperfections of the panel, and differences between the alignment of each panel in the test apparatus. A stiffness change occurs beyond 330°F, consis-

tent with the observations for tests Q2 and Q3, and possibly indicating temperature dependent material effects.

The load vs. strain responses for tests Z1 and Z4, with $[\pm 45/0_2]_s$ stacking sequences, are shown in Fig. 4-10. Test Z1 is loaded in end-shortening only, and test Z4 is heated first to 240°F, then loaded in end-shortening. The prebuckling and final postbuckling stiffnesses from both tests are essentially the same. The buckling load for test Z4, loaded at 240°F, is slightly lower than the buckling load of test Z1, which is loaded at room temperature. Note from the load vs. temperature curve that the load stays constant during panel heat-up, rather than immediately decreasing as expected from the analytical studies of $[\pm 45/0_2]_s$ laminates. This is likely due to the axial displacement of the panel due to drift of the lower load platen and thermal expansion of the steel fixtures.

The load vs. strain responses for test Z3, with a $[\pm 45/0_2]_s$ stacking sequence, are shown in Fig. 4-11. Test Z3 is loaded in end-shortening to -800 lbs., then heated slowly to 400°F. The measured load drops off rapidly when thermal loading begins, due to the negative axial coefficient of thermal expansion for the $[\pm 45/0_2]_s$ laminate. The load vs. temperature slope changes continuously after the initial drop, and eventually reaches an asymptote near -400 lbs. Although the exact reason for this asymptote is unknown, a number of possible conditions may have caused this behavior. One possibility is that the knife edge supports began to carry some of the load, due either to friction between the stabilizing blocks and the knife edge supports or to friction between
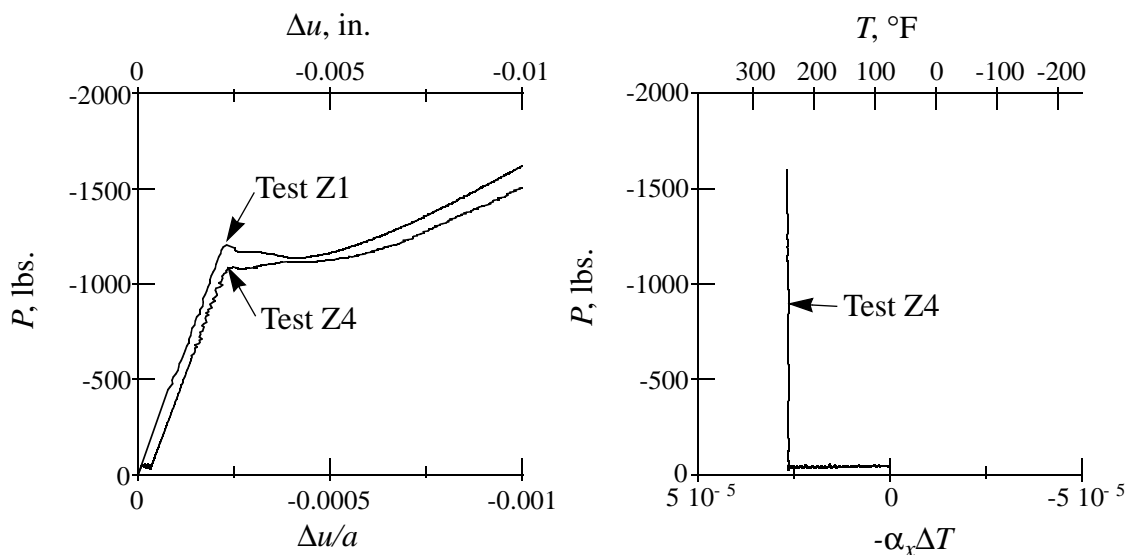
Figure 4-10 Load vs. strain responses for $[\pm 45/0_2]_s$ laminates, test Z1 and test Z4
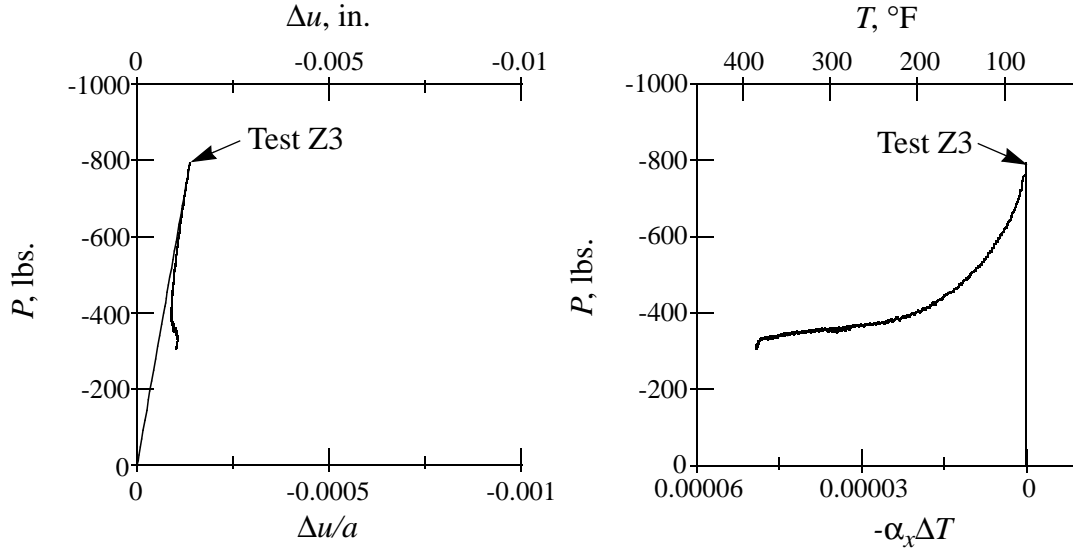
Figure 4-11 Load vs. strain response for a $[\pm 45/0_2]_s$ laminate, test Z3

the knife edge supports and the panel. Another possible cause is that the panel was carrying some load due to the weight of the load frame itself, resulting from imprecise tolerances in the load frame. From just one test result, the exact cause is unclear.

Because the experimental load frame apparatus was not designed to accommodate tensile loads, a pure thermal test of a $[\pm 45/0_2]_s$ laminate was not possible. Recall that this laminate was predicted to shrink in the axial direction when heated, resulting in a tensile load due to the fixed u-displacement boundary condition. As a substitute for this test, and to lend insight into the question of temperature dependent material properties, test Z2 was conducted as a free thermal expansion test. No loads or boundary conditions were applied, and the only data recorded were strains and temperatures.

The relationship between strains from axial and circumferential strain gages located at the center of the panel and the temperature change from test Z2, with a $[\pm 45/0_2]_s$ stacking sequence, is shown in Fig. 4-12. The slopes $\varepsilon/\Delta T$ of the curves are the coefficients of thermal expansion. At temperatures below 330°F, an increase in temperature produces a positive strain in the circumferential direction, indicating circumferential expansion, and a negative strain in the axial direction, indicating axial contraction or shrinking. The corresponding coefficients of thermal expansion are positive in the circumferential direction and negative in the axial direction. Above a temperature of 330°F, the panel begins to contract in the circumferential direction and to expand in the axial direction, as indicated by the changing slopes in Fig. 4-12. This change in slope implies a change

90
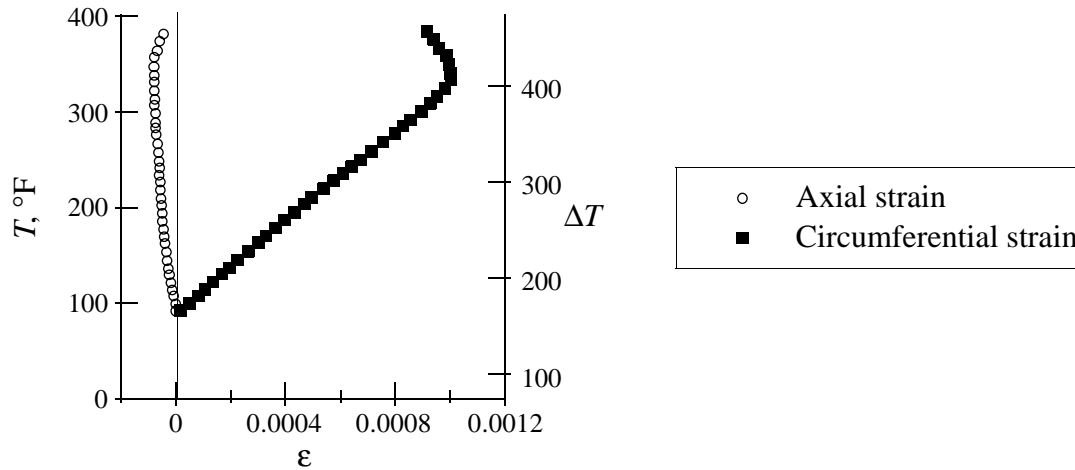
Figure 4-12 Free thermal expansion for a [±45/0₂]ₛ laminate, test Z2

in the sign of the coefficients of thermal expansion. At approximately 330°F, the coefficient of thermal expansion in the circumferential direction changes from positive to negative, while the coefficient of thermal expansion in the axial direction changes from negative to positive.

These changes in the coefficients of thermal expansion, coupled with a likely change in the material stiffness properties, could be an explanation for the loss of stiffness that occurred in tests Q2, Q3, N2 and N3 when heated to 400°F. Thus, the loss of stiffness that occurs at 330°F likely due to a change in material properties of this IM7/5260 material as opposed to a structural phenomenon.

A further examination of the material behavior as a function of temperature is included in Appendix C. Due to the unexpected changes in coefficients of thermal expansion at 330°F, the cure cycle of these panels was questioned. Although the details are included in Appendix C, it is important to note here that the cure cycle used to manufacture these panels was unusual. Therefore, all test results for temperatures greater than 330°F should not be attributed to regular IM7/5260 material behavior.

Chapter 5 - Experimental and Numerical Comparisons

Experimental results are compared to predictions obtained with the STAGS finite element code. In order to match the experimental conditions, numerous refinements were necessary in the base numerical model. The base model has clamped/sliding simple support boundary conditions, uniform temperature, and ideal geometry, as considered in section 3.2. There the base model was studied using both STAGS and the Rayleigh-Ritz approximate solution. In the following sections, the refinements to the numerical model will be considered one at a time for both temperature and end-shortening applied separately, then experimental results will be compared to the numerical models which incorporate all of the relevant refinements. Discrepancies between measured and predicted results will be noted and discussed.

5.1 Refinement of the Numerical Model

The base model was defined in section 3.2 and is repeated here in Fig. 5-1. Boundary conditions are clamped along the curved edges, with sliding simple supports along the straight edges. The geometry is assumed to be perfect, that is, no initial geometric imperfections are considered. The layer thickness is assumed to be 0.005 in., resulting in an eight-layer panel thickness of 0.04 in.
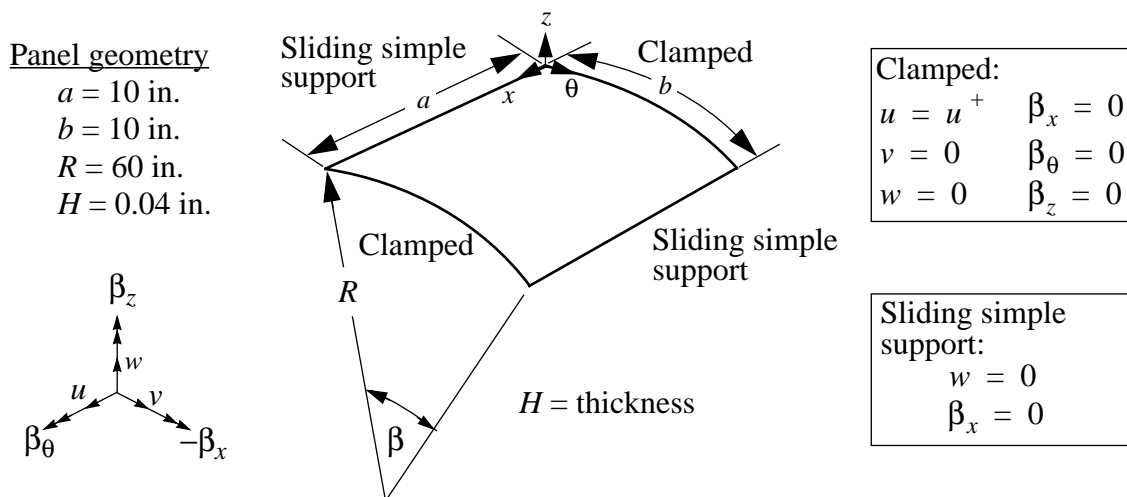
Figure 5-1 Panel geometry and boundary conditions for base model

Loading is due to either an axial end-shortening with no temperature change, or a uniform temperature change with axial end-shortening restricted to zero.

Experimental conditions were not as ideal as those assumed for the base model. Measured panel geometry, experimentally imposed boundary conditions, and thermal gradients contributed to small but significant discrepancies between the base model and experimental measurements of panel response. The following refinements were added to the base model in order to better represent experimental conditions.

1. Measured panel thickness was introduced.
2. Application of knife-edge simple support conditions was shifted 0.125 in. inward circumferentially from the edges of the panel (see Fig. 4-1).
3. Application of clamped support conditions was extended 0.375 in. inward axially from the curved ends of the panel (see Fig. 4-1).
4. Measured initial geometric imperfections were included in the model.
5. Through-thickness temperature gradients were included in the model.
6. Inplane temperature gradients were included in the model.
7. Clamped boundary conditions were relaxed to sliding clamped boundary conditions during thermal loading.

Each of these refinements will be considered separately to determine the relative effects of each refinement as compared to the base model. The effects of the refinements are considered for all three stacking sequences since each exhibits a unique response character. The buckling loads obtained from the refined models, N_x, are compared in Tables 5-1 and 5-2 to the buckling loads obtained from the simplified linear analysis, N_{cr} from Table 3-3. Also in Tables 5-1 and 5-2 are the differences between the base models and each of the refined models, listed as percentages.

5.1.1 Mechanical Response

For panels subjected to mechanical loading, the nonlinear response due to axial end-shortening is considered. For consistency with the analytical results of Chapter 3, nonlinear response results in Figs. 5-2 to 5-12 are normalized by the buckling loads obtained from the simplified linear analysis, N_{cr}, listed in Tables 5-1 and 5-2. Notice that the rows corresponding to the base model also correspond to Table 3-4, which lists the buckling values from STAGS for clamped/sliding simple support boundary conditions.

Table 5-1 Buckling loads for refined numerical models, Δu loading

Δu loading	$[\pm 45/0/90]_s$		$[\pm 45/90_2]_s$		$[\pm 45/0_2]_s$	
	N_x / N_{cr} N_{cr}=-141.0 lbs./in.	Difference from base model	N_x / N_{cr} N_{cr}=-145.0 lbs./in.	Difference from base model	N_x / N_{cr} N_{cr}=-100.3 lbs./in.	Difference from base model
Base model	0.96		0.91		1.18	
Measured thickness	1.17	+21%	1.10	+21%	1.49	+25%
Shifted simple supports	0.99	+2%	0.95	+4%	1.21	+2%
Extended clamped supports	1.00	+3%	0.91	0%	1.31	+11%
Initial geometric imperfections, panel number 3	0.85	-12%	0.79	-13%	1.09	-8%
Initial geometric imperfections, panel number 5	0.68	-29%	0.63	-31%	0.99	-17%

The first model refinement is to replace the base panel thickness of 0.04 in., from ref. [44], with a measured thickness. The representative measured thickness considered here is 0.0431 in. Measured thicknesses were obtained as the difference between the initial geometric imperfection scans of the inside and outside surfaces, from which an average panel thickness was calculated. Analyses were conducted by assuming this average value as the constant panel thickness.

The representative measured thickness is approximately 8% greater than the thickness assumed for the base model. The effects of measured thicknesses on the nonlinear response are shown in Fig. 5-2. The prebuckling stiffnesses, buckling loads, and initial postbuckling loads are substantially increased, but the postbuckling stiffness is relatively unaffected, compared to results for the thinner base model. From Eq. (2.30), for a panel with a large radius R it can be assumed that the buckling load is approximately proportional to the thickness cubed, so it is expected that an 8% increase in thickness would result in a 26% increase in the buckling load. The results in Table 5-1 suggest that this calculation provides a good approximation for the increase in buckling load as compared to the base model.

Table 5-2 Buckling loads for refined numerical models, ΔT loading

ΔT loading	$[\pm45/0/90]_s$		$[\pm45/90_2]_s$		$[\pm45/0_2]_s$	
	N_x/N_{cr} N_{cr}=-141.0 lbs./in.	Difference from base model	N_x/N_{cr} N_{cr}=-145.0 lbs./in.	Difference from base model	N_x/N_{cr} N_{cr}=-100.3 lbs./in.	Difference from base model
Base model	1.09		0.90		-1.36	
Measured thickness	1.39	+28%	1.09	+21%	-1.69	+25%
Shifted simple supports	1.15	+6%	0.94	+4%	-1.27	-6%
Extended clamped supports	1.13	+4%	0.90	0%	-1.37	+1%
Initial geometric imperfections, panel number 3	1.03	-5%	0.78	-13%	-1.31	-3%
Initial geometric imperfections, panel number 5	0.80	-26%	0.62	-31%	-1.26	-7%
Through-thickness temperature gradient	1.09	+1%	0.90	0%	-1.39	+3%
Midsurface temperature gradient	1.05	-3%	0.90	-1%	-1.33	-2%
Sliding clamped boundary conditions	0.94	-14%	0.90	-1%	does not buckle	

Since the curved end fixtures provide clamped support over 0.375 in. of the panel length at each end, and the knife edge supports are applied 0.125 in. inward from the straight edges, the analytical boundary conditions required modification from those used for the base model to represent the experimental boundary conditions. The constraint on the radial displacement, $w = 0$, was moved 0.125 in. inward circumferentially from the straight edges. Along the curved edges, the constraint on the radial displacement, $w = 0$, was extended 0.375 in. inward axially from the curved ends. The effect of these experimental boundary conditions on the analytical results are shown in Figs. 5-3 and 5-4.

(a) Model with measured thickness

(b) Nonlinear response, $[\pm 45/0/90]_s$

(b) Nonlinear response, $[\pm 45/90_2]_s$

(c) Nonlinear response, $[\pm 45/0_2]_s$
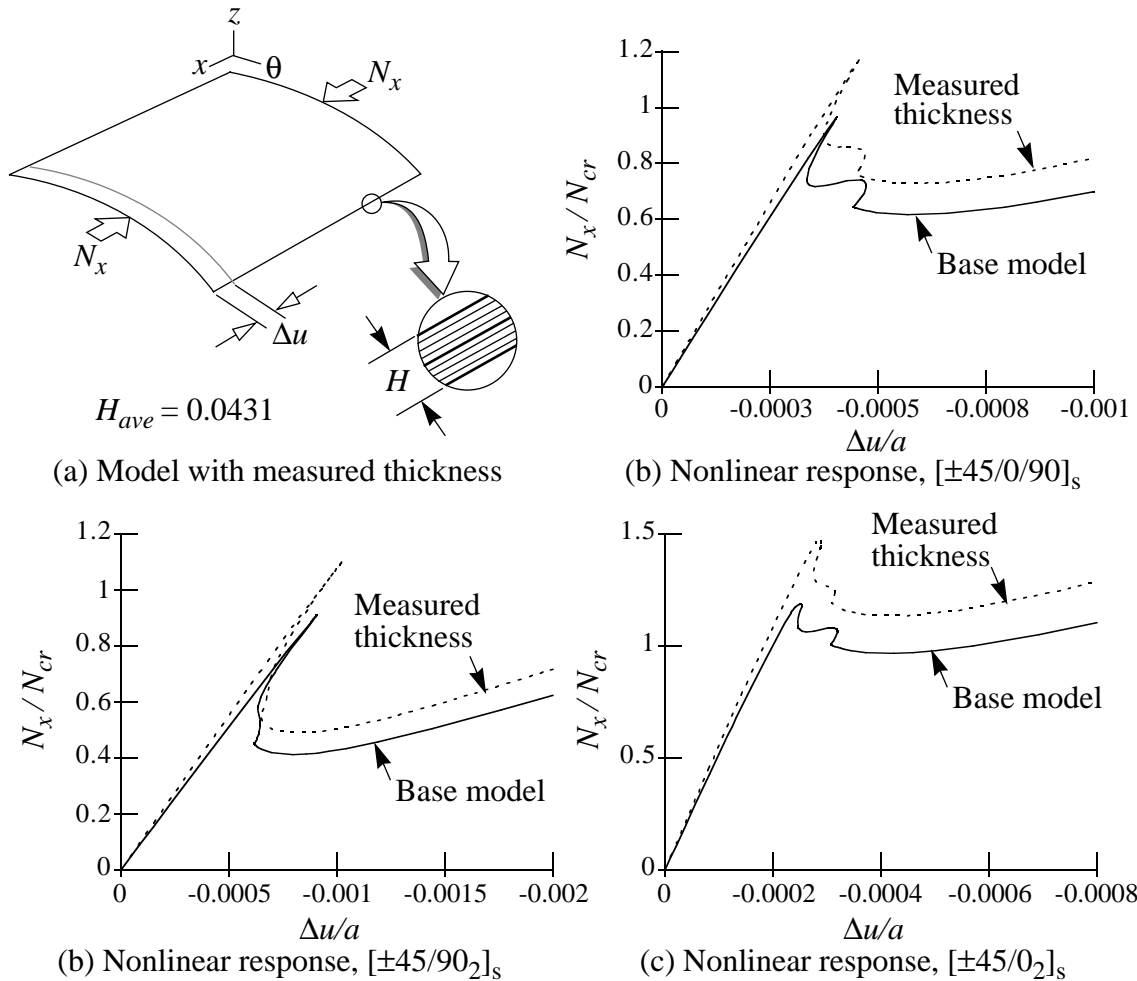
Figure 5-2 Effect of measured panel thickness on the nonlinear mechanical response

The analytical buckling loads due to end-shortening increase 2% to 4% for panels with shifted simple supports as compared to panels with base boundary conditions, as listed in Table 5-1. The postbuckling stiffnesses are higher for the shifted simple support boundary conditions than for the base model, although the initial postbuckling loads are unaffected by the change in boundary conditions. The increase in postbuckling stiffness may be due to the shortened unsupported arc length for the model with shifted edge supports as compared to the base model, leading to less panel material to form the postbuckled shape of one inward buckle.

For panels loaded in end-shortening with extended clamped boundary conditions, the buckling load is 0% to 11% greater than the buckling load for the base model. Postbuckling stiffnesses and initial postbuckling loads are essentially unaffected by the extended clamped supports. This sug-

(a) Model with shifted simple supports

(b) Nonlinear response, $[\pm 45/0/90]_s$

(c) Nonlinear response, $[\pm 45/90_2]_s$

(d) Nonlinear response, $[\pm 45/0_2]_s$
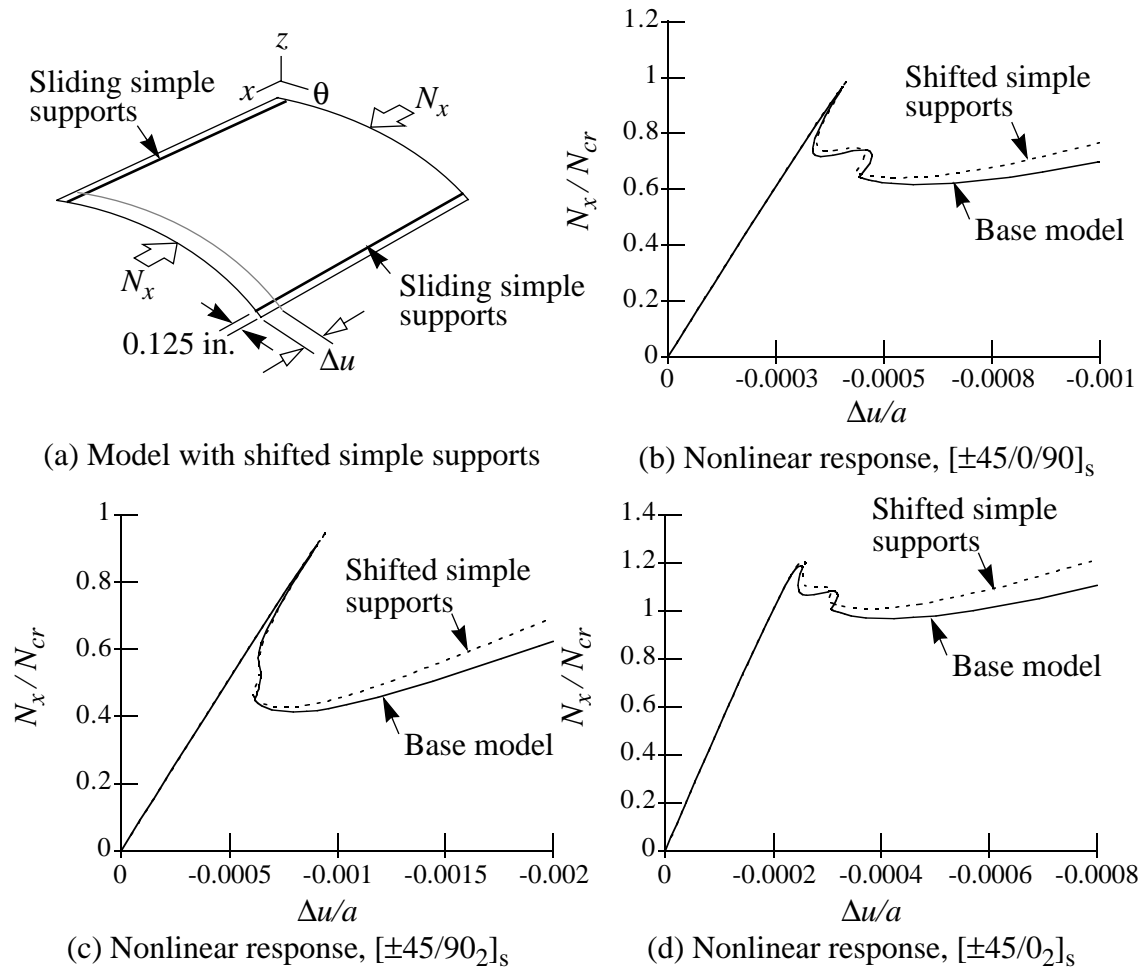
Figure 5-3 Effect of shifted simple supports on the nonlinear mechanical response

gests that little radial deflection occurs in the 0.375 in. of panel length nearest the curved ends, even when the original clamped supports of the base model are applied.

Initial geometric imperfections were measured and approximated with a Fourier series expansion according to the method described in Appendix B. The Fourier approximation for one of the initial geometric imperfections, measured from panel number 3 according to the designation of Table 4-2, is shown in Fig. 5-5(a). The radial imperfection $\bar{w}$ is normalized by the nominal layer thickness of 0.005 in. The magnitude of the maximum imperfection is on the order of two layer thicknesses, or 25% of the total panel thickness.

The nonlinear responses that are presented in Fig. 5-5 include the measured initial geometric imperfections of Fig. 5-5(a). Compared to the results for the base model, including this particular

(a) Model with extended clamped supports

(b) Nonlinear response, $[\pm45/0/90]_s$

(c) Nonlinear response, $[\pm45/90_2]_s$

(d) Nonlinear response, $[\pm45/0_2]_s$
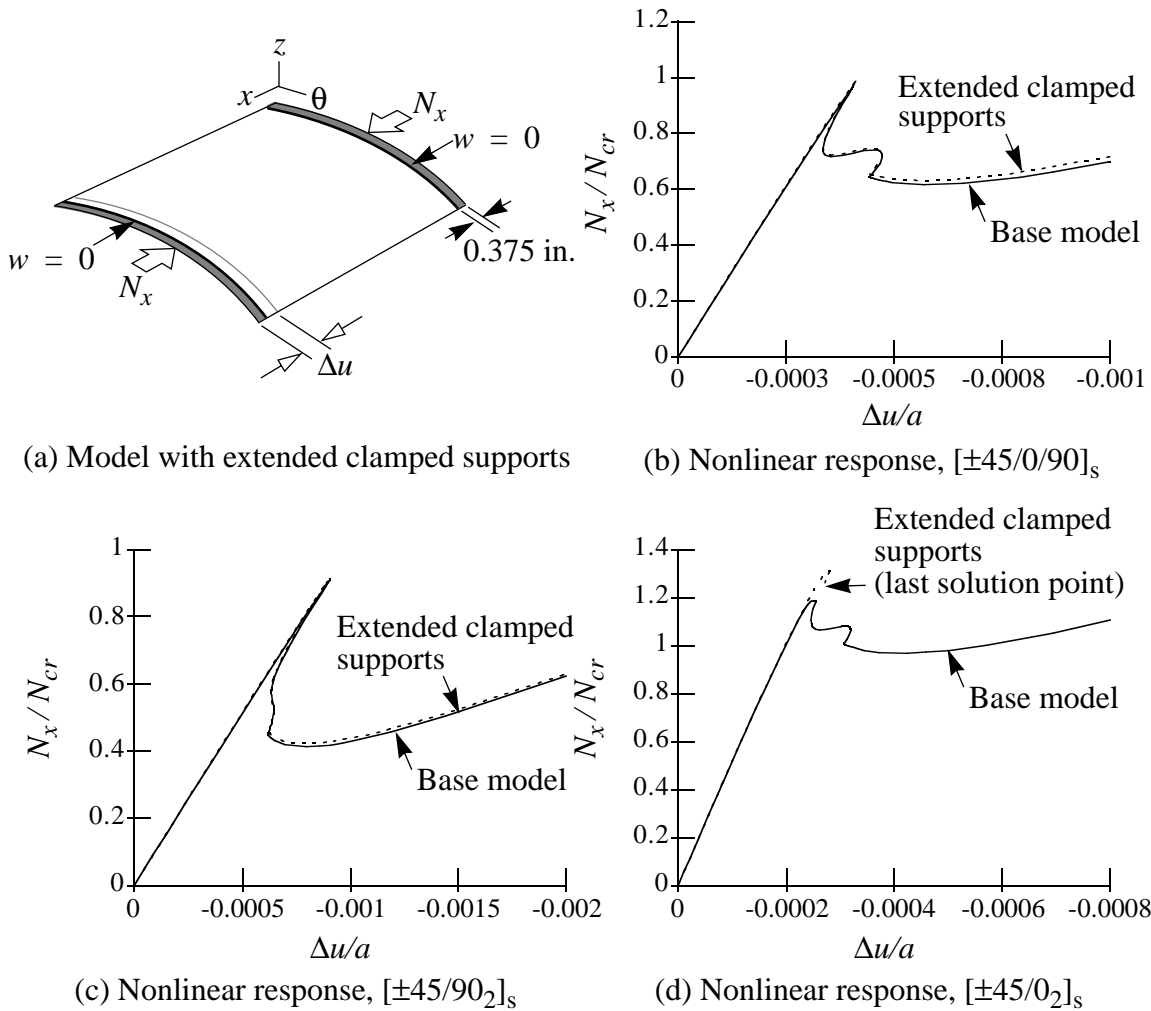
Figure 5-4 Effect of extended clamped supports on the nonlinear mechanical response

initial geometric imperfection has little effect on the panel stiffness due to end-shortening either before or after buckling, or on the initial postbuckling load. The bucking loads for end-shortening are decreased by 8% to 13% depending on the laminate, as shown in Table 5-1.

For completeness, the effects of a different initial geometric imperfection are shown in Tables 5-1 and 5-2 by considering the buckling loads. The initial geometric imperfection from panel number 5, shown in Appendix B, causes a substantial change in the buckling load as compared to the base model. The decrease in buckling load due to this particular measured imperfection is from 17% to 31%, shown in Table 5-1 for loading due to end-shortening. Comparing this decrease to the decrease noted with the imperfection from panel number 3, the specific geometry of the imperfec-
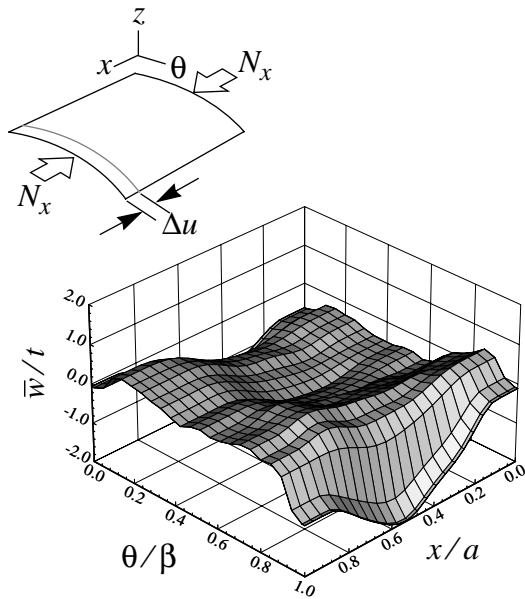
(a) Approximated geometric imperfections, panel number 3
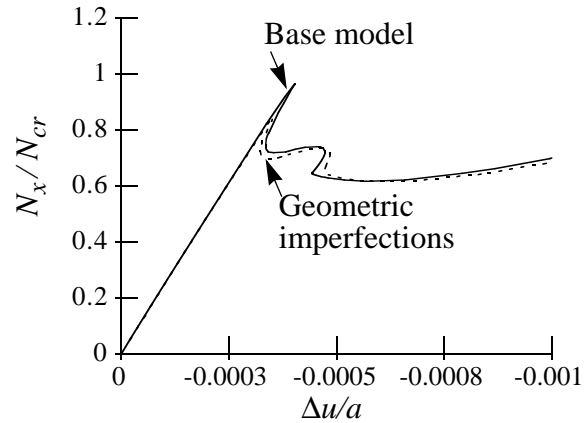
(b) Nonlinear response, $[\pm45/0/90]_s$
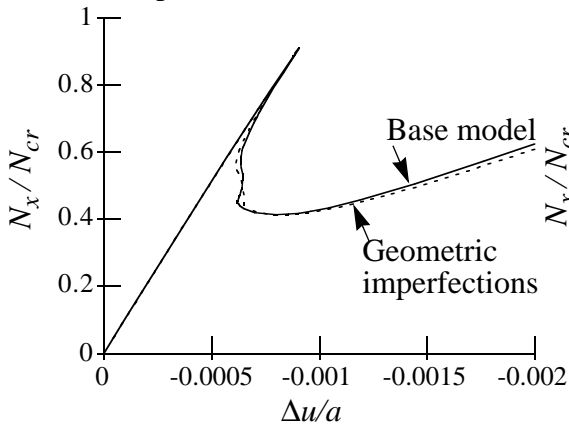
(c) Nonlinear response, $[\pm45/90_2]_s$
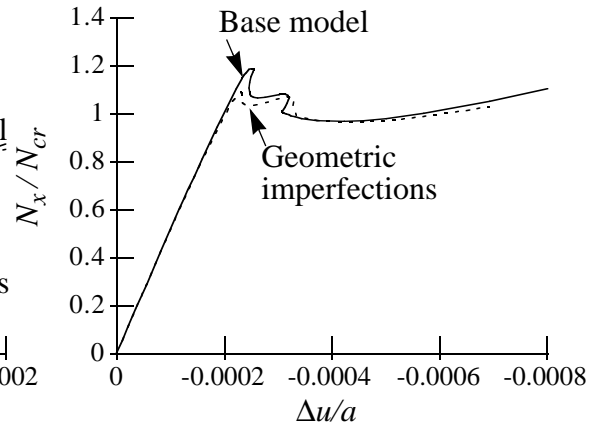
(d) Nonlinear response, $[\pm45/0_2]_s$

Figure 5-5 Effect of geometric imperfections on the nonlinear mechanical response

tion is seen to be important, resulting in either a very small or very substantial decrease in buckling load due to end-shortening.

5.1.2 Thermal Response

The thermal responses of the refined models as compared to the base model generally follow the observations noted for the mechanical responses. Additional refinements are also considered, including temperature gradients and sliding clamped boundary conditions along the curved end.

Again the response for a typical measured thickness of 0.0431 in. is compared to the response for a base thickness of 0.04 in, as obtained from ref. [44]. A 21% to 28% increase in the thermal buckling load is observed for the increased thickness model, as listed in Table 5-2.

The effects of measured thicknesses on the nonlinear response due to thermal loading are shown in Fig. 5-6. For the $[\pm45/0/90]_s$ and $[\pm45/90_2]_s$ laminates, the prebuckling stiffnesses and the buckling loads are substantially greater for the model with measured thickness compared to results obtained for the base model, as was observed for loading due to end-shortening. For the $[\pm45/0_2]_s$ laminate, the buckling load is similarly increased for the measured thickness as compared to the base model, but the prebuckling stiffness is unaffected. Repeating the approximation that the buckling load is proportional to the thickness cubed, the 8% increase in thickness resulting in a 26% increase in the buckling load again provides a good approximation.

(a) Model with measured thickness

(b) Nonlinear response, $[\pm45/0/90]_s$

(c) Nonlinear response, $[\pm45/90_2]_s$

(d) Nonlinear response, $[\pm45/0_2]_s$
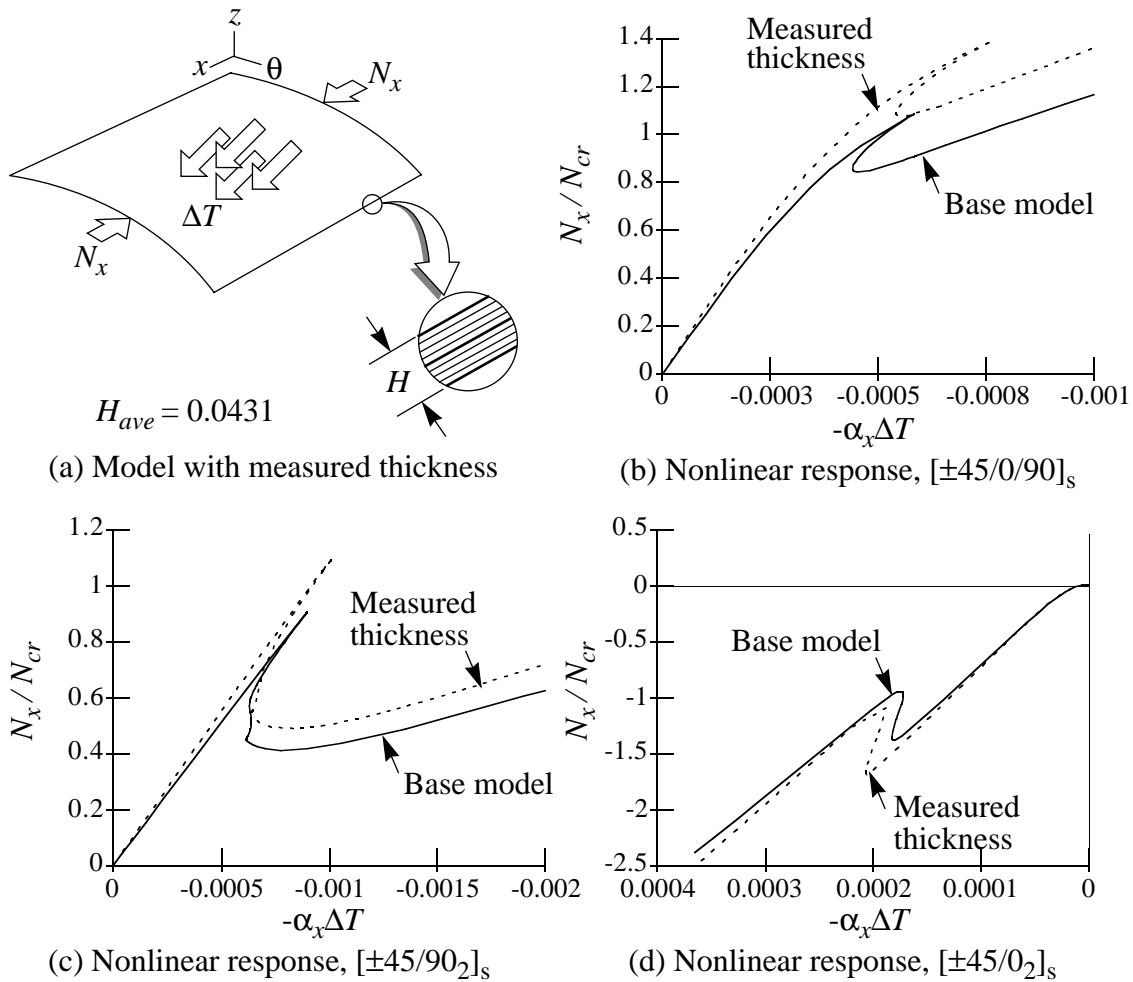
Figure 5-6 Effect of measured thickness on the nonlinear thermal response

The effects of shifted application of the knife edge supports 0.125 in. from the straight edge can be seen in Fig. 5-7 for loading due to temperature change. Each laminate responds to the change

(a) Model with shifted simple supports

(b) Nonlinear response, $[\pm45/0/90]_s$

(c) Nonlinear response, $[\pm45/90_2]_s$

(d) Nonlinear response, $[\pm45/0_2]_s$
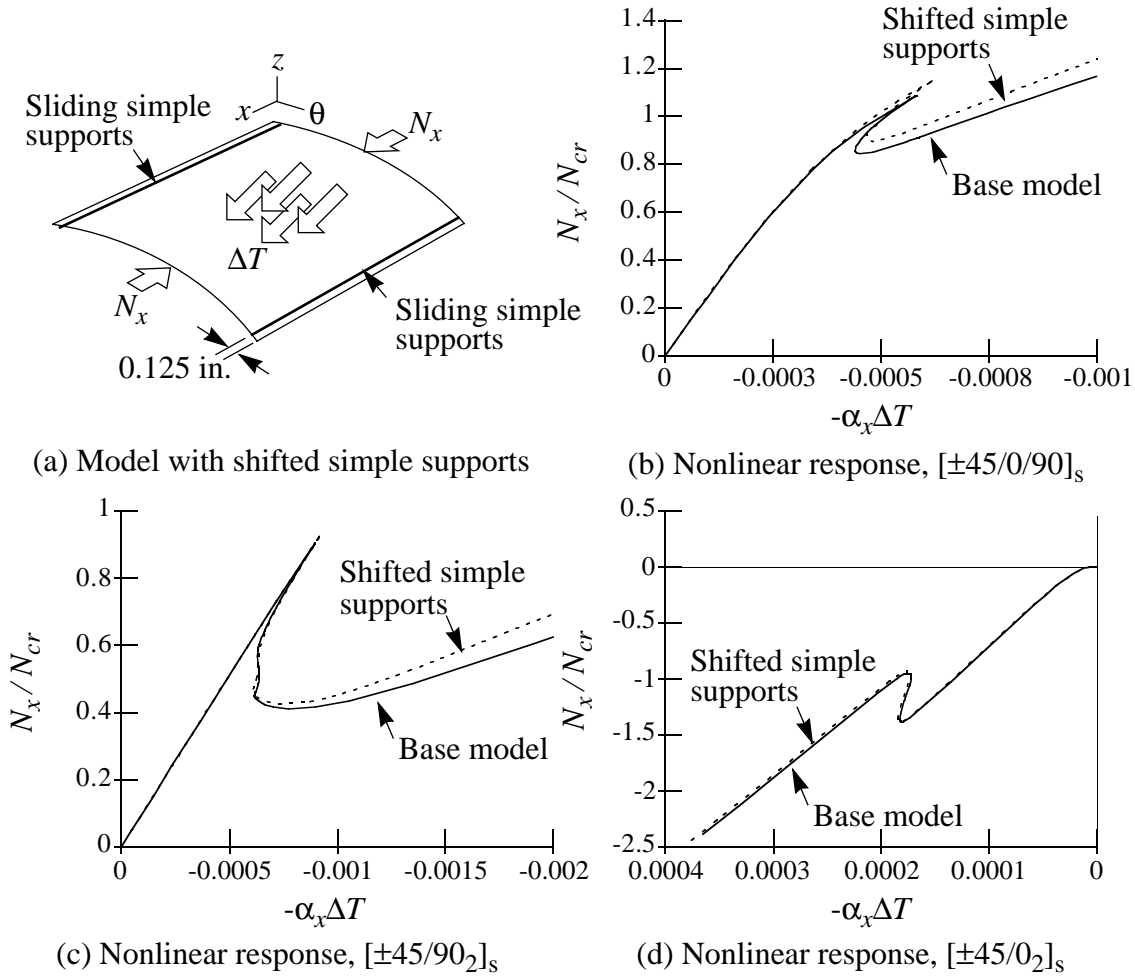
Figure 5-7 Effect of shifted simple supports on the nonlinear thermal response

in edge conditions differently. The $[\pm45/0/90]_s$ laminate shows a 6% increase in buckling load, an increased initial postbuckling load, and a slight increase in postbuckling stiffness. The $[\pm45/90_2]_s$ laminate shows a 4% increase in buckling load and an increased postbuckling stiffness with no change in initial postbuckling stiffness, similar to the noted response for loading due to end-shortening. The $[\pm45/0_2]_s$ laminate shows an 6% decrease in buckling load, but is otherwise unaffected.

Extending the clamped supports 0.375 in. from the curved ends has little effect on the thermal response of $[\pm45/0/90]_s$ and $[\pm45/90_2]_s$ laminates compared to the base model, as seen in Fig. 5-8.

(a) Model with extended clamped supports

(b) Nonlinear response, $[\pm45/0/90]_s$

(c) Nonlinear response, $[\pm45/90_2]_s$

(d) Nonlinear response, $[\pm45/0_2]_s$
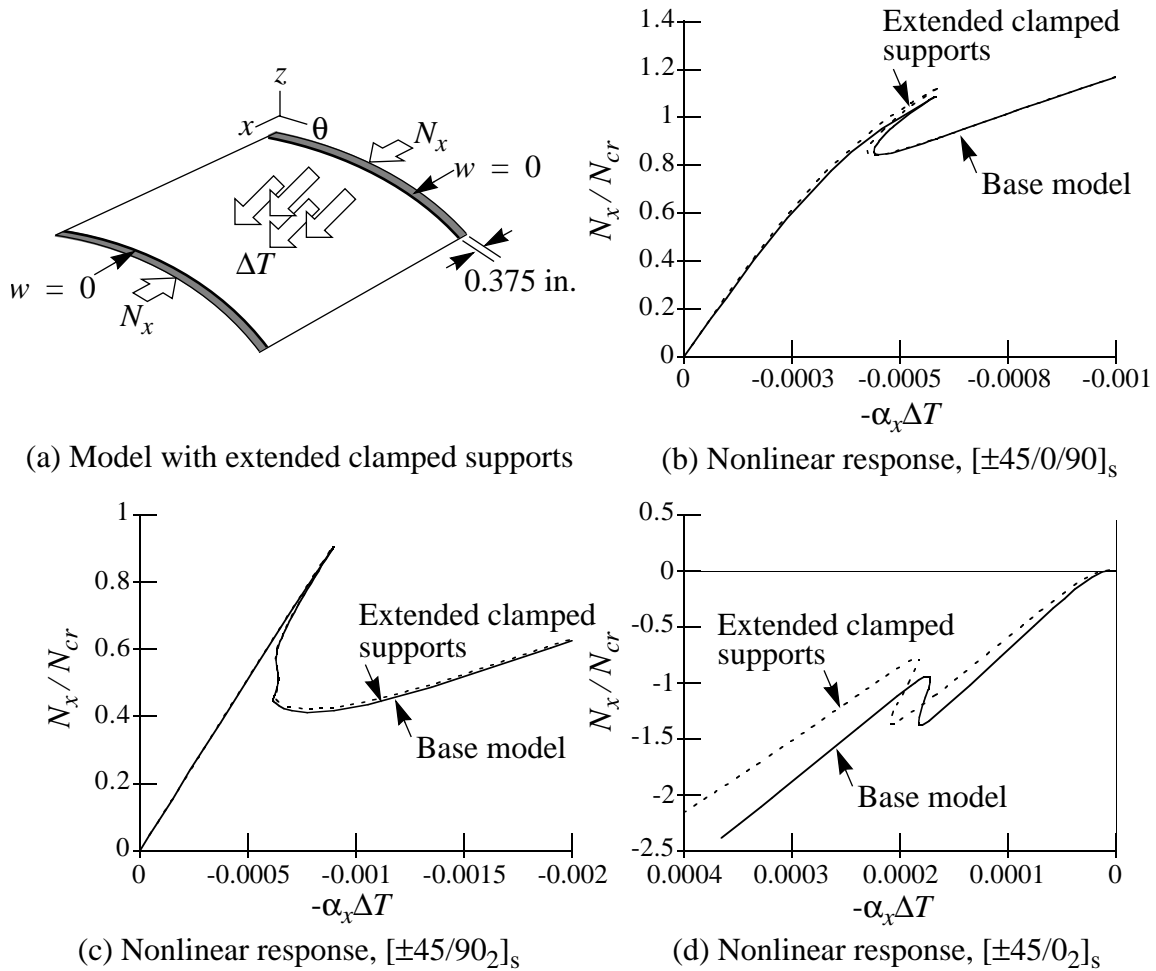
Figure 5-8 Effect of extended clamped supports on the nonlinear thermal response

For the $[\pm45/0_2]_s$ laminate, the response with extended clamped supports is surprisingly less stiff than the response for the base model, although the buckling load is virtually unchanged.

The Fourier approximation for the initial geometric imperfection measured for panel number 3 is shown in Fig. 5-9(a), where the radial imperfection $\bar{w}$ is normalized by the nominal layer thickness of 0.005 in. Considering the initial geometric imperfection of Fig. 5-9(a), a 3% to 13% reduction in the thermal buckling load is observed as compared to the buckling load of the base model, as seen in Table 5-2. Prebuckling stiffnesses, initial postbuckling loads, and postbuckling stiffnesses are, for the most part, unaffected. The initial imperfection for panel number 5, shown in Appendix B, has a more substantial effect on the buckling loads. The decrease in buckling loads as compared to the base model ranges from 17% to 31% for this imperfection, as shown in Table 5-2. Comparing the buckling load results for imperfections from panel number 3 and

(a) Approximated geometric imperfections,
panel number 3

(b) Nonlinear response, $[\pm 45/0/90]_s$

(c) Nonlinear response, $[\pm 45/90_2]_s$

(d) Nonlinear response, $[\pm 45/0_2]_s$
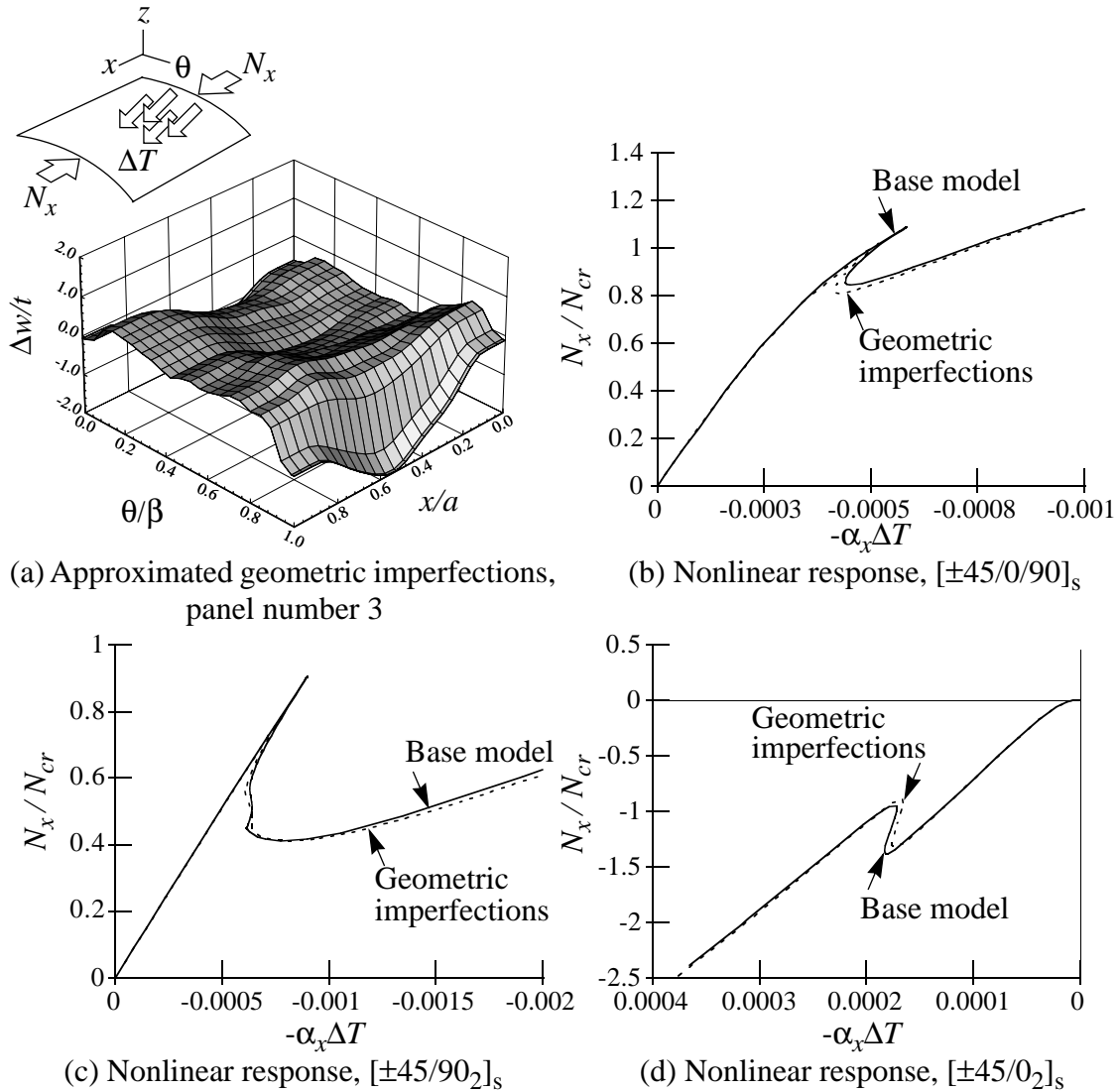
Figure 5-9 Effect of geometric imperfections on the nonlinear thermal response

imperfections from panel number 5, the specific geometry of the initial imperfection is seen to cause either a very small or very substantial decrease in the buckling load due to thermal loading.

The effects of thermal gradients are separated into through-thickness temperature gradients, which are assumed to be linear in the z-direction but zero in the x- and θ-directions, and midsurface gradients, which are assumed to be non-zero in the x-and θ-directions but zero in the z-direction.

The effects of through-thickness temperature gradients are shown in Fig. 5-10. For a gradient, it is assumed that the temperature of the outside surface of the curved panel is 0.75% greater than the temperature of the reference surface, and that the temperature of the inside surface is 0.75%

(a) Model of through-thickness
temperature gradient

(b) Nonlinear response, $[\pm45/0/90]_s$

(c) Nonlinear response, $[\pm45/90_2]_s$

(d) Nonlinear response, $[\pm45/0_2]_s$
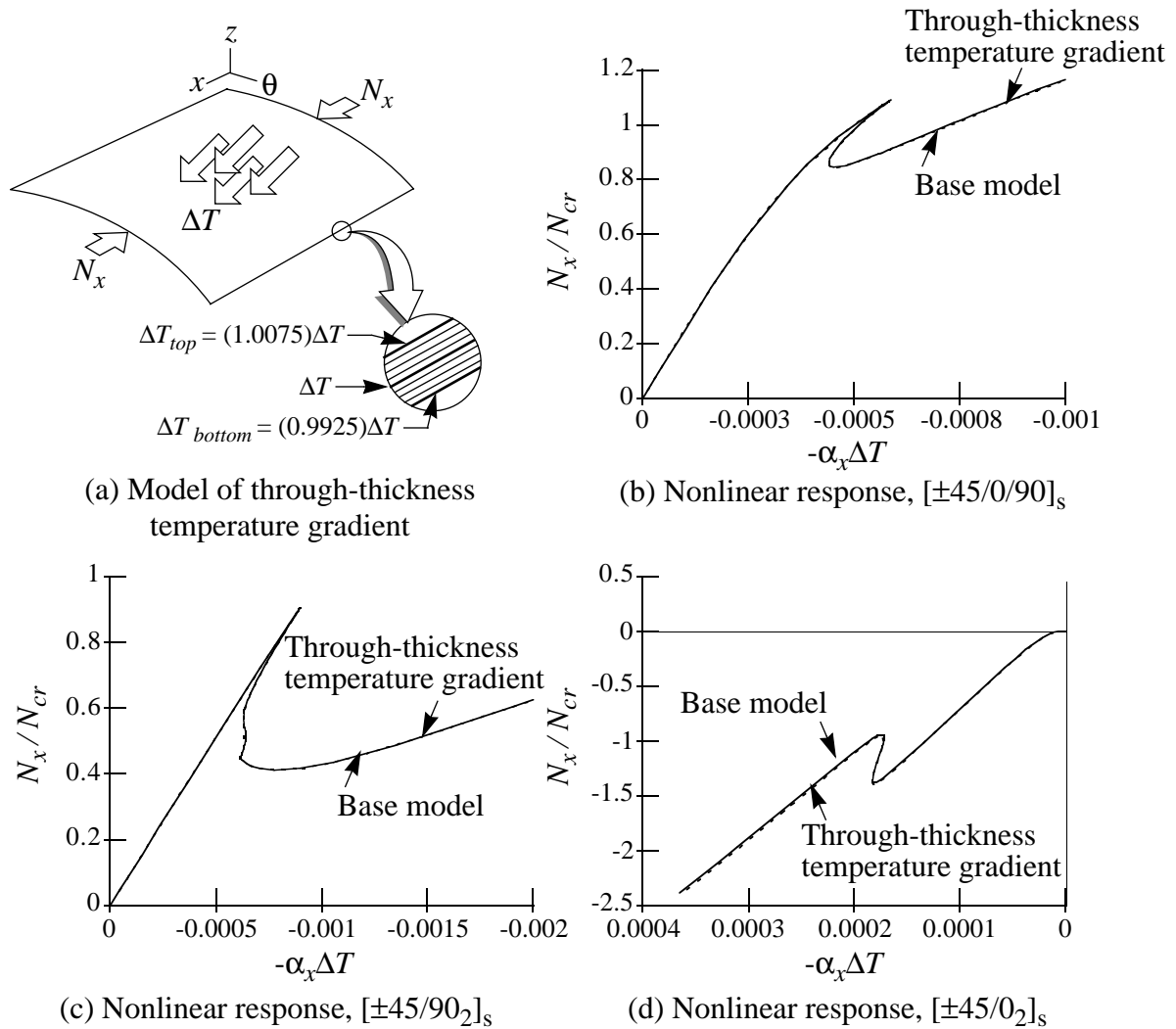
Figure 5-10 Effect of through-thickness temperature gradient on the nonlinear thermal response

less than the temperature of the reference surface, resulting in a 1.5% temperature gradient through the thickness. When the midsurface temperature ΔT=400°F, the difference between the inside and outside surface temperatures is 6°F. This 6°F difference in surface temperatures approximates the surface temperature difference noted in the experiments. The effects of this through-thickness temperature gradient are seen in Fig. 5-10(b-d). Response is virtually unaffected.

The typical midsurface temperature gradient shown in Fig. 5-11(a) was obtained by fitting a polynomial approximation to experimental data using the methods described in Appendix D. Nonlinear response curves are generated using ΔT_{ave}, which is the average temperature at the midsurface,
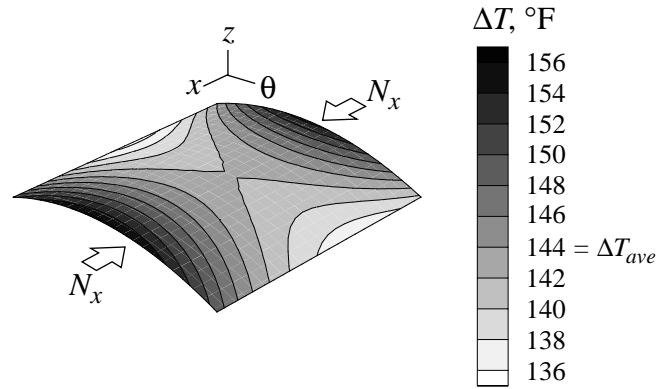
(a) Model of midsurface temperature gradient
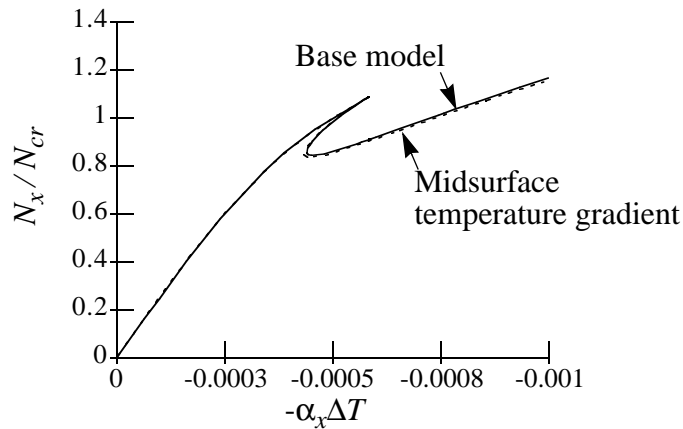
(b) Nonlinear response, $[\pm45/0/90]_\mathrm{s}$
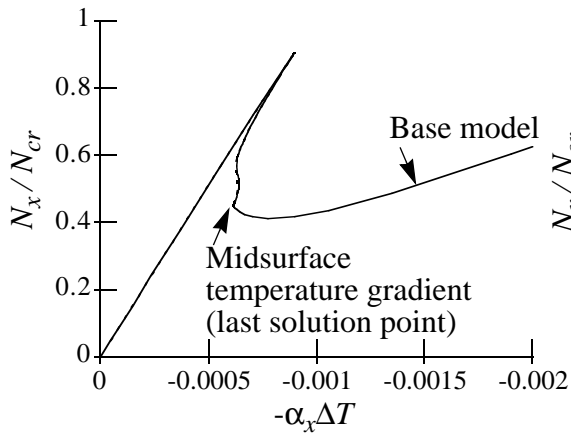
(c) Nonlinear response, $[\pm45/90_2]_\mathrm{s}$
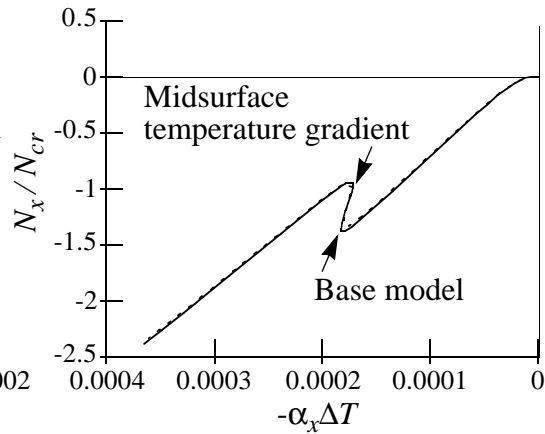
(d) Nonlinear response, $[\pm45/0_2]_\mathrm{s}$

Figure 5-11 Effect of midsurface temperature gradient on the nonlinear thermal response

obtained by summing the temperatures at each nodal location and dividing by the number of nodes in the finite element model. When ΔT_{ave}=216°F there is a maximum temperature difference of 20°F between the hottest and coolest points on the midsurface. The effects of this midsurface temperature gradient are shown in Fig. 5-11(b-d), where ΔT along the horizontal axis is actually ΔT_{ave} for the panel. The response with a midsurface temperature gradient is seen to be virtually the same as compared to the base model. Combined with the results in Fig. 5-10 for through-the-thickness temperature gradients, it can be concluded that the temperature gradients observed in the experiments are sufficiently small and thus the experiments can be expected to provide useful insight into the problem of uniform temperature change.

The final model refinement has to do with the thermal expansion of the end grip fixture used for clamping. The fixture was constructed of stainless steel, which has a coefficient of thermal expansion $\alpha = 6.0 \times 10^{-6}$ in./in./°F. As a result of this coefficient of thermal expansion, the circumferential displacement of the clamped ends of the panels were not zero during temperature changes. Instead, they moved in the circumferential direction. This boundary condition was referred to previously as sliding clamped/sliding simple supports. A comparison is made in Fig. 5-12 between the base model and a model with sliding clamped/sliding simple supports. The only difference between the two models is that for sliding clamped supports, $v \neq 0$ along the curved ends. The response is seen to differ greatly for the $[\pm 45/0/90]_s$ and $[\pm 45/0_2]_s$ laminates with sliding clamped boundary conditions as compared to the clamped boundary conditions of the base model. In fact, for the $[\pm 45/0_2]_s$ laminate, the classical postbuckling drop in load disappears altogether. Apparently the $v = 0$ condition on the clamped ends of the base model triggers the load drop phenomenon for this laminate. However for the $[\pm 45/90_2]_s$ laminate, the response is the same for both sliding clamped and clamped boundary conditions. These response characteristics are due to the very small negative coefficient of thermal expansion for the $[\pm 45/90_2]_s$ laminate as compared to the larger positive coefficients of thermal expansion for the other two laminates, listed in Table 3-2. As a result, the $[\pm 45/90_2]_s$ panel exhibits very little circumferentially movement during thermal loading whether or not v-displacement is restricted, so the nonlinear response is unaffected.

5.2 The Effects of Circumferential Restraint

A more detailed investigation on the effects of circumferential restraint is considered for three representative tests, including, for completeness, one test from each stacking sequence. A fully refined numerical model is considered, which includes the effects of measured thickness, shifted edge supports, extended clamped supports, initial geometric imperfections, and thermal gradients.
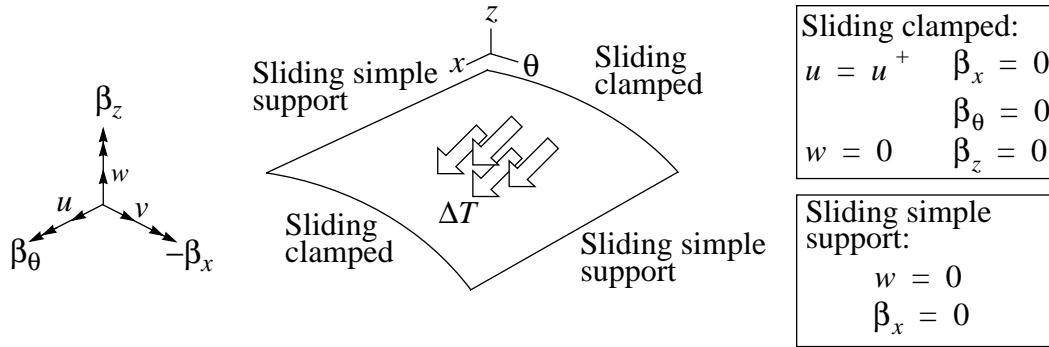
(a) Sliding clamped/sliding simple support boundary conditions
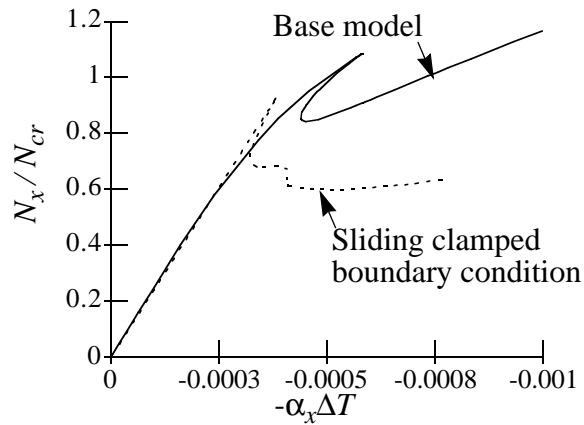
(b) Nonlinear response, $[\pm45/0/90]_s$
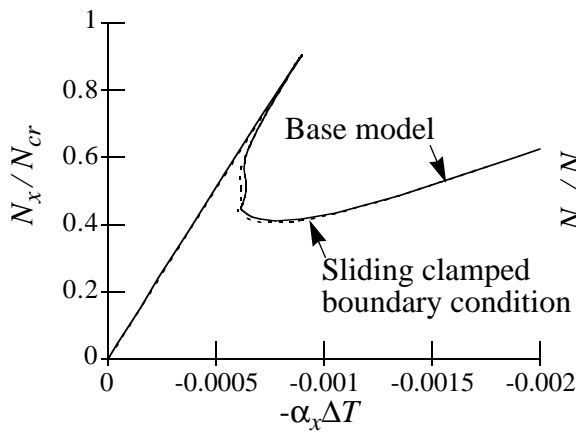
(c) Nonlinear response, $[\pm45/90_2]_s$
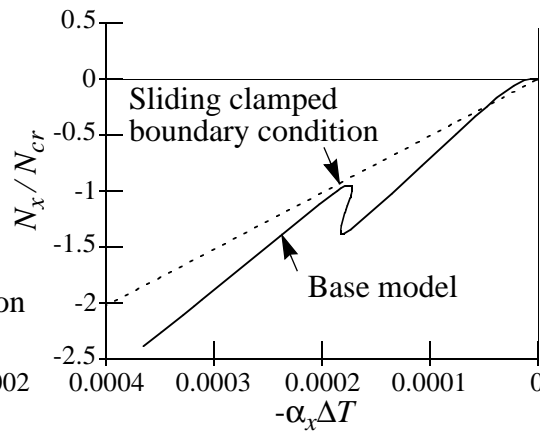
(d) Nonlinear response, $[\pm45/0_2]_s$

Figure 5-12 Effect of sliding clamped/sliding simple support boundary conditions on the nonlinear thermal response

A comparison between the experimentally determined buckling load and the buckling loads obtained using the fully refined numerical model and either clamped/sliding simple support or sliding clamped/sliding simple support boundary conditions is shown in Table 5-3 for these three representative tests. Also listed in Table 5-3 are the buckling loads obtained for models with specified v-displacements along the curved edges equal to the thermal expansion of steel. The expression for this specified v-displacement, assuming an origin at one corner of the panel, is

$$v^\circ = \alpha_s \Delta T \left(\theta R - \frac{b}{2} \right), \tag{5.1}$$

where $\alpha_s = 6 \times 10^{-6}$ is the coefficient of thermal expansion of steel.

Table 5-3 Buckling loads for different end support conditions

	Experiment P_{max}, lbs.	Clamped supports P/P_{max},	Sliding clamped supports P/P_{max},	Specified v-displacement P/P_{max},
$[\pm 45/0/90]_s$ Test Q3	-1350	does not buckle	0.95	0.74
$[\pm 45/0_2]_s$ Test Z4	-1090	1.81	0.94	0.79*
$[\pm 45/90_2]_s$ Test N3	-1270	0.93	0.84	0.75

* Does not correspond to a maximum load, but the load at the last solution on the linear prebuckling path.

Recall from Chapter 4 that the test Q3 is loaded first in end-shortening then heated to 400°F. The test Z4 is heated first to 250°F, then loaded in end-shortening. The test N3 is loaded first in end-shortening, then heated to 400°F. These three tests were selected because they demonstrated the clearest numerically predicted differences between clamped supports and sliding clamped supports among each of their respective stacking sequences. During loading by end-shortening, curved end boundary conditions are clamped supports. The sliding clamped support and specified v-displacement boundary conditions are imposed only during thermal loading to simulate the thermal expansion of the steel end grips.

For the quasi-isotropic $[\pm 45/0/90]_s$ laminate, the model assuming clamped supports does not predict buckling at all, while the model with sliding clamped supports predicts buckling at a load 5% below the experimental buckling load, and the model with a specified v-displacement predicts

buckling at a load 26% below the experimental buckling load. For the $[\pm 45/0_2]_\text{s}$ laminate, the model with clamped supports over predicts the buckling load by 81%, while the model with sliding clamped supports under predicts the buckling load by just 6%, and the model with a specified v-displacement underpredicts the buckling load by 21%. Clearly, for both $[\pm 45/0/90]_\text{s}$ and $[\pm 45/90_2]_\text{s}$ laminates, thermal loading should be modeled assuming sliding clamped supports, which allow v-displacement along the curved ends according to the expansion of the laminates.

For the $[\pm 45/90_2]_\text{s}$ laminate, the buckling load predicted from the model with clamped supports is 7% below the experimental buckling load, while the buckling load predicted from the model with sliding clamped supports is 16% below the experimental buckling load, and the model with a specified v-displacement is 25% below the experimental buckling load. For this laminate and this particular example, the buckling results suggest the use of clamped supports rather than either sliding clamped supports or a specified v-displacement. This is likely due to the nature of the experimental apparatus. The use of sliding clamped supports became necessary in order to account for the thermal expansion of the steel end supports, but the $[\pm 45/90_2]_\text{s}$ laminate contracts in the circumferential direction when heated, so allowing sliding clamped supports results in a compressive v-displacement rather than the tensile v-displacement suggested by the experimental conditions.

For all three laminates, assuming a specified v-displacement equal to the thermal expansion of the steel end grips, as in Eq. (5.1), results in a much lower buckling load that the experimental measurement. This suggests that some amount of sliding occurs between the curved end grip and the curved laminate during thermal loading, so that the correct boundary condition along the curved end is neither entirely clamped with v-displacement equal to zero, or perfectly fixed to the steel curved end grips, with v-displacement specified as in Eq. (5.1). The assumption of sliding clamped support boundary conditions seems a reasonable compromise between the two extremes.

5.2.1 Experimental and Analytical Considerations, $[\pm 45/0/90]_\text{s}$ Laminate

When analyzing experimental results, loading due to both end displacement and temperature change must be accounted for in the model. As described in Chapter 4, when attempting to hold a constant displacement, the lower load frame platen drifted downward with time due to a small hydraulic leak. Also during heating, the steel fixtures expanded, causing an axial end-shortening of the panel. As a result of these two factors, thermal loading was always accompanied by axial displacement, which could be obtained from experimental data. Therefore, loading of the model consisted of either end shortening alone, or temperature change coupled with end shortening. To

simulate the measured relationship between the two coupled loadings, Δu is applied as a linear or piecewise linear function of ΔT, and Riks' method [30] operates on the ΔT portion of loading. The outcome of the analysis is the axial load P that results from the applied temperature and end short-ening.

The nonlinear load vs. displacement and load vs. temperature responses for test Q3 with a $[\pm 45/0/90]_s$ stacking sequence are shown in Fig. 5-13. Experimental results are compared to numerical results for the fully refined models with clamped supports, sliding clamped supports, and a specified v-displacement. In the prebuckling range, all numerical models are seen to predict the same response. However, the model with sliding clamped supports is the only one to accurately predict buckling near the experimental buckling load.
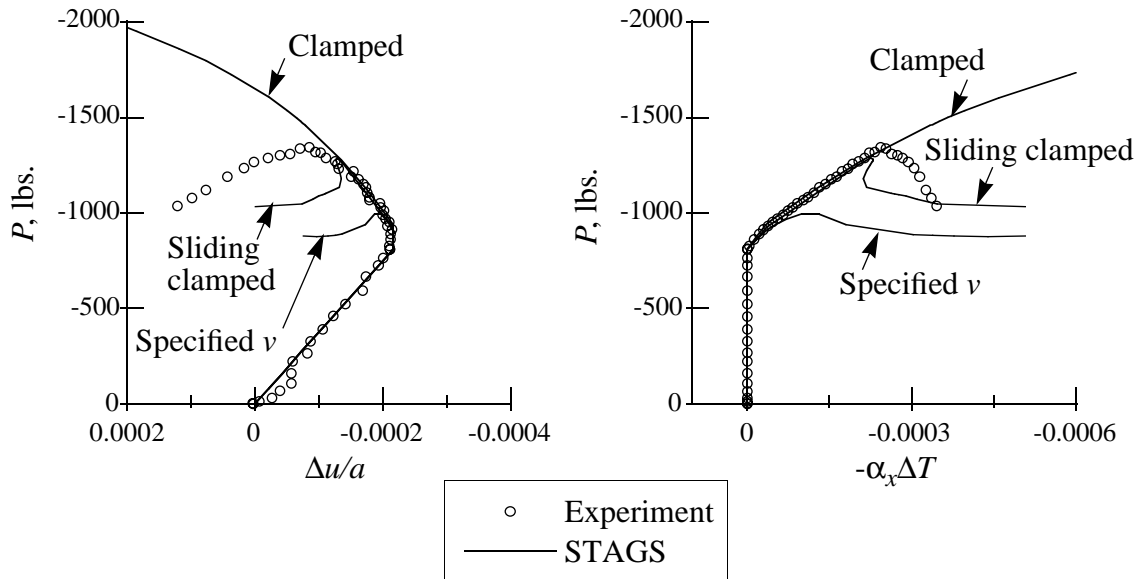
Figure 5-13 Nonlinear response with different boundary conditions, test Q3, $[\pm 45/0/90]_s$ laminate

A closer examination of the prebuckling response is obtained by examining the selected experimental strain gage results, shown in Fig. 5-14. As indicated in the strain gage diagram, gages are considered in back-to-back pairs with the even numbered gages located on the outside surface of the curved panel and the odd numbered gages located on the inside surface. Gages 7 and 8 and gages 37 and 38 are axial gages, while gages 19 and 20 and gages 27 and 28 are circumferential gages. Strain gages in back-to-back pairs can be used to access the bending or change in curvature of the panel, as described in Fig. 5-15. When back-to-back gages diverge, a positive or nega-
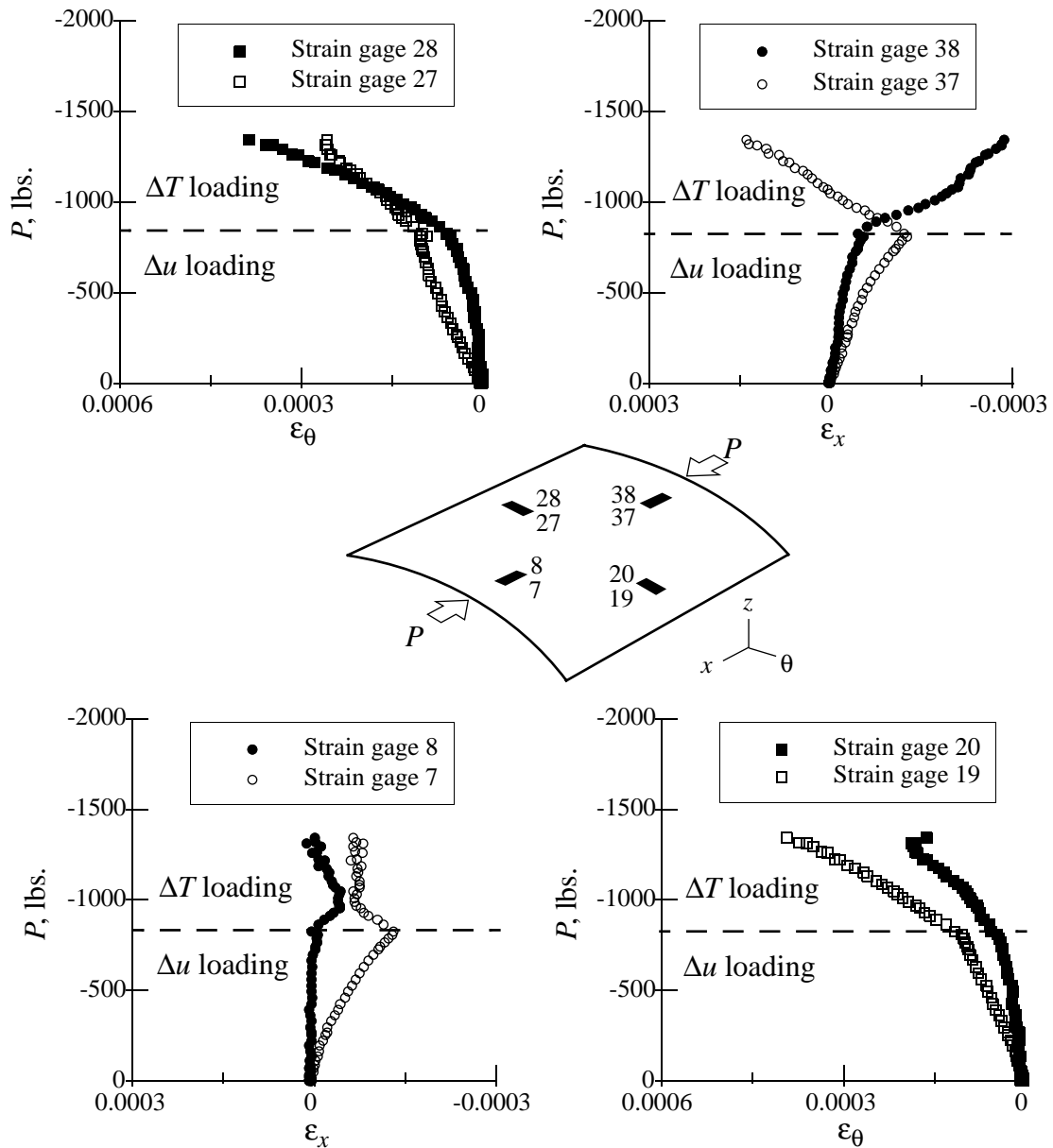
Figure 5-14 Prebuckling strains, test Q3, [±45/0/90]$_s$ laminate

tive change in curvature is indicated, depending on the relative value of the strains. When the strain of the even numbered outside gage is greater, algebraically, than the strain of the odd numbered inside gage, a positive change in curvature results.

For loads up to -800 lbs., test Q3 was loaded at room temperature by applying axial end-shortening. Beyond -800 lbs., the displacement of the load frame platen was fixed while the temperature was increased to 400°F. Prebuckling strains for test Q3 are shown in Fig. 5-14. Considering first
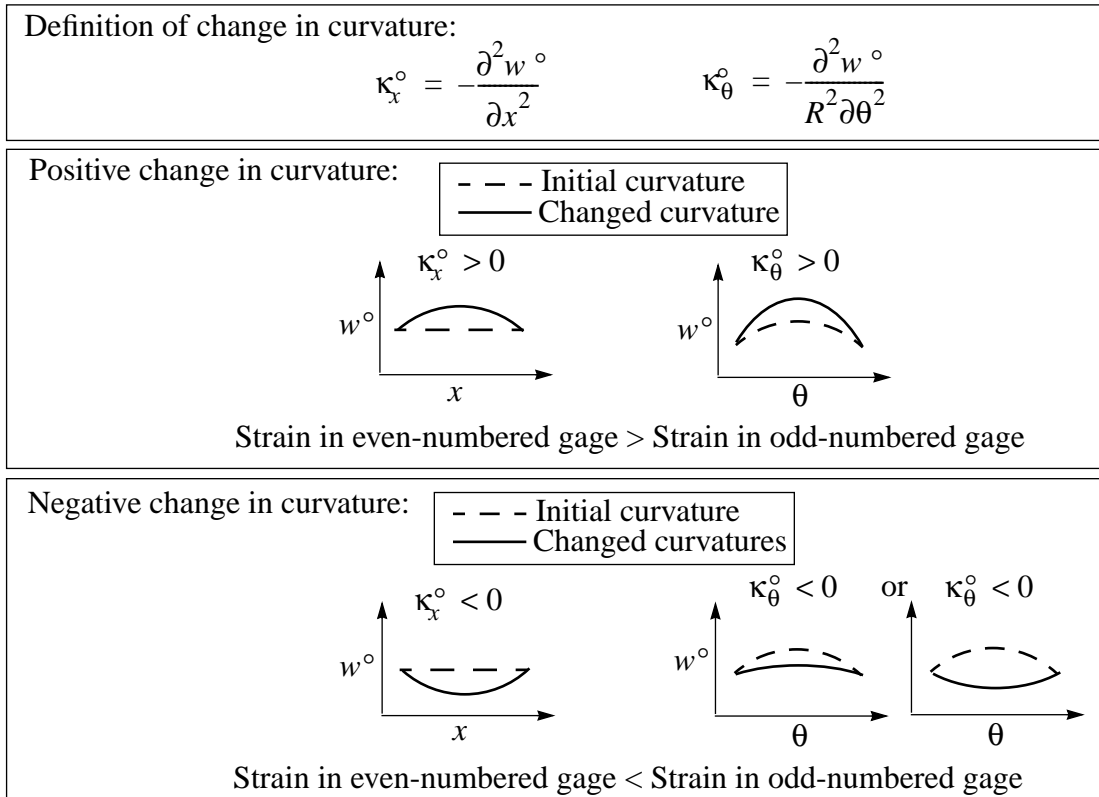
Figure 5-15 Sign convention of curvature and associated strain gage values

the Δu loading up to -800 lbs., axial gages 7/8 and 37/38 indicate positive curvature.   Circumferential gages 19/20 and 27/28 indicate negative curvature.   These observations are consistent with the deformation pattern of Fig. 5-16(a). Beyond -800 lbs., when ΔT loading is applied, axial gages 37/38 change from positive curvature to negative curvature, and circumferential gages 27/28 change from negative curvature to positive curvature. Considering Fig. 5-16(b), the model with clamped/sliding simple supports maintains the same deformation pattern during ΔT loading as it had during Δu loading, Fig. 5-16(a). The model with sliding clamped/sliding simple supports shows a new deformation pattern for ΔT loading, Fig. 5-16(c), as compared to Δu loading, Fig. 5-16(a). This change in deformation pattern is consistent with the changes in curvatures noted for gages 37/38 and 27/28, suggesting that sliding clamped supports are a more realistic representation of the actual experimental boundary conditions than are clamped supports. Note that gages 19/20 do not indicate a change in curvature when ΔT loading is applied, although Fig. 5-16(a) and (c) suggest that a change in curvature should occur. This discrepancy is likely due to a slight shift in the measured postbuckling deformation pattern due to an uneven load distribution across the curved end of the panel. The deformation pattern for the model with a specified v-displacement in shown in Fig. 5-16(d). This model also shows a new deformation pattern for ΔT loading as com-

(a) Δu loading, clamped supports

(b) ΔT loading, clamped supports

(c) ΔT loading, sliding clamped supports

(d) ΔT loading, specified v-displacement
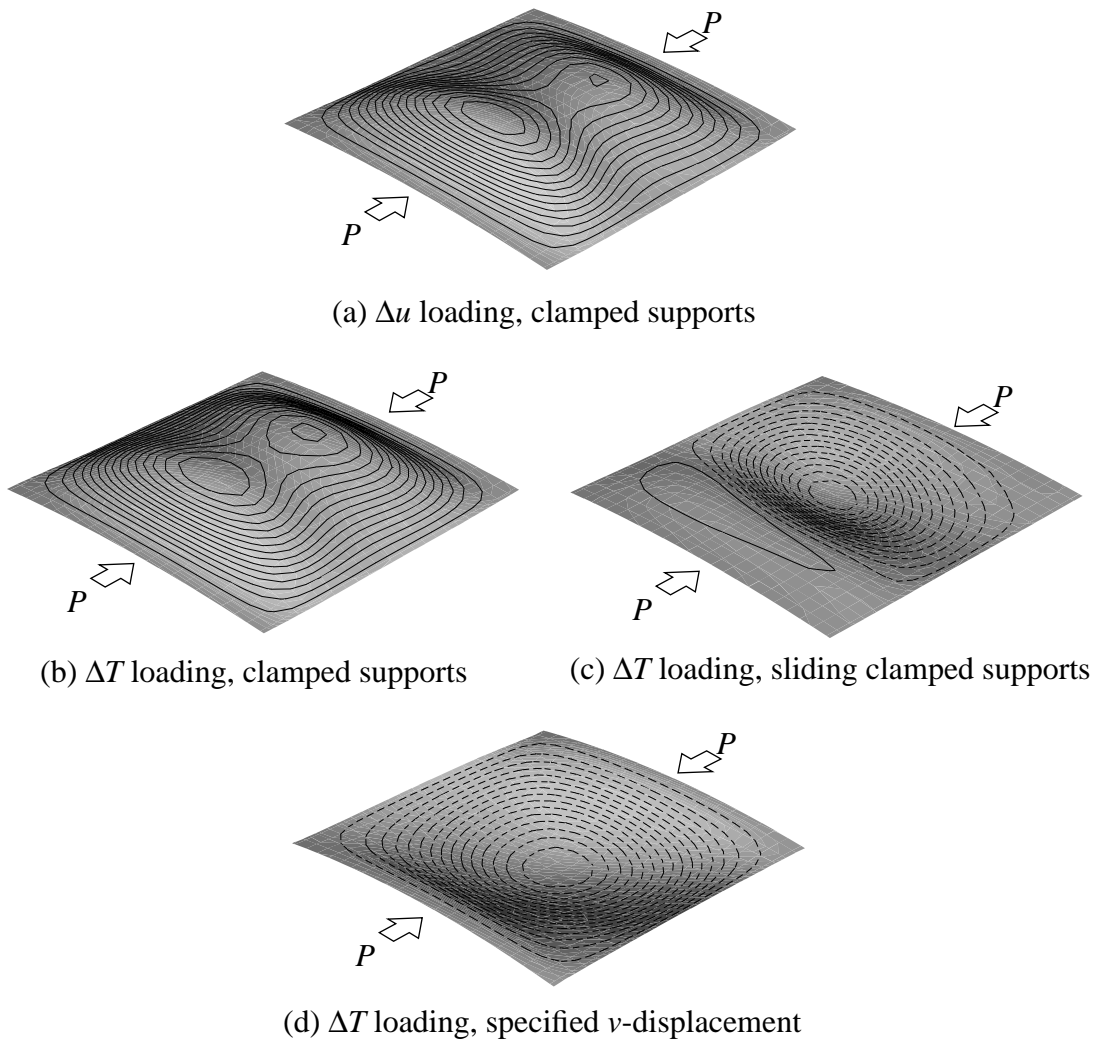
Figure 5-16 Prebuckling deformations, test Q3, [±45/0/90]$_s$ laminate

pared to the pattern for Δu loading, although this new pattern does not match the changes in curvature of the strain gages as well the model with sliding clamped supports, Fig. 5-16(c).

From Fig. 5-13, the assumption of sliding clamped boundary conditions significantly improves the predicted buckling load as compared to the model with clamped boundary conditions, but the postbuckling response is still not predicted correctly. In the experiment, the load gradually decreases after buckling, while the analysis with sliding clamped boundary conditions predicts a sudden drop in load. This suggests that, in the experiment, additional support is acting on the panel after buckling and preventing the expected sudden drop in load.

5.2.2 Experimental and Analytical Considerations, [±45/0$_2$]$_s$ Laminate

The nonlinear load vs. displacement and load vs. temperature responses for test Z4 with a [±45/0$_2$]$_s$ stacking sequence are shown in Fig. 5-17. Numerical results from the fully refined models with clamped supports, and sliding clamped supports, and a specified v-displacement are compared to experimental results. The panel is heated first to 250°F, then loaded in axial end-shortening. The prebuckling stiffness during end-shortening is slightly different for the three different boundary conditions, with the sliding clamped boundary condition providing the best match to experiment. At buckling, the model with sliding clamped supports provides a good estimate of both the buckling load and postbuckling stiffness, while the model with clamped supports predicts a much higher buckling load.

The strain gage results during thermal loading are shown in Fig. 5-18. The divergence of axial gages 7/8 and 37/38 indicate a negative change in curvature, as do the divergence of circumferential gages 19/20 and 27/28. The deformation pattern shown in Fig. 5-19(a) for clamped/sliding simple supports, ΔT loading, suggests positive curvature at the selected strain gage locations. The pattern of negative change in curvature indicated by the strain gages is consistent with the deformation pattern shown in Figs. 5-19(b) and 5-19(c) for the models with sliding clamped supports and a specified v-displacement, respectively.
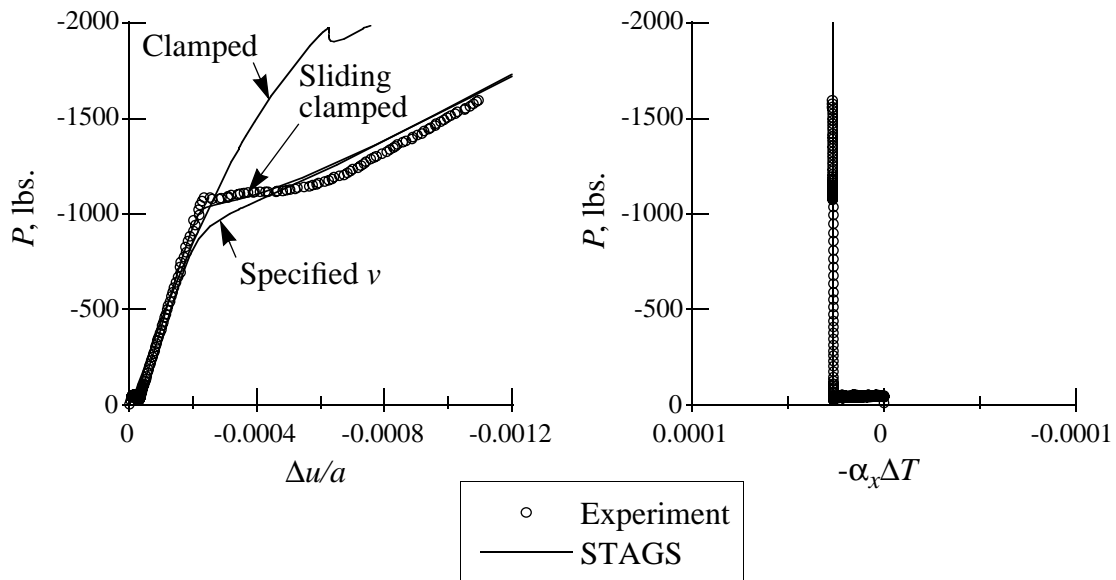
Figure 5-17 Nonlinear response with different boundary conditions, test Z4, [±45/0$_2$]$_s$ laminate
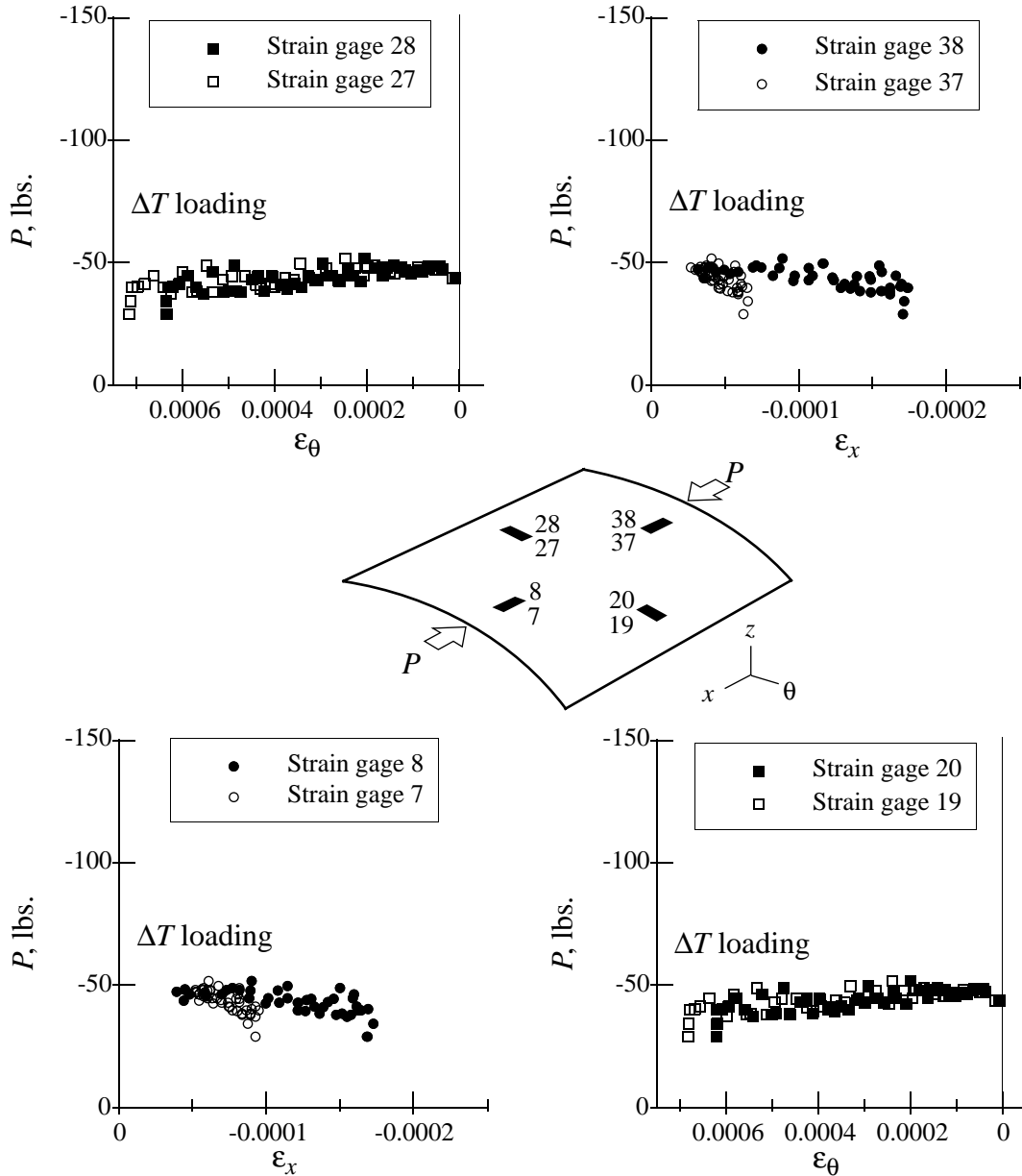
Figure 5-18 Prebuckling strains, test Z4, $[\pm 45/0_2]_s$ laminate

5.2.3 Experimental and Analytical Considerations, $[\pm 45/90_2]_s$ Laminate

The nonlinear load vs. displacement and load vs. temperature responses for test N3 with a $[\pm 45/90_2]_s$ stacking sequence are shown in Fig. 5-20. Experimental results and numerical results from the fully refined models with clamped supports, sliding clamped supports, and a specified *v*-displacement are compared. The panel is loaded first by applying end-shortening at room tem-

(a) ΔT loading, clamped supports

(b) ΔT loading, sliding clamped supports

(c) ΔT loading, specified v-displacement
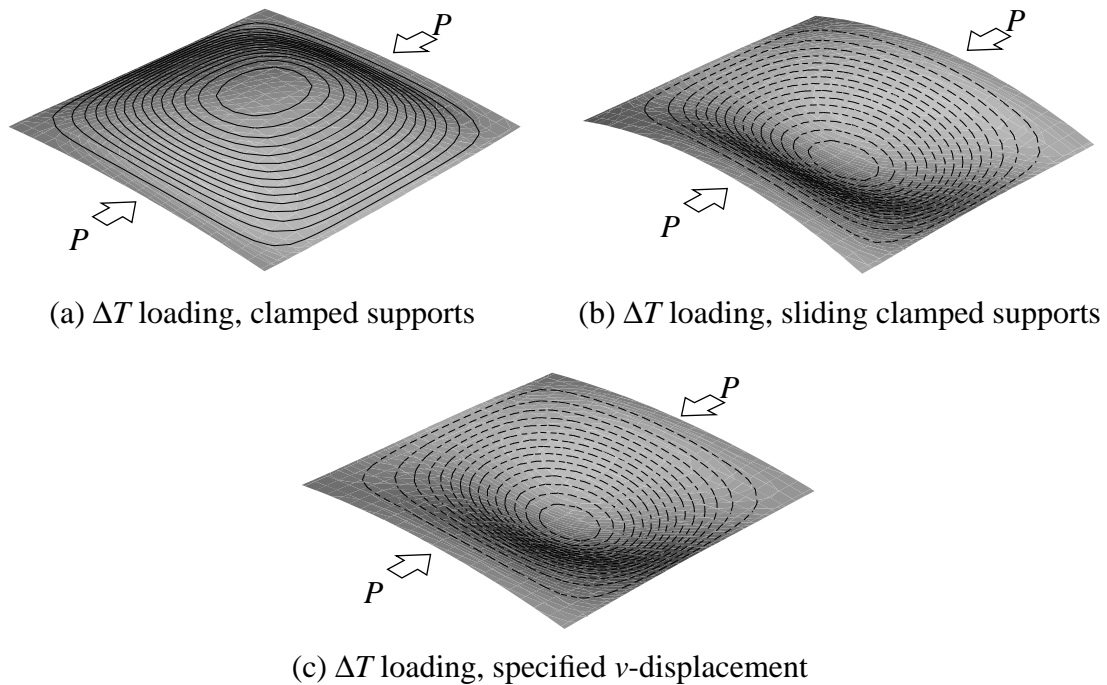
Figure 5-19 Prebuckling deformations, test Z4, $[\pm 45/0_2]_s$ laminate

perature, then by applying temperature to 400°F. The responses for the three refined models are seen to be relatively the same.   From the nonlinear response shown in Fig. 5-20, none of the boundary conditions clearly predicts experimental response better than the other boundary conditions.

Examining the prebuckling strain gage results of Fig. 5-21, the divergence of axial gages 7/8 and 37/38 indicate a positive change in curvature, gages 19/20 indicate no change in curvature, and gages 27/28 indicate a negative change in curvature.   This is consistent with the prebuckling deformation for Δu loading shown in Fig. 5-22(a) for clamped supports. During thermal loading, axial gages 7/8 and 37/38 change from a positive change in curvature to a negative change in curvature, while circumferential gages 27/28 maintain a negative change in curvature and gages 19/20 continue to indicate no change in curvature. The deformations for ΔT loading of the model with clamped supports, Fig. 5-22(b), indicates no substantial change from the deformation relative to that for Δu loading, Fig. 5-22(a). The deformations for ΔT loading shown in Fig. 5-22(c) for sliding clamped supports and Fig. 5-22(d) for a specified v-displacement boundary condition are in agreement with the strain gage results, although the buckling loads obtained from these models do not compare as well to experimental buckling loads as did the model with clamped
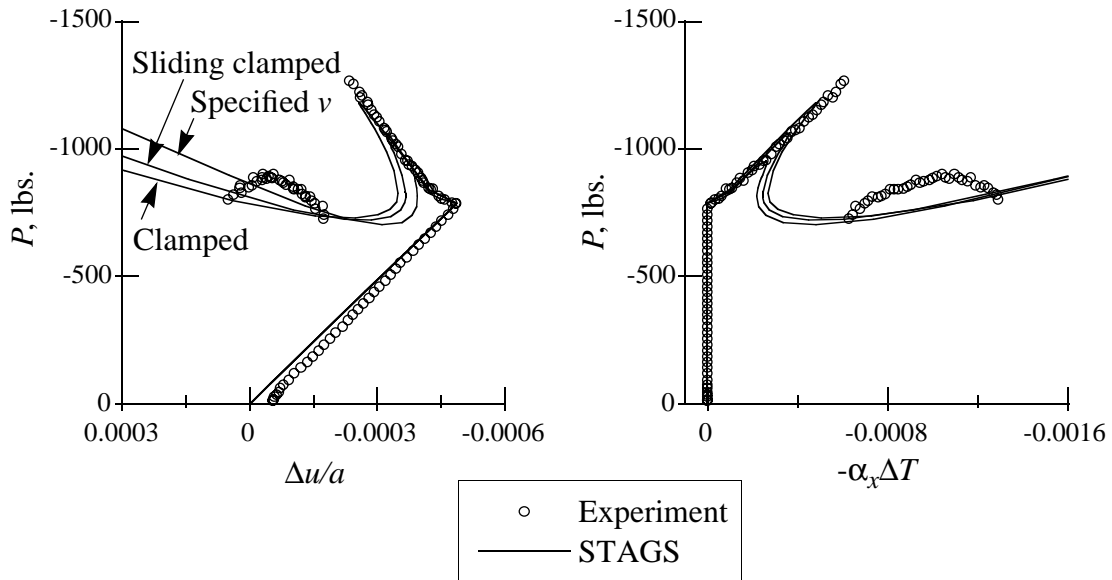
Figure 5-20 Nonlinear response with different boundary conditions, test N3, $[\pm 45/90_2]_s$ laminate

supports. In order to obtain a deformation during thermal loading consistent with the strain gages, and a more reasonable estimate of the buckling load, a model was constructed with a limited expanding v-displacement along the curved ends that is less than the thermal expansion of the steel curved end grips. Since no measurement of the actual v-displacement along the curved ends was obtained during testing, a displacement of

$$v^\circ \; = \; (0.15)(\alpha_s \Delta T)\left(\theta R - \frac{b}{2}\right) \qquad (5.2)$$

was assumed, where $\alpha_s = 6 \times 10^{-6}$ is the coefficient of thermal expansion of steel. With Eq. (5.2), the maximum v-displacement along the curved edge is 15% of the expansion of the steel end fixture.

The deformation pattern obtained using this limited v-displacement model, with v-displacement as given in Eq. (5.2), is shown in Fig. 5-22(e). The pattern shows the correct trends as compared to the change in curvature observations obtained from the strain gages.

Buckling loads obtained from experiment and the numerical models with clamped supports, sliding clamped supports, a specified v-displacement equal to the expansion of steel, and a limited v-displacement are compared for test N3 in Table 5-4. Three of these case have been seen before
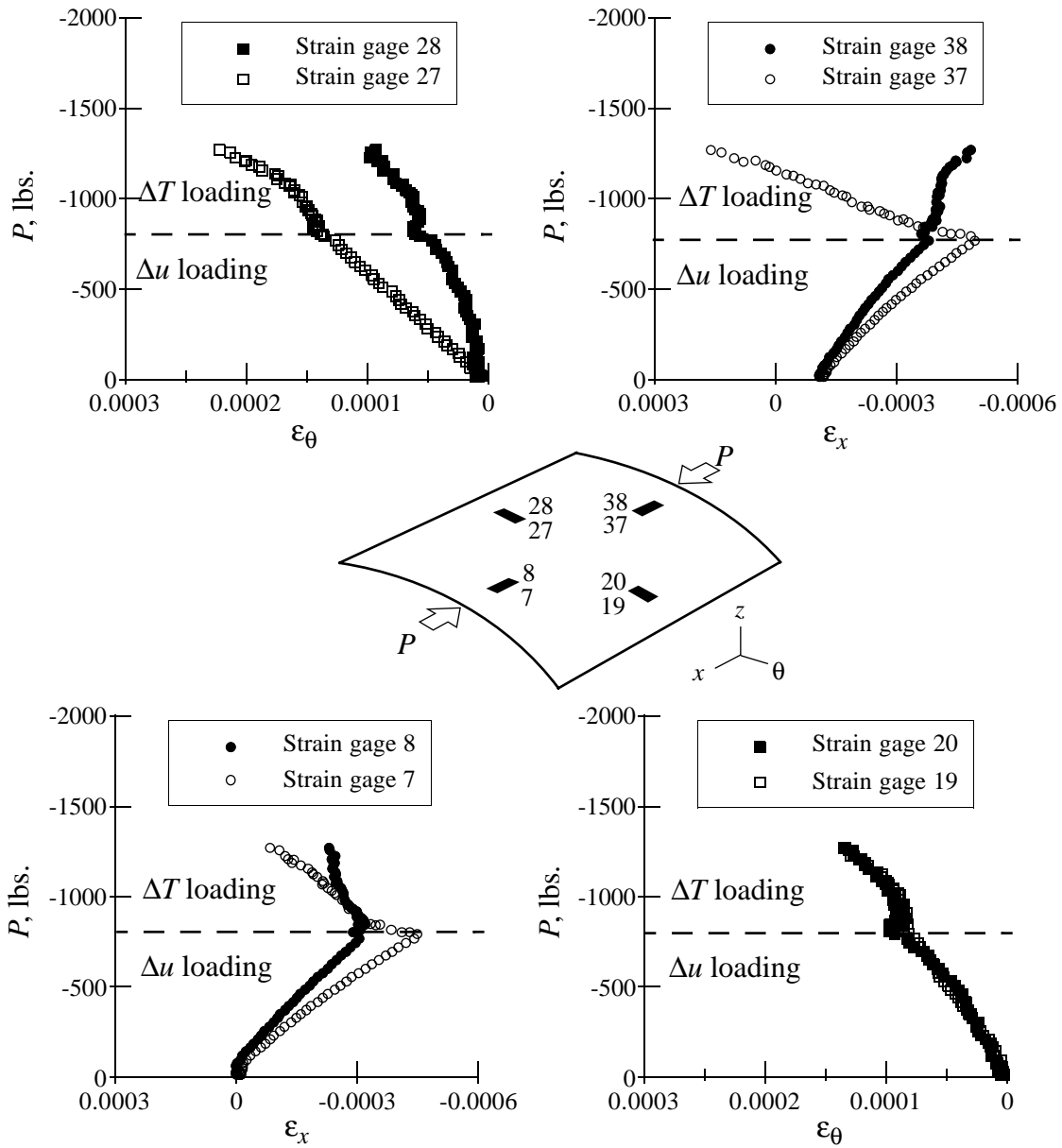
Figure 5-21 Prebuckling strains, test N3, [±45/90₂]ₛ laminate

in Table 5-3. All of the numerical models under predict the buckling load, with the best prediction being obtained from the model with clamped supports, which differs from experiment by only 7%. The model with a limited *v*-displacement under predicts the experimental buckling load by 13%.

The nonlinear load vs. displacement and load vs. temperature responses for test N3 are shown in Fig. 5-23 comparing experiment, clamped supports, and a limited *v*-displacement. The responses

118

(a) Δu loading, clamped supports

(b) ΔT loading, clamped supports

(c) ΔT loading, sliding clamped supports

(d) ΔT loading, specified v-displacement

(e) ΔT loading, limited v-displacement,
15% of steel expansion
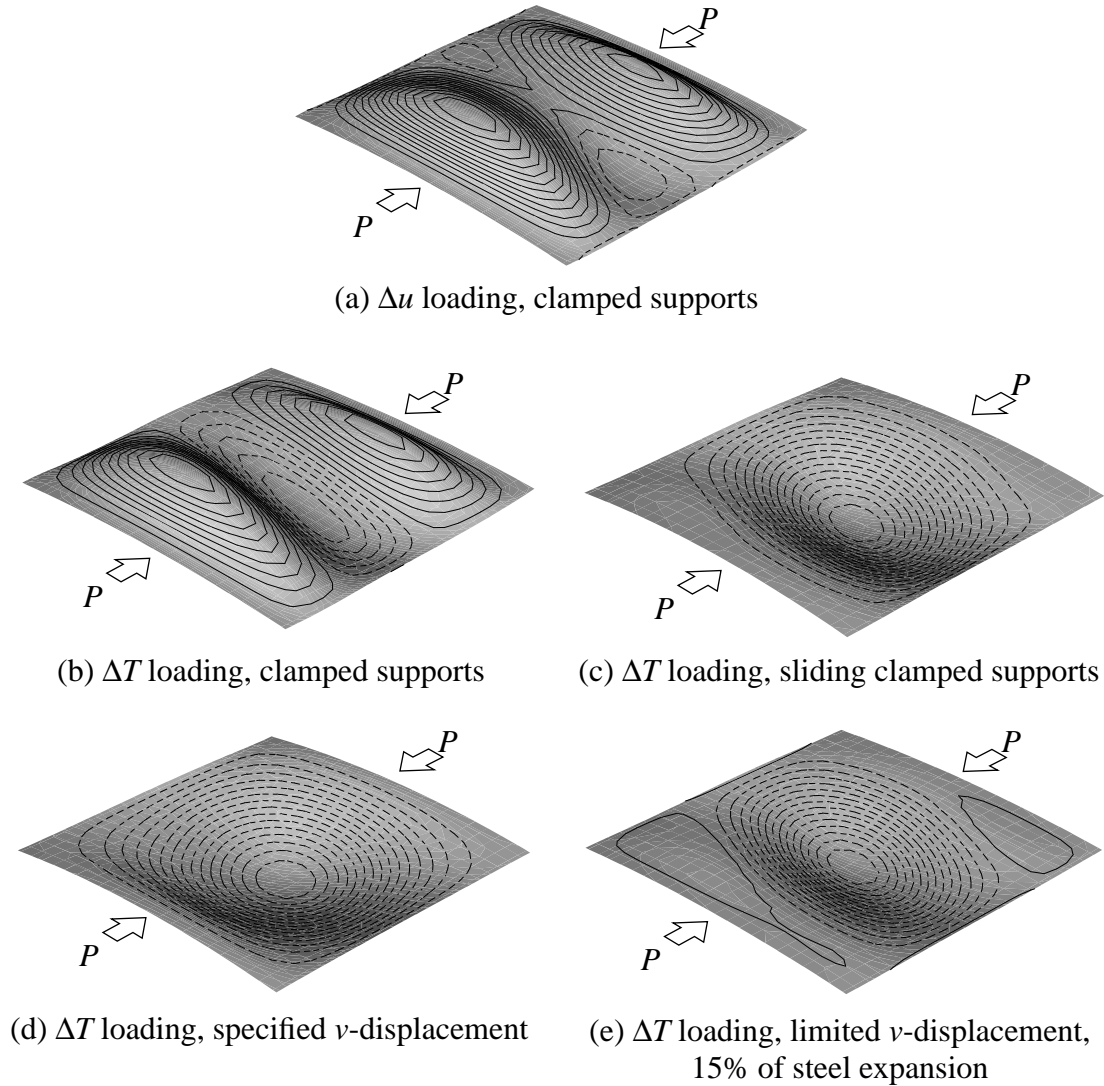
Figure 5-22 Prebuckling deformations, test N3, [±45/90$_2$]$_s$ laminate

Table 5-4 Buckling load comparison for circumferentially expanding supports

	Experiment P_{max}, lbs.	Clamped supports P/P_{max},	Sliding clamped supports P/P_{max},	Specified v-displacement P/P_{max},	Limited v-displacement P/P_{max},
[±45/90$_2$]$_s$ Test N3	-1270	0.93	0.84	0.75	0.87
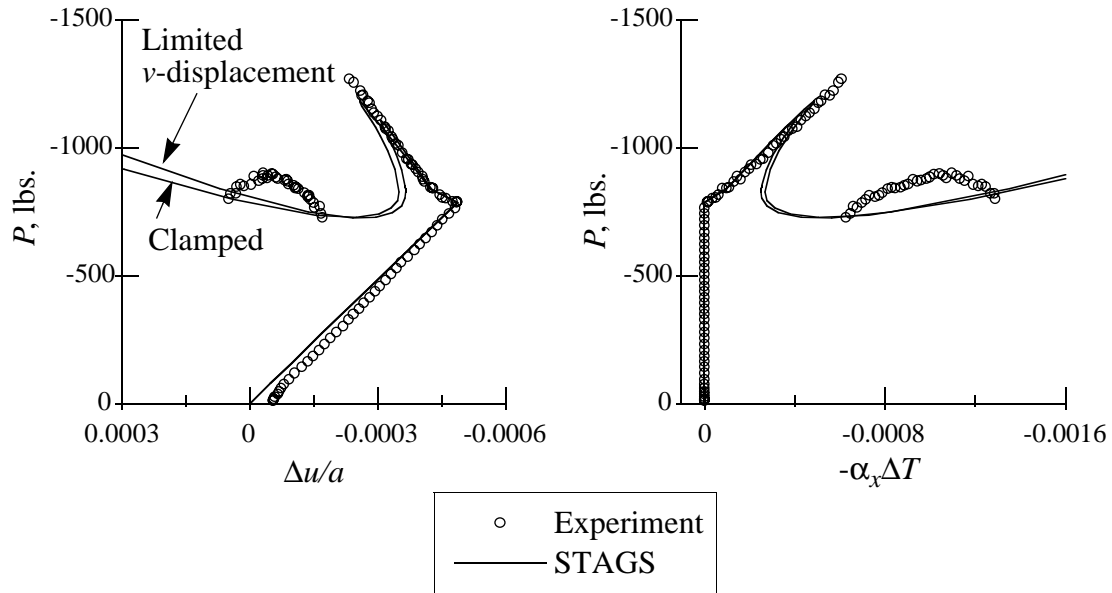
Figure 5-23 Nonlinear response with clamped vs. limited v-displacement boundary conditions, test N3, $[\pm 45/90_2]_s$ laminate

obtained from the two numerical models, clamped supports and a limited v-displacement, are nearly the same, and both show reasonable agreement with experiment. Additionally, the boundary condition variations illustrated in Fig. 5-20 also show reasonable agreement with experiment.

The question of which boundary condition best represents experimental conditions is not clear for this stacking sequence, the $[\pm 45/90_2]_s$ laminate. Examination of the prebuckling deformations suggests a model with sliding clamped supports or a limited v-displacement, comparison of buckling loads suggests clamped supports, and consideration of the nonlinear responses is inconclusive. Since no measurement is available for the circumferential v-displacement along the curved ends, the remainder of the tests on $[\pm 45/90_2]_s$ laminates will be compared to numerical models with clamped supports.

By comparing the experimental and predicted responses of all three laminates, Figs. 5-13, 5-17, and 5-20, and considering the laminate coefficients of thermal expansion, it may be possible to predict which laminates are best modeled by clamped boundary conditions and which are best modeled by sliding clamped boundary conditions during thermal loading. Note that the sliding clamped boundary condition model predicts the prebuckling, buckling and postbuckling responses of the $[\pm 45/0_2]_s$ laminate in test Z4 very accurately, shown in Fig. 5-17. In test Q3, with a $[\pm 45/0/90]_s$ laminate, the prebuckling and buckling behaviors are predicted well with the sliding

clamped boundary condition model, but postbuckling is not predicted as well, as shown in Fig. 5-13. For test N3, with a $[\pm45/90_2]_s$ laminate, the assumption of sliding clamped boundary conditions causes a worse buckling prediction than the model with clamped boundary conditions, shown in Fig. 5-20. With these observations in mind, consider the ratio of the laminate coefficients of thermal expansion to the coefficient of thermal expansion of steel, as listed in Table 5-5. Note that the best match between laminate and steel coefficients of thermal expansion occurs for a $[\pm45/0_2]_s$ laminate, which also shows the most accurate prediction of experimental results when sliding clamped boundary conditions are assumed. The next closest match between laminate and steel coefficients of thermal expansion occurs for the $[\pm45/0/90]_s$ laminate, which shows reasonable agreement between experiment and prediction when sliding clamped boundary conditions are used. Finally, the $[\pm45/90_2]_s$ laminate shows the greatest mismatch between laminate and steel coefficients of thermal expansion, and likewise shows little agreement between prediction and experiment when sliding clamped boundary conditions are assumed. From these observations, a correlation is suggested between similar laminate and steel coefficients of thermal expansion, and the accuracy of assuming sliding clamped boundary conditions.

Table 5-5 Circumferential thermal expansion of laminates compared to steel

	$[\pm45/0/90]_s$	$[\pm45/90_2]_s$	$[\pm45/0_2]_s$
$\dfrac{\alpha_y}{\alpha_{steel}}$	0.19	-0.03	0.72

5.3 Nonlinear Postbuckling Results

The experimental results are compared to the solutions obtained with the fully refined numerical model and considering the effects of circumferential restraint along the curved ends as described in section 5.2. The experimental and numerical buckling values for all of the buckling tests are listed in Table 5-6. The columns headed "STAGS" and "STAGS without imperfections" contain the numerical buckling loads normalized by the experimentally determined buckling loads for each particular test. The heading "STAGS" indicates the fully refined numerical model with sliding clamped/sliding simple support boundary conditions during thermal loading, and clamped/sliding simple support boundary conditions during mechanical loading, unless otherwise noted by an asterisk. The heading "STAGS without imperfections" indicates that the fully refined model without the effects of measured geometric imperfections is used. This column is included to help access the relative sensitivity of each test configuration to measured geometric imperfec-

Table 5-6 Experimental and numerical buckling loads

		Experiment P_{max}, lbs.	STAGS P/P_{max}	STAGS without imperfections P/P_{max}
Test Q1 $[\pm45/0/90]_s$	Δu only	-1670	0.87	1.04
Test Q2 $[\pm45/0/90]_s$	ΔT only	does not buckle	does not buckle	
Test Q3 $[\pm45/0/90]_s$	Δu then ΔT	-1350	0.95	1.09
Test Q4 $[\pm45/0/90]_s$	ΔT then Δu	-1920	0.71 0.81*	0.85 0.95*
Test N1 $[\pm45/90_2]_s$	Δu only	-1410	0.98*	1.17*
Test N2 $[\pm45/90_2]_s$	ΔT only	-1090	0.97*	1.48*
Test N3 $[\pm45/90_2]_s$	Δu then ΔT	-1270	0.93*	1.29*
Test N4 $[\pm45/90_2]_s$	ΔT then Δu	-1420	0.89*	1.15*
Test Z1 $[\pm45/0_2]_s$	Δu only	-1210	1.08	1.33
Test Z3 $[\pm45/0_2]_s$	Δu then ΔT	does not buckle	does not buckle	
Test Z4 $[\pm45/0_2]_s$	ΔT then Δu	-1090	0.94	1.29

* Indicates STAGS solution with clamped/sliding simple support boundary conditions. All other STAGS solutions use sliding clamped/sliding simple support boundary conditions during thermal loading, and clamped/sliding simple support boundary conditions during mechanical loading.

tions. Also, the refined model which incorporates measured initial geometric imperfections generally under predicts the experimental buckling load, while the model without measured initial geometric imperfections generally over predicts the experimental buckling load. This may be due to the assumption of constant panel thickness with a midsurface geometric imperfection. The

actual initial geometric imperfections may have included local thickness variations, in addition to midsurface geometric imperfections.

In general, $[\pm45/0/90]_s$ and $[\pm45/0_2]_s$ laminates are modeled using sliding clamped/sliding simple supports during thermal loading, and clamped/sliding simple supports during mechanical loading. An exception to this is test Q4, which is modeled both with sliding clamped/sliding simple supports during thermal loading, and with clamped/sliding simple supports throughout loading. Notice that the model with clamped supports provides a better estimate of the buckling load than the model with sliding clamped supports. Note also that even without imperfections, the numerical predictions are below the experimental buckling load.

Considering the sensitivity of the different stacking sequences to measured geometric imperfections, observe that the buckling loads of the $[\pm45/0/90]_s$ laminates change little when imperfections are included, while the buckling loads of the $[\pm45/90_2]_s$ and $[\pm45/0_2]_s$ laminates show substantial change due to including imperfections. This difference in behavior between laminates can be explained by recalling Tables 5-1 and 5-2, where it was shown that different measured imperfections can cause different changes in the buckling load. For the $[\pm45/90_2]_s$ and $[\pm45/0_2]_s$ laminates, including measured initial geometric imperfections always improves the prediction of buckling load as compared to the model without imperfections. For the $[\pm45/0/90]_s$ laminate, however, the model without imperfections provides a better buckling load prediction.

5.3.1 Nonlinear Response, $[\pm45/0/90]_s$ Laminates

The geometrically nonlinear load vs. displacement response of test Q1 is compared to numerical predictions in Fig. 5-24. Test Q1 was loaded in end-shortening at room temperature. Both the prebuckling and postbuckling responses predicted by STAGS agree well with the experimentally measured response. The only significant difference between the model with imperfections and the model without imperfections occurs in the predictions of the buckling load. The deformation mode shape of the postbuckling response is indicated by the photograph of the shadow moiré fringe pattern shown in Fig. 5-25 along with the predicted response from STAGS. The two deformation shapes agree qualitatively, with both indicating a single inward buckle pattern at the center of the panel.

Nonlinear load vs. displacement and load vs. temperature results for test Q2 are shown in Fig. 5-26. Although test Q2 was meant to access the effects of thermal loading only, mechanical loading occurs due to downward drift of the lower load platen and thermal expansion of the steel fixture and heated platen, as discussed in Chapter 4. The STAGS response does not predict buckling
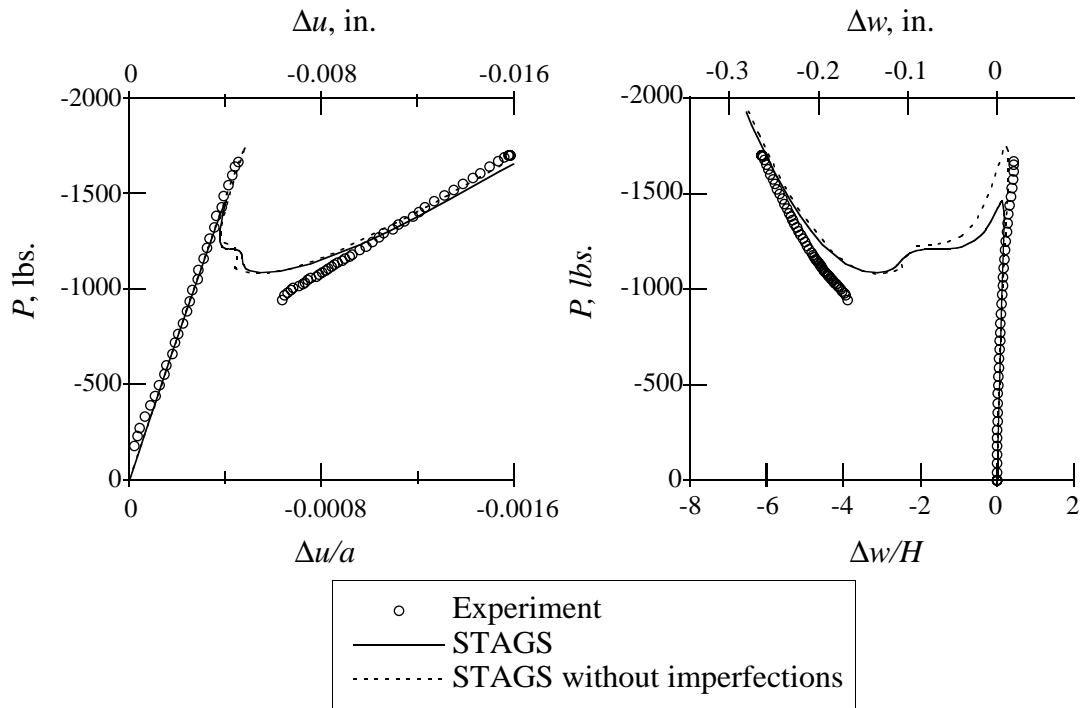
Figure 5-24 Nonlinear response, test Q1, $[\pm 45/0/90]_s$ laminate
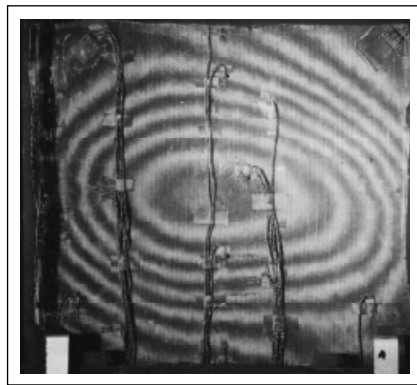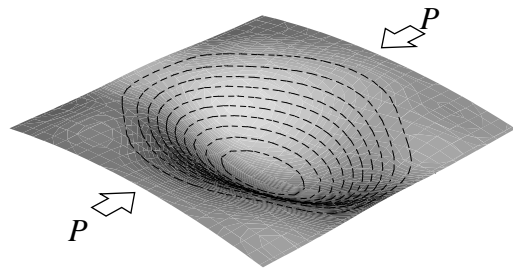
(a) Shadow moiré-fringe pattern   (b) STAGS contour, with imperfections

Figure 5-25 Postbuckling deformations, test Q1, $[\pm 45/0/90]_s$ laminate

in the temperature range considered. Since response with and without imperfections is the same during prebuckling, only response with imperfections is included here. Note that at a temperature of approximately 330°F, the measured response of the panel changes, and the load does not increase with increasing temperature. The STAGS model does not predict this behavior, because it does not include the change in material properties that may occur above 330°F.
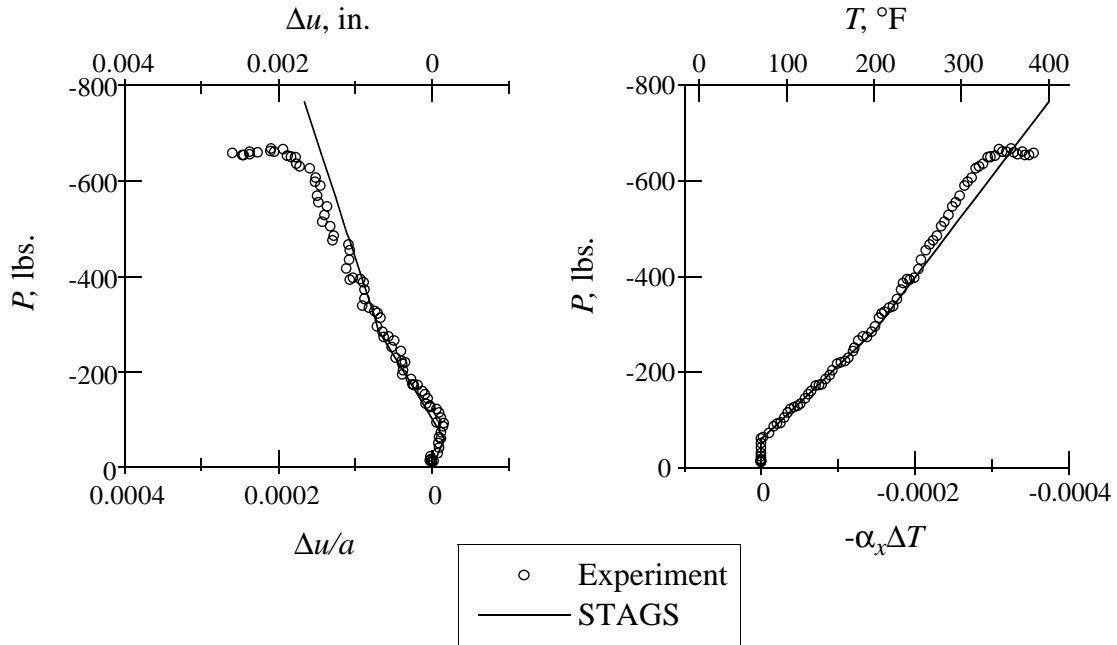
Figure 5-26 Nonlinear response, test Q2, [±45/0/90]$_s$ laminate

The nonlinear load vs. displacement and load vs. temperature responses of test Q3 are shown in Fig. 5-27. Test Q3 begins with mechanical loading to -800 lbs., then the panel is heated to 400°F while attempting to hold the end-shortening at a constant value. For loads prior to buckling, the STAGS predictions closely follow the experimental response. A good estimate of the buckling load is predicted, but the postbuckling response observed in experiment is not what the STAGS response suggests should happen. According to the predicted response, the load should drop off after buckling to a value of approximately -1080 lbs., but the experiment shows only a gradual decrease in load after buckling. This may be due to load being carried by the knife edge supports, which grip the panel increasingly tighter as the temperature is increased, or inaccurate modeling of the circumferentially expanding curved end boundary condition. A second discontinuity in stiffness can be seen at a temperature of approximately 330°F, due to the possible changes in material properties at temperatures above 330°F.

The nonlinear load vs. displacement and load vs. temperature responses of test Q4 are shown in Fig. 5-28 for sliding clamped/sliding simple support boundary conditions during thermal loading. Test Q4 is heated first to approximately 250°F while attempting to hold the end-shortening constant, then loaded in end-shortening while holding the temperature at a constant 250°F. From Fig. 5-28, it is seen that both the prebuckling and postbuckling stiffnesses at temperature are slightly
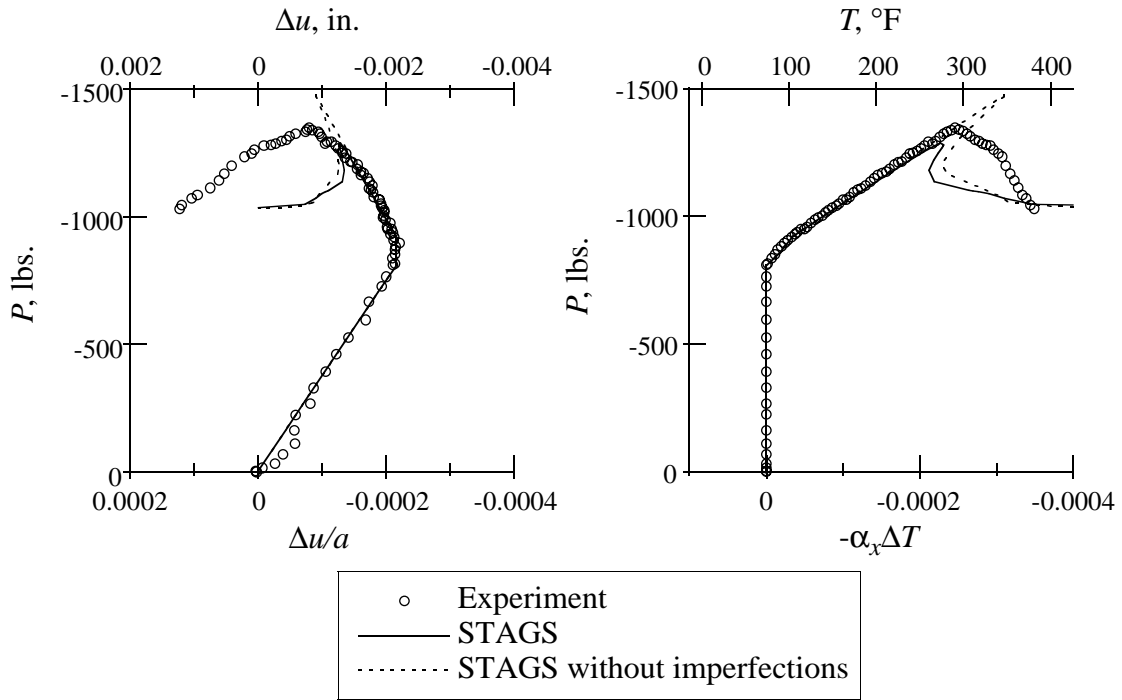
Figure 5-27 Nonlinear response, test Q3, [±45/0/90]$_s$ laminate
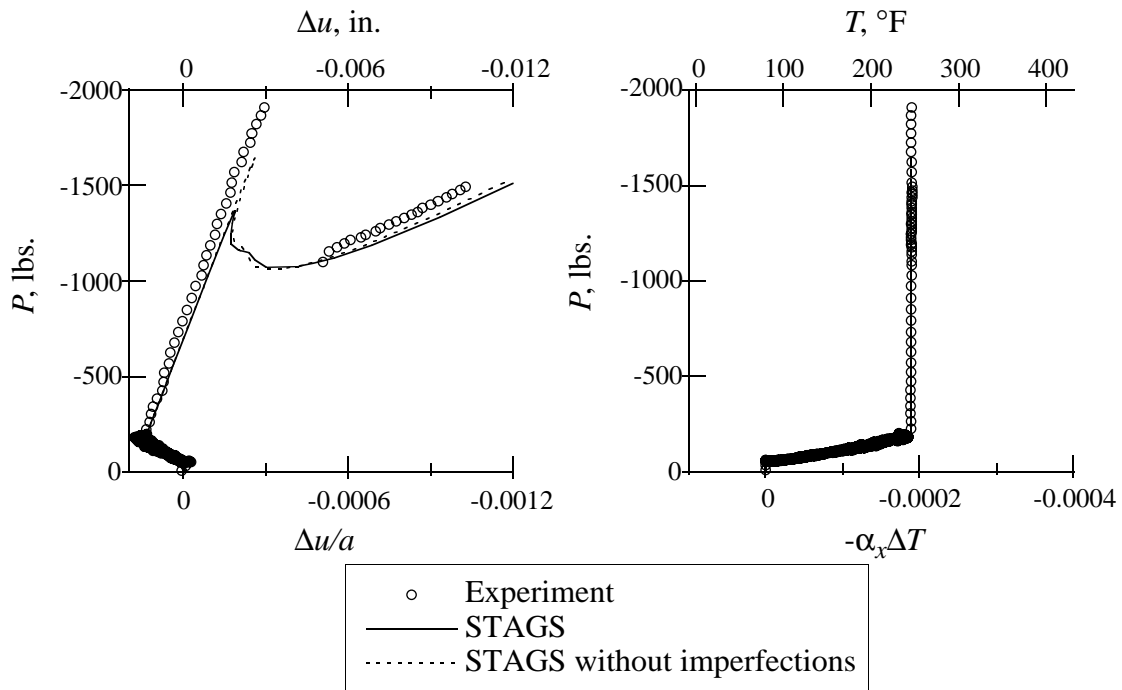
Figure 5-28 Nonlinear response with sliding clamped supports, test Q4, [±45/0/90]$_s$ laminate

greater for the experiment than were predicted by STAGS. The load that the panel carries after buckling is predicted accurately by the STAGS models. The buckling load is under predicted compared to the experimental results by both the model with imperfections and the model without imperfections.

In an attempt to improve the agreement between model and experiment, clamped/sliding simple support boundary conditions are considered for both mechanical and thermal loading, as shown in Fig. 5-29. The most notable difference between the previous model with sliding clamped/sliding simple supports during thermal loading and this model with clamped/sliding simple supports is in the values of the buckling loads. The model that assumes clamped/sliding simple supports more accurately predicts the experimentally determined buckling load, although the buckling load of the model with imperfections is still substantially less than the measured buckling load. The buckling load results bring into question the assumption of sliding clamped boundary conditions during thermal loading for a stacking sequence of $[\pm45/0/90]_S$. No final conclusion can be drawn from the limited experimental data presented here.
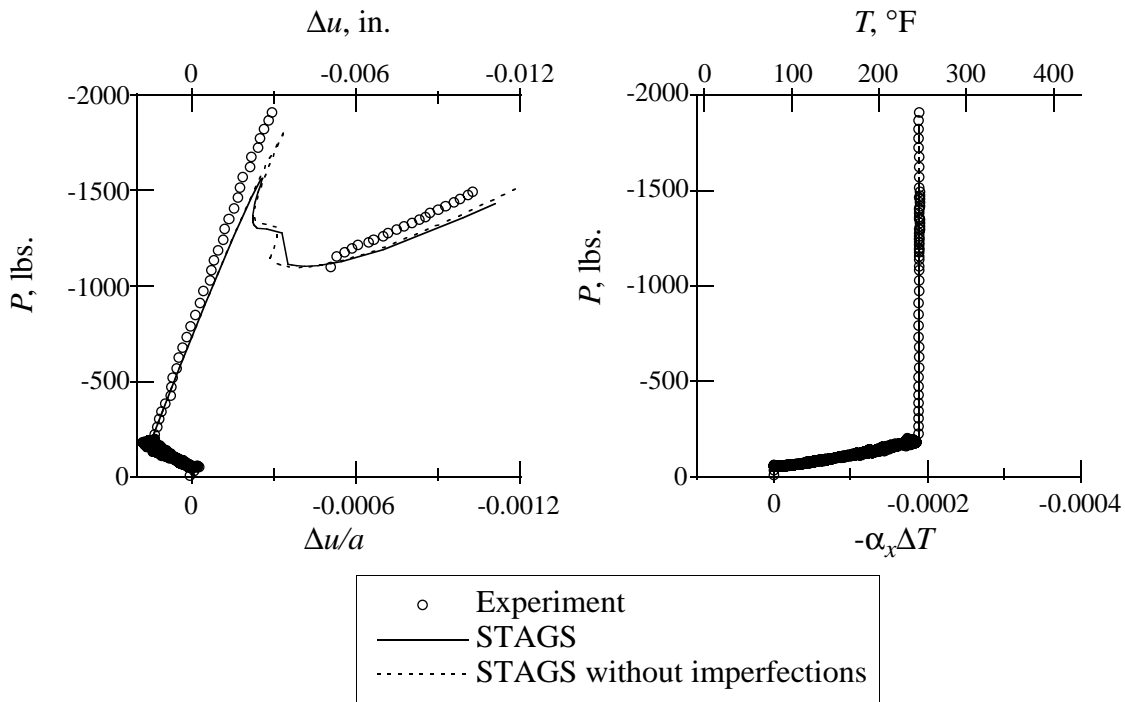
Figure 5-29 Nonlinear response with clamped supports, test Q4, $[\pm45/0/90]_S$ laminate

5.3.2 Nonlinear Response, $[\pm 45/90_2]_s$ Laminates

The nonlinear load vs. displacement response of test N1 with a $[\pm 45/90_2]_s$ stacking sequence is shown in Fig. 5-30. Test N1 is an end-shortening test conducted at room temperature. For all tests of $[\pm 45/90_2]_s$ laminates, the model boundary conditions are assumed to be clamped/sliding simple supports throughout testing. From Fig. 5-30, the STAGS models are seen to provide good predictions of the prebuckling stiffness, and the model with imperfections agrees well with the experimentally determined buckling load. The postbuckling stiffness predicted by the two models is less than the stiffness measured experimentally, although the initial postbuckling load shows good agreement between model and experiment. The deformation mode shape of the postbuckling response is represented in the shadow moiré fringe pattern shown in Fig. 5-31(a). It is seen to match qualitatively with the predicted deformation mode shape of Fig. 5-31(b), indicating a single buckle pattern at the center of the panel.

The nonlinear load vs. displacement and load vs. temperature responses of test N2 are shown in Fig. 5-32. Test N2 was meant to be pure thermal loading, so the only mechanical loading is due to the drift of the lower load frame platen and thermal expansion of the steel fixture and heated platen. The prebuckling stiffness and buckling load show good agreement between experiment
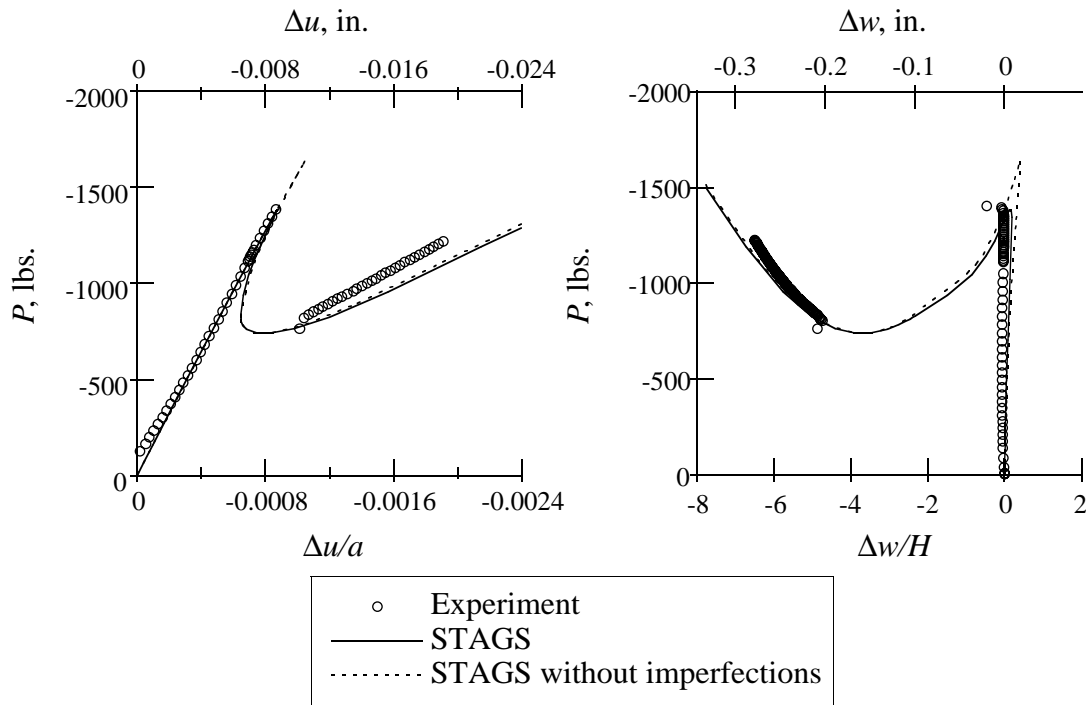
Figure 5-30 Nonlinear response, test N1, $[\pm 45/90_2]_s$ laminate
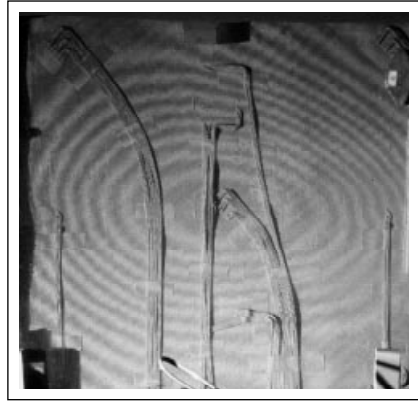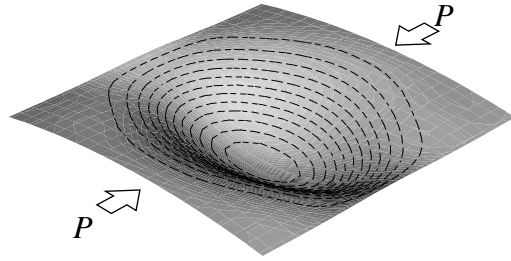
(a) Shadow moiré-fringe pattern   (b) STAGS contour, with imperfections

Figure 5-31 Postbuckling deformations, test N1, [±45/90$_2$]$_s$ laminate
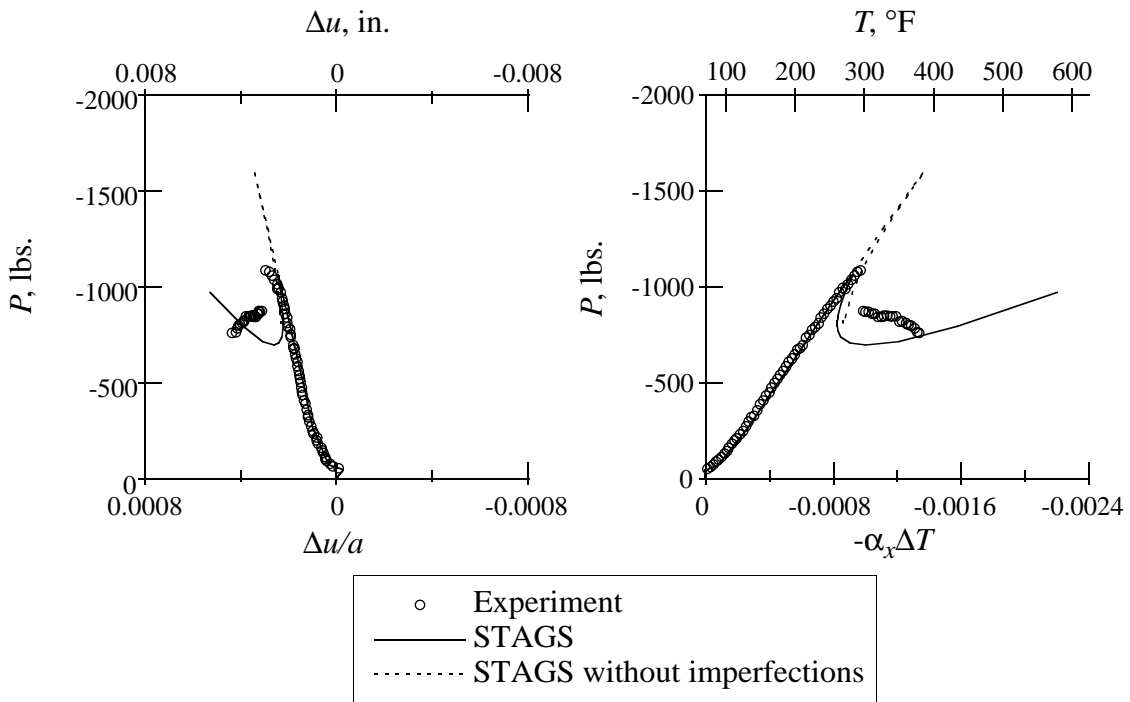
Figure 5-32 Nonlinear response, test N2, [±45/90$_2$]$_s$ laminate

and the STAGS models. After buckling, the model with imperfections predicts an initial post-buckling load of approximately -700 lbs., but the experimental results show an initial postbuckling load of approximately -880 lbs. As with test Q3, this may be due to load being carried by the knife edge supports, which grip the panel increasingly tighter as the temperature is increased, or an inaccurate modeling of the circumferentially expanding curved end supports. Note that both

tests N2 and Q3 involve buckling during thermal loading, and both show greater than predicted postbuckling load carrying capacity, suggesting an experimental problem at elevated temperatures. Returning to test N2, after the discrepancy in the initial postbuckling load, the postbuckling stiffness is also incorrectly predicted by the models. Note again the discontinuity in postbuckling stiffness that occurs near 330°F.

The nonlinear load vs. displacement and load vs. temperature responses of test N3 are shown in Fig 5-33. Test N3 begins with mechanical loading to -800 lbs. at room temperature, then thermal loading is applied to a temperature of 400°F while attempting to hold end-shortening constant. From Fig. 5-33, the prebuckling response and buckling load predicted by the STAGS model with imperfections are seen to agree well with the experimentally determined responses. The initial postbuckling load also shows good agreement, although the experimentally determined postbuckling stiffness is greater than the predicted stiffness, up to a temperature of approximately 330°F. Beyond this temperature, the measured postbuckling stiffness decreases, consistent with previous observations.

The nonlinear load vs. displacement and load vs. temperature responses for test N4 are shown in Fig. 5-34. Test N4 was heated first to approximately 240°F while attempting to hold end-shortening fixed, then loaded in end-shortening while maintaining a constant temperature. The predic-
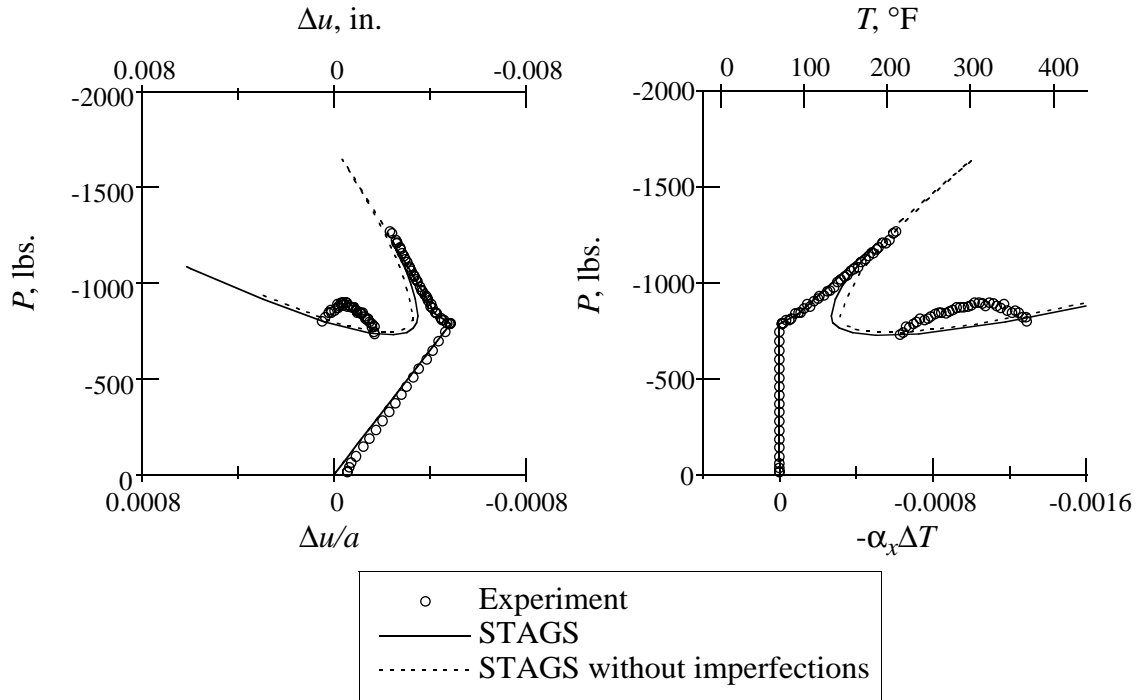
Figure 5-33 Nonlinear response, test N3, [±45/90$_2$]$_s$ laminate
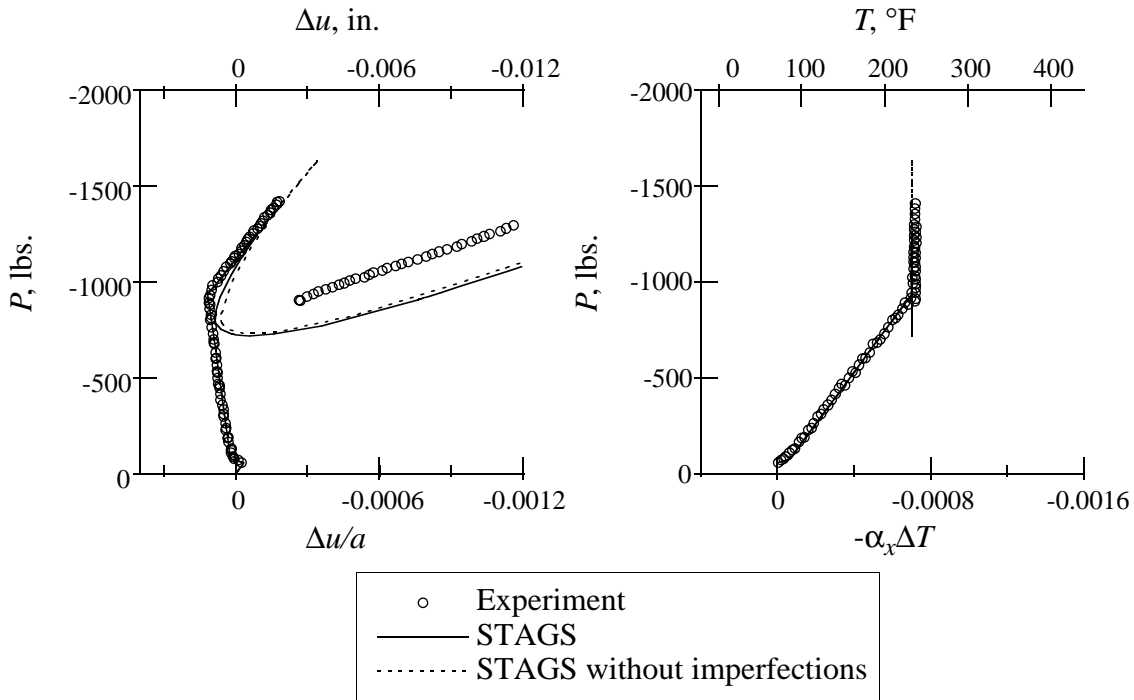
Figure 5-34 Nonlinear response, test N4, $[\pm 45/90_2]_s$ laminate

tions from the STAGS models agree well with experiments during prebuckling, and the STAGS model with imperfections provides a reasonable estimate of the buckling load. The experimentally determined initial postbuckling load is greater than predicted by the models, although the postbuckling stiffness shows good agreement between model and experiment.

5.3.3 Nonlinear Response, $[\pm 45/0_2]_s$ Laminates

The nonlinear load vs. displacement response for test Z1 is shown in Fig. 5-35. Test Z1 was an end-shortening test conducted at room temperature. The prebuckling stiffness shows good agreement between experiment and model. The buckling load is slightly over predicted by the STAGS model with imperfections, while the postbuckling stiffness is slightly under predicted, but both show reasonable agreement with experiment. The postbuckling deformations from a shadow moiré fringe pattern and the STAGS model with imperfections are shown in Fig. 5-36. Qualitative agreement is obtained, with both indicating a single inward buckle at the center of the panel.

The nonlinear load vs. displacement and load vs. temperature responses for test Z3 are shown in Fig. 5-37. Test Z3 was first loaded to -800 lbs. by applying end-shortening at room temperature, then heated to 400°F while attempting to hold the end-shortening constant. Model and experiment show excellent agreement. The measured load drops off rapidly when thermal loading
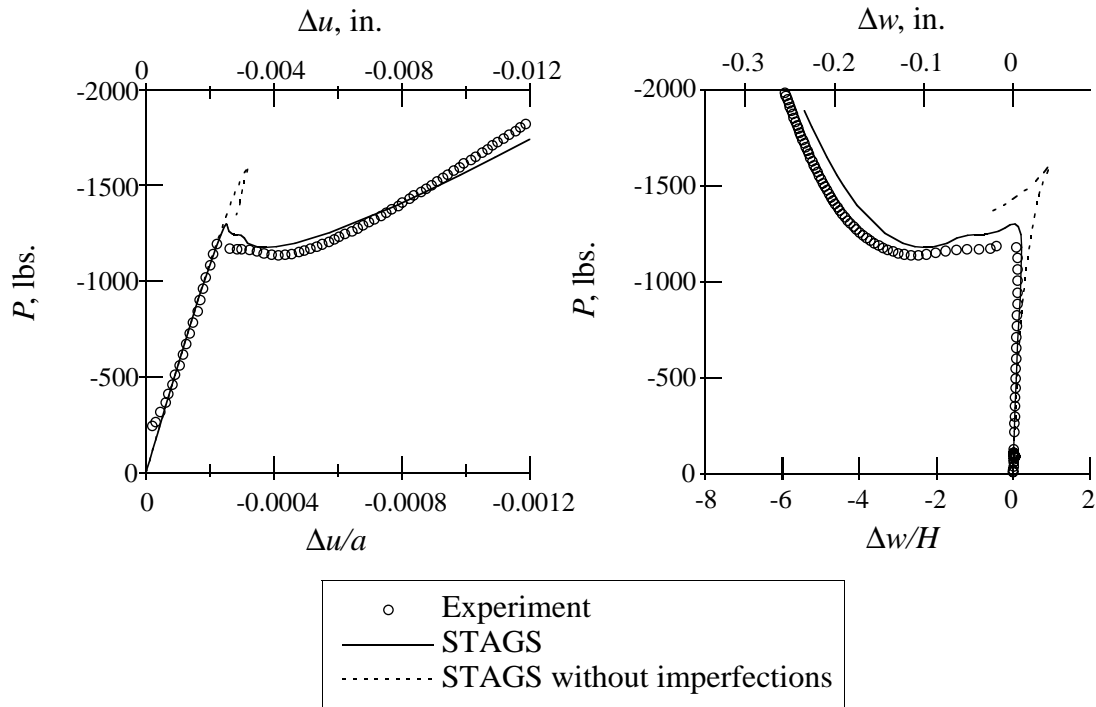
Figure 5-35 Nonlinear response, test Z1, [$\pm$45/0$_2$]$_\text{s}$ laminate
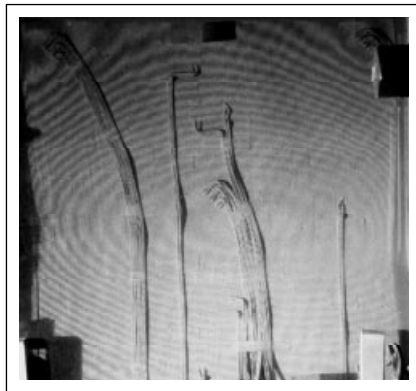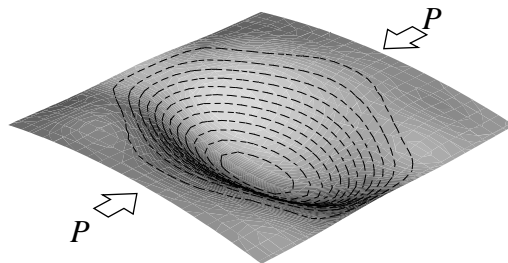
(a) Shadow moiré fringe pattern   (b) STAGS contour, with imperfections

Figure 5-36 Postbuckling deformations, test Z1, [$\pm$45/0$_2$]$_\text{s}$ laminate

begins, due to the negative axial coefficient of thermal expansion for the [$\pm$45/0$_2$]$_\text{s}$ laminate. The load vs. temperature slope changes continuously after the initial drop, and eventually reaches an asymptote near -400 lbs. As explained in Chapter 4, the cause of this asymptote is not fully understood but may be due to experimental error from either the knife edge supports or the load frame platen. The experiment and numerical model match because the actual panel end-shorten-
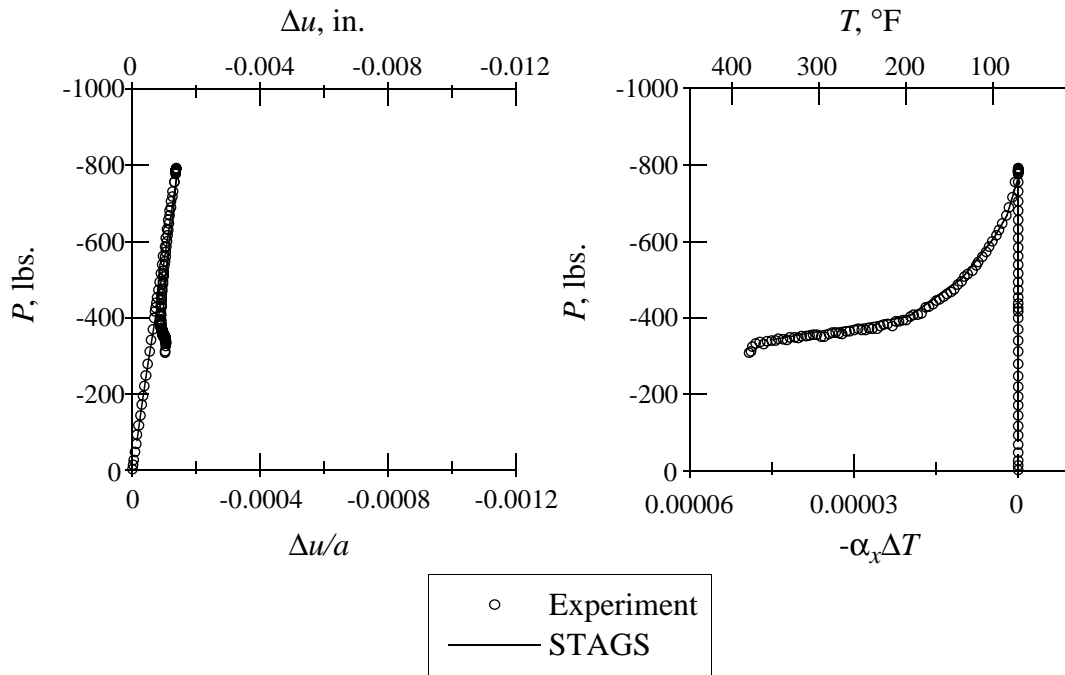
Figure 5-37 Nonlinear response, test Z3, $[\pm 45/0_2]_s$ laminate

ing, as obtained from strain gage readings, was included in the model, thus accounting for experimental errors due to hardware problems.

The nonlinear load vs. displacement and load vs. temperature responses of test Z4 are shown in Fig. 5-38. Test Z4 was heated first to approximately 240°F while attempting to hold end-shortening constant, then loaded in end-shortening while holding temperature constant. The prebuckling and buckling predictions obtained with the STAGS model that includes imperfections agree well with the experimental data. Beyond buckling, the initial response matches very well, but some discrepancy in both stiffness and load carrying capacity is observed as the end-shortening progresses.

This chapter has presented a considerable amount of information on the modeling aspect of thermal testing. The sections on model refinement reflect the realities of imperfect specimens and the physical characteristics of the test fixture. Deviations from perfection were seen to have minimal or no effect in some cases, as for thermal gradients, but potentially large effects for other cases, as for measured initial geometric imperfections. Boundary conditions, particularly the circumferential restraint component, were seen to play a large role in the predicted behavior. Because the actual boundary conditions are almost impossible to quantify exactly, the analysis was used to consider different possible conditions.
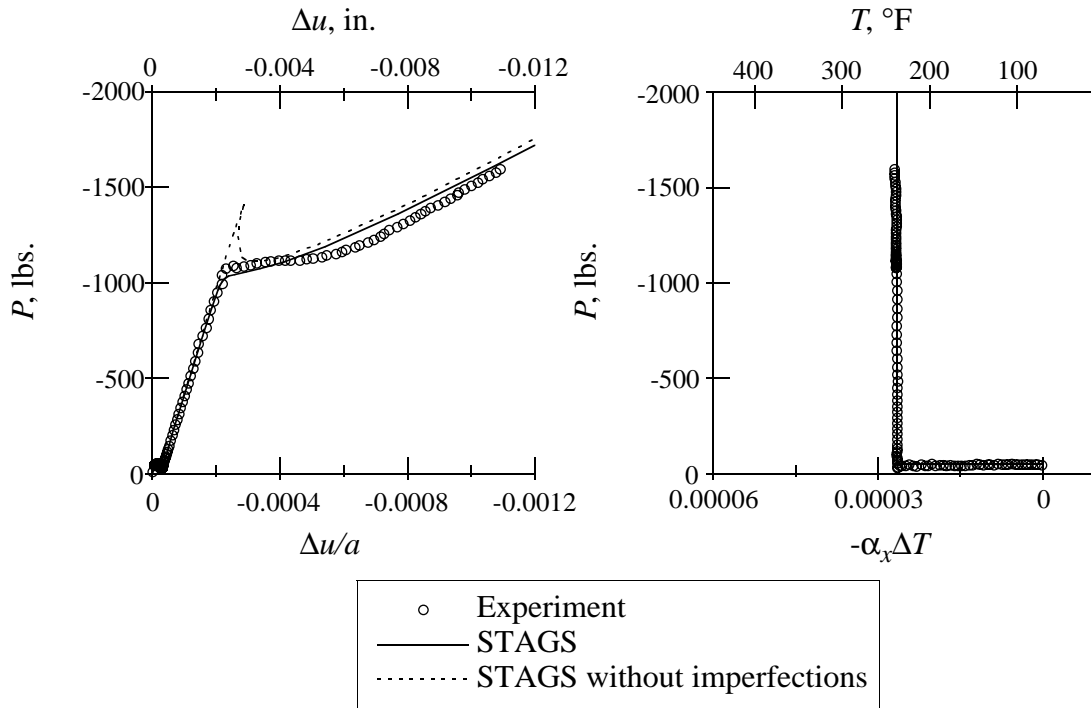
Figure 5-38 Nonlinear response, test Z4, [±45/0$_2$]$_s$ laminate

Thermal testing, in general, and the load frame used, in particular, had important bearings on the measured results. Drifting of the lower load frame platen and thermal expansion of the steel end grips prevented the application of pure thermal loading, and resulted in a net axial expansion of the panel during heating. However, this effect was successfully accounted for in the numerical analysis. Good agreement was obtained between measured response and numerical predictions for both stiffness and buckling results. Although the numerical model involved assumptions and did not account for all of the experimental anomalies, the validity of this type of modeling was verified. The nonlinear finite element code STAGS, using quadrilateral faceted shell elements, accounting for large rotations using a corotational formulation, and using Rik's method to obtain solutions along an unstable loading path, is appropriate for studies on the thermal buckling and postbuckling of composite shells.

As the first experimental thermal buckling study of composite shells, the results of the experimental investigation, in conjunction with the corresponding numerical studies, provide a unique contribution to the knowledge of thermal and mechanical buckling. Important conclusions can be drawn from the results, and improvements can be suggested for future thermal testing investigations. These are the subject of the final chapter.

6. Conclusions and Recommendations

The goal of this research was to study the buckling and postbuckling responses of curved composite panels subjected to combinations of thermal and mechanical loading. Experimental and numerical studies were planned. Curved composite panels were selected to simulate the unsupported sections of fuselage skin between stringers and stiffeners. Loading due to axial end-shortening and uniform temperature change were of particular interest, driven by the thermal stresses that arise when a structure is heated while restricting axial displacement. To study this topic in detail, a base geometry was chosen consisting of a 10 in. by 10 in. cylindrically curved panel with a 60 in. radius. Three lamination sequences were studied, including a quasi-isotropic $[\pm 45/0/90]_s$ laminate, an axially soft $[\pm 45/90_2]_s$ laminate, and an axial stiff $[\pm 45/0_2]_s$ laminate.

Boundary conditions for the base model were clamped edges along the curved ends, and simply supported with *v*-displacement unrestricted along the straight edges. This configuration was chosen because it simulated the boundary conditions of the experimental apparatus. A simplified linear buckling solution was presented for the curved panel by assuming simply supports on all four boundaries. For clamped/sliding simple support boundary conditions, the buckling load from a nonlinear prebuckling state was obtained using an approximate Rayleigh-Ritz solution and the geometrically nonlinear finite element code STAGS. Postbuckling responses were further studied using STAGS. A number of parametric studies were conducted to determine the effects of boundary conditions, radius, and combined loading on the nonlinear responses including postbuckling.

Experiments were conducted at room temperature and elevated temperatures up to 400°F to provide verification to the analyses. Tests were conducted on the three laminates of interest, loaded with end-shortening alone, with elevated temperature alone, with end-shortening followed by elevated temperature, and with elevated temperature followed by end-shortening. Load vs. axial strain results were compared to predictions from STAGS. Refinements to the base STAGS model were considered, including measured thicknesses, boundary conditions modified to reflect the test fixture, measured initial geometric imperfections, measured thermal gradients, and modifications to the circumferential component of the displacement at the curved end boundary conditions. It

135

was discovered during testing that axial end displacement of the panel occurs during the slow thermal heat-up of the panel. The magnitude of end displacement was determined and incorporated into the STAGS model. With the model refinements and inclusion of axial end displacement, the nonlinear STAGS predictions provided good correlation to the experimentally determined buckling loads and load vs. axial strain responses.

6.1 Conclusions

Conclusions are organized based on the different areas of emphasis for this study. The following presentation is meant to follow the order of the main text:

- The results of analytical parametric studies to determine the effects of boundary conditions, panel radius, and combined loading are summarized.

- The lessons learned while conducting thermal/structural experiments are detailed.

- The effects of modeling refinements to better simulate experimental conditions are noted.

- Comparisons are made between the load vs. axial strain responses predicted by the analyses and measured in the experiments.

6.1.1 Analytical Results and Parametric Studies

A simplified linear solution was presented for curved composite panels with simply supported boundary conditions loaded in end-shortening or uniform temperature change. A geometrically nonlinear Rayleigh-Ritz solution was developed for curved panels with either clamped/sliding simple supports or clamped/fixed simple supports, loaded in end-shortening and uniform temperature change. Comparison of the simplified linear solution and the approximate Rayleigh-Ritz solution suggested that the simplified solution could be used to provide an initial estimate of the buckling load in most cases. For the $[\pm45/0_2]_s$ laminate loaded by uniform temperature change, the simplified linear solution predicted a negative axial buckling load, while the nonlinear Rayleigh-Ritz solution showed that thermal buckling for this laminate would only occur in the presence of a tensile axial load and a compressive circumferential load.

Parametric studies were performed using the geometrically nonlinear finite element code STAGS with the following results:

- The effects of boundary conditions were studied by first restricting the circumferential displacement of the straight edges, creating a boundary condition termed clamped/fixed simple

supports, then by freeing the circumferential displacement along the curved ends, for a boundary condition termed sliding clamped/sliding simple supports. The base model with clamped/sliding simple supports was found to buckle due to bifurcation. Thermal and mechanical responses for a given laminate may be either the same or entirely different, depending on the specific laminate considered. Clamped/fixed simple supports induce buckling at a limit point with buckling loads that are higher than those of clamped/sliding simple supports. The character of response is significantly different than clamped/sliding simple supports. Sliding clamped/sliding simple supports buckle at a bifurcation point and have lower buckling loads than clamped/sliding simple supports. For mechanical loading, clamped/sliding simple supports and sliding clamped/sliding simple supports have similar response characteristics, but for thermal loading, different responses are noted for the two boundary conditions.

• The effect of varying the panel radius is considered. As the radius decreases, the prebuckling stiffness remains constant while buckling load increases. Beyond $R = 30$ in., the character of the postbuckling response changes. For $[\pm 45/0/90]_s$ and $[\pm 45/90_2]_s$ laminates, the postbuckling deformations for small radii approach the deformation pattern expected for a full cylinder. For the $[\pm 45/0_2]_s$ laminate, buckling is dominated by circumferential strains that are not similar to full cylinders.

• The effects of combined loading are considered by simulating the loading of panels either with end-shortening followed by temperature change or with temperature change followed by end-shortening. Panels loaded by either sequence reach the same solution (load and deformation pattern) for the same loading combinations, although the response path to reach that solution may be notably different.

6.1.2 Lessons Learned From Conducting Experiments

While conducting elevated temperature experiments and attempting correlation to previously conducted analyses, the following lessons were learned that may aid in future elevated temperature testing:

• Axial displacement occurs during thermal loading due to drift of the load frame platen and thermal expansion of the steel fixtures. Although other types of equipment may have eliminated the platen drift, thermal expansion of steel supports is inevitable. The resulting axial displacement affects the panel response. Three methods have been suggested for determining this axial displacement using a combination of measured and calculated quantities.

- For the specific heating arrangement chosen, thermal gradients occurred in the panel with a maximum temperature difference between the hottest and coldest points of approximately 20°F. This difference was established by 200°F and continued throughout the test. Based on analytical comparisons of models with and without the thermal gradient, this gradient was found to have a negligible effect of the load vs. axial strain response of the panel.

- Boundary conditions along the curved ends are difficult to determine during thermal testing. Comparison to analytical results suggests that circumferential displacement occurs in the panel as a result of the thermal expansion of the steel end grips. The actual magnitude of the panel expansion was unknown for these experiments.

6.1.3 Model Refinements

The base finite element model with clamped/sliding simple supports that was originally considered for parametric studies required the following minor modifications to accurately represent experimental conditions:

- The average measured panel thickness was used, which was about 8% greater than the panel thickness originally assumed for parametric studies. Since the buckling load is approximately proportional to the thickness cubed, this thickness increase resulted in approximately a 26% increase in buckling load.

- To better match boundary conditions as they were applied by the experimental apparatus, the sliding simple supports were shifted 0.125 in. inward from the straight edges and the clamped supports were extended 0.375 in. inward from the curved ends. These changes had little effect on the buckling load, although postbuckling stiffnesses generally increased due to the shift of the sliding simple supports.

- Measured initial geometric imperfections caused a decrease in the buckling load but did not substantially alter either the prebuckling or postbuckling stiffnesses. The percent decrease in buckling load depended strongly on the particular imperfection used.

- The typical measured temperature gradient, consisting of a linear through-thickness variation of 6°F and a second order polynomial variation in the x - and θ-directions with a maximum temperature difference of 20°F, has negligible effect on the buckling load or nonlinear response.

- Sliding clamped boundary conditions along the curved ends during thermal loading improves

the correlation with experiments for $[\pm 45/0/90]_s$ and $[\pm 45/0_2]_s$ laminates, but not for $[\pm 45/90_2]_s$ laminates. Allowing the circumferential expansion of the panel to equal the thermal expansion of the steel end grips does not improve correlation with experiments. The best correlation for the $[\pm 45/90_2]_s$ laminate occurs when a small outward circumferential expansion is applied to the panels. However, the improvement over clamped supports is small, and no measure of the actual circumferential expansion is available.

6.1.4 Comparison Between Analysis and Experiment

Analytical results from the STAGS geometrically nonlinear analysis are compared to the experimental results with the following observations:

- Good agreement is obtained between the experiments and the geometrically nonlinear STAGS analyses for the overall load vs. axial strain response. To obtain this agreement, sliding clamped/sliding simple support boundary conditions are assumed during thermal loading of the $[\pm 45/0/90]_s$ and $[\pm 45/0_2]_s$ laminates, and clamped/sliding simple support boundary conditions are assumed during thermal loading of the $[\pm 45/90_2]_s$ laminates and during all mechanical loading. Model refinements and the axial displacement of the panel that occurs during thermal loading are also accounted for by the model.

- The refined STAGS model generally underpredicts the measured buckling loads, and the STAGS model that neglects measured geometric imperfections generally overpredicts the measured buckling load.

- By considering the free thermal expansion of a $[\pm 45/0_2]_s$ laminate, and noting a discontinuity in the response of the other laminates, it is suggested that the coefficients of thermal expansion of this panel material change sign at a temperature of approximately 330°F. Since these panels did not undergo the complete recommended cure cycle, this result is not necessarily expected for all structures made from IM7/5260.

6.2 Recommendations For Future Work

Although the buckling and postbuckling response of curved composite panels has been studied extensively in this work, further improvements to the effort are possible. Future work in this area can be divided into refinements to the current study, and new topics to be explored.

6.2.1 Further Refinements To This Study

The following improvements to the study could be made to further improve correlation between analysis and prediction:

- Consider imperfections in the axial direction, i.e. *u*-displacement, and include an uneven load distribution in the model. This would likely allow correlation of individual strain gage results with analytical predictions, which would be necessary in a more complex structure where failure prediction might be of interest.

- Include radial or *w*-displacement imperfections as thickness variations rather than just midsurface strain imperfections.

- Further investigate the issue of circumferential displacement along the curved ends during thermal loading, perhaps by conducting more experiments, while taking special care to instrument the specimens close to the ends.

- Measure the temperature dependent nature of the material properties of properly cured IM7/5260, and incorporate this into the analysis if necessary.

6.2.2 Related Areas To Explore

As an extension of the current work, the following might be considered as the next issues of interest, leading to the final goal of designing a high temperature composite fuselage structure:

- Consider the effects of stiffeners, particularly stiffeners with a different coefficients of thermal expansion than their adjacent skin.

- Apply additional mechanical loading schemes, including pressure loading and/or shear loading.

- Conduct additional parametric studies to determine the effects of increasing the number of layers, changing the aspect ratio of the panel to better represent the unsupported skin between stiffeners, and applying boundary conditions to represent a curved panel which is really a portion of a complete cylinder.

References

Thermal Response Review Papers

1.   Starnes, J. H. Jr., and Camarda, C. J., "Analysis and Design Technology for High-Speed Aircraft Structures," in *Computational Structures Technology for Airframes and Propulsion Systems*, NASA-CP-3142, 1992, pp. 137-172.

2.   Thorton, E. A., "Thermal Structures: Four Decades of Progress," *Proceedings of the 31st AIAA/ASME/ASCH/AHS Structures, Structural Dynamics and Materials Conference*, Long Beach, CA, 1990, pp. 794-814.

3.   Tauchert, T. R., "Thermally Induced Flexure, Buckling and Vibration of Plates," *Applied Mechanics Review*, Vol. 44, No. 8, 1991, pp. 347-360.

4.   Noor, A. K. and Burton, W. S., "Computational Models for High-Temperature Multilayered Composite Plates and Shells," *Applied Mechanics Review*, Vol. 45, No. 10, 1992, pp. 419-445.

5.   Thornton, E. A., "Thermal Buckling of Plates and Shells," *Applied Mechanics Review*, Vol 46, No. 10, 1993, pp. 485-506.

Axial Compression of Curved Panels

6.   Donnell, L. H., "A New Theory for the Buckling of Thin Cylinders Under Axial Compression and Bending," *Transactions Am. Soc. Mech. Engr.*, Vol. 56, 1934, pp. 795-806.

7.   Levy, S., "Large-Deflection Theory of Curved Sheet," NACA Technical Note 895, 1943.

8.   Leggett, D. M. A., "The Buckling of a Long Curved Panel under Axial Compression," Aeronautical Research Council, Reports and Memoranda, No. 1899, 1942.

9.   Koiter, W. T., "Buckling and Post-Buckling Behavior of a Cylindrical Panel under Axial Compression," Report S. 476, National Aeronautical Research Institute, Amsterdam, 1956.

References

10.   Tamate, O. and Sekine, H., "Postbuckling Behavior of Thin Curved Panels Under Axial Compression," *Bulletin of JSME*, Vol. 12, No. 51, 1969, pp. 415-420.

11.   Hsueh, P. S. and Chajes, A., "Buckling of Axially Loaded Cylindrical Panels," *Journal of the Engineering Mechanics Division, Proceedings of the American Society of Civil Engineers*, Vol. 97, No. EM3, 1971, pp. 919-933.

12.   Wilkins, D. J., "Compression Buckling Tests of Laminated Graphite-Epoxy Curved Panels," *AIAA Journal*, Vol. 13, No. 4, April 1975, pp. 465-470.

13.   Wilkins, D. J., "Anisotropic Curved Panel Analysis," Report FZM-5567, General Dynamics, Fort Worth, TX, May 1973.

14.   Soldatos, K. P., and Tzivanidis, G. J., "Buckling and Vibration of Cross-Ply Laminated Circular Cylindrical Panels," *Journal of Applied Mathematics and Physics*, Vol. 33, 1982, pp. 230-239.

15.   Soldatos, K. P., "Buckling of Axially Compressed Antisymmetric Angle-Ply Laminated Circular Cylindrical Panels According to a Refined Shear Deformable Shell Theory," ASME PVP 124, 1987, pp. 63-71

16.   Whitney, J. M., "Buckling of Anisotropic Laminated Cylindrical Panels," *AIAA Journal*, Vol. 22, No. 11, 1984, pp. 1641-1645.

17.   Reddy, J. N. and Liu, C. F., "A Higher-Order Shear Deformation Theory of Laminated Elastic Shell," *International Journal of Engineering Science*, Vol. 23, 1985, pp. 319-330.

18.   Sanders, J. L. Jr., "An Improved First-Approximation Theory for Thin Shells," NASA TR R-24, 1959.

19.   Palazotto, A. N. and Linnemann, P. E., "Vibration and Buckling Characteristics of Composite Cylindrical Panels Incorporating the Effects of a Higher Order Shear Theory," *International Journal of Solids and Structures*, Vol. 28, No. 3, 1991, pp. 341-361.

20.   Hui, D., "Asymmetric Postbuckling of Symmetrically Laminated Cross Ply, Short Cylindrical Panels Under Compression," *Composite Structures*, Vol. 3, 1985, pp. 81-95

21.   Satyamurthy, K., Khot, N. S. and Bauld, N. R., "An Automated, Energy-Based, Finite-Difference Procedure for the Elastic Collapse of Rectangular Plates and Panels," *Computers and Structures*, Vol. 11, 1980, pp. 239-249.

References

22.   Bauld, N. R., Jr., and Khot, N. S., "A Numerical and Experimental Investigation of the Buckling Behavior of Composite Panels," *Computers and Structures*, Vol. 15, No. 4, 1982, pp. 393-403.

23.   Khot, N. S. and Bauld, N. R., Jr., "Further Comparison of the Numerical and Experimental Bucking Behaviors of Composite Panels," *Computers and Structures*, Vol. 17, No. 1, 1983, pp. 61-68.

24.   Becker, M. L., Palazotto, A. N. and Khot, N. S., "Experimental Investigation of the Instability of Composite Cylindrical Panels," *Experimental Mechanics*, Vol. 22, No. 10, Oct. 1982, pp. 372-376.

25.   Zhang, Y. and Matthews, F. L., "Postbuckling Behavior of Cylindrically Curved Panels of Generally Layered Composite Materials with Small Initial Imperfections of Geometry," *Composite Structures 2*, edited by I. H. Marshall, 1983, pp. 428-441.

26.   Zhang, Y. and Matthews, F. L., "Large Deflection Behavior of Simply Supported Laminated Panels Under In-Plane Loading," *Journal of Applied Mechanics*, Vol. 52, Sept. 1985, pp. 553-558.

27.   Snell, M. B. and Morley, N. T., "The Compression Buckling Behavior of Highly Curved Panels of Carbon Fibre Reinforced Plastic," *Proceedings of the Fifth International Conference on Composite Materials ICCM-V*, 1985, pp. 1327-1354.

28.   Kobayashi, S., Sumihara, K., and Koyama, K., "Compressive Buckling Strength of Graphite-Epoxy Laminated Curved Panels," *Proceedings of the 15th Congress of the International Council of the Aeronautical Sciences*, 1986, pp. 244-254, ICAS-86-4.2.2.

29.   Knight, N. F. Jr. and Starnes, J. H. Jr., "Postbuckling Behavior of Selected Graphite-Epoxy Cylindrical Panels Loaded in Axial Compression," *Proceedings of the 27th AIAA/ASME/ASCH/AHS Structures, Structural Dynamics and Materials Conference*, 1986, pp. 142-158.

30.   Riks, E., "Progress in Collapse Analysis," *Collapse Analysis of Structures*, ASME PVP-Vol. 84, 1984, pp. 51-67.

Thermal Response of Curved Panels

31.   Mahayni, M. A., "Thermal Buckling of Shallow Shells," *International Journal of Solids and Structures*, Vol. 2, 1966, pp. 167-180.

References

32.   Birman, V., Bert, C. W. and Elishakoff, I., "Effect of Aerodynamic Heating on Deformation of Composite Cylindrical Panels in a Gas Flow," *Composite Structures*, Vol. 15, 1990, pp. 259-273.

33.   Khdeir, A. A., Rajab, M. D., and Reddy, J. N., "Thermal Effects on the Response of Cross-Ply Laminated Shallow Shells," *International Journal of Solids and Structures*, Vol. 29, No. 5, 1992, pp. 653-667.

34.   Chen, L. W. and Chen, L. Y., "Thermal Buckling of Laminated Cylindrical Plates," *Composite Structures*, Vol. 8, 1987, pp. 189-205.

35.   Chen, L. W. and Chen, L. Y., "Thermal Buckling Analysis of Laminated Cylindrical Plates by the Finite Element Method," *Computers and Structures*, Vol. 34, No. 1, 1990, pp. 71-78.

36.   Chandrashekhara, K., "Thermal Buckling of Anisotropic Laminated Cylindrically Curved Panels," *Proceedings of the 32nd AIAA/ASME/ASCH/AHS Structures, Structural Dynamics and Materials Conference*, Baltimore, MD, 1991, pp. 933-937.

37.   Chang, J. S. and Chui, W. C., "Thermal Buckling Analysis of Antisymmetric Laminated Cylindrical Shell Panels," *International Journal of Solids and Structures*, Vol. 27, No. 1, 1991, pp. 1295-1309.

38.   Huang, N. N. and Tauchert, T. R., "Large Deflections of Laminated Cylindrical and Doubly-Curved Panels Under Thermal Loading," *Computers and Structures*, Vol. 41, No. 2, 1991, pp. 303-312.

39.   Kossira, H. and Haupt, M., "Buckling of Laminate Plates and Cylindrical Shells Subjected to Combined Thermal and Mechanical Loads," J. F. Jullien, ed., Buckling of Shell Structures, on Land, in the Sea and in the Air, New York: Elsevier Applied Science, 1991, pp. 201-212.

40.   Averill, R. C. and Reddy, J. N., "Thermomechanical Postbuckling Analysis of Laminated Composite Shells," *Proceedings of the 34th AIAA/ASME/ASCH/AHS Structures, Structural Dynamics and Materials Conference*, 1993, pp. 351-360.

41.   Patlashenko, I. and Weller, T., "Cubic B-Spline Analysis of Postbuckling Behavior of Panels, Including Temperature Dependent Material Properties and Transverse Shear," *Proceedings of the 33rd AIAA/ASME/ASCH/AHS Structures, Structural Dynamics and Materials Conference*, Dallas, TX, 1992, pp. 212-218.

References

42. Librescu, L., Lin, W., Nemeth, M. P. and Starnes, J. H. Jr., "Thermomechanical Postbuckling of Geometrically Imperfect Flat and Curved Panels Taking Into Account Tangential Edge Constraints," *Journal of Thermal Stresses*, Vol. 18, 1995, pp. 465-482.

43. Madenci, E. and Barun, A., "Thermal Postbuckling Analysis of Cylindrically Curved Composite Laminates with a Hole," *International Journal for Numerical Methods in Engineering*, Vol. 37, 1994, pp. 2073-2091.

44. Noor, A. K and Starnes, J. H. Jr., "Nonlinear and Postbuckling Responses of Curved Composite Panels with Cutouts," *Proceeding of the 36th AIAA/ASME/ASCE/AHS/ASC Structures, Structural Dynamics, and Materials Conferenc*e, New Orleans, LA, 1995, pp. 2116-2144.

Thermal-Structural Testing

45. Heldenfels, R. R. and Roberts, W. M., "Experimental and Theoretical Determination of Thermal Stresses in a Flat Plate," NACA TN 2769, 1952.

46. Hill, D. W., "Buckling of a Thin Circular Cylindrical Shell Heated Along an Axial Strip," AFSOR-TN-59-1250, 1959.

47. Johns, D. J., "Local Circumferential Buckling of Thin Circular Cylindrical Shells," Collected Papers on Instability of Shell Structures - 1962, NASA TN D-1510, 1962.

48. Anderson, M. S. and Card, M. F., "Buckling of Ring-Stiffened Cylinders Under a Pure Bending Moment and a Nonuniform Temperature Distribution," NASA TN D-1513, 1962.

49. Ross, B., Mayers, J, and Jaworski, A., "Buckling of Thin Cylindrical Shells Heated Along an Axial Strip," *Experimental Mechanics*, Vol. 8, No. 8, 1965, pp. 247-256.

50. Ross, B., Hoff, N. J. and Horton, W. H., "The Buckling Behavior of Uniformly Heated Thin Circular Cylindrical Shells," *Experimental Mechanics*, Vol. 6, No. 11, 1966, pp. 529-537.

51. Bushnell, D and Smith, S., "Stress and Buckling of Nonuniformly Heated Cylindrical and Conical Shells," *AIAA Journal*, Vol. 9, No. 12, 1971, pp. 2314-2321.

52. Frum, Y. an Baruch, M., "Buckling of Cylindrical Shells Heated Along Two Opposite Generators Combined with Axial Compression," *Experimental Mechanics*, Vol. 16, No. 4, 1976, pp. 133-139.

References

53.   Ari-Gur, J., Baruch, M. and Singer, J., "Buckling of Cylindrical Shells Under Combined Axial Preload, Nonuniform Heating, and Torque," *Experimental Mechanics*, Vol. 19, 1979, pp. 406-410.

54.   Percy, W. C. and Fields, R. A., "Buckling Analysis and Test Correlation of Hat Stiffened Panels for Hypersonic Vehicles," AIAA -90-5219, 1990.

55.   Thompson, R. C. and Richards, W. L., "Thermal-Structural Panel Buckling Tests," NASA-TM-104243, 1991.

56.   Thorton, E. A., Coyle, M. F. and McLeod, R. N., "Experimental Study of Plate Buckling Induced by Spatial Temperature Gradients," *Proceedings of the 33rd AIAA/ASME/ASCH/ AHS Structures, Structural Dynamics and Materials Conference*, Dallas, TX, 1992, pp. 1038-1051.

Computational Aids

57.   Brogan, F. A., Rankin, C. C., and Cabiness, H. D., *STAGS User Manual*, LMSC PO32594, Lockheed Palo Alto Research Laboratory, Palo Alto, CA, March 1994.

58.   Wolfram, S., *Mathematica: A System for Doing Mathematics by Computer, 2nd Ed.*, Addison-Wesley Publishing Co., Redwood, CA, 1991.

59.   IMSL MATH/Library User's Manual, IMSL inc., Houston, TX, 1987.

60.   More, J., Garbow, B., and Hillstrom, K., *User Guide for MINIPACK-1*, Argonne National Labs Report AND-80-74, Argonne, IL, 1980.

61.   Rankin, C. C. and Brogan, F. A., "An Element-Independent Corotational Procedure for the Treatment of Large Rotations," *Collapse Analysis of Structures*, ASME PVP-Vol. 84, 1984, pp. 85-100.

62.   Rankin, C. C., and Brogan, F. A., "Computational Structural Mechanics Testbed Structural Element Processor ES5: STAGS Shell Element," NASA CR-4358, May 1991.

General Topics

63.   Brush, D. O. and Almorth, B. O., *Buckling of Bars, Plates, and Shells*, McGraw-Hill, Inc., 1975.

References

64. Yamaki, N., *Elastic Stability of Circular Cylindrical Shells*, Elsevier Science Publishers B. V., Amsterdam, The Netherlands, 1984.

65. Waters, W. A. and Sikora, J., personal communication, Sept. 1994.

Appendix A - Convergence of the Rayleigh-Ritz Solution

Convergence of the geometrically nonlinear Rayleigh-Ritz solution is based on the calculated difference between the approximate solution and a solution perceived as exact. An actual exact solution was not available for this problem, which is why the Rayleigh-Ritz method was used. Instead of an exact solution, a Rayleigh-Ritz solution is used that has a very high number of terms in the assumed displacement series. Convergence is determined when the difference between this solution and a more approximate solution, one with fewer terms in the displacement series, is sufficiently small and unchanging.

Displacements were calculated from the Rayleigh-Ritz coefficients every 1/2 in. over the surface of the panel. Displacements are given by

$$u°(x, \theta) = \frac{x\Delta u}{a} + \sum_{i=1}^{2N}\sum_{j=0}^{2N} U_{ij}^c \sin\left(\frac{i\pi x}{a}\right)\cos\left(\frac{j\pi\theta}{\beta}\right) + \sum_{i=1}^{2N}\sum_{j=1}^{2N} U_{ij}^s \sin\left(\frac{i\pi x}{a}\right)\sin\left(\frac{j\pi\theta}{\beta}\right)$$

$$v°(x, \theta) = \sum_{i=1}^{2N}\sum_{j=0}^{2N} V_{ij}^c \sin\left(\frac{i\pi x}{a}\right)\cos\left(\frac{j\pi\theta}{\beta}\right) + \sum_{i=1}^{2N}\sum_{j=1}^{2N} V_{ij}^s \sin\left(\frac{i\pi x}{a}\right)\sin\left(\frac{j\pi\theta}{\beta}\right)$$

$$w°(x, \theta) = \sum_{i=1}^{N}\sum_{j=1}^{N} W_{ij}\left[\cos\left(\frac{(i-1)\pi x}{a}\right) - \cos\left(\frac{(i+1)\pi x}{a}\right)\right]\sin\left(\frac{j\pi\theta}{\beta}\right),$$

(A.1)

for clamped/sliding simple supports, and by

$$u°(x, \theta) = \frac{x\Delta u}{a} + \sum_{i=1}^{2N}\sum_{j=0}^{2N} U_{ij}^c \sin\left(\frac{i\pi x}{a}\right)\cos\left(\frac{j\pi\theta}{\beta}\right)$$

$$v°(x, \theta) = \sum_{i=1}^{2N}\sum_{j=1}^{2N} V_{ij}^s \sin\left(\frac{i\pi x}{a}\right)\sin\left(\frac{j\pi\theta}{\beta}\right)$$

$$w°(x, \theta) = \sum_{i=1}^{N}\sum_{j=1}^{N} W_{ij}\left[\cos\left(\frac{(i-1)\pi x}{a}\right) - \cos\left(\frac{(i+1)\pi x}{a}\right)\right]\sin\left(\frac{j\pi\theta}{\beta}\right),$$

(A.2)

for clamped/fixed simple supports. The displacement solutions for $N = 5$ in Eqs. (A.1) and (A.2) were used for comparison to the solutions for $N = 4, 3, 2$ and 1, except for the case of $[\pm 45/0_2]_s$ laminate with clamped/fixed simple supports, where the $N = 7$ solution was used for comparison. The errors in the displacement solutions are given by

$$u \;\; error = \sqrt{\frac{\sum (u_{N=5} - u)^2}{\sum (u_{N=5})^2}} \; , \tag{A.3}$$

$$v \;\; error = \sqrt{\frac{\sum (v_{N=5} - v)^2}{\sum (v_{N=5})^2}} \; , \tag{A.4}$$

$$w \;\; error = \sqrt{\frac{\sum (w_{N=5} - w)^2}{\sum (w_{N=5})^2}} \; , \tag{A.5}$$

where u, v, and w represent displacement solutions for $N = 4, 3, 2$, and 1. These errors are shown graphically in Fig. A-1 for clamped/sliding simple supports and Fig. A-2 for clamped/fixed simple supports.

Note that Fig. A-1(f), representing the thermal loading of the $[\pm 45/0_2]_s$ laminate with clamped/ sliding simple supports, has a maximum of $N = 5$ terms. Recall from Chapter 3 that $N = 5$ does not represent a converged solution for this case, according to comparison with the STAGS finite element solution.

By examining Figs. A-1 and A-2, it can be seen that for mechanical loading only, errors are very small for $N = 3$, while for thermal loading the errors in the displacements are still substantial at $N = 4$. This can be attributed to the difficulty in matching u-displacement that is encountered in the thermal loading solution. For the mechanical loading solution, u-displacement is dominated by $(x/a)\Delta u$, representing the overall inplane deformation of a panel of length a due to an end displacement Δu. This provides a very good approximation even for $N = 1$.

Comparing Fig. A-1 for clamped/sliding simple supports with Fig. A-2 for clamped/fixed simple supports, the convergence of the v-displacement is generally seen to be much faster when v is fixed along the straight edges, as in Fig. A-2. An exception to this is the thermal loading of the $[\pm 45/0_2]_s$ laminate with clamped/fixed simple supports, Fig. A-2(f), which cannot be modeled with any accuracy using fewer than $N = 3$ terms.

Appendix A - Convergence of the Rayleigh-Ritz Solution

(a) Convergence of [±45/0/90]$_s$, Δu=-0.0035 in.

(b) Convergence of [±45/0/90]$_s$, ΔT=300°F

(c) Convergence of [±45/90$_2$]$_s$, Δu=-0.0070 in.

(d) Convergence of [±45/90$_2$]$_s$, ΔT=200°F

(e) Convergence of [±45/0$_2$]$_s$, Δu=-0.0015 in.

(f) Convergence of [±45/0$_2$]$_s$, ΔT=300°F
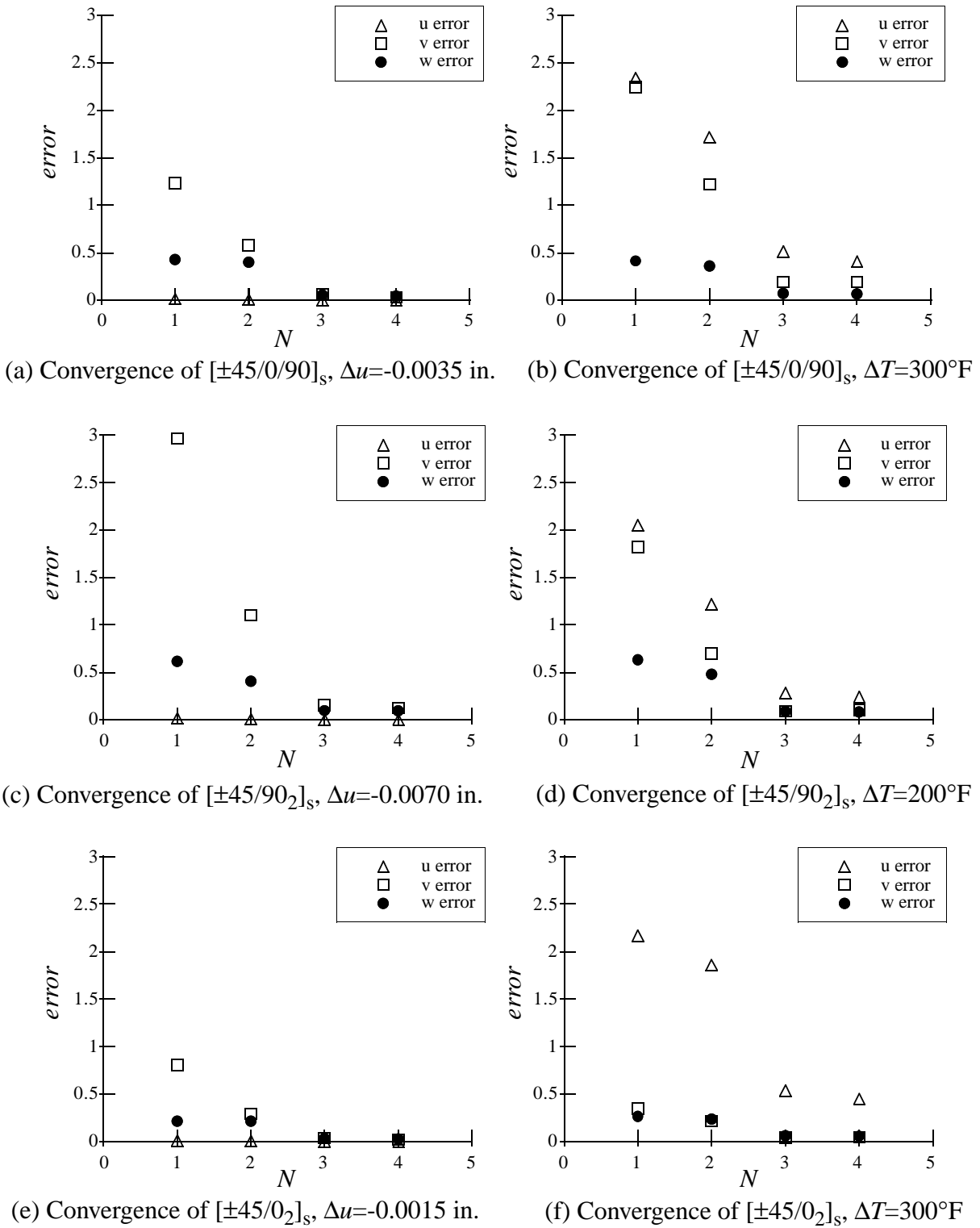
Figure A-1 Convergence of Rayleigh-Ritz solution, clamped/sliding simple supports

Appendix A - Convergence of the Rayleigh-Ritz Solution
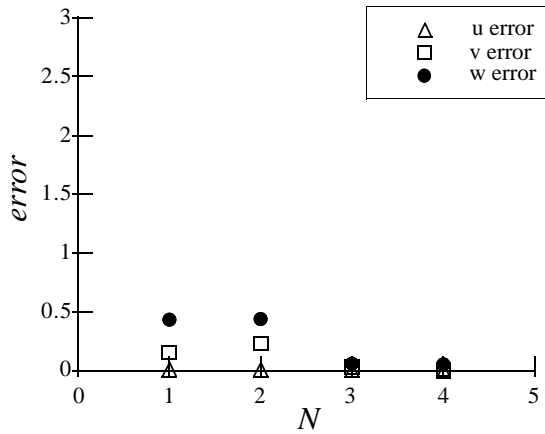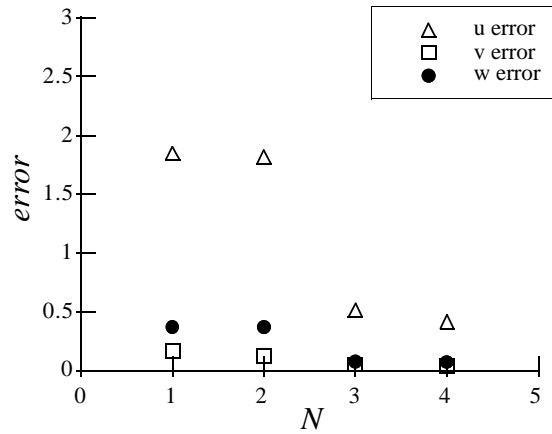
(a) Convergence of $[\pm45/0/90]_s$, Δu=-0.0035 in.

(b) Convergence of $[\pm45/0/90]_s$, ΔT=300°F
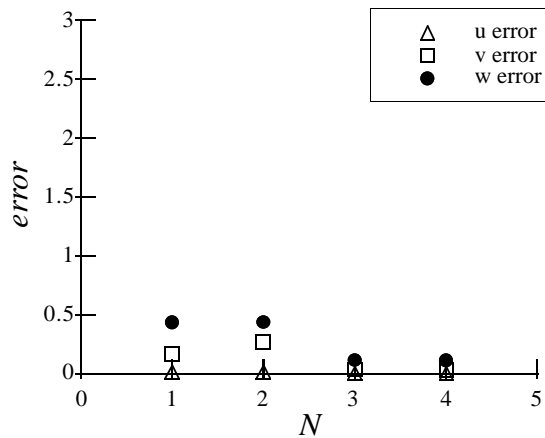
(c) Convergence of $[\pm45/90_2]_s$, Δu=-0.0070 in.
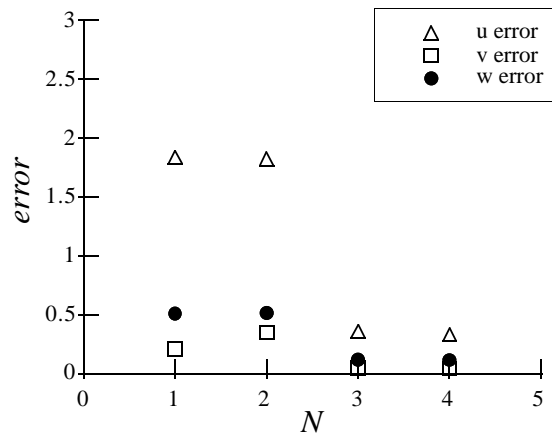
(d) Convergence of $[\pm45/90_2]_s$, ΔT=200°F
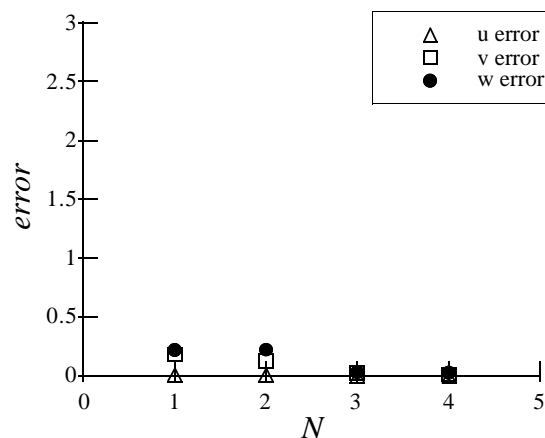
(e) Convergence of $[\pm45/0_2]_s$, Δu=-0.0015 in.
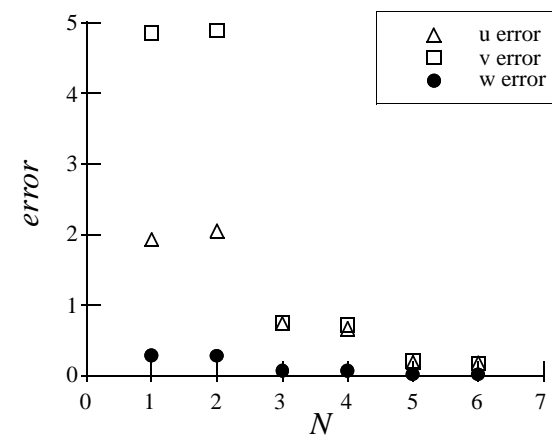
(f) Convergence of $[\pm45/0_2]_s$, ΔT=300°F

Figure A-2 Convergence of Rayleigh-Ritz solution, clamped/fixed simple supports

Appendix B - Measured Imperfections

Specimens were installed in the curved panel compression test fixture for measurement of surface imperfections. The surface imperfections of the specimens were measured every 0.125 in. along the axial and circumferential directions, with measurements taken on both the inside radius and outside radius surfaces of the panels. Subtracting the inside surface measurements from the outside surface measurements yielded a thickness measurement. The average thickness for each specimen was used in the STAGS analysis. These average measured thicknesses are given in Table B-1. The corner displacement listed in Table B-1 is a measure of the initial warpage

Table B-1 Panel designation and measured panel geometry

	Panel Number	Test Number	Average Measured Thickness, in.	Corner Displacement, in.
$[\pm45/0/90]_\mathrm{s}$	1	Q1 and Q4	0.0431	0.192
	2	Q2	0.0430	0.106
	3	Q3	0.0431	0.108
$[\pm45/90_2]_\mathrm{s}$	4	N1	0.0428	0.102
	5	N2	0.0428	0.072
	6	N3	0.0432	0.098
	7	N4	0.0429	0.039
$[\pm45/0_2]_\mathrm{s}$	8	Z1	0.0429	0.085
	9	Z3	0.0425	0.096
	10	Z2 and Z4	0.0428	0.115

observed in the panels at room temperature, before they were installed in the curved panel compression test fixture. When three corners of a panel were held against a flat surface, the corner displacement was measured as the maximum deflection of the other corner of the panel, at $x = a$ and

Appendix B - Measured Imperfections

$\theta = 0$. Proper installation of the panels in the compression test fixture required the four corners of the panels to be planar, so a warpage measurement was not intentionally included in the surface imperfection measurements.

Imperfections were incorporated into STAGS by representing the measured imperfections as a double Fourier series. At each measurement point, an average of the inside and outside imperfections was used to estimate the imperfection at the midsurface. The Fourier series representation of the midsurface imperfection was calculated using a trapezoid rule for numerical integration. The Fourier series was in the form

$$\overline{w}(x, \theta) = \sum_{n=0}^{n_{max}} \sum_{m=0}^{m_{max}} A_{mn} \cos\left(\frac{m\pi(x - x_0)}{a}\right) \cos\left(\frac{n\pi(\theta - \theta_0)}{\beta}\right), \tag{B.1}$$

where (x_o, θ_o) is the origin of the imperfection data. Imperfections beyond the region of measurement, including the portions of the specimens inside of the end grips and beyond the knife edge supports, were assumed to be the same as the nearest measured point.

Since the measured imperfection data included surface roughness due to a porous release cloth in the manufacturing process, a limited number of terms were included in the Fourier series to filter out the unwanted surface effects. Due to the relatively large size of the elements, approximately 0.45 in. square, compared to the 0.125 in. grid of measurement points, too much accuracy in the Fourier representation could result in a choppy or discontinuous finite element representation. A series with $n_{max} = 6$ and $m_{max} = 14$ was found to give satisfactory results, based on an error calculation given by

$$error = \sqrt{\frac{\sum (w_{measured} - \overline{w})^2}{\sum (w_{measured})^2}} \tag{B.2}$$

where the summation is taken over the total number of measurement points. The error for $n_{max} = 6$ and $m_{max} = 14$ was sufficiently small for all of the panels, and showed little improvement when additional terms were added to the Fourier approximation.

The measured imperfections and the Fourier approximation as incorporated into STAGS are shown in Figs. B-1 through B-12. The radial imperfection is normalized by the layer thickness, t, where t is one-eighth of the total panel thickness.
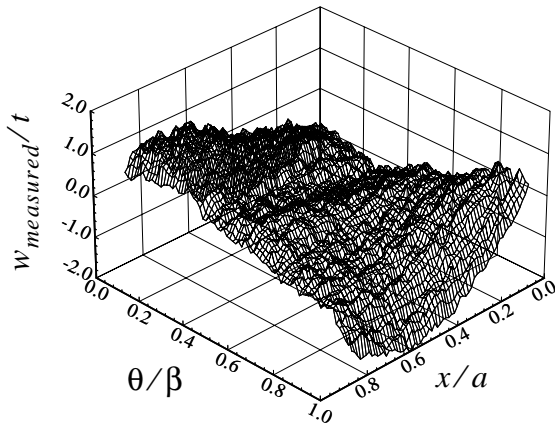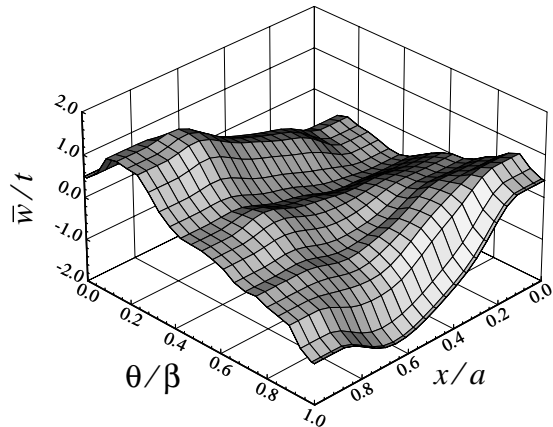
(a) Measured imperfections   (b) Approximated imperfections

Figure B-1 Geometric imperfections for panel number 1, tests Q1 and Q4, [±45/0/90]$_s$ laminate
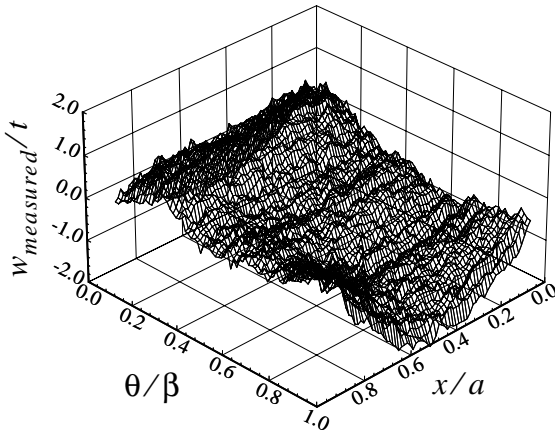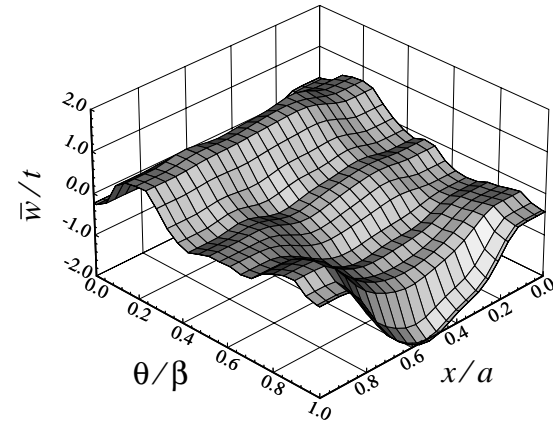
(a) Measured imperfections   (b) Approximated imperfections

Figure B-2 Geometric imperfections for panel number 2, test Q2, [±45/0/90]$_s$ laminate
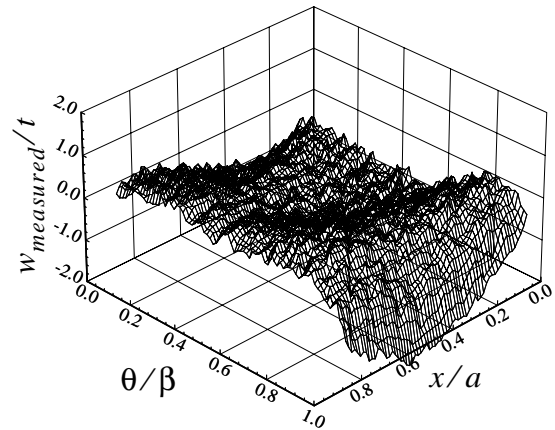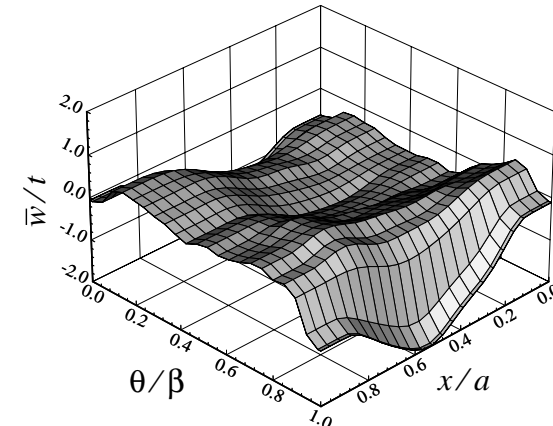
(a) Measured imperfections   (b) Approximated imperfections

Figure B-3 Geometric imperfections for panel number 3, test Q3, [±45/0/90]$_s$ laminate
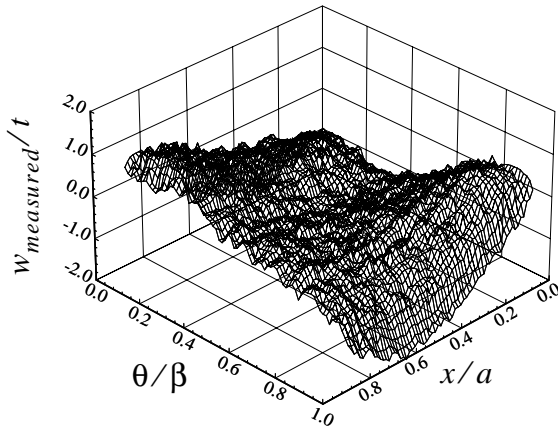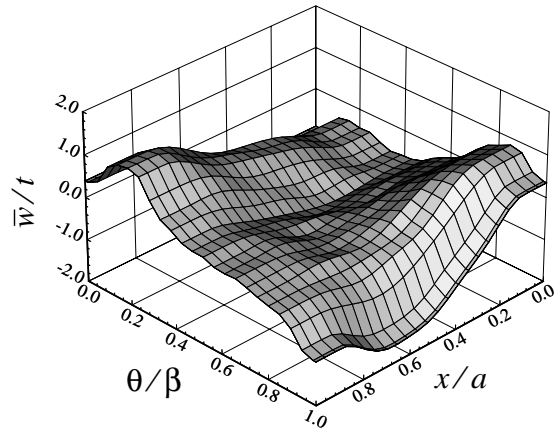
(a) Measured imperfections   (b) Approximated imperfections

Figure B-4 Geometric imperfections for panel number 4, test N1, $[\pm 45/90_2]_s$ laminate
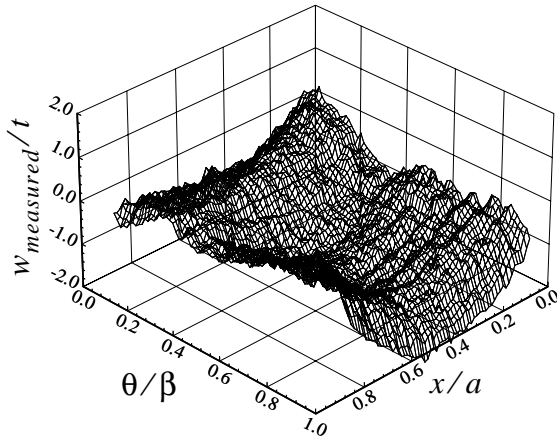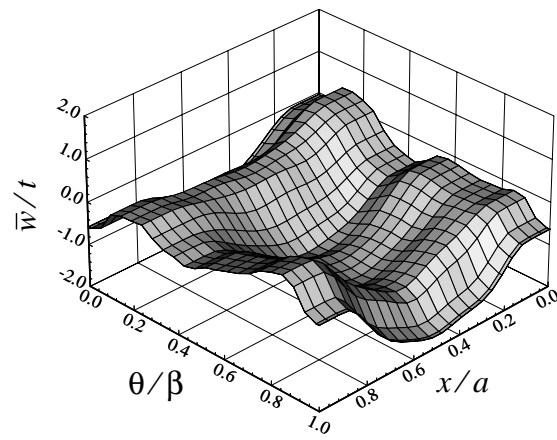
(a) Measured imperfections   (b) Approximated imperfections

Figure B-5 Geometric imperfections for panel number 5, test N2, $[\pm 45/90_2]_s$ laminate
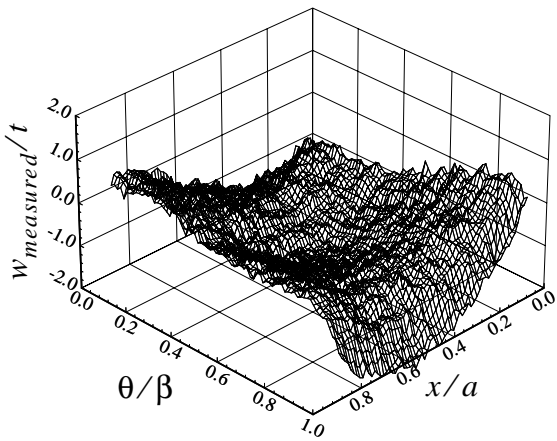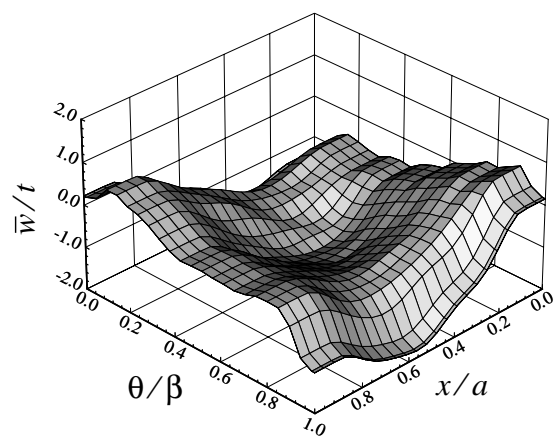
(a) Measured imperfections   (b) Approximated imperfections

Figure B-6 Geometric imperfections for panel number 6, test N3, $[\pm 45/90_2]_s$ laminate

155
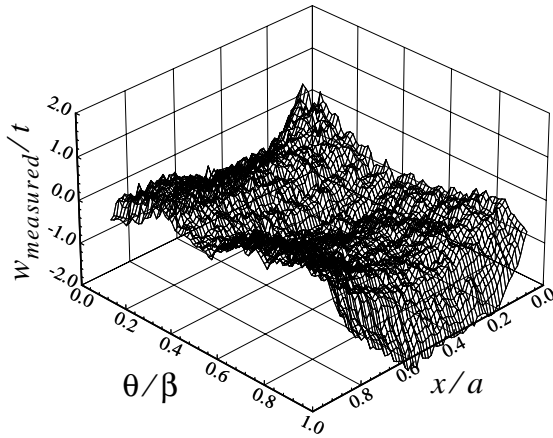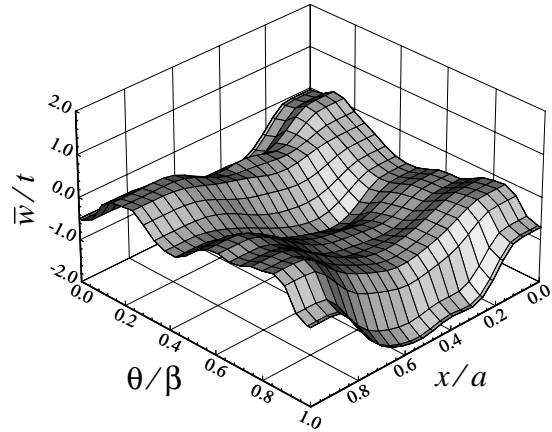
(a) Measured imperfections   (b) Approximated imperfections

Figure B-7 Geometric imperfections for panel number 7, test N4, [$\pm$45/90$_2$]$_s$ laminate
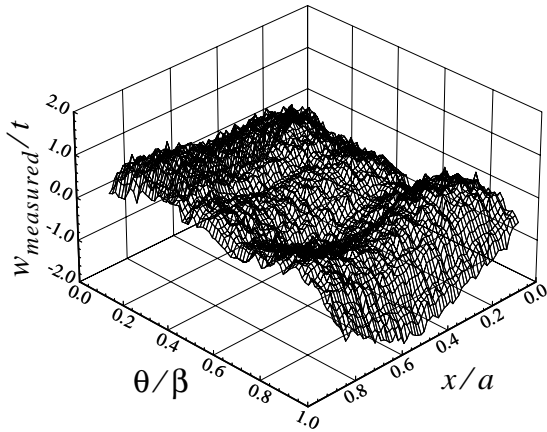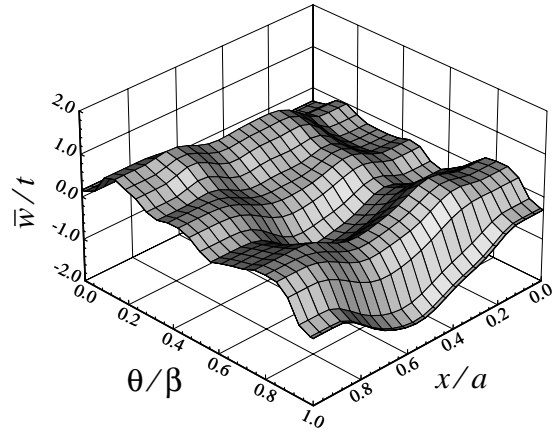
(a) Measured imperfections   (b) Approximated imperfections

Figure B-8 Geometric imperfections for panel number 8, test Z1, [$\pm$45/0$_2$]$_s$ laminate
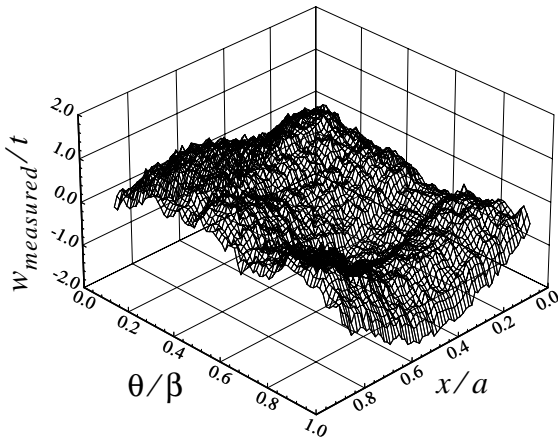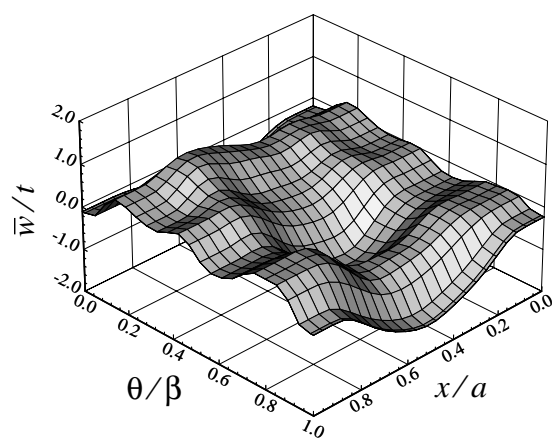
(a) Measured imperfections   (b) Approximated imperfections

Figure B-9 Geometric imperfections for panel number 9, test Z3, [$\pm$45/0$_2$]$_s$ laminate

(a) Measured imperfections   (b) Approximated imperfections

Figure B-10 Geometric imperfections for panel number 10, tests Z2 and Z4, $[\pm 45/0_2]_s$ laminate

Appendix C - Panel Cure Effects

In an effort to better understand the apparent change in material properties that occurred at a temperature of 330°F, a thermal analysis of the 5260 BMI resin system was performed. Using an edge scrap from one of the original 22 in. by 22 in. panels, a differential scanning calorimetry (DSC) test was conducted, with the results shown in Fig. C-1. A DSC test measures the amount of energy required to maintain a reference sample and the test sample at the same temperature during heating, as explained in ref. [C1]. The increase in the energy that occurred near 318°F, according to the DSC results shown in Fig. C-1, indicates that an exothermic chemical reaction began at this temperature. This behavior was unexpected, and indicates that the resin system in the panel scrap was not completely cured.
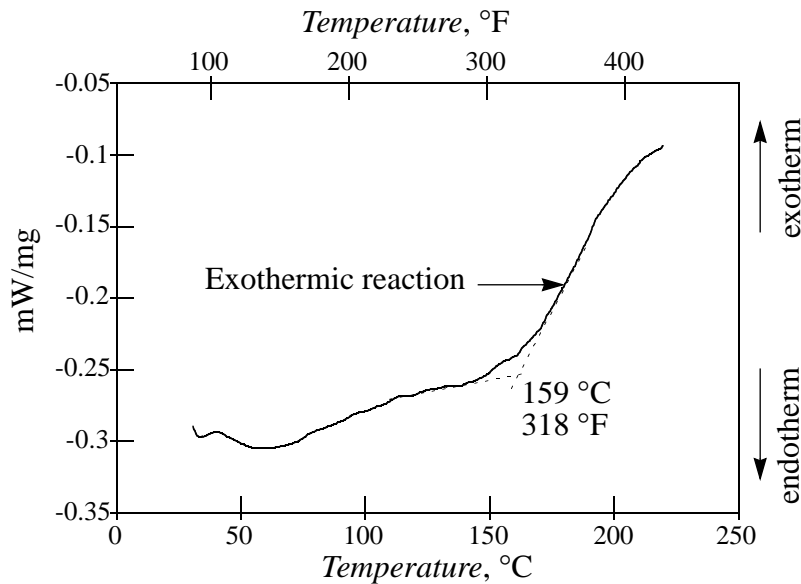
Figure C-1 DSC test result for IM7/5260 as manufactured for this study

Further investigation of the actual curing cycle used in the manufacture of these panels uncovered an error. The recommended cure cycle of the 5260 resin system is shown in Fig. C-2(a) as obtained from ref. [C2]. The actual cure cycle used to manufacture the panels used in this study is

Appendix C - Panel Cure Effects

(a) Recommended cure cycle   (b) Actual cure cycle
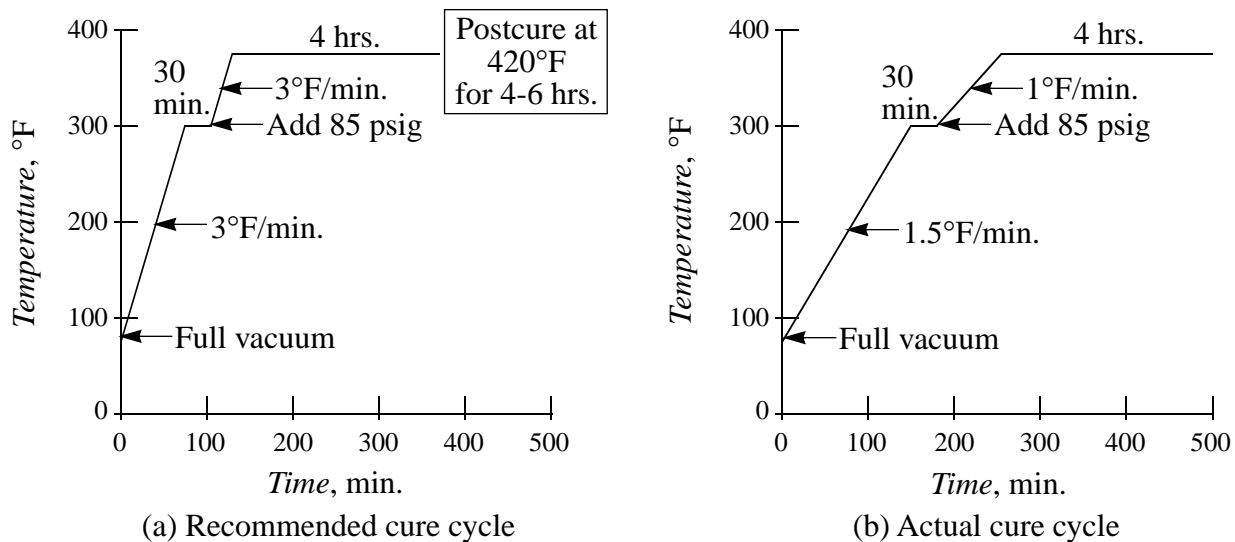
Figure C-2 Cure cycles for IM7/5260 BMI

shown in Fig. C-2(b). The panels were apparently never postcured, resulting in incomplete curing of the resin.

It is noted that material changes in the panel scrap began at approximately 318°F, as indicated in Fig. C-1, compared to changes at 330°F that were seen in the panels during thermal testing. This small discrepancy is likely the result of a partial postcure of the panels which occurred during instrumentation, but did not occur for the panel scrap. Namely, elevated temperature strain gages, Micromeasurements, Inc. type WK-00, were applied to the panels undergoing thermal testing. The gage adhesive was cured for 2 hours at a temperature of 250°F. Since the gages were put on in groups of 8 to 10 gages, the cure time for each panel ranged from 8 to 10 hours at a temperature of 250°F. After all of the gages were mounted, each panel was postcured for 1 hour at 375°F. The combined gage adhesive thermal curing, particularly the 1 hour postcure at 375°F, likely provided a partial postcure of the 5260 resin system of the panel that was not present in the panel scrap.

To determine definitively whether or not the panels were fully cured, one last test was conducted. A second scrap of the original panel was postcured at 420°F for 5 hours, and a DSC test was performed for comparison to the previous DSC results. The results of this test are shown in Fig. C-3, where the curve labeled "Before postcure" represents the first scrap, and the curve labeled "After postcure" represents the second scrap which has been postcured. The presence of a glass transition temperature, T_g, and the lack of an exothermic reaction in the second scrap, indicates that the first scrap was indeed not fully cured. It is therefore concluded that the apparent material property

159

changes occurring near 330°F in the panels used for thermal structural testing, which had a thermal history closely matching that of the first scrap, can be attributed to an incomplete cure cycle. Therefore, results from thermal structural tests at temperatures above approximately 318°F are specific to these particular panels with their incomplete cure cycles.
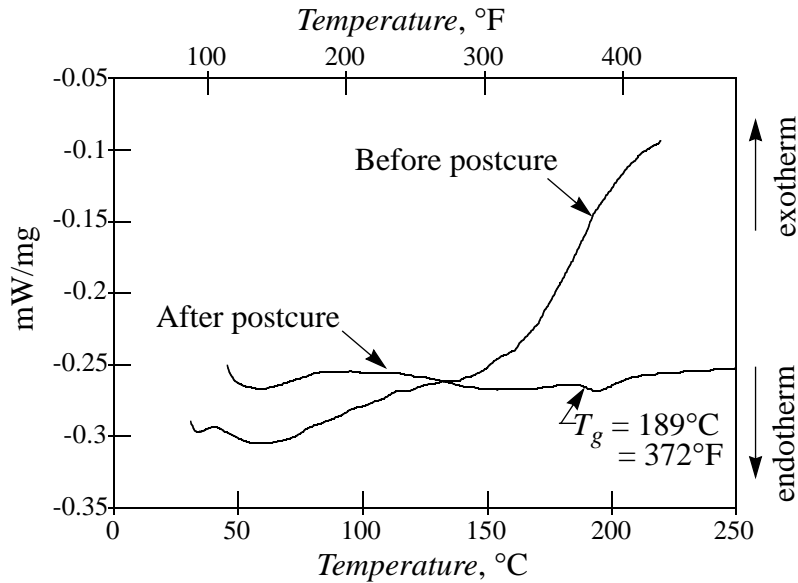
Figure C-3 DSC test result for IM7/5260 before and after postcure at 420°F for 5 hrs.

References

C1.   Sperling, L. H., Introduction to Physical Polymer Science, 2nd Ed., John Wiley & Sons, Inc., New York, 1992.

C2.   Cano, R. J. and Dow, M. B., "Properties of Five Toughened Matrix Composite Materials", NASA Technical Paper 3254, Oct. 1992.

Appendix D - Measured Temperature Gradients

Temperature gradients within the test specimens were measured using eighteen type K thermo-couples distributed evenly on the inside and outside radius surfaces of the panels, as shown in Fig. D-1. Thermocouples were located approximately 1/2 inch from the edges, and at the center of the panel. Measurements were collected once per second for the duration of the test, including the two hour heat-up cycle to bring the panels slowly to 400°F.
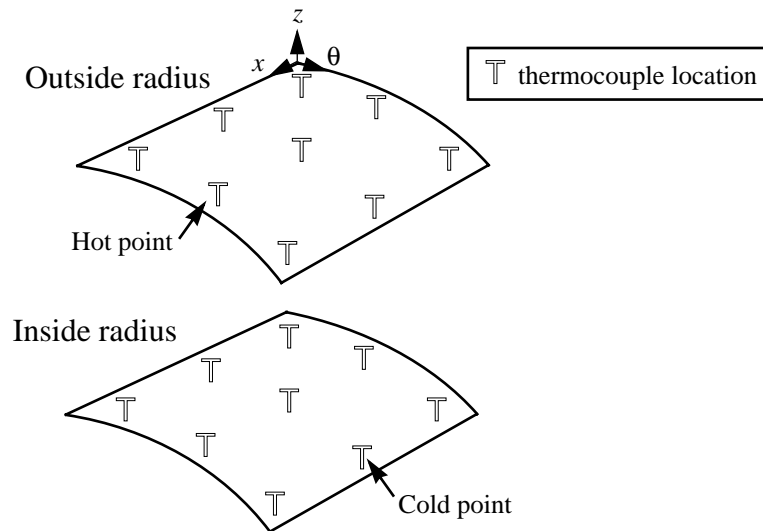
Figure D-1 Thermocouple locations for elevated temperature testing

For incorporation of the thermal gradients into the numerical analysis using the STAGS finite ele-ment package, one set of measurements was used, representing temperatures at one instant in time. The set of measurements was chosen at an average temperature of approximately 220°F. This average temperature was chosen because it was reached by all elevated temperature tests and because it allowed time for a steady temperature gradient to be established in the panels. The time vs. temperature relations for the hottest and coldest points on the panels can be seen in Figs. D-2 through D-10. The locations of the hot point and cold point are shown in Fig. D-1.

The finite element representation required a continuous thermal gradient over the surface of the panel, so that a different temperature could be considered at each nodal locations. For both the

inside and outside radius surfaces, and second order polynomial approximation was fit through the data having the form

$$\Delta T(x, \theta) = C_1 x^2 \theta^2 + C_2 x^2 \theta + C_3 x^2 + C_4 x \theta^2 + C_5 x \theta + C_6 x + C_7 \theta^2 + C_8 \theta + C_9, \qquad \text{(D.1)}$$

where the constants C_1-C_9 were determined from the nine temperature readings on each surface. The change in temperature, ΔT, represents the difference between the measured temperature and the initial room temperature. Through-thickness thermal gradients were assumed to be linear.

The approximate temperature distributions for each panel are shown in Figs. D-2 through D-10, as obtained from Eq. (D.1). The gradients remained relatively steady throughout the test, and are likely due to partially obstructed air flow and thermal shading within the insulated box. Contributors to the obstruction and shading include the knife edge support fixtures, the instrumentation wires, and the internal LVDT's.
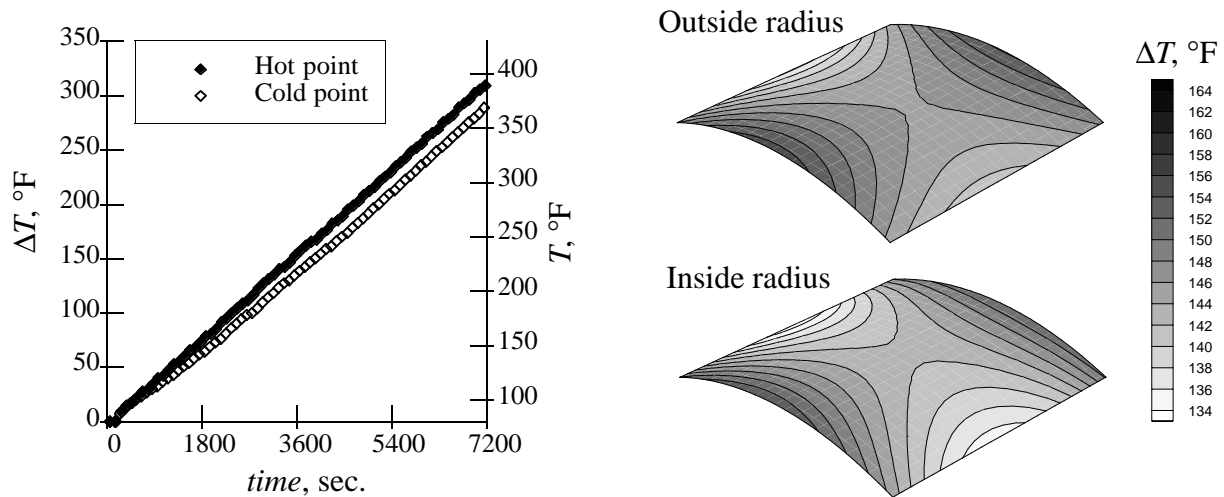
Figure D-2 Temperature distribution for test Q2, [±45/0/90]$_s$ laminate
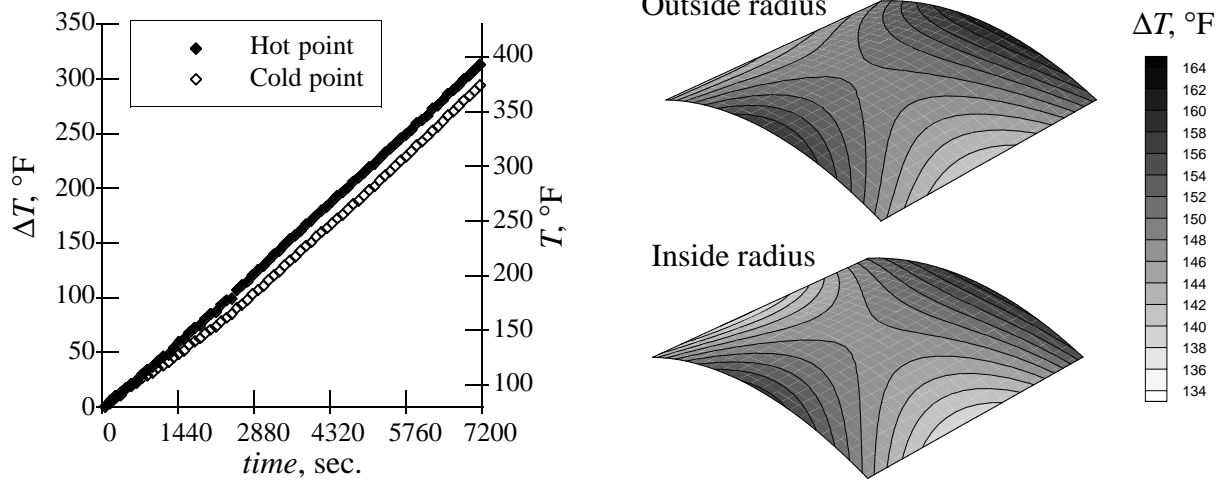
Figure D-3 Temperature distribution for test Q3, [±45/0/90]$_s$ laminate
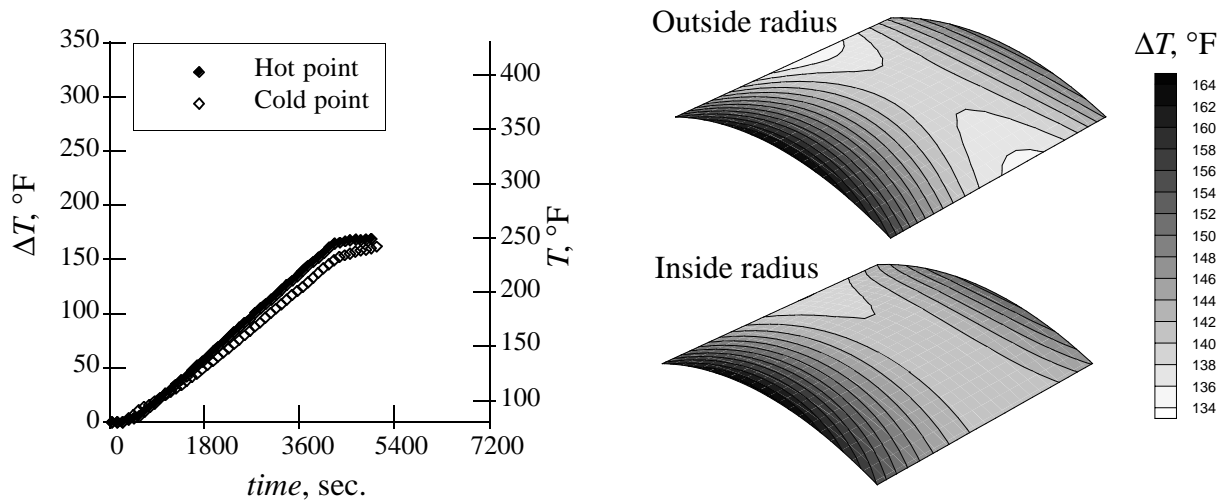
Figure D-4 Temperature distribution for test Q4, [±45/0/90]$_s$ laminate
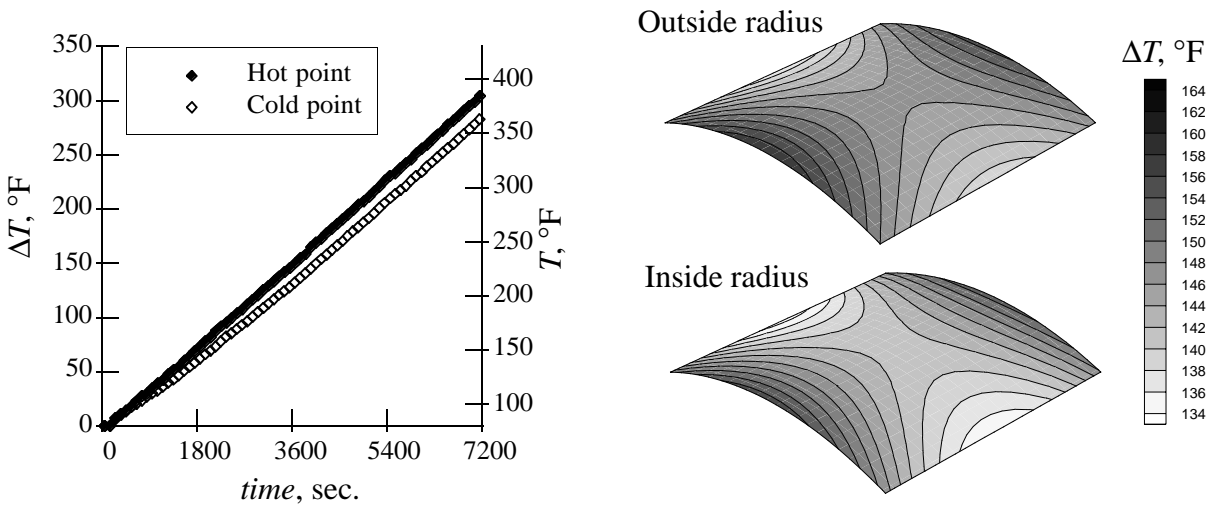
Figure D-5 Temperature distribution for test N2, [±45/90$_2$]$_s$ laminate
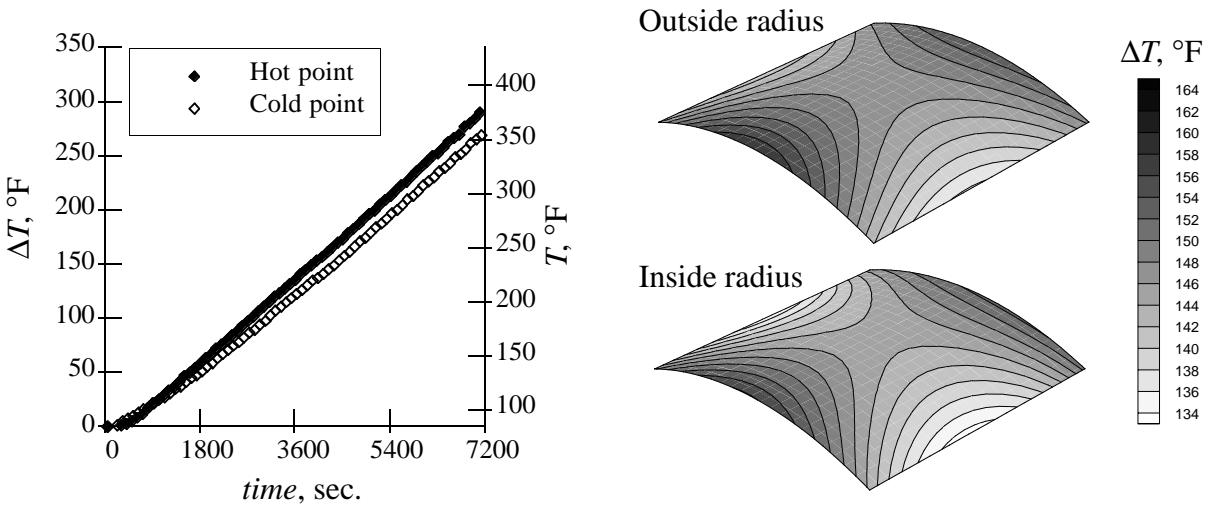
Figure D-6 Temperature distribution for test N3, [±45/90$_2$]$_s$ laminate
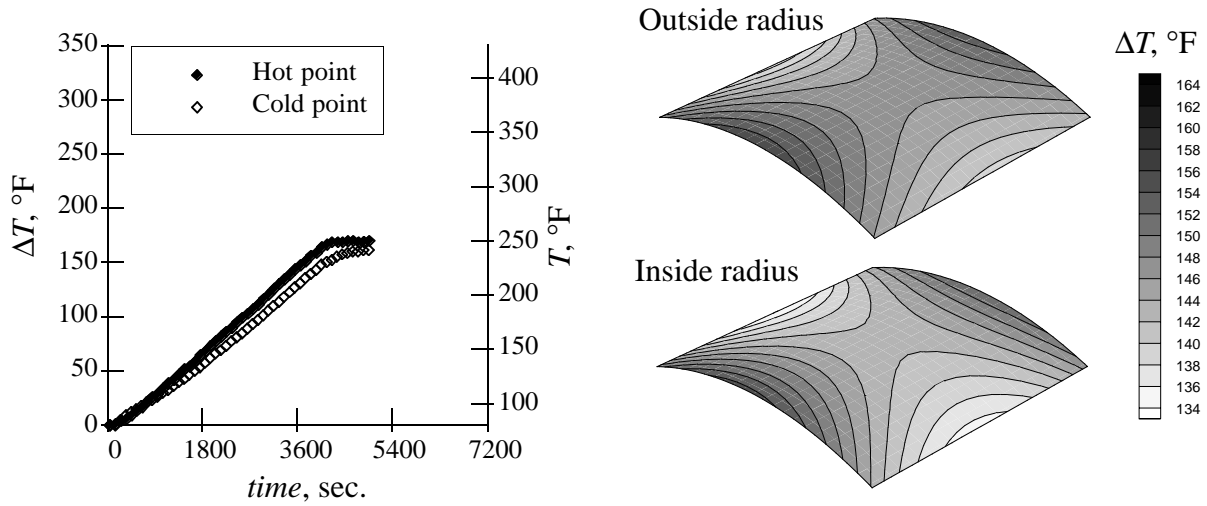
Figure D-7 Temperature distribution for test N4, [±45/90$_2$]$_s$ laminate
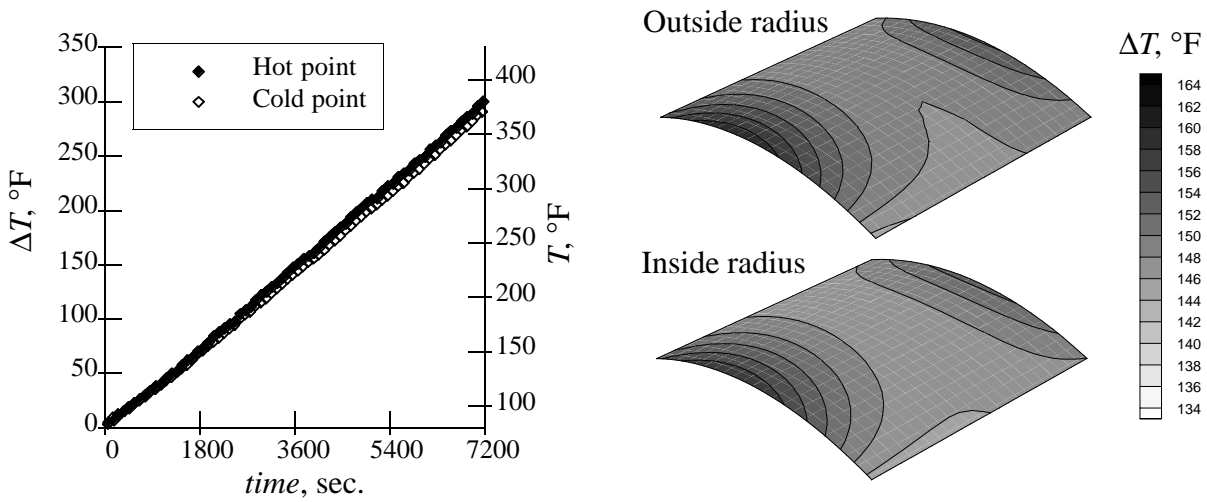
Figure D-8 Temperature distribution for test Z2, [±45/0$_2$]$_s$ laminate
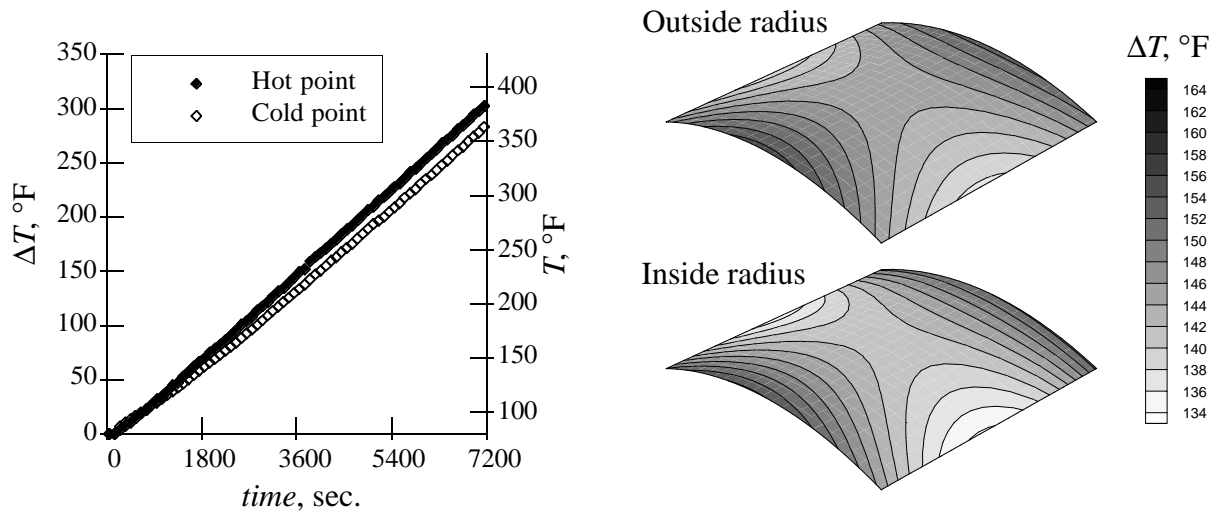
Figure D-9 Temperature distribution for test Z3, [±45/0₂]ₛ laminate
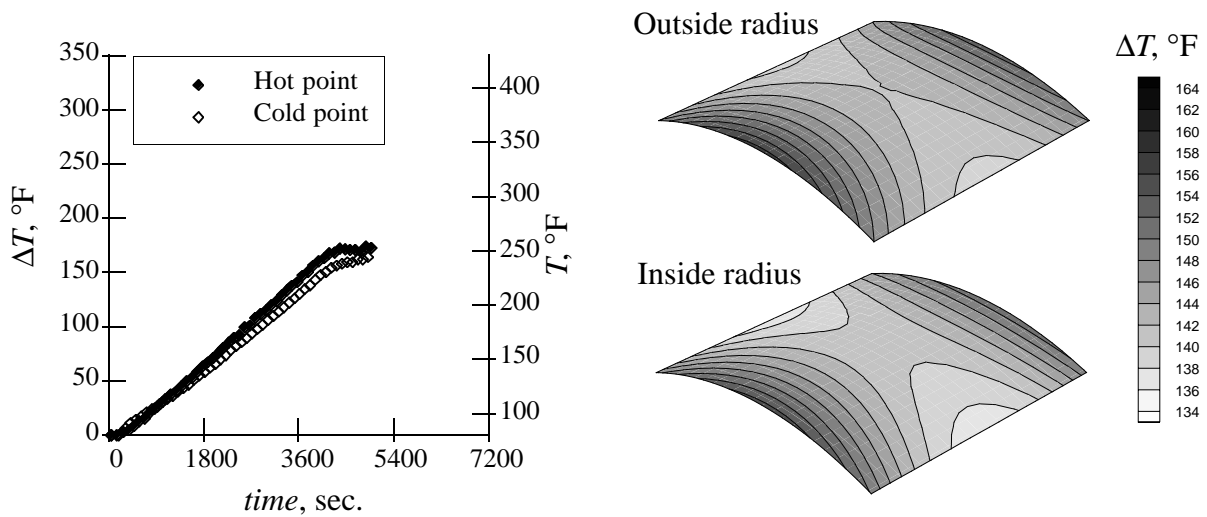
Figure D-10 Temperature distribution for test Z4, [±45/0₂]ₛ laminate

Vita

Nicole L. Breivik was born on January 24, 1967 in Duluth, Minnesota. She graduated from Duluth East High School in June 1985. She enrolled at the University of Minnesota in Minneapolis, Minnesota and completed her Bachelor of Science degree in Mechanical Engineering in December, 1989. While an undergraduate student, she participated in the cooperative education program as an employee of the Saturn Corporation in Troy, Michigan. After completion of her bachelor's degree, she began graduate studies at Virginia Polytechnic Institute and State University in the Department of Engineering Science and Mechanics. As part of her research, which was funded by the NASA Virginia Tech Composites Program, she spent a four month residency at NASA Langley Research Center in the Mechanics of Materials Branch. Upon completion of her Master of Science degree in Engineering Mechanics, she continued graduate studies at Virginia Tech, still funded by NASA Langley Research Center. A two and a half year residency was spent at NASA Langley Research Center, this time in the Structural Mechanics Branch, for completion of the research and experiments associated with her Ph.D. degree. Upon completion of this degree, she will remain at the NASA Langley Research Center as a National Research Council post-doctoral fellow in the Structural Mechanics Branch.